Design of Bumpers for Impact Resistant Gloves

By

Kendra Jade Hartley

A thesis submitted in partial fulfilment of the requirements for the degree of

Master of Science

in

MATERIALS ENGINEERING

Department of Chemical and Materials Engineering
University of Alberta

Abstract

Hand injuries, due to impact, are common workplace injuries. Many work gloves afford impact protection through design of add-on components known as bumpers. Glove design criteria are complex (e.g., limitations from human factors, dexterity, use case, hand size variability) and commercial bumpers exhibit a wide variation in their geometry, placement, colour, and material of construction. In addition, manufacturers aim to meet or exceed standards for glove testing and rating (e.g., cut, abrasion, puncture, chemical, and impact resistance).

Polymeric bumper materials simultaneously meet many design criteria (e.g., low stiffness for dexterity, manufacturing into complex geometries, high volume production, and high energy absorption on a mass basis); however, current knowledge gaps of how polymer material properties and dimensions reduce the transmitted force of impacts provided motivation for this work.

Drop testing was performed using the ANSI/ISEA 138-2019 impact standard as a guideline. Due to the multitude of variables involved, no single ideal design or material was identified. Nonetheless, insights from this work include: 1) different materials, and their local thickness and dimensions, have potential to reduce transmitted force and should be further explored; 2) a characteristic length scale (associated with the standard impact testing apparatus) was identified and produced a transition in material behaviour resulting in a dip in transmitted force; 3) the testing locations of the impact standard, when contrasted against injury statistics, should be revisited against high frequency injury locations for greater potential protection. The findings of this work culminate in a preliminary design for a prototype for future testing.

Acknowledgements

Thanks to:

Table of Contents

List of Tables

List of Figures

List of Symbols

A   Surface area (m^2)

E   Young's modulus (GPa)

F   Force (N)

F_t Transmitted Force (N)

g   Gravitational constant ($N \cdot m^2/kg^2$)

H   Shore hardness (A)

h   Thickness (m)

I   Impulse ($N \cdot s$)

I_m Second moment of inertia

KE   Kinetic Energy (J)

K   Spring constant ($N \cdot m$)

L   Length (m)

m   Mass (kg)

P   Momentum ($kg \cdot m/s$)

PE   Potential Energy (J)

S   Stiffness ($N \cdot m^2$)

tanδ Tan delta (GPa/GPa)

v   Velocity (m/s)

W   Work (J)

ρ Density (kg/m^3)

List of Abbreviations

ANSI   American National Standards Institution

ARIT   Accelerated Repeated Impact Testing

DMA   Dynamic Mechanical Analysis

FEA   Finite Element Analysis

HSV   High Speed Videography

NIOSH National Institute for Occupational Safety and Health

PE   Polyethylene

PPE   Personal Protective Equipment

PVC   Polyvinyl chloride

TPR   Thermoplastic Rubber

Chapter 1 : Introduction

1.1 Motivation: The Need for Impact Resistant Gloves

Hand injuries are common in the workplace with over 500,000 injuries occurring in Canada every year [1]. The U.S. Bureau of Labor Statistics reported that the most frequent reason for lost time injuries were those to the upper extremities, with a frequency of 346,710 cases in 2014 [2]. Approximately 40% of those injuries involved the hand. Injuries to the hand had an incident rate of 12.7 per 10,000 full time workers and a median of 5 days away from work. The frequency of the hand injuries was the second most frequent after back injuries, which had a frequency 18.5 per 10,000 full-time workers (in 2014). Many of these injuries could have been prevented, as the U.S. Bureau of Labor Statistics reported that approximately 70% of hand injuries in the workplace were due to the worker not wearing gloves [2]. The injury data shows that even with proper safety measures, such as employee safety training, there is a great need to create protection for the hands. By not wearing the gloves, the workers are jeopardizing their ability to do everyday tasks like eating, driving, and jotting down notes [3].

After cuts, crushes and fractures are the most frequent hand injuries in the workplace [4]. For industries such as mining, oil and gas, forestry, and construction, crush and fracture injuries are most likely to occur from impacts on the back (dorsal side) of the hand [5]. These injuries are classified as blunt force trauma injuries, which will be outlined in Chapter 2.

Impact resistant gloves currently used in the industry were designed to have a protective layer on the back of the hand to protect the vulnerable areas of the hand from impact. Figure 1.1 below illustrates an example of an impact resistant glove; the protective layer to protect the hand (bumper) is colored green. Until recently, there was no standard in place to evaluate the glove's effectiveness at impact protection. This absence of consensus meant that each glove manufacturing company was left to make their own judgments of where the protection was needed and how effective the protection was. A lack of regulation also left the consumer to evaluate the effectiveness of the protection by banging their knuckles against a wall with the glove on to see if it would work [6]. Such a situation was non-ideal—for the consumer or the manufacturer.

50 mm

Figure 1.1: A impact resistant glove. The bumpers (green) are used to absorb the impacts.

In 2019, the American National Standards Institution (ANSI) introduced a new ANSI/ISEA 138-2019 standard for workplace gloves to address the gaps in evaluating dorsal hand protection in the industry [7]. The standard states that each glove will be drop-tested nine times on the dorsal side of the hand; the locations and procedure for testing the gloves will be discussed in Chapter 2. The standard also specifies how much transmitted force is permitted to meet a specified performance level when a fixed mass is dropped onto the top of the material with 5 J of kinetic energy. For example, to meet the first performance level (level 1) each impact must be below 11.3 kN of transmitted force and the average of all nine impacts must be under 9 kN. As of November 2020, there are three performance levels the glove can be classified under, with level 1 being the lowest level of protection and level 3 being the highest level of protection. The details of each level are summarized in Table 1.1 below. The chance of injuring the bone for the specific level is given on the far left column [8]. Note that meeting level 3 still has a 50% chance of injuring the bone [8] (see Chapter 2 for further details).

Table 1.1: Classification for Impact Resistance. ANSI/ISEA 138-2019 impact standard [7]. The data for the % chance of injuring the bone was taken from [8].

Performance Level	Mean (kN)	All Impacts (kN)	Chance of Injuring Bone (%)
1	≤9	<11.3	99%
2	≤6.5	≤8.1	80%
3	≤4	≤5	50%

Achieving level 3, meaning that the average of all the impacts are under 4kN, has now become the "gold standard" of the industry. Thus, creating a glove that meets the new standard has become the market target for manufacturers and consumers. Finding a glove design that meets this market need is not an easy problem to solve as the variables to achieve great impact protection performance conflict with the human factors of user dexterity, comfort, cost, and manufacturability.

1.2 The Design Process

The design process for glove creation is similar to the one outlined in *Materials Selection in Mechanical Design* by Michael Ashby [9]. In the Ashby design process, a solution neutral market need is identified in order to prevent narrow thinking of preconceptions [9]. After that, all the different concepts that can meet the market need are envisioned and funneled down into a design solution. The way to funnel down the concepts is to identify the "use case" scenarios for the design which will determine the functional constraints the design has. The concepts that can meet the design constrains are then analyzed in the next stage, which is embodiment. Embodiment is the stage where materials selection and sizing of the components occur. The final step before producing a product in the Ashby method is the detail stage. The detail stage is where the specifications of the components are drafted and tested (i.e., prototyping). In addition, the final materials selection and production methods are analyzed and costed [9].

Figure 1.2 below illustrates the Ashby design process for the back of the hand protection, starting with the market need, and then funneling the solutions into a designed product. In the figure, each stage of the Ashby method for back of the hand protection is shown on the right and the correlating stage it belongs to is on the left. For back of the hand protection, the solution neutral market need is identified as a way to protect the hands from impact, as discussed in Section 1.1 of Chapter 1. One of the many concepts to protect hands from impact is to create gloves with bumpers on the back of the hand, which is discussed in detail in Chapter 2. Within the glove design concept, there are multiple

sub-concepts of the general areas of the hand the bumpers should cover. For example, it is possible to have a glove that meets the ANSI/ISEA 138-2019 standard that does not protect all the vulnerable areas of the hand (refer to Chapter 2, Section 2.7). The embodiment stage of the glove design process will look into the specific geometry of the glove (i.e., the dimensions and shape of the bumper) and the materials selection of the bumper. The embodiment stage is highlighted in Figure 1.1 as it is the primary focus of the thesis and will be the focal point of Chapters 4, and 5, as well as Appendix C. The detail stage of the design process and possible final products will be discussed in Chapter 6.
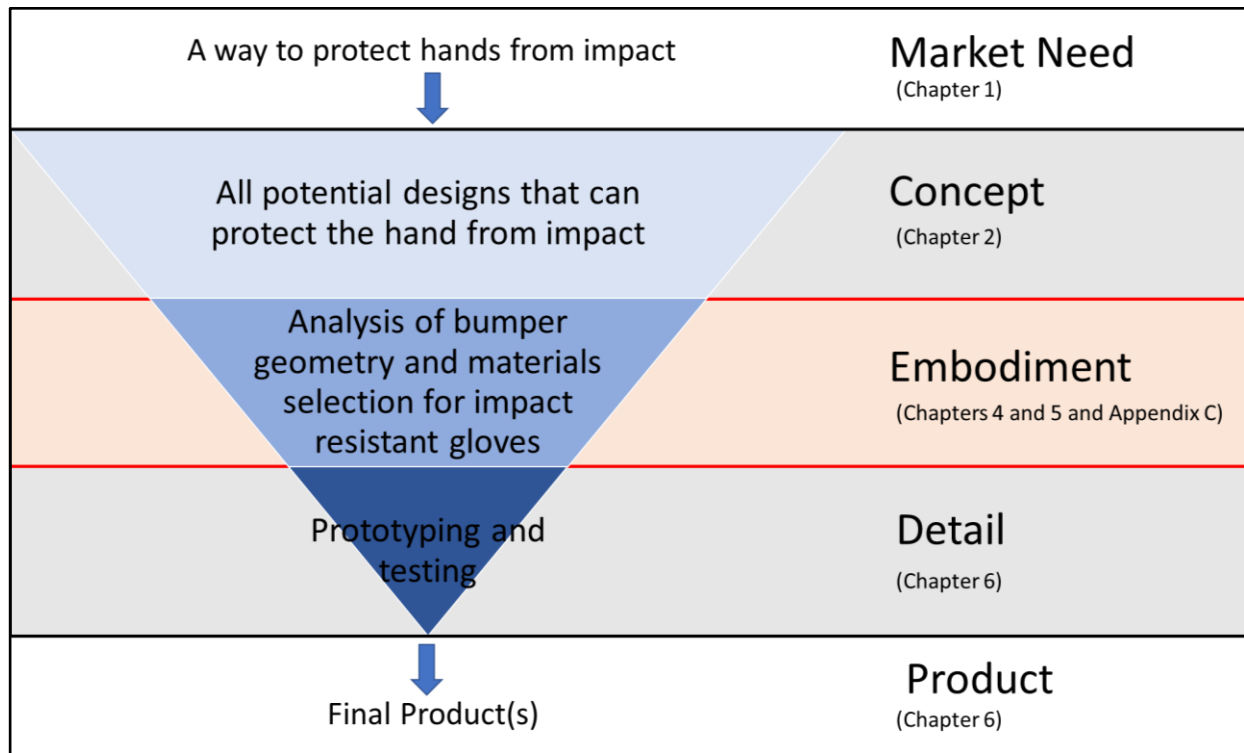
Figure 1.2: The Ashby design method applied for the design of back of the hand protection. In the Ashby design method, a market need is identified (i.e., a way to protect hands from impact). From there, all of the possible designs are funneled down into a final product through a concept, embodiment, and detail stage. The details for the glove design stage (left side) correlate with the design stage (right side). The embodiment stage is highlighted as it is the primary focus of the thesis. The figure was generated using ideas from [9].

One of the most important parts in the Ashby design method is to identify the function, constraints, objective, and free variables of the design. Identifying the design requirements provides a framework or path for the design to follow to help select a solution. Table 1.2 below shows a summary of the design requirements for the bumpers of impact resistant gloves. The table outlines the function of the gloves, the variety of performance needs of the user and producer (constraints), the wants of the user and producer (objectives), and the free variables for the design of the gloves. A more detailed table with quantitative values can be found in Chapter 2 (Table 2.4).

Table 1.2: A summary of the design criteria for the bumpers of impact resistant gloves.

Design Requirements for a Bumper on an Impact Resistant Glove	
Function	• Protect vulnerable areas of the hand from blunt force trauma
Constraints	• Transmitted Force: limited to values outlined in ANSI/ISEA 138-2019 • Stiffness: must be low enough to allow for adequate dexterity • Surface Area: must be large enough to protect vulnerable areas of the hand, but small enough to fit the hand • Durable: is flame resistant, oil resistant, water resistant and does not degrade from mechanical wear • Cost: cost of materials and production must be under $9 CAD • Temperature: maintains impact performance in a variety of temperatures • Processing: easy to process and form
Objective	• Maximize tan delta • Minimize mass • Minimize thickness
Free Variables	• Choice of material • Shape of bumper

1.2.1 Existing Solutions and Materials Used in the Market

Table 1.2 demonstrates that creating a glove design to meet all the design constraints is a complex problem with many variables—the very reason there is a proliferation of bumper designs currently used by glove manufacturers (further discussed in Chapter 2). Almost all the designs for impact resistant gloves use elastomers, a subset of polymers, or thermosets as the materials to construct the bumpers. This material selection is because elastomers and thermosets have desired mechanical behaviors (e.g., low modulus, high elasticity, and can be formed into many shapes) to meet the constraints at an economical cost [10]. One major gap of the current impact resistant glove market is that there is a lack of gloves that meet the Level 3 protection outlined in the ANSI/ISEA 138-2019 standard.

1.3 Research Questions

This research aims to identify a suitable material along with minimum dimensions for a glove bumper in order to achieve each of the levels outlined in ANSI/ISEA 138-2019 while also satisfying the human factors of the users. In order to achieve this research goal, the research questions addressed in this thesis are:

(1) Is there a material currently not used by the glove industry that can enhance the impact performance of gloves? (Chapter 4)

(2) What material should be used for the glove bumpers based on the use case of the gloves? (Chapter 4 and Chapter 5)

(3) What are the effects of thickness, surface area, and volume on reducing transmitted force? (Chapter 5)

(4) When keeping thickness consistent, when does the lateral size (surface area) of the bulk material have diminishing returns on impact performance? (Chapter 5).

(5) What is the effect of geometry on transmitted force? (Preliminary model addressed in Appendix C).

(6) How can modelling be used to accurately predict a design's ability to reduce transmitted force? (Preliminary model addressed in Appendix C).

1.4 Objectives

The work done for this thesis was in collaboration with Superior Glove Works Ltd. (Superior Glove). The primary objective for the research is to identify how material properties and dimensions can reduce the transmitted force of impacts. Achieving this objective would allow designers to have a better understanding of how to create gloves in order to achieve a certain level of protection. Identifying how to reduce transmitted force through material choice and dimensions could also give designers a starting point when they are trying to generate ideas and designs for impact resistant gloves.

The secondary objective of the research is to use the knowledge of materials and the kinematics of drop testing, in conjunction with physical testing, to develop a method to model the impact test. The desired model will be constructed using finite element analysis (FEA) software (preliminary work in Appendix C). The ideal outcome of this objective is to allow the designer to be able to predict the effectiveness of their design through modeling and running simulations before a physical prototype

is produced. Being able to predict the performance of a prototype can save the designer and developing company valuable resources, such as time and materials.

1.5 Thesis Overview

Chapter 2 provides a summary of the literature related to information the designer would need to know to create the gloves, including: details of the impact standard, kinematics of the drop test, anatomy of the hand and common impact related injuries, properties of elastomers, energy absorption of elastomers, energy absorption of different structures, and existing solutions for impact protection in various scenarios. Chapter 3 details the specific materials used for experimentation, the equipment used, and how the tests were performed. Chapter 4 describes a design approach to identify materials for use in impact resistant gloves. Analysis of the dimensional effects on transmitted force are examined in Chapter 5. Chapter 6 describes the recommendation for future tests as well as a summary of the results. The creation of a preliminary predictive numerical model is presented in Appendix C, which also includes predictions of shape effects on transmitted force.

Chapter 1 References

[1] Canada, Employment and Social Development. Our Hands at Work! 2013; Available from: https://www.canada.ca/en/employment-social-development/services/health-safety/reports/hands.html. [cited Dec 2,2019].

[2] TED: The Economics Daily. Type of injury or illness and body parts affected by nonfatal injuries and illnesses in 2014 : The Economics Daily: U.S. Bureau of Labor Statistics. Available from: https://www.bls.gov/opub/ted/2015/type-of-injury-or-illness-and-body-parts-affected-by-nonfatal-injuries-and-illnesses-in-2014.htm. [cited Nov 29,2019].

[3] 7 Dangerous Jobs That Involve Working with Your Hands. 2019; Available from: https://cestusline.com/blogs/news/dangerous-jobs-working-with-your-hands. [cited Nov 4,2020].

[4] Here are the most common work-related hand injuries. 2018; Available from: https://www.ishn.com/articles/108061-here-are-the-most-common-work-related-hand-injuries?v=preview. [cited Dec 2,2019].

[5] Olson A. Dorsal defense: Guard against impact & abrasion injuries. 2015; Available from: https://www.ishn.com/articles/100623-dorsal-defense-guard-against-impact-abarsion-injuries?v=preview. [cited Nov 3, 2020].

[6] Geng J. Everything You Need To Know About ANSI/ISEA 138 – The New Impact Standard. 2019; Available from: https://www.superiorglove.com/blog/everything-you-need-to-know-about-ansi-isea-138-the-new-impact-standard. [cited Oct 8, 2020].

[7] American national standard for performance and classification for impact resistant hand protection. . International Safety Equipment Association 2019 February.

[8] Carpanen D, Kedgley AE, Shah DS, Edwards DS, Plant DJ, Masouros SD. Injury risk of interphalangeal and metacarpophalangeal joints under impact loading. Journal of the Mechanical Behavior of Biomedical Materials 2019 September; 97:306-311.

[9] Ashby MF. Materials selection in mechanical design. 4th ed. Burlington, MA: Butterworth-Heinemann; 2011.

[10] Nielson LE, Landel RF. Mechanical properties of polymers and composites . 2nd ed. 6000 Broken Sound Parkway NW, Suite 300 Boca Raton, FL: Taylor and Francis Group; 1993

Chapter 2 : Literature Review

2.1 Introduction

The following chapter introduces the basic information needed to design impact resistant gloves. When designing the gloves to meet a specific impact standard, the designer must have knowledge of:

1. The details of the ANSI/ISEA 138-2019 standard
2. Impact mechanics
3. Anatomy of the hand
4. Common impact-related injuries
5. Relevant material properties and how they respond to impact
6. How bumper structure influences the absorption of impact energy
7. Existing products on the market
8. Impact protection strategies in similar markets (e.g., helmets)

The background knowledge associated these areas will provide a framework for the design of impact resistant gloves. Understanding the details of the standard will establish a definitive performance criterion that the gloves must meet. The mechanics of the drop testing process need to be established and mathematically broken down so that a predictive performance model could be generated. Obtaining knowledge of the anatomy of the hand and common injuries from impact determines the dimensional constraints and positioning of the bumpers in the design. Awareness of the material properties and impact response of the material will ensure that the best material is selected for the design. Knowing how the structure of the bumper influences the transmitted force will maximize the impact protection of a single material. Lastly, studying impact-related products and gloves on the market can allow for design inspiration, as well as identify knowledge gaps in the industry.

2.2 Drop Testing: Standard and Kinematics

2.2.1 ANSI/ISEA 138-2019 Standard

The ANSI/ISEA 138-2019 standard for evaluating dorsal hand protection is used to gauge the performance of impact resistant gloves at the knuckles and fingers [1]. The standard uses a vertical drop test method to test nine impact sites on a pair of size 9 or 10 gloves (size defined by EN

420:2009). Figure 2.1 illustrates the location of the nine impact sites. To determine the knuckle impact sites (red triangles), three assessors with the appropriate size hand don the glove and grip a cylindrical bar with a diameter 32 mm ± 5 mm [1]. The position of the most prominent point of the four knuckles will be marked (black dots in Figure 2.1). A triangle will be drawn between the three points and the center of the triangle will be the location of the test (drawn "x"). For the fingers, one assessor will don the glove and measure and mark three fingers 25 mm from the tip (blue solid lines in Figure 2.1) and two fingers 50 mm from the tip (blue dashed lines).
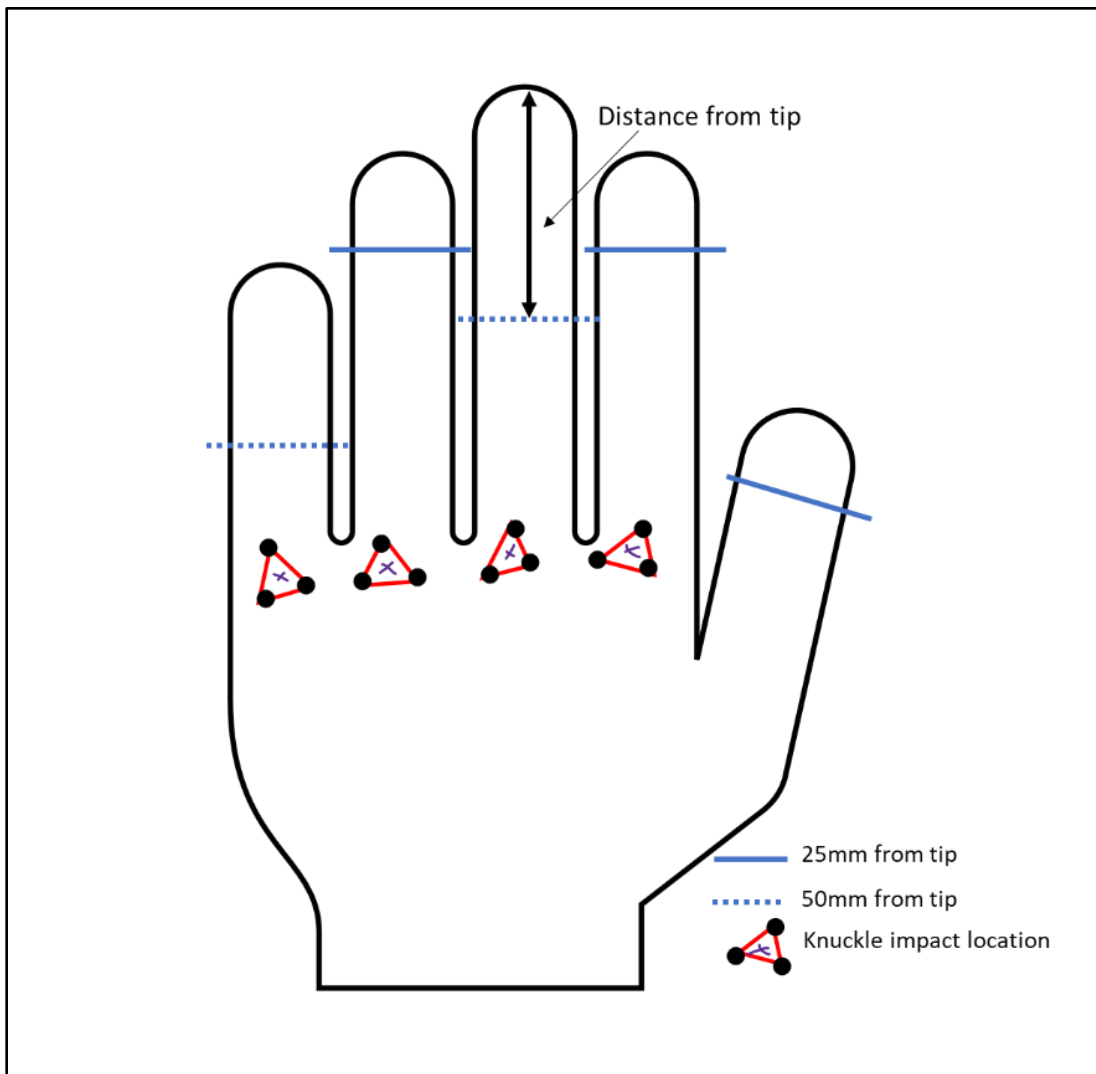
Figure 2.1: A schematic of the finger and knuckle impact locations of the ANSI standard (not to scale). Adapted from ANSI/ISEA 138-2019 [1].

Once the gloves are measured, the palm side of the glove is cut out to allow the dorsal surface to lie flat on the testing apparatus. Figure 2.2 displays a glove that has been prepared for testing with the

palm removed. The locations of the testing were marked with a permanent marker (one location site is indicated with a red arrow).

Figure 2.2: A glove specimen prepared for testing. The impact test sites have been marked (red arrow indicates one marking) for testing and the glove has been cut open to allow the glove to lie flat on the apparatus.

A simple schematic of the testing apparatus is shown in Figure 2.3 (a) (not to scale). The testing apparatus consists of an anvil mounted to a load sensor to measure the transmitted force, and a striker that has a guided vertical path so that the center of the falling mass coincides with the center axis of the anvil [1]. The dimensional specifications for the anvil are also shown in Figure 2.3 (b). The standard states that the mass of the striker (including the part that guides the striker) must be 500 g ± 10 g and the anvil and transducer assembly must be attached to a minimum mass of 500 kg [1].
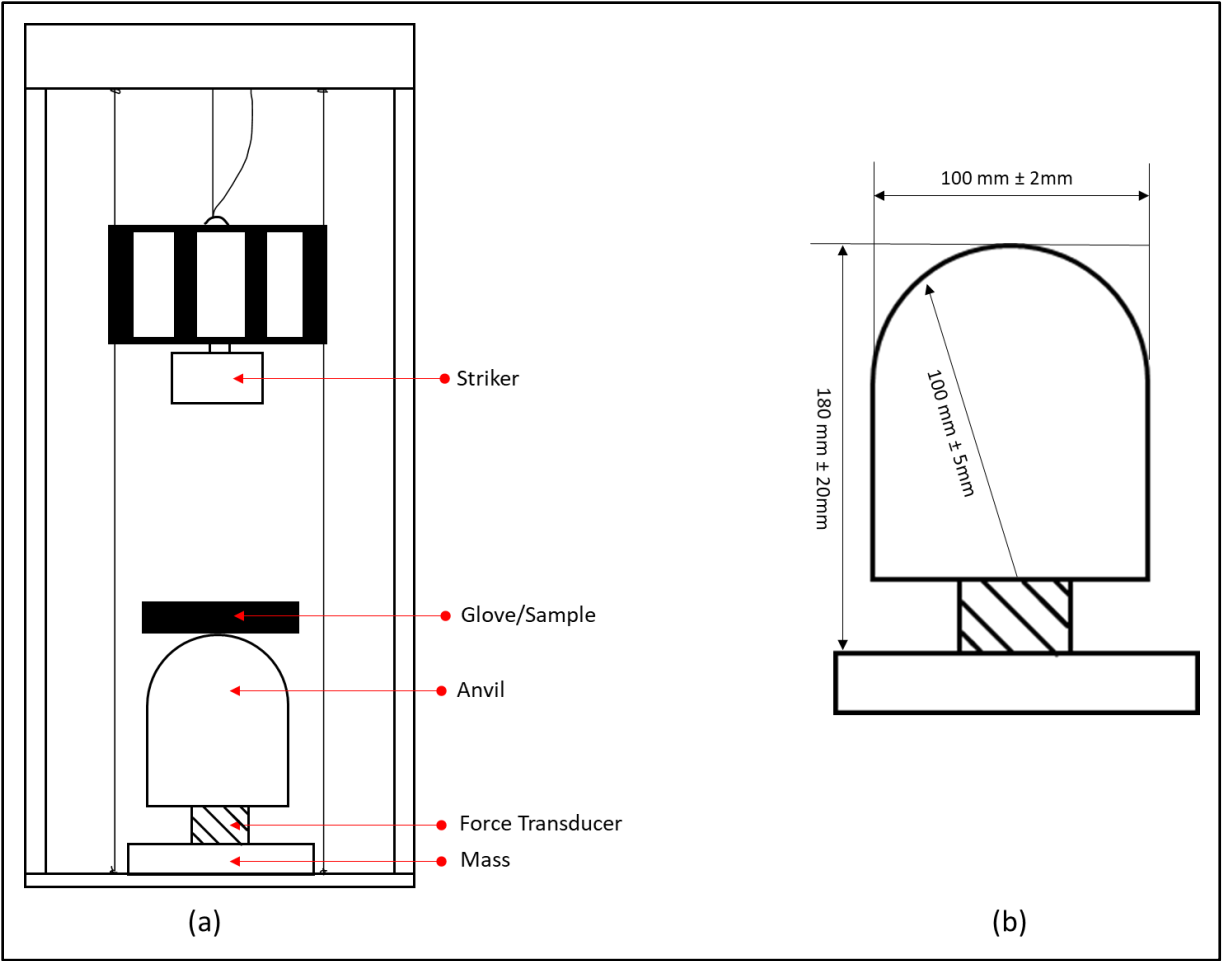
Figure 2.3: A schematic of the testing apparatus used in ANSI/ISEA 138-2019; (a) is the entire apparatus, with a striker guided by wires, a specimen or glove to be tested resting on the anvil, a force transducer to record the force, and a mass to which the anvil is secured (not drawn to scale). Not included in the schematic are the time gate, ruler, and data screen; and (b) shows the measurements specified by the standard (not drawn to scale and adapted from the standard [1]).

A picture of the actual testing apparatus used in the experimentation is shown in Figure 2.4 below. The apparatus is a CADEX mini twin wire machine and is discussed in greater detail in Chapter 3. In the figure, the striker, anvil, and mass are visible (labeled). The force transducer is not visible in the figure as it is hidden by a custom wooden stand that was fabricated to keep the glove from shifting out of place during testing. The wooden table was used by Superior Glove in their testing as well as experimentation in this thesis; creating a way to secure the specimen without interfering with the anvil and striker is common in the glove industry.
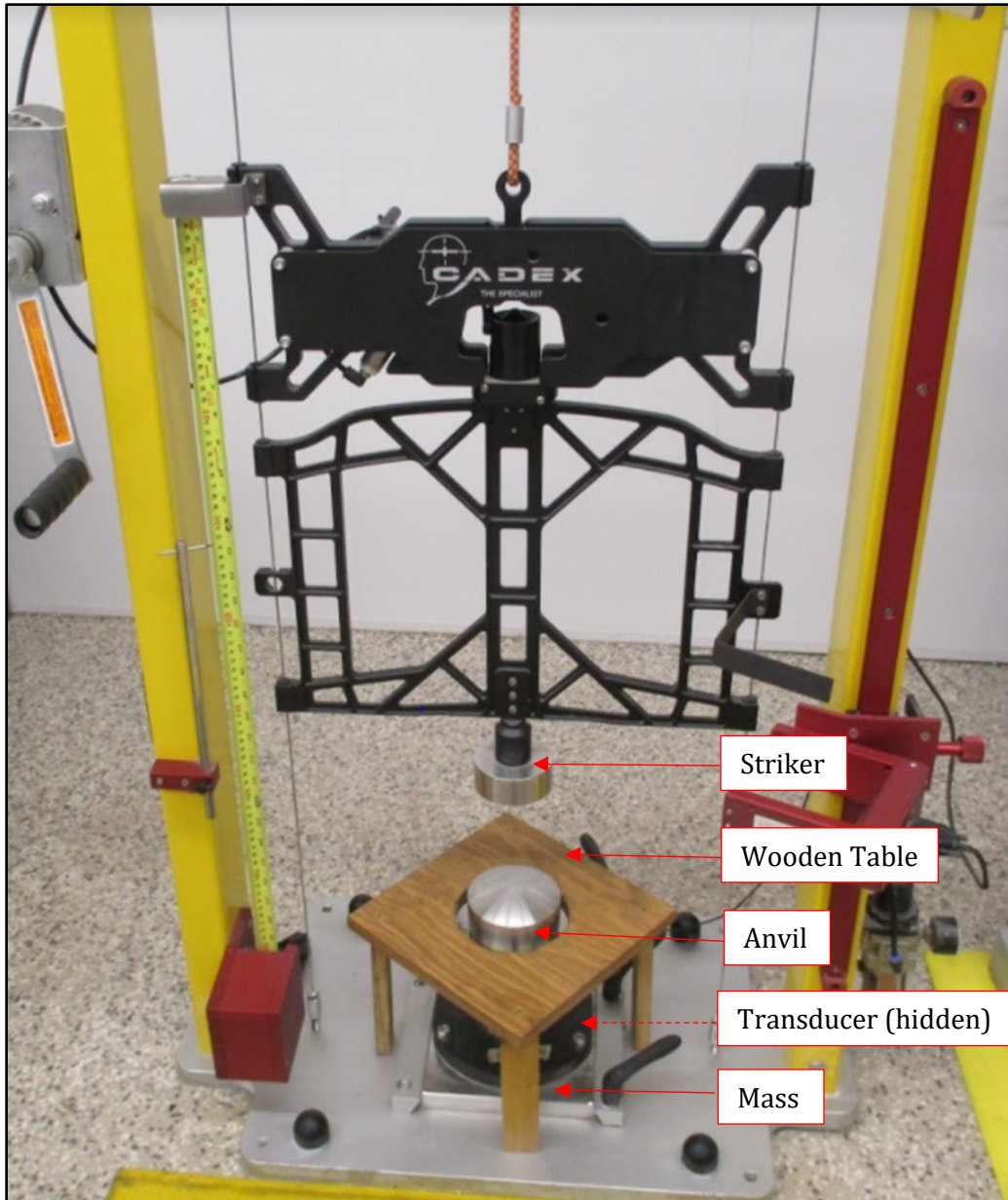
Figure 2.4: The CADEX mini twin wire machine used during experimentation. The corresponding parts from Figure 2.3 are indicated. The transducer is not visible in the figure as it is hidden by a custom wooden table that was created to prevent the specimen from shifting out of place during testing. The wooden table was fabricated by Superior Glove for their own glove testing and the table was also used during experimentation in this thesis.

During the test, the impact site to be tested is placed in the center of the anvil. The mass is then raised to a height so that when dropped it impacts the specimen with 5 J of energy. Using the principle of potential energy, to achieve 5 J of energy, the striker must be raised to a minimum height of 20 cm – assuming there will be a 100% conversion of potential energy to kinetic energy (e.g., no losses due to friction). When the test is completed, the load cell will record the peak force and time of the test.

Each drop is recorded on each glove, generating 18 separate drops (per pair of gloves). The standard specifies the maximum transmitted force for each drop as well as the maximum average of all 18 drops to achieve a certified level. Recall a summary of the levels as shown in section 1.1 in Chapter 1.
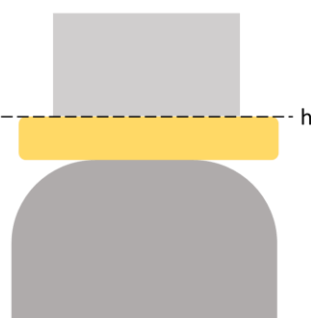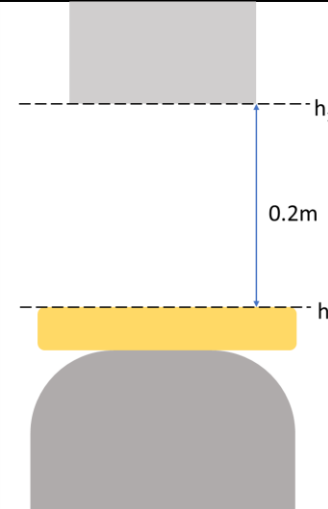
2.2.1.1 Limitations of the Standard

There are some key limitations that arise from the standard. Only impacts perpendicular to the bumpers of the glove are tested. For example, in an industry such as construction, it is possible for the hands to be struck from multiple angles – not just perpendicular to the bumper. A second limitation is that the surface of the striker is flat with an 80 mm diameter. It is possible that changing the surface area of the striker (e.g., end of a hammer) or changing the surface topography of the striker will result in a different performance of the bumper. A third limitation is that bumpers can be placed only on the nine locations specified by the standard and meet the certified level of protection – leaving large areas of the hand vulnerable to impacts. This standard-based limitation is explored in further detail in Section 2.7 of Chapter 2.

2.2.2 Kinematics of the Drop Test

The ANSI 138-2019 standard, in the simplest terms, is a vertical drop test with seven distinct stages from the top of the drop to the peak transmitted force at the bottom of the drop. Identifying these stages is necessary in order to mathematically calculate the performance of the tested specimen. In addition, identifying the distinct stages provides more information for the drop test verification when the drop test is simulated using finite element analysis (FEA). The following Table 2.1 illustrates the seven distinct stages of the start of the drop test to the bottom of the impact, as well as the beginning of the first recovery stage. In Table 2.1, the start of the stage is indicated on the left and the end of the stage is on the right. The information and stage number are provided below the corresponding stage images. The variables in Table 2.1 are used to calculate the meachincs of the impact at diffrent stages in order to be able to mathematically define and predict the impact.

Table 2.1: The kinematics of the drop test from the start of the test to the bottom of the drop, where the maximum transmitted force is recorded. The drop test can be defined in seven distinct stages for the start to bottom of the drop. The details of each stage are given visually and numerically.

Start of Stage	End of Stage
m_1= 2.5kg h_0= 0 m $\vec{v}_0$= 0 m/s $\dot{\vec{F}}_t$= 0 N KE = 0 J PE = 0 J $\vec{P}$ = 0 kg·m/s I = 0 N·s	m_1= 2.5kg h_1= 0.2 m $\vec{v}_0$= 0 m/s $\dot{\vec{F}}_t$= 0 N KE = 0 J PE = 5 J $\vec{P}$ = 0 kg·m/s I = 0 N·s

Stage (1): The striker with a mass (m_1) is vertically raised to a theoretical height (h_1) of 20 cm above the initial height (h_0), corresponding to the top of the specimen to be tested. The height is calculated by assuming that all the potential energy created will be converted to 5 J of kinetic energy:

$$h = \frac{(PE)}{mg} \tag{2.1}$$

where h is the height the striker is to be raised, PE is the potential energy required, m is the mass of the striker, and g is the gravitational constant.

At this stage, the striker velocity (v_0) is 0m/s; therefore, the striker has no momentum (P). The kinetic energy (KE) for the end of this stage is 0 J, and the potential energy (PE) is 5 J.

$m_1 = 2.5$ kg
$h_1 = 0.2$ m
$\vec{v}_0 = 0$ m/s
$\vec{F}_t = 0$ N
KE = 0 J
PE = 5 J
$\vec{P} = 0$ kg·m/s
$I = 0$ N·s

$m_1 = 2.5$ kg
$h_2 = h_0 = 0$ m
$\vec{v}_1 = -2$ m/s
$\vec{F}_t = 0$ N
KE = 5 J
PE = 0 J
$\vec{P} = 5$ kg·m/s
$I = 0$ N·s
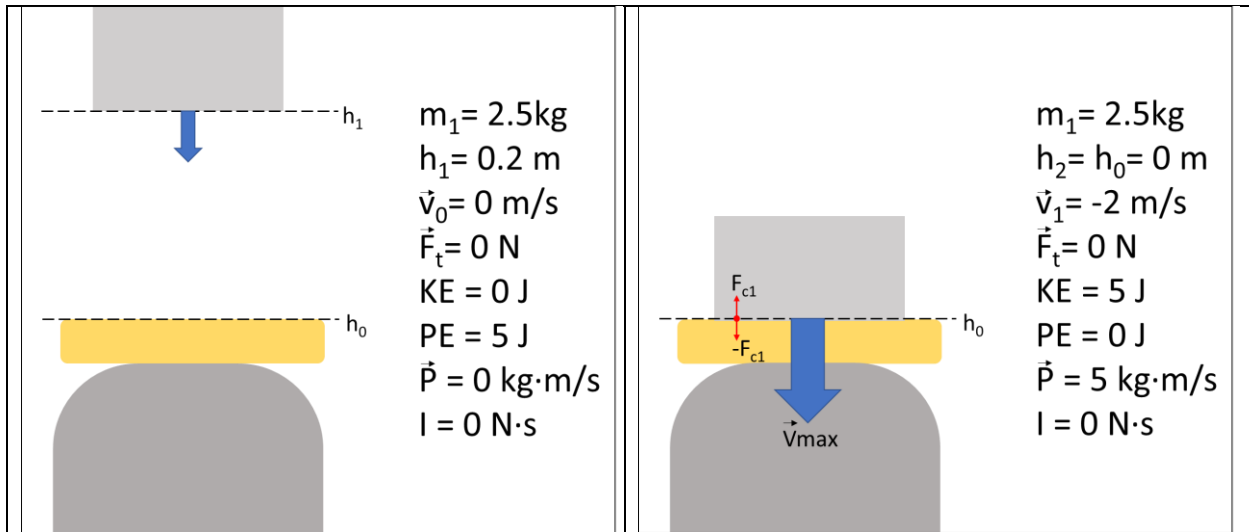
Stage (2): When the striker is released Stage 2 begins. The end of Stage 2 is when the striker initially contacts the specimen, generating an initial contact force (F_{c1} in the diagram). At the end of this stage, using the principle of the conservation of energy, the striker has 5 J of kinetic energy and a velocity of the striker is 2 m/s (v_1). The velocity at the end of Stage 2 is also the maximum velocity the striker and assembly will have in the test. The velocity was calculated from equating the potential energy and kinetic energy and rearranging for velocity:

$$\vec{v_1} = \sqrt{2gh} \qquad (2.2)$$

The momentum (P) of the striker at this stage is 5 kg*m/s, which is found by multiplying the velocity and mass of the striker:

$$\vec{P} = m_1 v_1 \qquad (2.3)$$

$m_1 = 2.5$ kg
$h_2 = h_0 = 0$ m
$\vec{v}_1 = -2$ m/s
$\vec{F}_t = 0$ N
KE = 5 J
PE = 0 J
$\vec{P} = 5$ kg·m/s
$I = 0$ N·s

$m_1 = 2.5$ kg
$h_3 = -x_1$
$\vec{v}_2 < -2$ m/s
$\vec{F}_t = 0$ N
KE < 5 J
PE > 0 J
$\vec{P} = P_2$
$I = I_1$
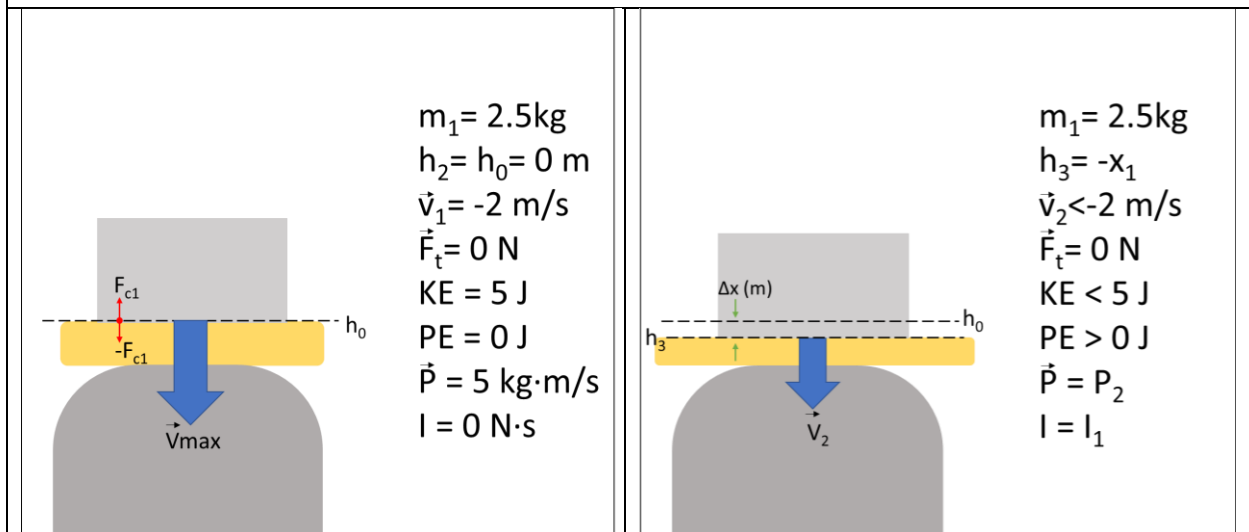
Stage (3): The impact of the striker will generate stress waves perpendicular to the motion of impact, causing the specimen to deform under the load. Stage 3 is when most of the energy the material is capable of absorbing will occur. In addition, Stage 3 is when an impulse is generated. Impulse (I) is defined as the change in momentum (ΔP), which is the force (F) is applied over a change in time (Δt):

$$I = \Delta P = F\Delta t \tag{2.4}$$

The velocity at the end of Stage 3 is less than 2m/s, with the exact value changing from test to test depending on the material and dimensions of the specimen. The kinetic energy is also reduced below 5J of energy.
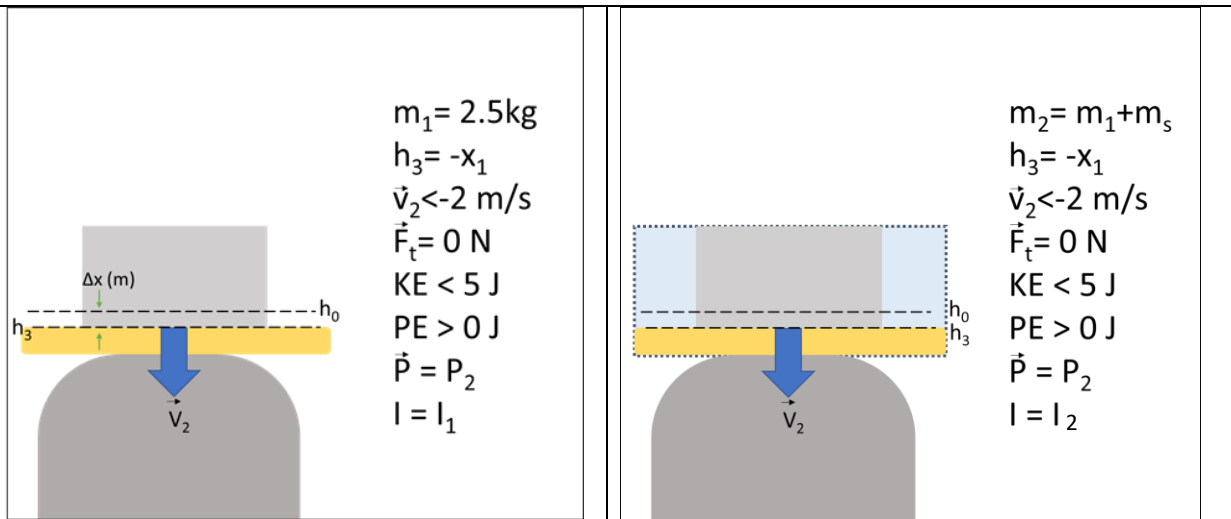
Stage (4): The specimen has reached its peak thickness deformation (x_1) under the striker load at Stage 4 and the new height of the top of the specimen is h_3. If the specimen has not absorbed all 5 J of energy, it will continue to move with the striker (whole system moving is denoted with a box) with the residual kinetic energy from the striker. Thus, the new mass of the system is m_2 as the mass of the specimen (m_s) is added to the mass of the striker (m_1).

$m_2 = m_1 + m_s$
$h_3 = -x_1$
$\vec{v}_2 < -2$ m/s
$\vec{F}_t = 0$ N
$KE < 5$ J
$PE > 0$ J
$\vec{P} = P_2$
$I = I_2$

h_0 h_3 v_2

$m_2 = m_1 + m_s$
$h_4 = -x_1 + -x_2$
$\vec{v}_4 < \vec{v}_3$
$\vec{F}_t > 0$ N
$KE < 5$ J
$PE > 0$ J
$\vec{P} = P_3$
$I = I_3$

$\Delta x_2 (m)$ F_{c2} $-F_{c2}$ h_3 h_4 v_4
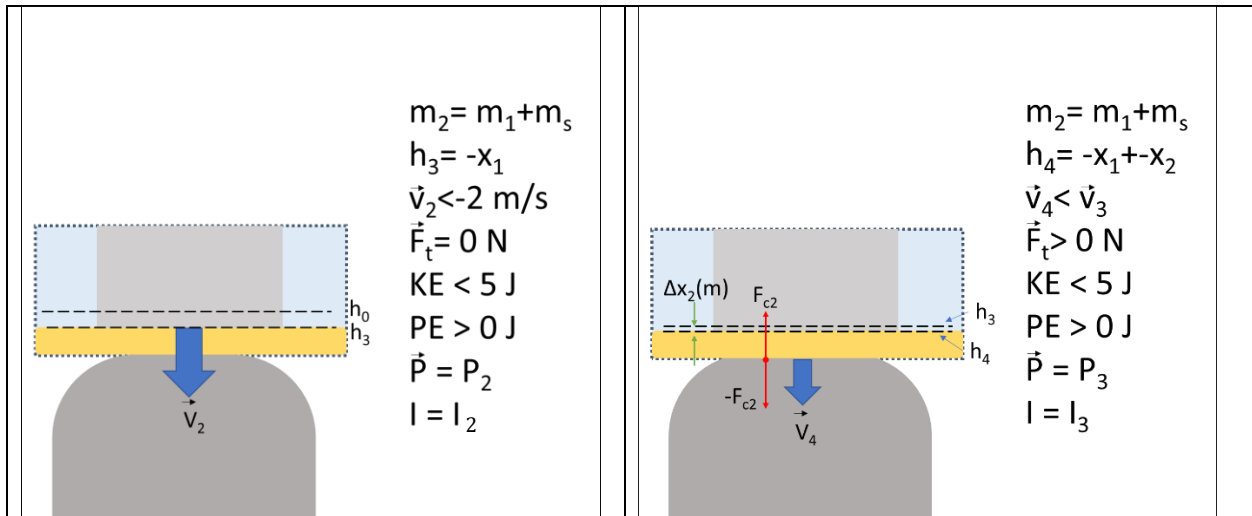
Stage (5): The striker and specimen move as one unit a distance of x_2 until they come into contact with the anvil at a height defined as h_4, generating an initial contact force and transmitted force. Stage (5) can occur during stage (3), as the onset of the transmitted force is subject to the Poisson's ratio of the material.

$m_2 = m_1 + m_s$
$h_4 = -x_1 + -x_2$
$\vec{v}_4 < \vec{v}_3$
$\vec{F}_t > 0$ N
$KE < 5$ J
$PE > 0$ J
$\vec{P} = P_3$
$I = I_3$

h_4 v_4

$m_3 = m_2 + m_a$
$h_5 = -x_1 + -x_2 + -x_3$
$\vec{v}_5 = 0$ m/s
$\vec{F}_t > 0$ N
$KE = 0$ J
$PE > 0$ J
$\vec{P} = 0$ kg·m/s
$I = 5$ N·s

$\Delta x = 0.5$mm h_4 h_5 v_5
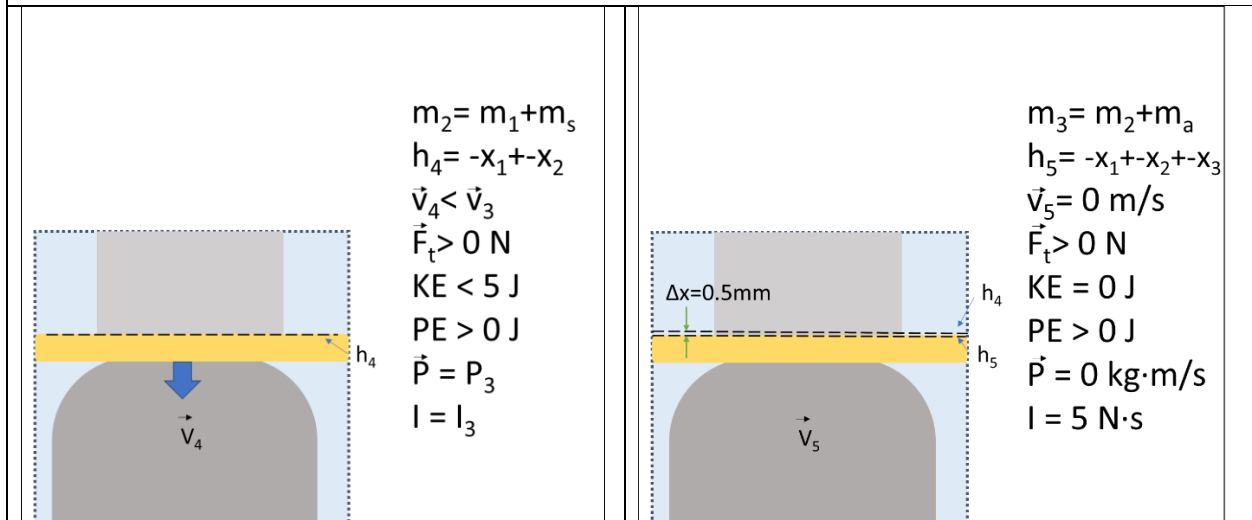
Stage (6): The striker, specimen, and anvil will move as a unit against the transducer. This movement was found to be less than 0.5 mm from the results of high speed videography (HSV) discussed in Chapter 3.

$m_3 = m_2 + m_a$
$h_5 = -x_1 + -x_2 + -x_3$
$\vec{v}_5 = 0 \text{ m/s}$
$\vec{F}_t = \text{max}$
$KE = 0 \text{ J}$
$PE > 0 \text{ J}$
$\vec{P} = 0 \text{ kg·m/s}$
$I = I_4$

h_0
h_5

$\overrightarrow{V_5} = 0\text{m/s}$
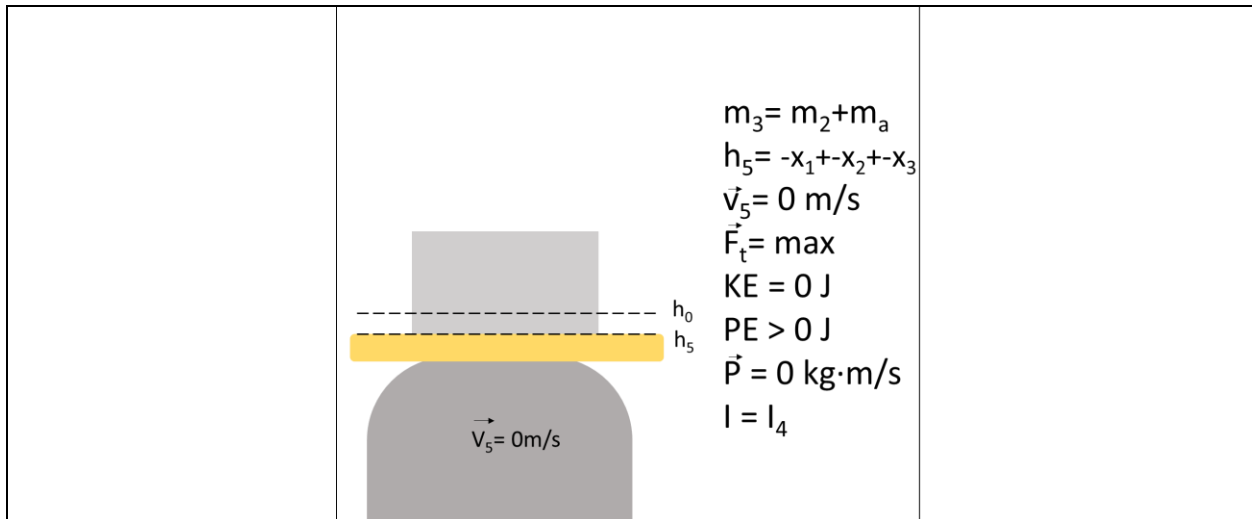
Stage (7): The bottom of the impact. Here, the velocity of the striker is zero, kinetic energy of the impact is zero, and the maximum transmitted force has been generated by the impact. The transducer will have recorded this impact in the form of an impulse curve (force vs time graph)

$$F = \frac{mv}{t} \tag{2.5}$$

$m_3 = m_2 + m_a$
$h_5 = -x_1 + -x_2 + -x_3$
$\vec{v}_5 = 0 \text{ m/s}$
$\vec{F}_t = \text{max}$
$KE = 0 \text{ J}$
$PE > 0 \text{ J}$
$\vec{P} = 0 \text{ kg·m/s}$
$I = I_4$

h_0
h_5

$\overrightarrow{V_5} = 0\text{m/s}$

$\overrightarrow{V_6}$

$m_3 = m_2 + m_a$
$h_5 = -x_1 + -x_2 + -x_3$
$\vec{v}_6 > 0 \text{ m/s}$
$\vec{F}_t < \text{max}$
$KE > 0 \text{ J}$
$PE > 0 \text{ J}$
$\vec{P} = 0 \text{ kg·m/s}$
$I = I_5$

h_0
h_5
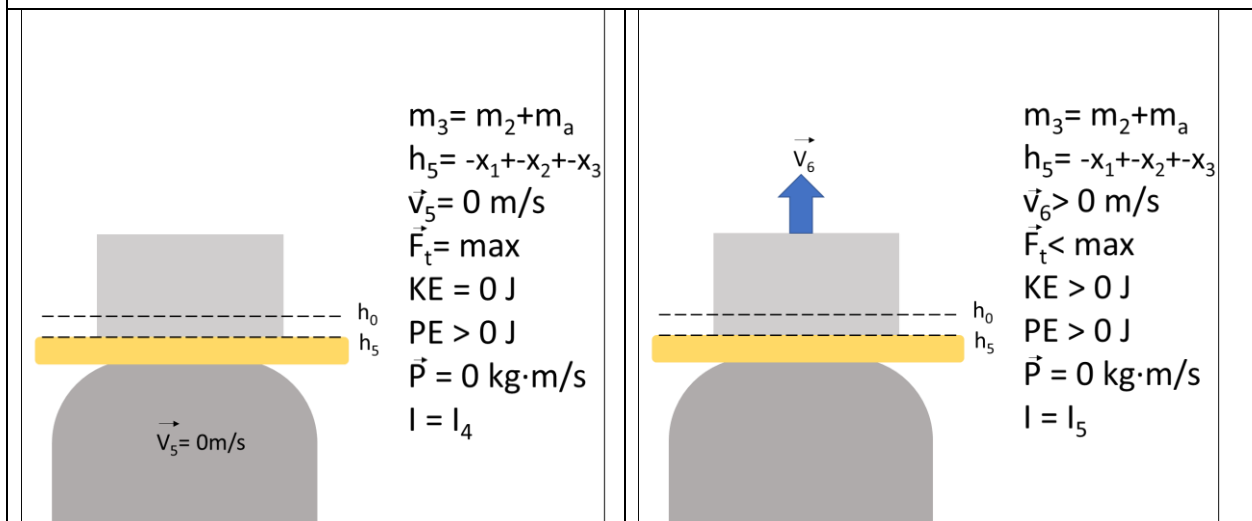
Stage (8): The kinetic energy that was absorbed as elastic strain energy by the specimen, anvil, and transducer is released to accelerate the striker upwards.

2.3 Hands: Critical Anatomy and Common Injuries

The following section will focus on the anatomy of the hand and how it is injured from impacts. Hand anatomy is important to glove design as it will dictate where the bumpers should be placed and how

they should be created to allow maximum protection as well as mobility of the hand. In addition, having knowledge of the more vulnerable areas of the hand is ideal to ensure that the energy is adequately absorbed in such areas.

2.3.1 The Anatomy of the Hand

It is important to know the parts of the hand when designing impact resistant gloves to ensure that they are providing adequate protection. The anatomy of the hand can be broken down into seven structures: skin, fat, bones and joints, ligaments and tendons, muscle, nerves, and blood vessels. In addition, the hand has two surfaces. The palm-side of the hand is known as the palmar surface and the back of the hand is the dorsal surface. Impact resistant gloves focus on protecting the dorsal surface of the hand; therefore, the next section will focus on the anatomy of the dorsal surface. The following is a relatively basic overview of the hand, for a more in-depth overview the reader is guided to the *Surgical Anatomy of the Hand and Upper Extremity* by James R. Doyle [2]. Skin and fat tissues are not as varied as the other tissues in the hand, nor as location specific, and because they have little influence on bumper design their anatomy has not been discussed herein.

2.3.1.1 Bones and Joints

The hand has 27 bones that can be grouped into three sections: carpals, metacarpals, and phalanges [3]. Figure 2.5 below illustrates the bones as viewed from an anterior view of the palmar surface of the right hand. There are 8 carpal bones which allow for wrist mobility (indicated in Figure 2.5). This group of bones are adjacent to the radius and ulna bones of the forearm. The radius and ulna bones are the two large bones in the forearm (not shown). The ulna bone is located on the pinky side of the hand and the radial bone, which rotates when the hand is rotated, is located on the thumb side of the hand.

Going from the wrist to the tips of the fingers, the next group of bones are the metacarpals (yellow bones in Figure 2.5). There are five of them total and they are ordered numerically, with the first metacarpal located at the thumb and the fifth located at the pinky [3]. Each metacarpal can be divided into four regions: the head, neck, shaft, and base (see inset of Figure 2.5) [2]. The last section of bones are the finger bones, known as the phalanges. The second through fifth phalanges are comprised of three bones each: the proximal phalanx (adjacent to metacarpal), the middle or intermediate phalanx, and the distal phalanx (tip of the finger) [2]. The first phalange (thumb) only has a proximal and distal phalanx.
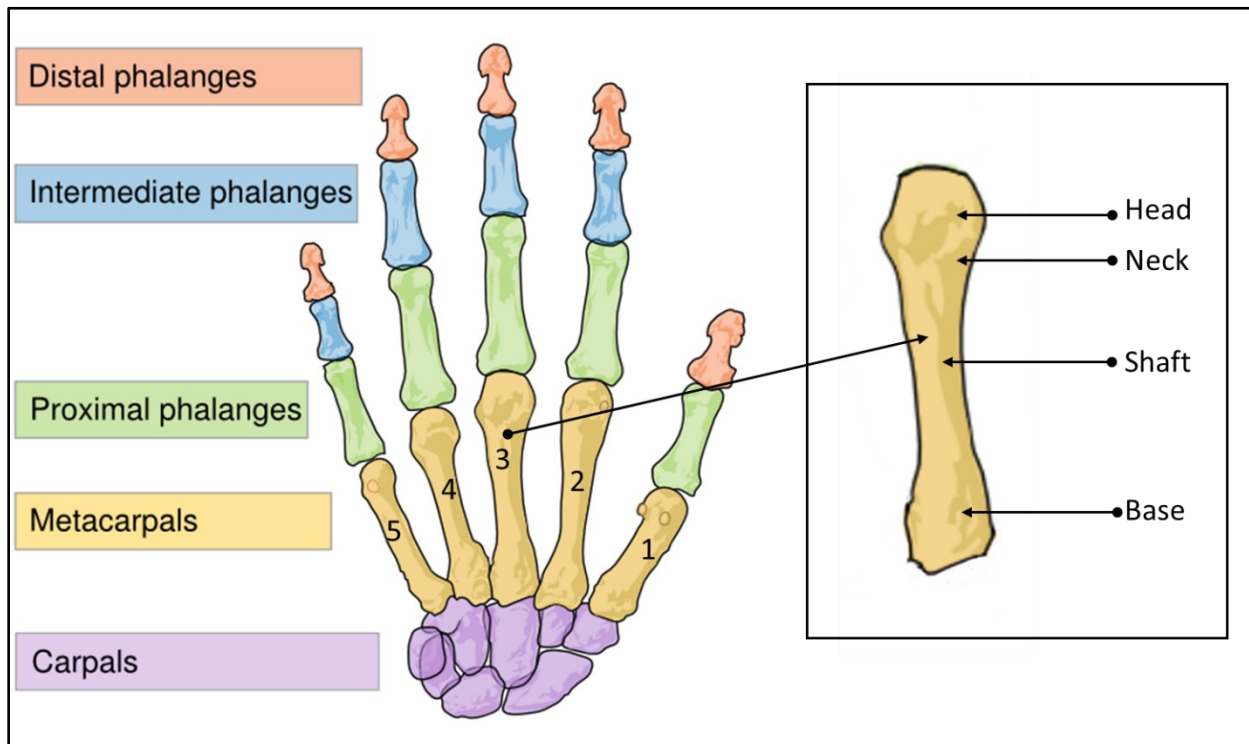
Figure 2.5: Anterior view of the bones of the hand coded by specific region of the hand and the parts of the metacarpal bone. Modified from [4].

The joints in the hand act as hinges between the bones so that the fingers can be bent and straightened. All the joints are covered with articular cartilage, which absorbs sudden mechanical forces and provides a smooth surface for motion [3]. The main joints in the hand are the knuckle joints, called metacarpophalangeal joints (MCP joints), which are located between the metacarpal bones and proximal phalanges. The phalanges in each finger are separated by the interphalangeal joints (IP joints). The thumb has one IP joint, and the other fingers have two [3].

2.3.1.2 Ligaments and Tendons

Ligaments are a band of tough tissue that hold bones in place [3]. On the dorsal surface of the hand, only the collateral ligaments are exposed. These ligaments are located on either side of the MCP and IP joints, as shown in Figure 2.6.
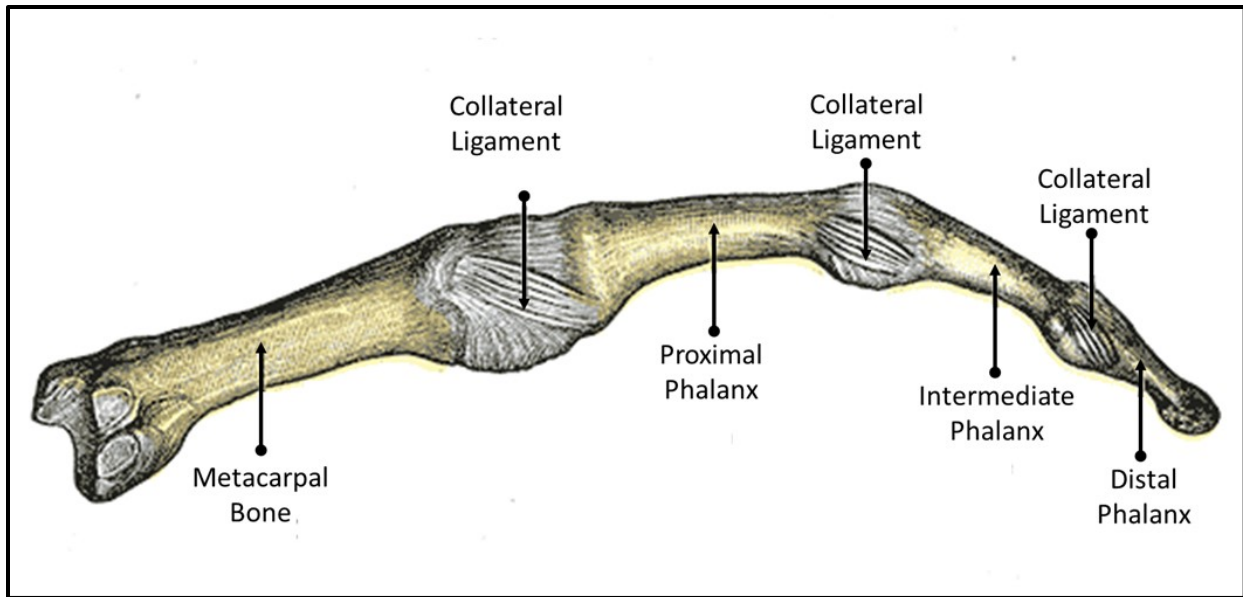
Figure 2.6: The locations of the collateral ligaments in the finger. These ligaments connect the phalanges together and the proximal phalanx to the metacarpal bone. Figure modified from [5].

Tendons are fibrous connective tissue which attach muscles to the bone [3]. For the dorsal side of the hand, there is a series of tendons, called extensor tendons, that run through the hand and attach at the middle and distal phalanx of each finger in an area known as the central slip [3]. These tendons are responsible for extension of the hand when the muscle, located in the forearm, is activated [2].
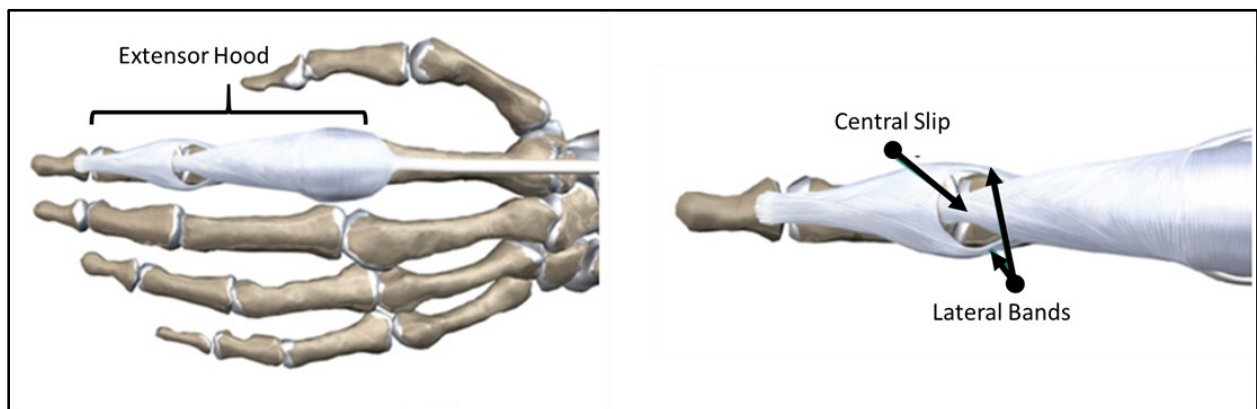
Figure 2.7: Posterior view of the extensor tendons of the hand, which are controlled by the muscles in the forearm. Images modified from [3].

2.3.1.3 Muscles

The palmar surface of the hand is where the muscles responsible for hand grip and thumb opposition are located. These muscles start at the carpal bones and extend to the pinky and thumb [3] [6]. The dorsal surface of the hand contains the intrinsic muscles of the interossei, which are shown in Figure 2.8. These muscles are located between the metacarpal bones and they are responsible for fine motor movements [3]. The other muscles that are responsible for the contraction and extension of the hand are located in the forearm (not shown) [2].
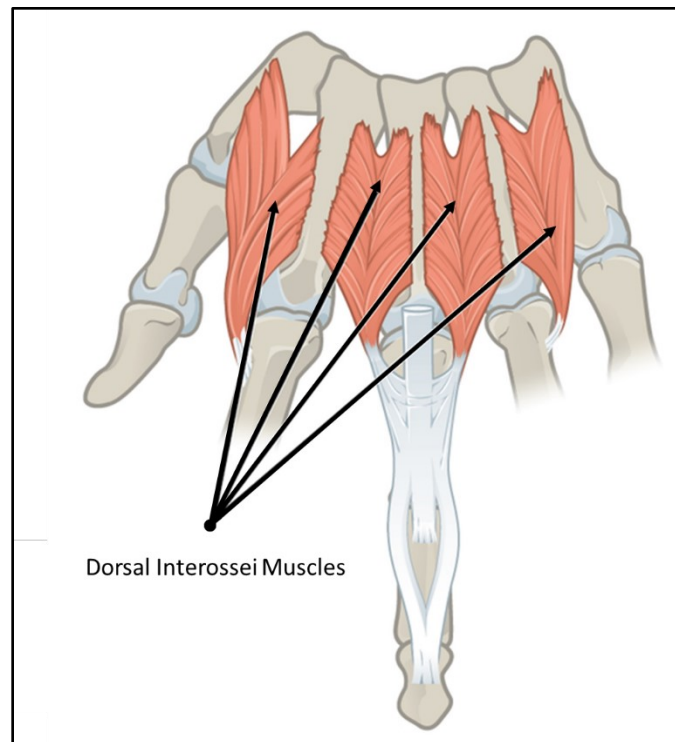
Figure 2.8: The intrinsic interossei muscles of the hand that are exposed on the dorsal side of the hand. Image modified from [7].

2.3.1.4 Nerves

The hand has three nerves: the radial nerve, ulnar nerve, and median nerve [3]. These nerves are responsible for carrying signals to the brain to move the hand muscles, as well as sensory information such as pain and temperature [2]. The radial nerve is located only on the dorsal surface of the hand and runs on the radius side edge of the hand. It covers the thumb, half of the index finger, and half of the middle finger. The ulnar nerve is located on the ulna side edge of the hand and it is on both the palmar and dorsal surfaces of the hand. It covers sensations in the pinky to the ring finger. The median nerve is primarily on the palmer surface of the hand and covers the thumb to the middle of

the ring finger. On the dorsal surface of the hand, the median nerve covers the tips of the thumb, index finger, middle finger, and half of the ring finger. The locations and areas of sensation the nerves are responsible for are shown in Figure 2.9 below.
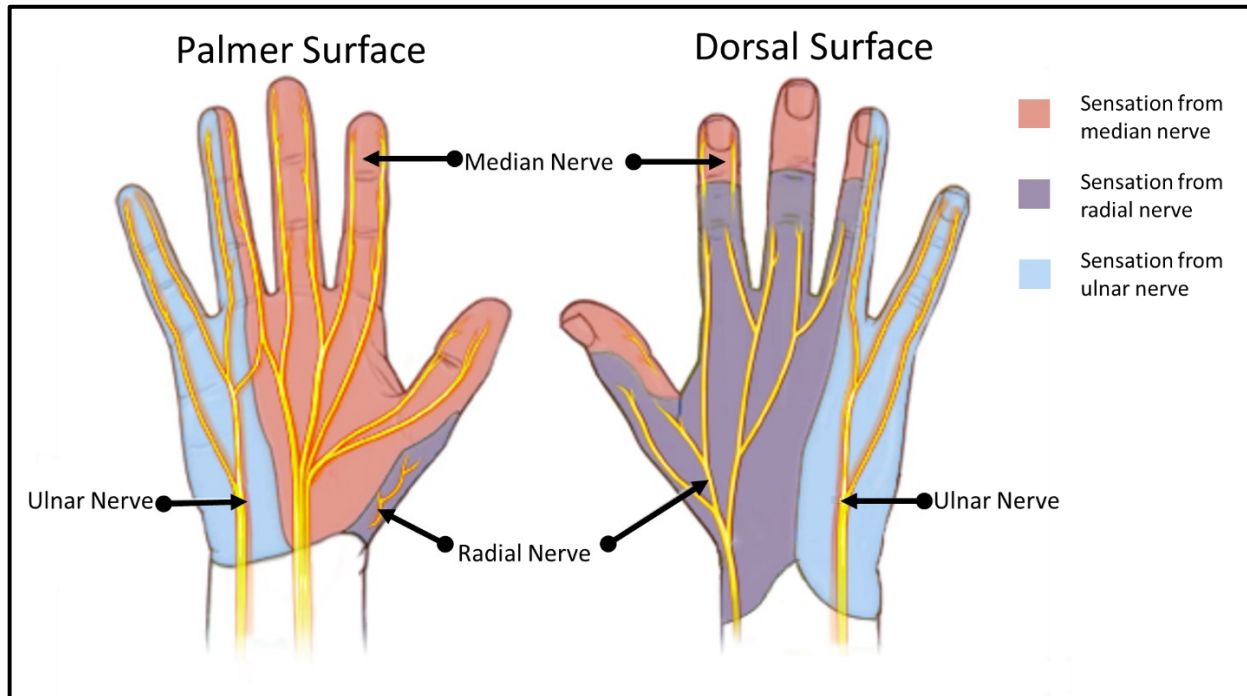
Figure 2.9: The locations of sensation for the three nerves in the hand. The palmer surface of the hand is shown on the left and the dorsal surface is shown on the right. The pink shaded area is the sensation from the median nerve, the purple shaded area is the sensation experienced from the radial nerve, and the blue shaded area is the sensation from the ulnar nerve. Image modified from [8].

2.3.1.5 Arteries

There are two arteries in the hand: the ulnar artery and radial artery [3]. The purpose of the arteries is to supply blood to their respective sides of the hand. The ulnar artery supplies blood to the ulna side of the hand and the radial supplies blood to the radial side of the hand. Both of these arteries are exposed on the dorsal and palmar surface of the hand [2]. Figure 2.10 below shows the locations of the ulnar and radial arteries on the dorsal surface of the hand.
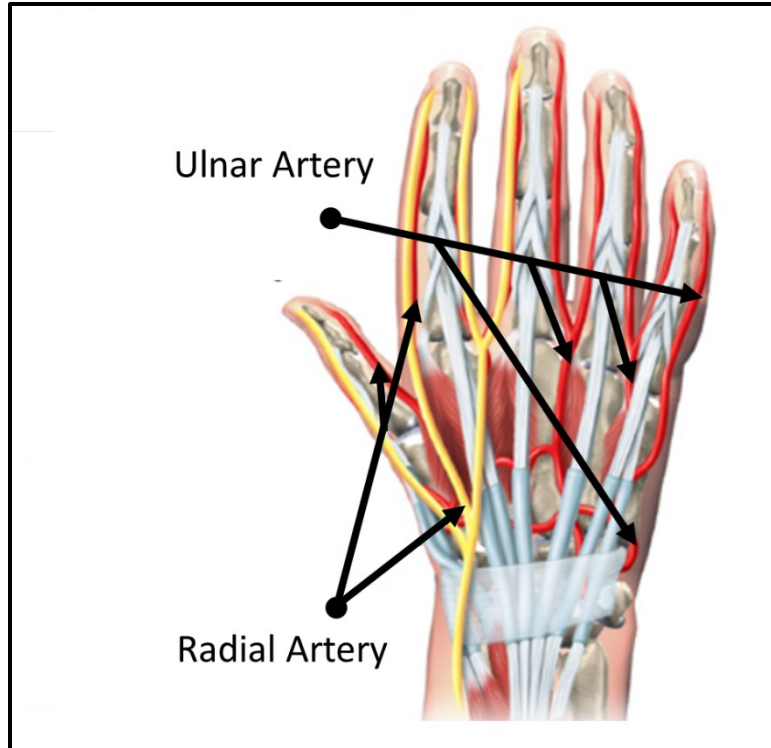
Figure 2.10: The locations of the ulnar and radial arteries on the dorsal surface of the hand. Image modified from [3].

2.3.2 Variation in Hand Size

The human hand can come in all shapes and sizes and there is a definite difference between the size of the average male and female hand [9]. It is important to know the variance in hand size of humans to identify the "footprint" and ranges in dimensions for bumpers.

Using the data collected in the book *The Measure of Man and Woman* by Alvin R. Tilley (published in 1993) Table 2. below shows the different dimensions of the hand for men and women aged 20 to 65 [9]. The data in the book was gathered from anthropometrical studies of the world's population and plotted on a Gaussian distribution curve [9]. The book then specified the average (50th percentile) measurements for the hand as well as the 99th percentile and the 1st percentile measurements.

25

Table 2.2: The various measurements of the hand for men and woman for the 99, 50, and 1 percentiles measured in milimeters. The measurements for men are shaded in green and the measurements for women are shaded in blue. Information retrieved from pages 22-25 of [9].

Measurement	Man			Woman		
	99 Percentile	50 Percentile	1 Percentile	99 Percentile	50 Percentile	1 Percentile
Length of hand (Wrist to fingertips) (mm)	213	190	168	198	175*	152
Length of wrist to thumb (mm)	132	117	102	122	107	94
Length of wrist to middle of palm (mm)	84	78	69	84	71	64
Width of Hand (mm)	117	104	94	104	91	81
Width of Fingers (excluding thumb) (mm)	102	86	78	86	76	64

Book states that this measurement is 75mm, which was assumed to be a typo of 175mm

From the data, it is apparent that there is a drastic difference between the size of hands of the "99 percentile man" when compared to the "1 percentile woman". For hand width alone, the bumper would have to be 36mm larger for the 99 percentile man to provide the same protection, assuming the entire width of the hand needs to be covered. It should also be noted that the ratio of the length of the hand to width of the hand for men is approximately 1.8, whereas it is 1.9 for females. This ratio indicates that women's hands tend to have slightly longer fingers than men for the same hand width.

2.3.3 Defining Injury Due to Low Velocity Impact

Injuries to the hand due to an object falling onto the hand, or the hand striking a hard object are categorized as blunt force trauma [10] which is when the "...relatively low-velocity impacts are over a large surface area" [10]. Blunt force trauma is opposed to sharp force trauma, where the impact involves a narrow surface area at lower velocities (e.g., an axe), or an injury from a projectile, where the object is travelling at high velocities (e.g., a bullet) [10]. It is important to distinguish that the injuries that the gloves under consideration for this thesis will be designed to mitigate are from blunt force trauma as the types of injuries that arise from the other categories of impact, and the way to prevent them, will be different.

2.3.4 Common Blunt Force Trauma Injuries

Blunt force trauma injuries in the workplace can occur from either an object striking the hand or the hand striking an object. In industries such as construction, mining, and oil and gas, the hands are prone to being either in a clenched fist position, as the hand is used to hold tools, or a flat position with the palm resting on a surface. Each of these positions will have different injury outcomes to the blunt force trauma [10].

2.3.4.1 Bone Fractures

The most severe and common injury from blunt force trauma to the dorsal surface of the hand is the fracturing of the bones [10]. Bones can be classified as an anisotropic ceramic-polymer composite material as they can withstand larger compressive forces than tensile forces and have a molecular orientation [10]. Similar to all materials, bones also have a yield strength and failure point when subjected to certain stresses and strains [10]. When the force applied to the bone exceeds the yield strength, micro fractures in the bone form [10]. The bone fully fractures at the failure point. In a study by Carpanen *et al.* that measured the likelihood of the bones in the hand fracturing, it was determined that 4000 N of force has a 50% chance of fracturing bone, while there is a 99% chance of fracturing the bone with 8000 N of force [11]. In another study conducted, it was found that a sharp blow to the rib in boxing delivers 3,300 N of force and has a 25% chance of fracturing an "average person's" rib [12].

Data shows that 20% of all hand fractures are to the fifth or first metacarpals [10]. The fifth metacarpal is the most likely to be injured due to its exterior anatomical positioning on the hand. The first metacarpal is the next likely to be injured due to its structural difference and edge-based anatomical location [10]. Figure 2.11 below highlights the fifth and first metacarpal bones. In addition, Figure 2.11 shows where each metacarpal is likely to get fractured. Fractures from blows or impact are most likely to occur at the neck of the bone for metacarpals 1,2, and 5 and midshaft for 3 and 4. The third and fourth metacarpals tend to break simultaneously from impact [10].
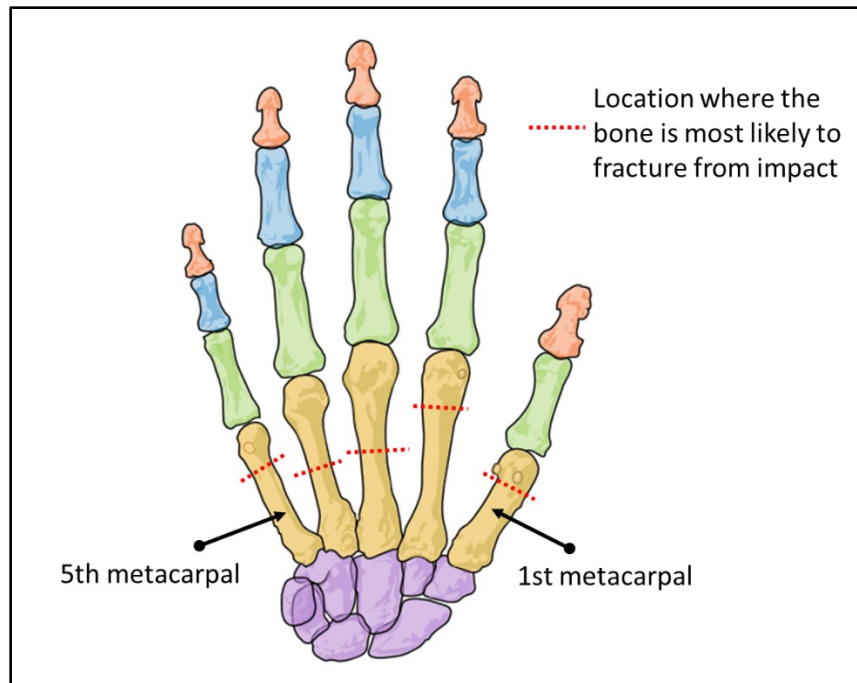
Figure 2.11: The locations where each metacarpal bone is most likely to be fractured from impact. The fifth metacarpal (indicated) is the most frequent metacarpal that is fractured followed by the first metacarpal (indicated). Modified from [4].

The uneven distribution of the frequency of bone fractures in the hand are due to the placement of the hand during impact [10]. If the hand is in a clenched position, the metacarpals are more vulnerable. If the hand were to strike an object, the most likely injury is a boxer's fracture, where there is a 60% chance the fracture occurs in the fourth and fifth metacarpal [10]. The phalanges are more vulnerable when the hand is extended. The common injury mechanism for the phalanges is getting crushed by machinery or getting caught between colliding objects [10]. 50% of the fractures occur on the middle or proximal phalanx [10]. The carpal bones are not likely to get injured from a blunt force to the dorsal side of the hand; they are more likely to be injured due to a person falling [10].

2.3.4.2 Contusions

Contusions are another consequence of blunt force trauma. Contusions can occur in the presence or absence of the bones fracturing. A contusion is when the blood vessels are torn and form a bruise [13]. Contusions can cause swelling, which can impinge the muscles, tendons, and nerves in the hand. The consequence of the impingement is the loss of fine motor movements of the hand [13].

2.3.4.3 Lacerations and Tears

Lacerations are a type of injury that can occur from blunt force trauma to the back of the hand [14]. A laceration is a wound that is produced by tearing the soft body tissue (skin, muscle, and tendons) [15]. Lacerations can range in severity from a tear to the skin (minor cut) to a complete tear of the tendons and muscles in the back of the hand. A laceration to the tendons in the back of the hand will result in the inability to extend (straighten) a joint or finger [14].

2.3.4.4 Nerve Damage

Blunt force trauma can cause nerve damage. Damage to the ulnar nerve results in the loss of sensation in the hand at the ring and little fingers, loss of coordination, pain, loss of grip strength, and paralysis [16]. Damage to the radial nerve is similar to the ulnar nerve except that there is a loss of sensation in the thumb, index, and middle finger on the hand [16]. In addition, the ability to straighten the wrist will be compromised if the radial nerve is damaged [16].

2.4 Polymers and Elastomers

Polymers are a class of organic materials. Due to the nature of their structure and bond interactions, polymers possess the unique ability to be flexible and strong, which makes polymers desirable for many design applications [17]. The following section describes the structure of polymers and elastomers and their structure-sensitive mechanical properties.

2.4.1 Polymer and Elastomer Structure

The microstructure of a polymer is most frequently a series of carbon atom chains (C-C) as a backbone. In most polymers, each individual carbon has four free electrons, allowing it to covalently bond with four other carbon atoms or other elements creating multiple chains [18]. The simplest form of a polymer is polyethylene (PE), which is a series of ethylene molecules (ethene; the monomer) bound together through a process known as polymerization to form a linear chain of the molecules (the polymer) [17]. Figure 2.12 shows the basic structure of PE as well as some of the most common single chains of polymers. The monomers of each of the polymers in Figure 2.12 are enclosed in a blue box. To create polyvinyl chloride (PVC), for example, a chlorine atom replaces one out of the four hydrogen atoms in the functional group connected to the carbon chain. Silicone, on the other hand, is a chain of silicon and oxygen atoms instead of carbon [17].

Polymer Chain	Polymer Name

Figure 2.12: The polymer chain structures of polyethylene (PE), polyvinylchloride (PVC), Teflon (PTFE), and polypropylene (PP). The monomer, or smallest repeatable unit of each polymer is enclosed in a blue box. Figure modified from [17],[18].

A single chain of a polymer can have many different forms. Figure 2.13 below displays the line representation of various forms of polymer structures. A single linear chain of polymer is represented by a line (Figure 2.13(a)). The polymer chains can also have multiple side chains when a third or forth carbon atom is covalently bonded to a carbon atom, making it branched as shown in Figure 2.13(b). The longest continuous connection of carbon atoms in a polymer is deemed to be the main chain [18] (indicated in Figure 2.13(b)). The chain of polymer can also be cross-linked through chemical processes such as the vulcanization process in rubber (only possible for thermosets) [18], which is shown in Figure 2.13(c).
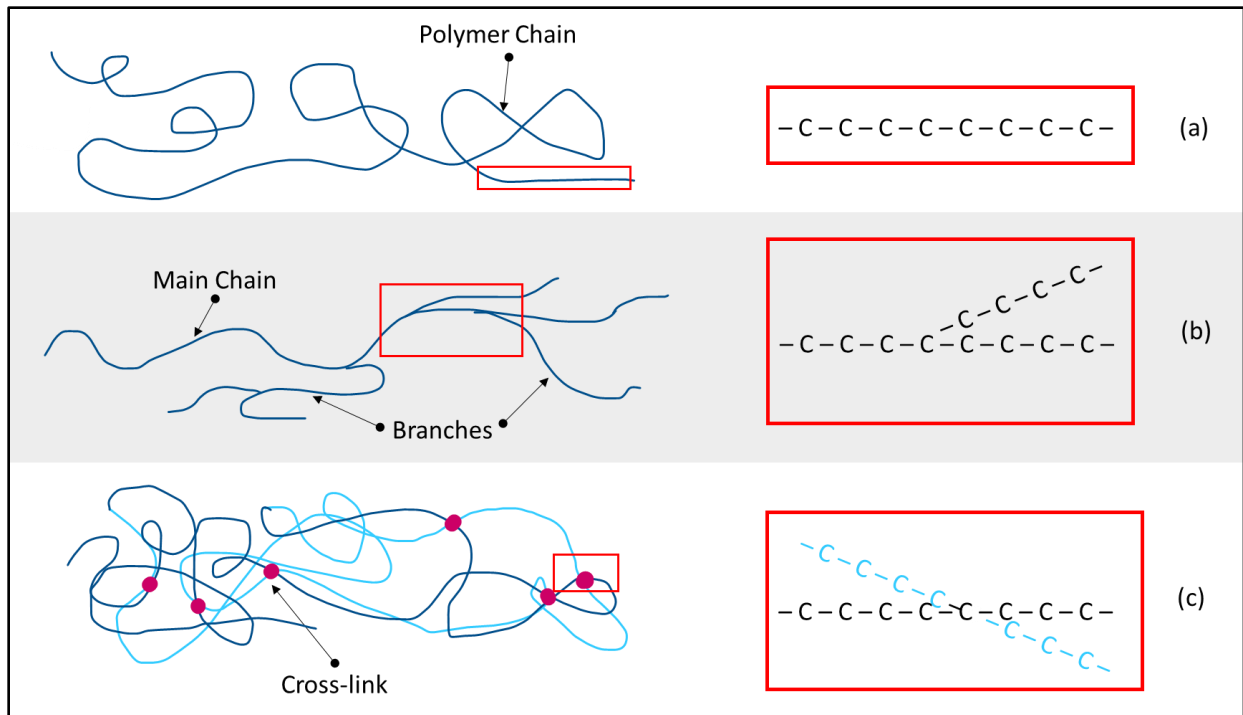
Figure 2.13: The various microstructures of a single polymer chain. The left side of the figure illustrates the line method of representing polymer microstructure and the right side displays the chemical composition annotation: note that on "C" represents an ethylene group (CHx). (a) shows a single chain of a polymer, which is a linear structure. (b) shows a branched chain of a polymer with the main chain indicated. (c)shows a cross-linked thermoset polymer chain (the cross-links are the magenta dots). Figure modified from [17].

When multiple chains are close together, the hydrogen atoms will attract each other through weak intermolecular forces, causing the chains to become ordered for small segments along the chain [17]. These weak forces cause the chains to have no order and look similar to a bowl of spaghetti, where each chain is a single noodle. These chains can also be cross-linked together, with the higher number of cross-links resulting in a stiffer material. Keeping with the spaghetti analogy, cross-linking would be as if two noodles were chemically attached at a point of contact. Figure 2.14 shows the broad microstructure of multiple polymer chains that are non-cross-linked (a) or cross-linked (b). Each blue line of a different shade is a separate polymer chain in Figure 2.14.
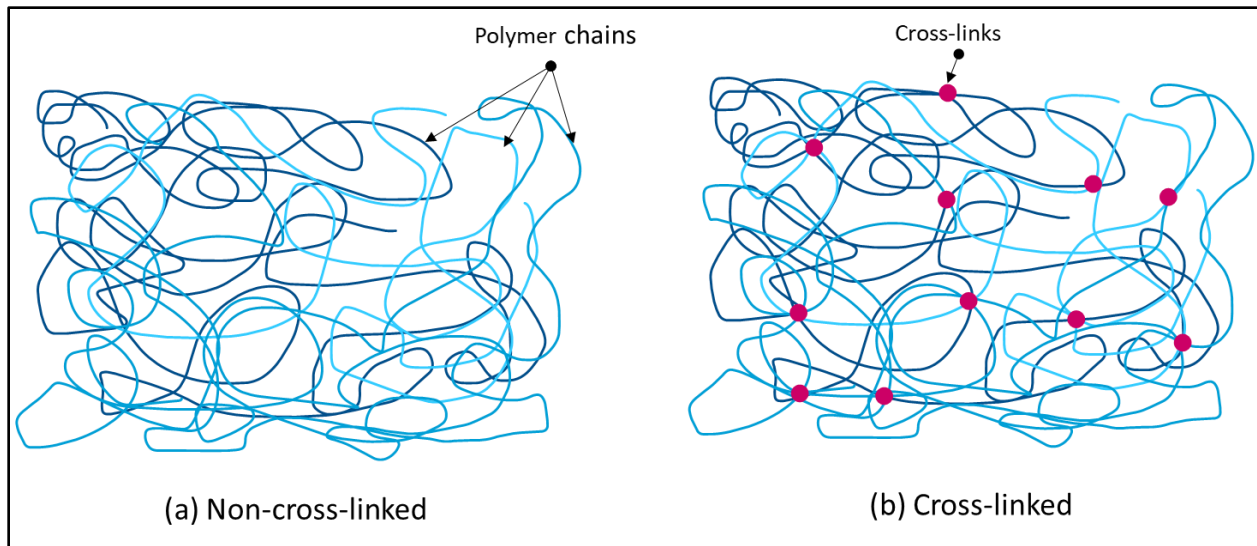
Figure 2.14: The large-scale microstructure of multiple PE chains. Each different shade of blue line represents a separate PE chain. (a) illustrates a non-cross-linked PE and (b) represents a cross-linked PE (cross-links are the magenta dots). Figure modified from [17].

The microstructures can vary in terms of how long the chain is, the degree to which they are cross-linked, and how much they are ordered (crystallinity); however, many polymers tend to be amorphous materials, meaning that the microstructure is not ordered [18]. The result of the amorphous aspect of polymers is that they are often isotropic – their properties do not differ with the direction of applied forces [18].

2.4.1.1 Thermosets and Thermoplastics

There are two major categories of polymers: thermosets and thermoplastics, which, in addition to their intermolecular bonding structure, are differentiated based on their behaviour when temperature is increased [19]. Thermosets are a type of polymer that have been cross-linked; therefore, thermosets cannot be remolded after the initial forming without compromising the chemical structure [19]. In contrast, thermoplastics are not cross-linked and can be remolded without any chemical changes. Due to the lack of cross-linking, thermoplastics are prone to melting at lower temperatures than thermosets [19]. Thermoplastics also have a higher strength when compared to thermosets. Table 2.2 below outlines common thermoplastics and thermosets. Materials that were used for the experimentation in the thesis are bolded in Table 2.2.

Table 2.2: Examples of materials that are thermosets and thermoplastics [19]. Materials that were used during experimentation in the thesis are bolded.

Thermosets	Thermoplastics
- Fluoropolymers - Natural Rubber - Neoprene - Polyester **Silicone** - Structural foams	- Acrylic (ABS) - Nylon - Polyethylene (PE) - Polypropylene (PP) - Polystyrene (PS) **Polyvinylchloride (PVC)** - Teflon (PTFE) **Thermoplastic Rubber (TPR)**

2.4.1.2 Elastomers

Elastomers are a subset of thermoset polymers that have a low stiffness [17]. The low stiffness is due to the limited cross-linking of the polymer chains. The cross-linking also gives the material the ability to be stretched well beyond the original length and recover to its original size when released [17]. Without the cross-links, the material would behave as a viscous liquid and have no stiffness at all [17]. An example of an elastomer is silicone.

2.4.2 Properties of Polymers and Elastomers

The properties of elastomers are dependent on many factors, such as temperature and time (strain rate) [18]; however, they retain their properties associated with elasticity over a wide temperature range [17]. This temperature range will vary depending on the material [18].

In general, within the rubbery regime of the material, the properties and characteristics of polymers and elastomers are:

- Low elastic modulus (low material stiffness) – 500-5000 times less than metals [17]
- High strength per unit mass [17]
- Low density [20]
- High toughness (resistance to cracking/fracture) [17]
- High damping coefficient [17]
- The ability to be stretched beyond the original length [17]
- High Poisson's ratio [20]

- Low electrical conductivity [20]
- Low thermal conductivity [17]
- Easy to form and mold [20]

All of the "low" and "high" characteristics of elastomer properties are relative to other classes of materials such as metals, ceramics, and ceramic glasses [17]. Many of the above properties of elastomers can be manipulated by cross-linking and adjusting the molecular weight and degree of crystallinity [17]. For example, increasing the cross-linking of the material will increase the elastic modulus and increase the fracture toughness [17]. In addition, when compared to metals, polymers do not generally require finishing operations, such as polishing, which makes them easy to form and mold directly into the desired shape with desired surface finish [17].

2.4.2.1 Effects of Temperature on Elastic Modulus

The elastic modulus of thermoplastic polymers and, to a lesser extent, elastomers and thermosetting polymers, varies with temperature [17]. At low temperatures, the elastic modulus is higher, causing the material to be stiffer. At high temperatures, the elastic modulus is low, and the thermoplastic materials enter a viscous flow regime. Figure 2.15 illustrates a typical graph of temperature vs. elastic modulus, as measured using dynamic mechanical analysis (DMA). There are four key regions to highlight in the figure: the first is the temperature region below the glass transition temperature (T_g, indicated) of the material (denoted by 1 in Figure 2.15). In this region, the molecules in the polymer have limited movement as they are tightly compressed [21]. As the temperature increases, the polymers begin to have the ability to bend and stretch, as well as have movement in the side groups. The movement of the chains will allow the material to develop some toughness [21]. Each stage of molecular movement will have its own transition; however, these transitions are faint and can only be picked up through DMA testing [21]. In the range between T_β (indicated) and T_g, known as the glass plateau, the material is stiff but is flexible enough not to shatter under low strains [21]. The next key region is the glass transition temperature (denoted by 2 in Figure 2.15). The glass transition temperature is the temperature under which the material has the most dramatic change in modulus and goes from having glass-like properties to having rubbery properties due to coordination of large-scale motion of the chains [21]. Knowing this temperature is ideal when designing with polymers as it defines one end of the operating range of the material. The third region (3 in Figure 2.15) is known as the rubbery plateau. The rubbery plateau is where the material behaves as a rubber. In this region, as the temperature increases, the chains will lengthen and become more ordered [21]. Eventually,

the chains will be able to slide past each other and the material flows (region 4 in Figure 2.15). The point at which the material flows occurs is known as the melting temperature (indicated in Figure 2.15).
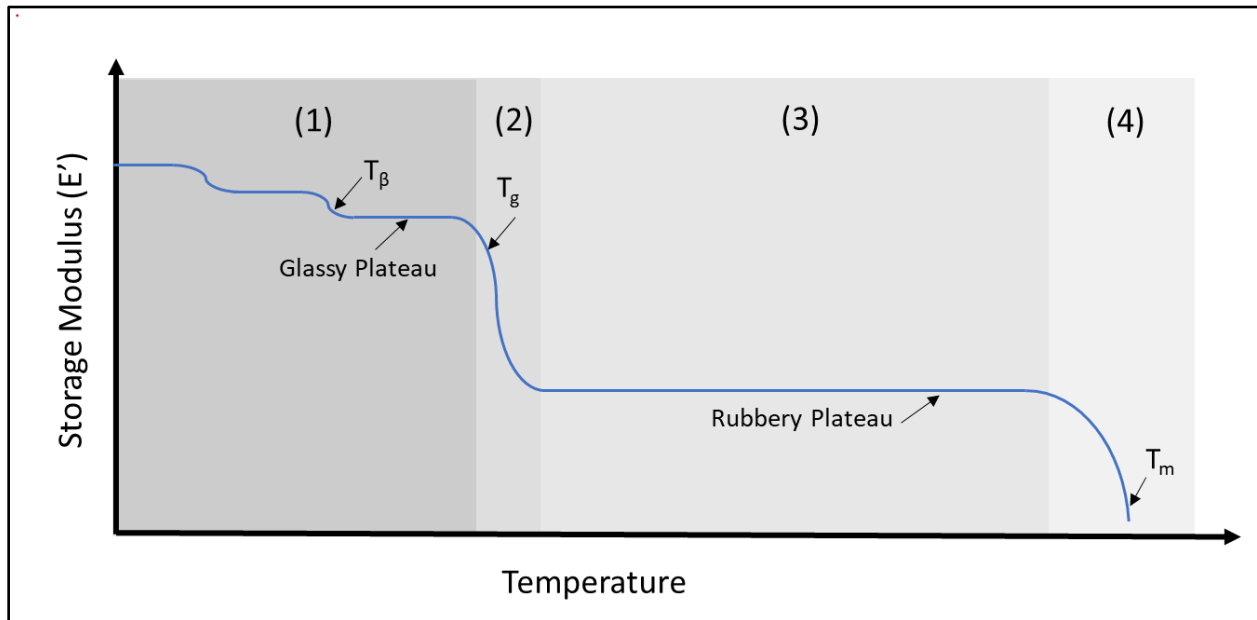
Figure 2.15: The typical storage modulus behaviour of polymers when temperature is changed. (1) is where the polymer behaves as a glass; (2) is the transition temperature range where the polymer goes from glass to rubber in behaviour; (3) is the rubbery plateau region where the polymer behaves as a rubber; (4) is the temperature range at which the polymer melts.

2.4.3 Stress-Strain Curves

The stress-strain behaviours of materials are most often determined from conducting a tensile test on the material [22]. During a tensile test, a uniform tensile load is applied to a specimen until failure. The equipment measures the force required to lengthen a specimen. From the force-displacement data the stress (force per unit area) and strain (how much a specimen deforms compared to its original length) are calculated for the test. Graphing the stress-strain data enables the ability to calculate many properties of a material, such as the elastic modulus, elastic and plastic regimes, and various strengths (e.g., yield strength, tensile strength).

A typical engineering stress-strain behaviour of different polymers at room temperature is shown in Figure 2.16; (A) illustrates the behaviour of a brittle polymer, (B) a plastic polymer, and (C) displays the behavior of a highly elastic (elastomeric) polymer. Each of these materials will exhibit an elastic region, where the material will retain its original shape (strain is recoverable) if the elastic limit has not been reached [22]. As shown, highly elastic polymers, such as elastomers and thermosets, can

withstand higher strain and retain their elastic properties as contrasted to the other polymers. Once each material is loaded beyond the elastic limit, the material will begin to yield and plastically (permanently) deform. If the material fails soon after reaching the elastic limit it is considered brittle [22]. When the material fails, the stress at failure is known as the fracture stress or rupture strength (denoted with an x in Figure 2.16). As observed in Figure 2.16, elastomeric polymers have low rupture strength and ultimate tensile strength when compared to other types of polymers.
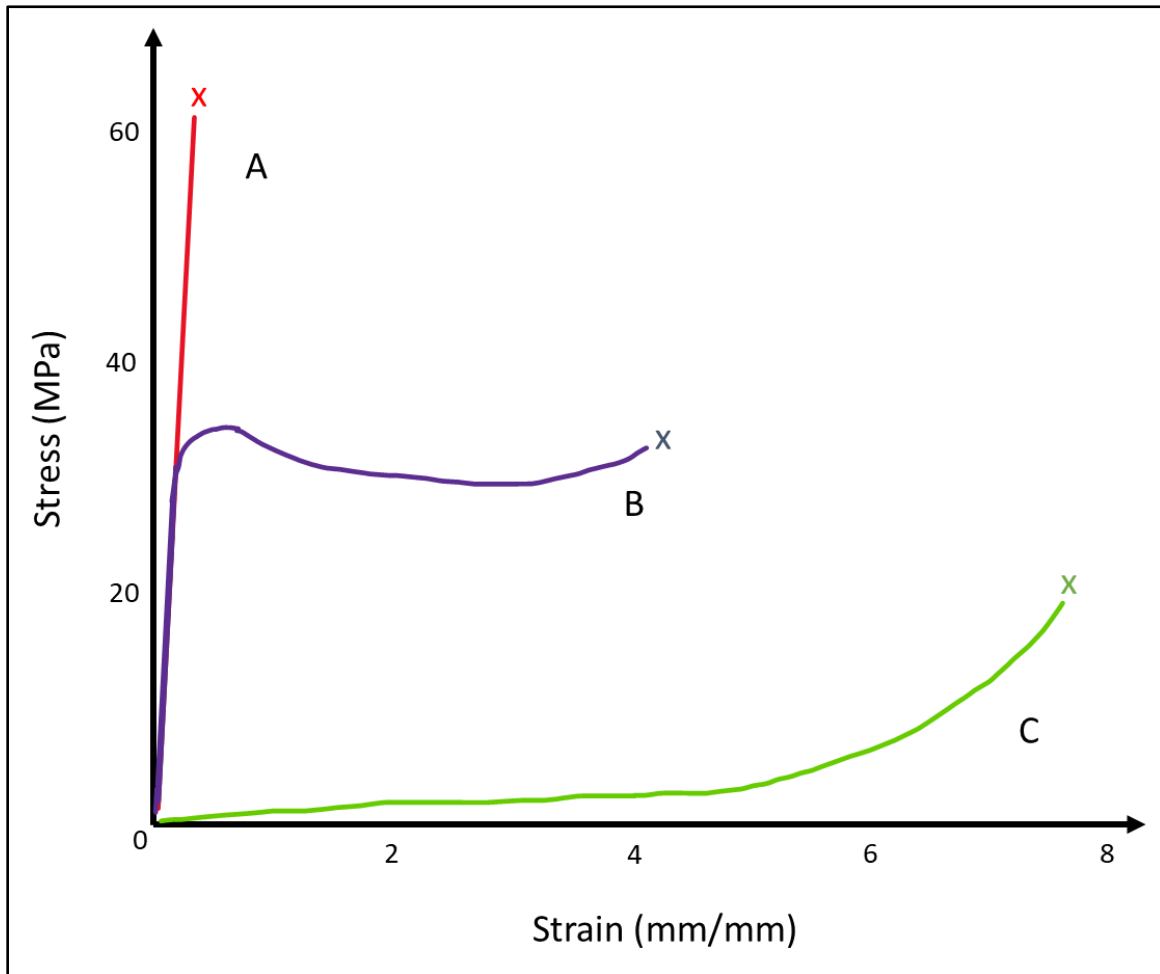
Figure 2.16: The stress-strain curves for different polymers. (a) is a brittle polymer; (b) is a plastic polymer; (c) is a highly elastic polymer. Figure adapted from [22].

2.4.3.1 Effects of Temperature and Strain Rate on the Stress-Strain Curve

The properties of polymers are time dependent. Increasing the strain rate or decreasing the temperature of the material will cause it to be more rigid and cause the stress-strain curve to shift to the top left corner, as illustrated by Figure 2.17 below [22]. The increase in material stiffness due to

the increase in strain rate is a result of the van der Waals forces generated between chains inhibiting the free movement of the chains, causing the material to be stiffer [23]. The stiffness can be due to the ordering of the chains in the direction of the load applied [23]. The opposite of strain rate hardening is creep, which is the stress relaxation of the material over a long period of time [22] (rate and period of time for creep is dependent on the material).
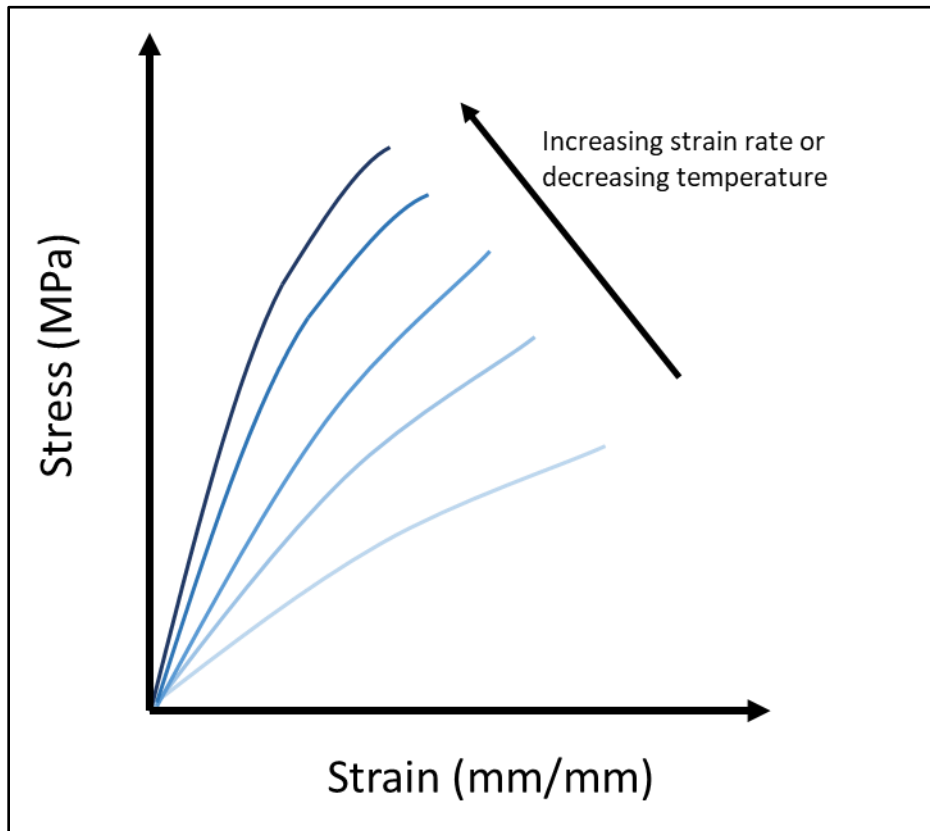
Figure 2.17: The effects of increasing strain or decreasing the temperature on the stress-strain curve of polymers. Figure adapted from [23].

2.4.4 High strain rate failure

Elastomers can fail due to multiple sources such as: temperature, light, radiation, humidity, chemical degradation, bio-organisms, mechanical stress, and electrical stress [23]. For failure from impacts, only high strain rate failures will be examined herein. The common plastic deformation and visual failure indicators of elastomers under high strain rate loading are cracking, crazing, color change, and stress bands [18] [22]. Cracking is initiated in areas with high stress concentrations, for example a void in the material, and will propagate due to the increased stress of the impact [18]. Visually, many

elastomers will also develop crazes, which are load bearing fibrils that bridge the two surfaces of a micro crack together [23].

Color change is another visual indication of failure in an elastomer. The color change is due to the chains breaking within the elastomer [24]. In fact, one elastomer, a spiropyran mechanophore (SP) blend (SP-PDMS), was specifically developed to have a drastic color change in order to study the strain failures of elastomers for ballistic purposes [24]. When the carbon-oxygen bond in SP breaks due to impact, it forms a longer colored merocyanine (MC) chain, which results in a change of color [24].

2.5 Energy absorption

If a structure is adequately designed, both the material and the geometry (structure) of a component (such as a bumper) have the ability to absorb energy through conversion to elastic energy and plastic deformation. Other forms of energy absorption, such as sound and heat, do occur under impact, specifically in the first collision phase, but are negligible compared to the effects of geometry and material [25]. Under dynamic loads, the effectiveness of a bumper will depend on a combination of material properties, such as yield strength, as well as its ability to deform, both plastically and elastically. The design must be able to absorb the kinetic energy by either storing it as another form of energy (e.g., elastic strain energy from compression of atomic bonds) or convert it into inelastic energy via plastic deformation [25]. According to Lu and Yu, for low-velocity impacts, "plastic deformation of structures and materials is the most effective mechanism for absorbing energy of ductile materials and has the widest practical applications" [25].

2.5.1 Energy Absorption via Materials

The energy absorbed by a material is the area under its stress-strain curve (recall section 2.4.3) [17]. When the material is impacted, the impact will generate stress waves that propagate the strain energy away from the impact [25]. The initial kinetic energy absorption by the material will transform the energy into elastic vibrations or store it as elastic strain energy when the intermolecular bonds move [25]. If the stress of the impact is greater than the elastic threshold of the material, the remaining kinetic energy (energy not absorbed elastically) will be absorbed through plastic deformation of the material [25]. Microstructurally, the kinetic energy will be absorbed by breaking the bonds of the chains of polymers or stretch the bonds to the point they will not restore

to their original length, causing permanent deformation [25]. This permanent deformation can be observed via fracture or lasting changes to the original shape of the material.

It should be noted that the area under the stress strain curve only shows the potential for the material to absorb energy at the strain rate tested. Materials that are stiff with a large area under the stress-strain curve do not perform as well for impact absorption as materials with a lower elastic modulus, even if the area under the curve is less. For example, the research by Jones compared the energy absorption capabilities of steel and aluminium tubes of identical dimensions. Steel has a higher strength and elastic modulus than aluminium; however, aluminium was more effective at absorbing energy due to its low elastic modulus [26]. The low material stiffness allowed for the structure to deform progressively, inducing more strain into the entire structure to result in much more material being strained. The steel tubes did not allow for as much strain; therefore, the steel did not absorb as much energy compare to the aluminium [26].

2.5.2 Energy Absorption via Structure and Geometry

Structure and geometry are important to the creation of glove bumpers as changing the geometry can also provide additional energy absorption for the design. To find the energy absorbed by a structure, the force required to displace the material is recorded and plotted against the distance it was displaced. Finding the energy absorbed can be done through tensile testing or done through axial loading experiments through crushing (static impact). The area under the force-displacement curve is the energy absorbed since 1 Nm = 1 J. Figure 2.18 below gives an example schematic of a force-displacement graph from an axial loading experiment. Specimen 1 (blue line) has the potential to absorb more energy than specimen 2 (red line) as it has the larger area under the force-displacement curve.
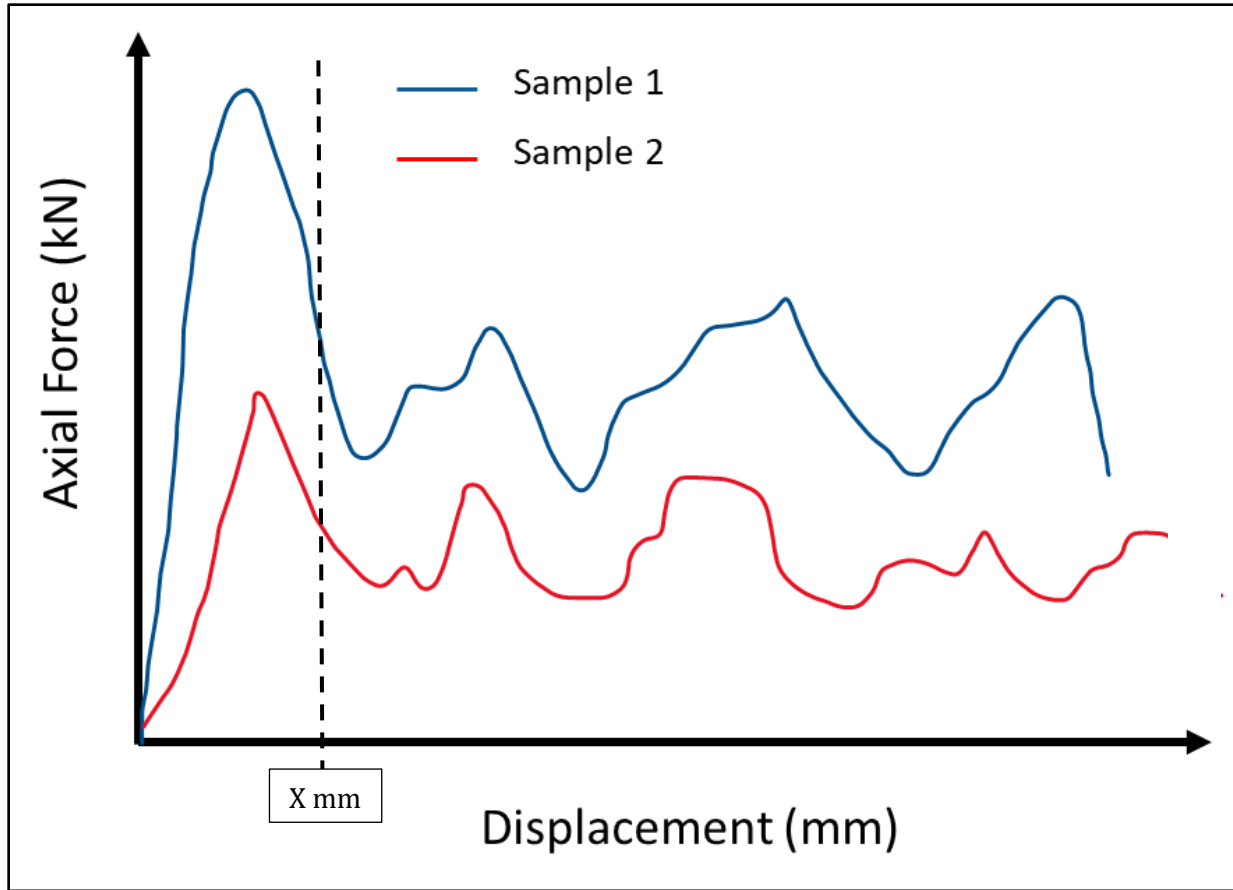
Figure 2.18: A schematic of a force-displacement graph from an axial loading experiment. In the figure, specimen 1 (blue) has a higher potential to absorb more energy than specimen 2 (red) due to the larger area under the curve.

It should be noted that Figure 2.18 only shows the potential ability of each specimen to absorb energy under static loads. Whether or not the specimen will be able to effectively absorb the energy depends on the quotient of the total energy that can be absorbed into the system to the maximum energy up to failure in a normal tensile specimen, which is known as the energy-absorbing effectiveness factor [26]. For example, if specimen 1 in Figure 2.18 above only deforms to X mm (indicated) before there is failure in the material, its energy-absorbing effectiveness factor is low, and it is inefficient at absorbing energy. Thus, a material with a low enough stiffness to allow for deformation (strain) and a geometry that maximizes the deformation will be effective in absorbing energy. This is why thin-walled tubes are used as energy absorbers as they allow for more deformation through progressive buckling [25]

2.5.2.1 Variation in External Geometry

2.5.2.1.1 Cross Section

There have been many studies conducted to show the effectiveness of energy absorption by changing the cross-sectional geometries of steel tubes via crushing (static) and impact (dynamic) loading [27], [28], [29]. In these experiments, tubes were impacted in in compressive axial impact loading . These geometrical experiments have a general consensus that circular geometries absorb more energy than square or rectangular cross-section geometries of the same volume and increasing the tube thickness increases the energy absorbed up until a certain point [30], [31], [32]. For example, in the experiment conducted by Alavi Nia and Hamedani [31], seven cross-sectional shapes of thin-walled tubes were tested via axial compression (static impact) with the same volume and average section area. All of the specimens were composed primarily of aluminium and tested in two wall thicknesses of 1 mm and 1.5 mm. Figure 2.19 below shows the shapes and dimensions of the tubes. The seven cross sectional shapes were a circle with a diameter of 60 mm, a hexagon with a rib length of 31.4 mm, a square with a length of 47.1 mm, a rectangle with outer dimensions of 31.4 mm and 62.8 mm, a triangle with a side length of 62.8 mm, a frustum (bottom portion of a sectioned cone or pyramid) with a minimum diameter of 43.32 mm, and a rectangular pyramid with a minimum cross section of 40 x 41.37 mm.

Figure 2.19: The different geometries of specimens tested by Alavi, Nia and Hamedani [31].

The results of the experiment showed that the circular cross-section tube absorbed the most energy per unit mass, followed by the frustum. For the uniform polygon sections, the higher the number of sides, the higher the energy absorbed. For the maximum force required to crush the tube, the circular and hexagonal cross-sections were the greatest. Figure 2.20 below illustrates the results of the 1.5 mm thick tube tests, (a) is the energy absorbed by each cross-section, numerically and experimentally, and (b) shows the maximum and mean force of each cross-section in the force-

displacement graph. Each cross-sectional shape in Figure 2.20 is denoted with the first two letters of its name with the exception of the circle (Cr) and pyramid (Pr). When comparing the 1.5 mm to the 1 mm specimens, the order of the shapes did not change; however, the 1.5 mm thick specimens absorbed more energy than the 1 mm specimens [31].
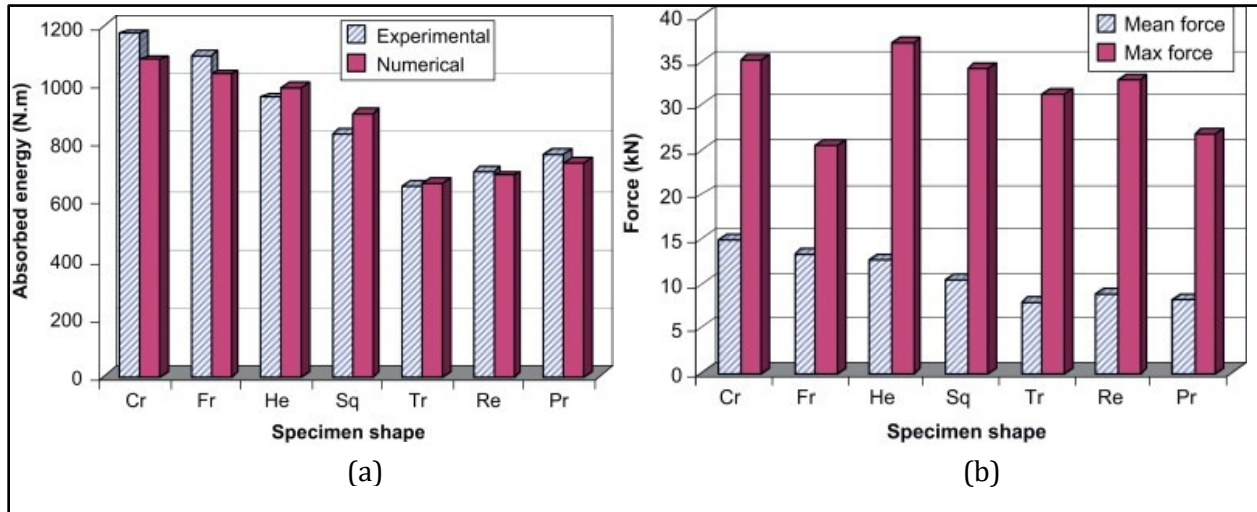
Figure 2.20: The energy absorption of the shapes outlined in Figure 2.19 above, modified from [31].

In Figure 2.20 (a), the absorbed energy was higher in the experimental data for the circle, frustrum, rectangle, and pyramid geometries. The shapes that had a lower experimental absorbed energy were the shapes that did not progressively deform during testing, as observed by Alavi Nia and Hamedani [31]. The numerical data showed comparable results to the experimental data in terms of energy absorbed, with the largest discrepancy of the numerical data being 100 N·m for the circle and square shapes [31].

2.5.2.1.2 External Surface Geometry

Guler *et al.* [33] attempted to look at the energy absorption of different conical shell structures. In the experiment, multiple metallic cones were axially crush tested. The wall thickness of the cones was varied (0.5-2.5 mm) and three geometric cross-sections were studied: hexagons, squares, and circles. Modifications to the baseline geometries were also made by putting ribs or holes into the surface of the cone. Figure 2.21 below shows the different modifications made. The results of this experiment concluded: (1) increasing wall thickness will absorb energy up to a certain value (the value depends on the geometry of the tube), (2) the circular cross-section with 2 mm thickness absorbed the most energy, (3) circular cross-sections performed better than the other geometries, and (4) the

corrugated tubes (S1-S7 in Figure 2.21), performed better as they acted as a guide for plastic deformation, allowing for more places of concentrated stress, and maximized the plastic strain at the corrugation locations.
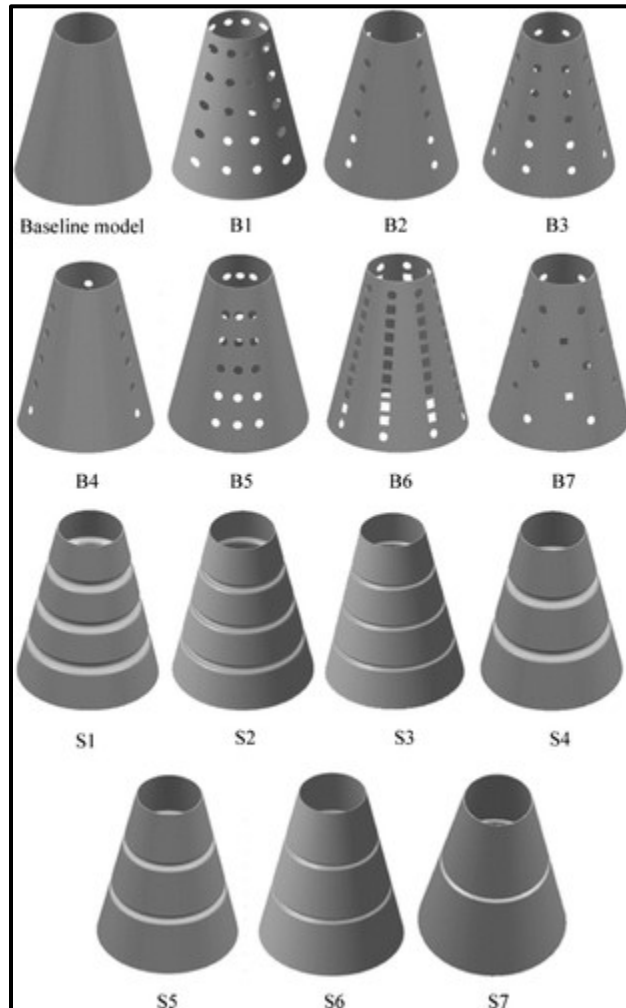
Figure 2.21: The different conical geometries created by Guler et al. to test energy absorption [33]

Many other experiments have been conducted to ascertain the effects of changing the external surface geometry of tubes [34] [35] [36]. Some of the experiments introduced ribbing to the tubes [34], while others made complex origami structures [36]. The results of changing the external geometry were similar to Guler *et al.* [33], where the energy absorbed will be greater in structures that guide the plastic deformation because these geometries allow for the complete deformation of the *entire* structure.

2.5.2.2 Variation in Internal Geometry

2.5.2.2.1 Honeycomb Structures

In a two-part study by Gong *et al.* the effect of creating various layers of tubular honeycomb structures on impact performance was detailed [37]. The orientation of the honeycomb cross-section differed from the other experiments above in that the tube axis was perpendicular to the direction of impact ((a) in Figure 2.22).
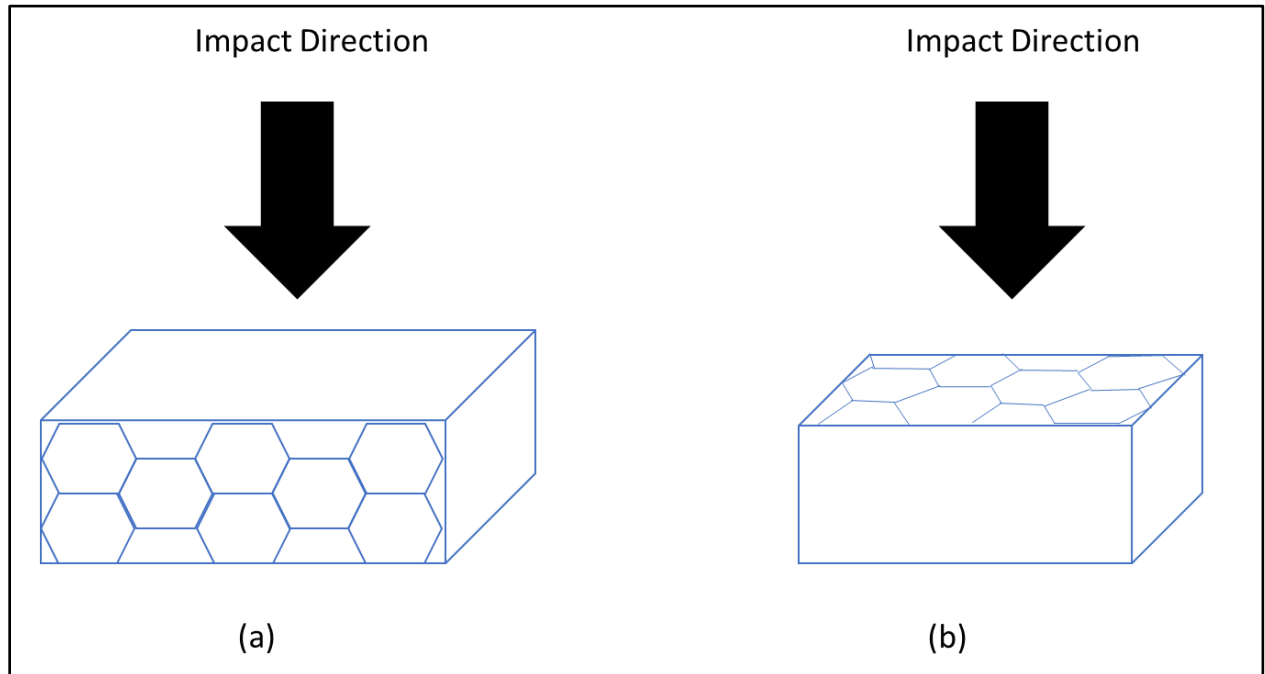
Figure 2.22: The difference of specimen orientation for the honeycomb experiment in relation to impact direction. (a) is the orientation of the specimen by Gong et al. [37]; (b) is the orientation of the specimens during other axial crushing experiments.
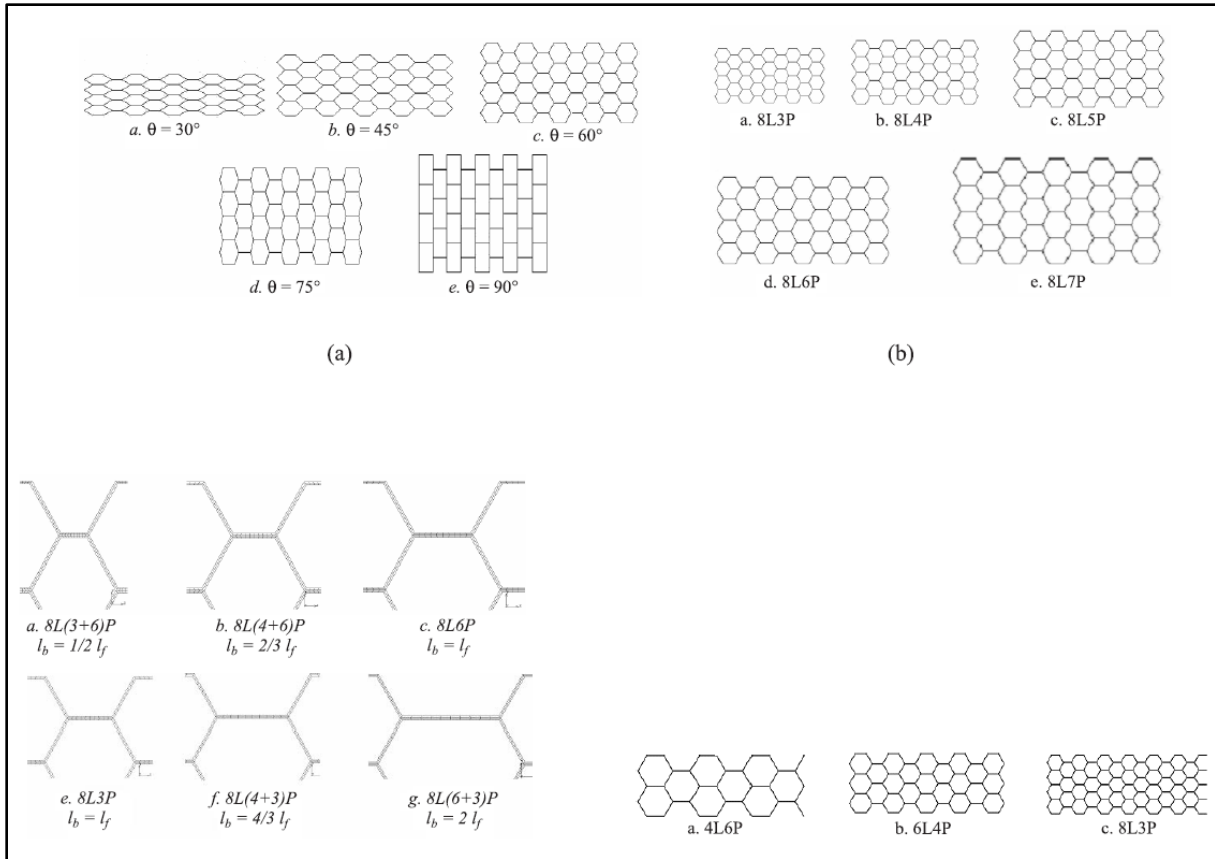
Figure 2.23: The different honeycomb structures analyzed by Gong et al. Taken from [37].

These honeycomb structures were made from textile composites and varied in the cell size of the hexagons, overall thickness of the structure, as well as the cell density [37]. In the experiment, each specimen was tested through drop-testing with 8.3 J of energy at impact. The authors concluded that as long as there was no plastic deformation in the specimen, the energy absorbed by the specimens was similar. The transmitted force, however, did have variations. For the specimens with a greater overall thickness in the direction of the impact, the transmitted force was reduced. The greater the density of the honeycomb structure, the greater the transmitted force – or in other words, the smaller the cell size, the greater the transmitted force [38].

2.5.2.2.2 Internal Lattice

Energy absorption for thin-walled tubes discussed above can be further increased by inserting a lattice structure. In the research conducted by Cetin and Baykasoglu [38], different base centered cubic (BCC) lattice structures were created with varying tube thicknesses and number of lattice cells. These structures were tested for performance independently and as a hybrid with the thin wall tubes.

Figure 2.24 below displays five of the specimens used in the research, with (a) having the smallest number of lattice cells and (e) having the most. The specimens shown were also made with varying tube thicknesses and cell diameters [38].
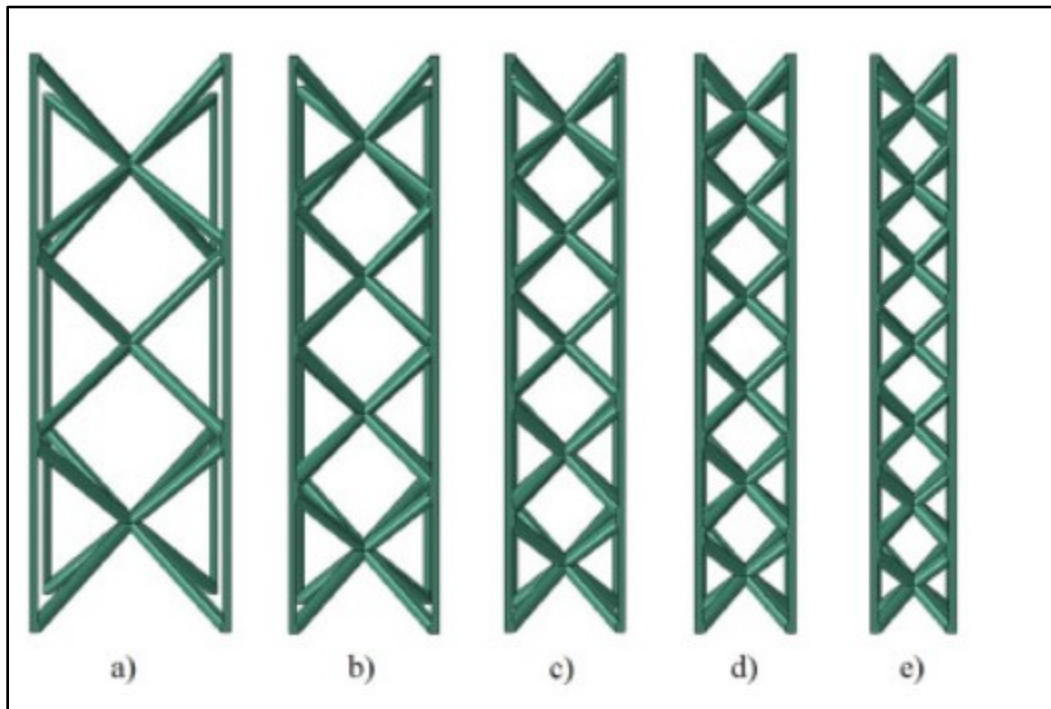
Figure 2.24: The five specimens used in the research conducted by Cetin and Baykasoglu. Taken from [38].

The results of the research showed that the structures with the thicker tube diameter (1.5 mm vs. 0.5 mm) and the larger lattice cells had a higher energy absorption. One reason for the larger lattice cells increasing the energy absorbed was due to the deformation mechanics of the structure – larger cells and low aspect ratios caused the structures to deform and buckle progressively within the structure ensuring that it buckled in multiple locations and not just at one site. The research also showed that adding these structures to the thin-walled tubes will increase the overall energy absorption (the whole is greater than the sum of the parts) [38].

2.5.2.2.3 Air Inclusions

Generating air inclusions into a material has been shown to effectively reduce transmitted force and increase energy absorption [39]. The reduction of transmitted force due to air inclusions can be exemplified by the energy absorption capabilities of foam and bubble wrap [39]. Another example is the foaming of a bulk polymer ethyl vinyl acetate (EVA). For specimens of EVA (with the same

dimensions), inducing 10% air porosity has shown to decrease the transmitted force by 5% for a 4.4 J impact if the pores are fully closed and 30% of the pores are open at the surface [39].

2.5.2.3 Thickness

Thickness is another geometric variable that can influence energy absorption and transmitted force. As demonstrated in the study conducted for honeycombs (see section 2.5.2.2.1) and the study of the impact protection of mouthguards (see section 2.6.3), increasing thickness in the direction of the impact will reduce the transmitted force. For a bulk material, increasing thickness will also increase the energy absorbed. However, there is a trade off point where increasing thickness will not substantially reduce the transmitted force for similar specimens.

2.6 Design Applications of Energy Absorption: Case Studies

There are many impact applications that require kinetic energy absorption in the design. These include, but are not limited to, impact-related sports, bullet proof vests, car collisions, protecting fragile objects during transportation, rock fall protection, and corrugated guardrails [25]. The following section will look more specifically into blunt-force trauma impact protection that is worn on the head as they are similar to gloves in that the design is dictated by impact performance and user comfort.

2.6.1 Type I Helmets (Hardhats)

Type I helmets are helmets where the impact is absorbed by a suspension belt system [40]. There are commonly known as hardhats and are used in industries such as oil and gas, construction, forestry, and mining [40]. For example, in the construction industry, there is a high instance of head and neck injuries from falling objects. Hardhats were developed to protect the head from these impact related injuries by having a hard, plastic shell to distribute the impact over a large area and suspension system to dissipate the energy [40]. The design of the hardhat has the ability to reduce the peak load of a falling object with 50 J of energy [40].

2.6.2 Type II Helmets

Type II helmets are sports and industrial helmets where the shock is absorbed by liner materials (typically foam) [40]. Bicycle helmets were developed to protect the user's head if they fell from their bicycle and crashed onto the road surface while having a mass less than 300 g [40]. The designs of the bicycle helmets must be able to protect from impacts with 100 J of energy as per the international standards [40]. In this scenario, the design should convert most of the energy to irreversible inelastic

energy, as converting the energy to elastic strain energy will result in the stored elastic strain energy being converted back into kinetic energy in the opposite direction of the impact [40]. The elastic strain energy being converted back into kinetic energy could lead to a more serious consequence as the head and neck would be subjected to multiple severe acceleration and decelerations [40]. Thus, helmet designs consist of a hard outer shell and the inner layer is comprised of foam or other lightweight structures that will undergo irreversible plastic deformation on impact.

2.6.3 Mouth Guards

Mouth guards are similar to impact resistant gloves in that they are used to prevent injuries to the scull by absorbing and reducing transmitted force, but the design is dictated by the comfort of the user [39]. A study by Westerman *et al.* [39] attempted to find the ideal thickness of a mouth guard that balanced protection with user comfort using EVA with a shore hardness of 80 A as the material. The experiment tested specimens ranging from 1-6 mm and used the Charpy impact test method to impact the pieces with 4.4 J. The results of the impact experiment showed that there was no significant reduction in transmitted force (or increase in absorbed energy) on specimens thicker than 4 mm.

In addition, it was found that doctors recommended that the area around the incisal edges of the teeth were 2 mm and the labial edges (front) were 4 mm. The difference in thickness is because for the use-case of mouthguards, most of the impacts will be from external blows (direct impacts) to the front teeth. Having the mouthguard reduced to 2 mm on the incisal edges will allow for the user comfort while still adequately protecting the user as the impacts in these locations tend to be from secondary (indirect) impacts of the teeth contacting each other.

The same researchers also conducted a separate experiment where they injected various amounts of hydrocerol (chemical foaming agent) to the EVA in order to make it a closed-cell foam [39]. The results were that the EVA containing 10% weight of hydrocerol reduced transmitted force by 5%. The researchers compared this result to a previous study that used larger open celled bubbles, in which they found there was a reduction in transmitted force by almost 30% for the EVA foam.

2.7 The Design Process

2.7.1 Identifying a Market Need

The design process for glove creation is similar to the one outlined in *Materials Selection in Mechanical Design* by Michael Ashby where a general market need is identified and funneled down into a design solution [41]. The first step in the Ashby design process is to identify a solution-neutral market need. As described above, the frequency of dorsal hand injuries has created a market need: a device that protects the hands from blunt force impact. To fulfill the market need, there are many concepts that can be created. Figure 2.25 illustrates some design concepts generated by the author. In each of the concepts, a hazard of a falling block (red) and a unique control to reduce the risk of injury (green) is shown. Concept (a) shows that robotic equipment or tools could be used to keep the hands away from the hazard; concept (b) shows a shield-like device, where the hands are free to move independent of the structure; concept (c) shows a wearable device, where the structure and hand move together (i.e., a glove). These concepts can be considered as engineering controls or personal protective equipment (PPE) as they do not prevent the hazard from happening, but minimize the severity of the incident; thus, lowering the risk of the incident occurring [42]. In the hierarchy of controls outlined by the National Institute for Occupational Safety and Health (NIOSH), engineering controls - which isolate people from the hazard - should be used before PPE. Thus, the concept of using a robotic design should be used over the other two when possible; however, the best design would be to simply eliminate the falling block hazard according to NIOSH [42].
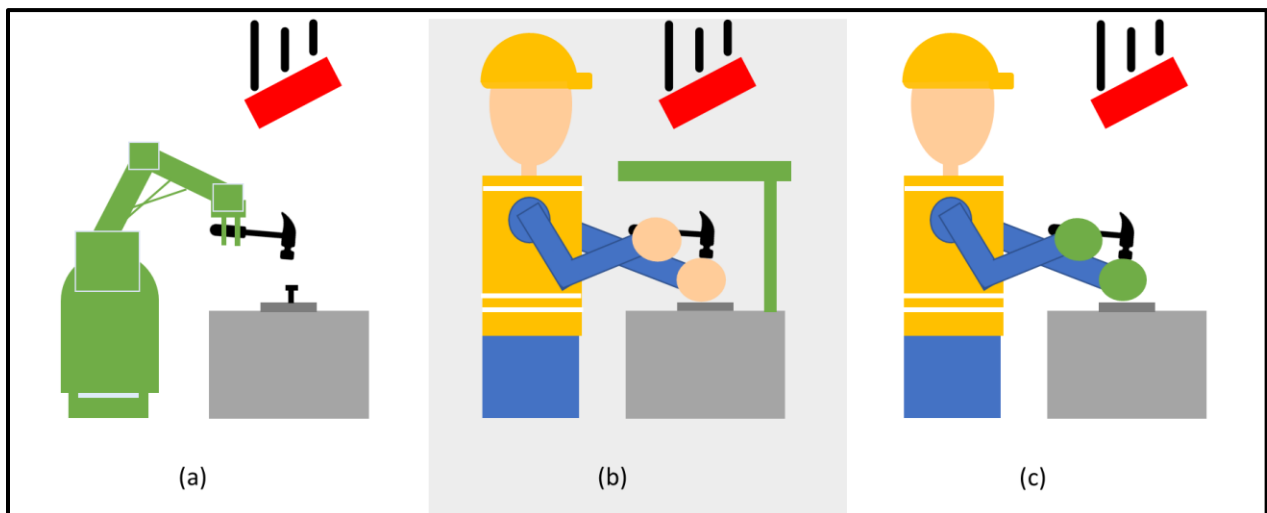
Figure 2.25: Design concepts to protect hands from impacts. From left to right: (a) Is a robotic design without a user, (b) is a shield-like device where the hands operate independently from the device, and (c) is a glove-like device where the hands operate with the device to protect from impacts.

The concepts shown in Figure 2.25 are just a few devices of many that could be created to protect hands from impact. From each of these concepts, many different variances of the device can be developed, creating a multitude of potential prototypes and designs. To narrow down the scope, it is crucial to identify the limitations of each of the devices. For example, although concept (a) is preferred as it minimizes injuries by keeping the person out of the line of fire, using robotic equipment can create more hazards for the user [43]. In addition, there might not be enough space for the robotic equipment to operate. Concept (b) is limited by the usable workspace area too and does not protect the hands from impacts from hand-held tools. Concept (c) increases the dexterity of the user and it is the concept that most likely will result in the hands coming into direct contact with the hazard.

2.7.2 Use Case Scenarios: Selecting the Ideal Concept

Another way to narrow the scope is to identify the use case scenarios that drive the market to need a way to protect hands. Many of the injuries discussed in Chapter 1 occurred in the mining, forestry, construction, and oil and gas industries. All of these industries have similar working conditions in North America and Europe [44]:

- The jobs require working inside buildings as well as outside, where the workers are exposed to temperatures that can range from -40°C to 40°C;
- The jobs require the working environment to change frequently, introducing a variety of new hazards that the worker must be protected against each time the environment changes;
- The jobs all use a form of heavy equipment and machinery;
- The tasks of the job require the user to use handheld tools as well as use fine motor movements to complete the tasks.

For example, take an employee working in Fort McMurray, Canada in the oil and gas industry, where 50% of the incidents are hand and finger injuries [45]. When working outside in Fort McMurray, the temperature can range from a daily low average of -22.5°C in January to a daily high average of 23.7°C in July [46]. With the record lowest temperature and record highest temperature considered, the employee could be subjected to temperatures ranging from -50°C to 40°C [47]. The daily tasks for this employee involve: lifting heavy objects, reaching overhead, bending, pushing and pulling heavy loads, working with high pressure lines and equipment, using handheld tools, and working in confined spaces [48]. Thus, some of the impact related injuries workers are exposed to are:

- Objects falling onto hands;

- Hands getting crushed in between two objects;

- Striking a hand with a handheld tool (e.g., hammer);

- Having a hand slip from equipment or be knocked against different surfaces by the equipment.

Understanding the everyday tasks of workers in the mining, forestry, construction, and oil and gas industries, eliminates concepts (a) and (b) from Figure 2.25 as possibilities. Although both concepts are valid, they are not feasible for the use case due to the shear volume of the variety of tasks, the variety of working conditions, and limited and unpredictable working space for some tasks. Thus, the concept of the glove (concept (c)) should be used as a method for protecting hands when elimination of the hazard and introducing engineering controls are not possible. It is also an effective solution as many workers in these industries already wear gloves to protect hands from other hazards, such as abrasion [44]. In addition, some companies have found that wearing gloves reduces the rate of hand injuries by 50% [45].

2.7.3 Designing Bumpers for Gloves

The creation of the ANSI/ISEA 138-2019 standard demonstrates that there is a demand towards the use of gloves as a method to reduce impact-related hand injuries in the market. The creation of the standard has resulted in creating a secondary market need: a glove that will achieve level 3 protection. To achieve level 3, the glove must be able to reduce the transmitted force of a 5 J drop to less than 5 kN in the nine locations determined on the standard. Reducing the transmitted force is commonly done by placing a bumper on the back of the hand. Some of the possible designs that can meet the standard are shown in Figure 2.26. The designs pictured are: (a) bumpers placed on the nine locations tested by the standard; (b) a large two-piece rigid plate-like bumper covering the entire hand and thumb; (c) a thin bumper with separate pieces for the fingers, wrist, and hand; (d) a thick bumper with separate pieces for the fingers, wrist, and hand; (e) a bumper with individual circular pieces covering the fingers and back of hand; and (f) a bumper with individual diamond pieces covering the fingers and back of hand.
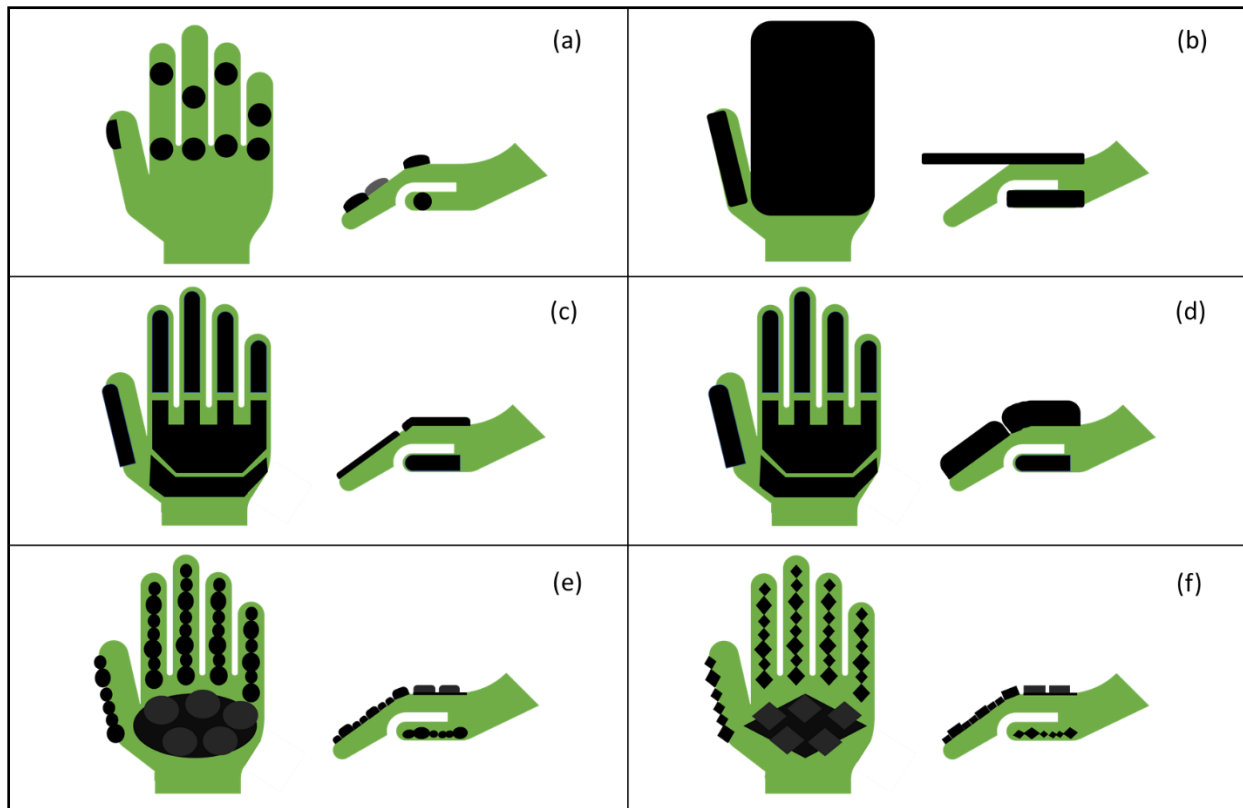
Figure 2.26: Various design prototypes of bumpers on the gloves that can be made to achieve the ANSI 138-2019 standard. The glove is shown in green and the bumper is black. (a) is a design where the bumpers placed only on the nine testing locations. (b) is a plate design covering the whole hand. (c) and (d) are the same design with various thicknesses where the bumpers have separate regions for the hand. (e) and (f) are the same design with changes to the shape of the bumpers.

Each of the designs shown in Figure 2.26 would meet the standard; however, many of them are not feasible as they do not take into the account the needs and wants of the user and producer. For example, design (a), meets the standard but leaves many areas of the hand vulnerable to impact. Another example is design (b), where the rigid plate might be cost efficient due to minimal processing and have great impact performance capabilities due to the volume of material, it does not consider the use case scenario of the user. Having a rigid plate could cause more hazards if the plate gets caught in machinery and it reduces the ability for the hand to fit into confined spaces. The lack of comfort and poor ability to complete the task could lead to the user removing the glove to perform a task and risk a hand injury. In fact, workers are more likely to make mistakes or remove the gloves when they cannot maneuver their hands properly [45]. Thus, designs (a) and (b) can be eliminated as possibilities.

Designs (c)-(f) are all valid possibilities for impact resistant gloves and worth looking into further as they provoke many design questions. Take (c) and (d) for example. Design (c) has a thin bumper on

the glove that will be great for user dexterity; however, is there a material that can be made into a thin bumper and still meet the requirements of the material? What is the cost of that material? On the other hand, design (d) is thick and could limit dexterity; thus, at what thickness does the bumper significantly reduce dexterity? For designs (e) and (f) the question that arises is: what is the effect of shape on dexterity and impact performance?

In addition to the user, a good glove design will also take the producer into consideration. Producers are a business and thus value the profitability of a product, as well as customer satisfaction. Some basic needs of the producer are as follows: a glove with low costs of materials; a glove that is easily produced or worked into a production line; a glove the consumer will wear due to adequate protection and dexterity. Thus, there is an overlap of the needs and wants of the glove user and the needs and wants of the glove producer.

2.7.4 Summary of the Bumper Design Criteria

Table 2.3 below shows a summary of the design criteria for the bumpers of impact resistant gloves. The table outlines the function of the gloves, the variety of performance needs of the user and producer (constraints), the wants of the user and producer (objectives), and the free variables for the design of the gloves.

Table 2.3: A summary of the design criteria for the bumpers of impact resistant gloves.

Design Requirements for a Bumper on an Impact Resistant Glove	
Function	• Protect vulnerable areas of the hand from blunt force trauma
Constraints	• Strength: Must reduce the transmitted force to values outlined in ANSI/ISEA 138-2019 • Stiffness: must be low enough to allow for adequate dexterity • Surface Area: must be large enough to protect vulnerable areas of the hand, but small enough to fit the hand • Durable: is flame resistant, oil resistant, and does not degrade from mechanical wear • Temperature: maintains impact performance in a temperature range of -40°C to 40°C • Processing: easy to process and form • Cost of materials below $9 CAD before processing
Objective	• Maximize tan delta • Minimize thickness • Minimize mass
Free Variables	• Choice of material • Geometry of bumper

2.7.5 Existing Solutions and Materials Used in the Market

As it is shown in Table 2.3, creating a glove design that can meet the design constraints identified is a complex problem with many variables—the very reason there is a proliferation of bumper designs currently used by glove manufacturers, as shown in Figure 2.27 [49]. All of the designs pictured in Figure 2.27 have a bumper placed on the fingers and knuckles to satisfy the impact standard drop locations. The gloves also have varying levels of protection for the metacarpals on the dorsal side. Each design is unique in the shapes and colors of the bumpers. Design 1, 9 and 15, for example, use a skeleton like design of the bumper. Designs 13 and 18 use a single piece for the knuckles and fingers, where most of the designs use separate pieces for the knuckles and fingers.

Figure 2.27: An example of the different designs used for glove bumpers and how there is a lot of variation in design, acquired from [49].

Almost all the designs in the impact glove manufacturing industry use elastomers, a subset of polymers, as the material to construct the bumpers. This material selection is because elastomers have the desired mechanical behaviors to meet identified the constraints at an economical cost [50]. One major gap of the current impact resistant glove market is that there is a lack of gloves that meet the Level 3 protection outlined in the ANSI/ISEA 138-2019 standard. The lack of Level 3 protection shows that there is an opportunity to enhance the design of the impact resistant gloves, which was one of the key motivations for this thesis.

Chapter 2 References

[1] American national standard for performance and classification for impact resistant hand protection. . International Safety Equipment Association 2019 February.

[2] Doyle JR, Botte MJ, Roselius E, Krames C. Surgical anatomy of the hand and upper extremity. Philadelphia, Pennsylvania: Lippincott Williams & Wilkins; 2003.

[3] Hand anatomy. 2015 July 8,.

[4] Human Hand Bones Anatomy N2 image. Available from: https://pixy.org/1356057/. [cited Nov 5,2020].

[5] Carter HV, Gray H, Book St. Metacarpophalangeal articulation and articulations of digit. ulnar aspect. 1858 before date QS:P,+-00-00T00:00:00Z/7,P1326,+-00-00T00:00:00Z/9.

[6] Shahid S. Anatomy of grip. Available from: https://www.kenhub.com/en/library/anatomy/anatomy-of-grip. [cited Nov 4,2020] .

[7] English: Based off: 2015 14 October.

[8] Skin Feeling of the Hand. Available from: https://myhealth.alberta.ca:443/Health/pages/conditions.aspx?hwid=zm6309. [cited Dec 9,2020] .

[9] Tilley AR. The measure of man and woman. 1. publ. ed. New York: Whitney Libr. of Design; 1993.

[10] Galloway A. Broken bones. Springfield, Ill: Charles C Thomas; 1999.

[11] Carpanen D, Kedgley AE, Shah DS, Edwards DS, Plant DJ, Masouros SD. Injury risk of interphalangeal and metacarpophalangeal joints under impact loading. Journal of the Mechanical Behavior of Biomedical Materials 2019 September; 97:306-311.

[12] Choi CQ. Brute Force: Humans Can Sure Take a Punch. 2010; Available from: https://www.livescience.com/6040-brute-force-humans-punch.html. [cite dOct 20,2020] .

[13] What Is a Contusion? Bone Contusions, Muscle Contusions, and Causes. 2018; Available from: https://www.healthline.com/health/what-is-a-contusion. [cited Nov 9,2020] .

[14] Flexor and Extensor Tendon Laceration. Available from: http://www.rushortho.com/body-part/hand/flexor-extensor-tendon-laceration. [cited Nov 10,2020] .

[15] Heller JL. Laceration versus puncture wound: MedlinePlus Medical Encyclopedia Image. 2019; Available from: https://medlineplus.gov/ency/imagepages/19616.htm. [cited Nov 10,2020] .

[16] TREATING NERVE DAMAGE IN THE HAND & WRIST. Available from: https://www.muirortho.com/treatments/hand-wrist/treating-nerve-damage-in-the-hand-wrist/#:~:text=Damage%20to%20the%20nerves%20that,problems%20positioning%20the%20hand%20correctly. [citedNov 4,2020] .

[17] Ashby MF, Shercliff H, Cebon D. Materials: Engineering, science, processing and design. Oxford, UNITED KINGDOM: Elsevier Science & Technology; 2007.

[18] Askeland DR, Wright WJ. The science and engineering of materials. 7. ed., SI ed. Boston, Mass: Cengage Learning; 2016.

[19] Thermoset vs. Thermoplastics - A Comparison of Materials, Advantages and Disadvantages. Available from: https://www.thomasnet.com/articles/plastics-rubber/thermoset-vs-thermoplastics. [citedDec 10,2020] .

[20] Granta Design Limited. Granta edupack . Level 3 2020;20.1.1.

[21] Menard KP. Dynamic mechanical analysis. first edition ed. Boca Raton, FL [u.a.]: CRC Press; 1999.

[22] Callister WD. Materials science and engineering. 7. ed. ed. New York, NY: Wiley; 2007.

[23] Harper CA. Handbook of plastics, elastomers, and composites. 4th ed. New York: McGraw-Hill; 2002.

[24] Xia Z, Alphonse VD, Trigg DB, Harrigan TP, Paulson JM, Luong QT, et al. 'Seeing' strain in soft materials. Molecules 2019 Feb 1,;24(3).

[25] Lu G, Yu TX. Energy absorption of structures and materials. Cambridge: Elsevier Science & Technology; 2003.

[26] Jones N. Energy-absorbing effectiveness factor. International Journal for Impact Engineering 2010 June;37(6):754-765.

[27] Zhang Z, Sun W, Zhao Y, Hou S. Crashworthiness of different composite tubes by experiments and simulations. Composites Part B: Engineering 2018;143:86-95.

[28] Bambach MR, Elchalakani M, Zhao XL. Composite steel–CFRP SHS tubes under axial impact. Composite Structures 2009;87(3):282-292.

[29] Salehghaffari S, Tajdari M, Panahi M, Mokhtarnezhad F. Attempts to improve energy absorption characteristics of circular metal tubes subjected to axial loading. Thin-Walled Structures 2010;48(6):379-390.

[30] Alavi Nia A, Haddad Hamedani J. Comparative analysis of energy absorption and deformations of thin walled tubes with various section geometries. Thin-Walled Structures 2010;48(12):946-954.

[31] Niknejad A, Abdolzadeh Y, Rouzegar J, Abbasi M. Experimental study on the energy absorption capability of circular corrugated tubes under lateral loading and axial loading. Proceedings of the Institution of Mechanical Engineers, Part D: Journal of Automobile Engineering 2015 February 2,;229(13):1739-1761.

[32] Othman A, Abdullah S, Ariffin AK, Mohamed NAN. Investigating the quasi-static axial crushing behavior of polymeric foam-filled composite pultrusion square tubes. Mater Des 2014;63:446-459.

[33] Guler MA, Cerit ME, Bayram B, Gerçeker B, Karakaya E. The effect of geometrical parameters on the energy absorption characteristics of thin-walled structures under axial impact loading. null 2010;15(4):377-390.

[34] Zahran MS, Xue P, Esa MS, Abdelwahab MM, Lu G. A new configuration of circular stepped tubes
reinforced with external stiffeners to improve energy
absorption characteristics under axial impact . Latin American Journal of Solids and Structures 2017 Feb;14(2):292-311.

[35] Sulaiman S, AlHajji M, Jaafar CNA, Aziz FA, Zuhair T. Effect of composite material distribution and shape on energy absorption systems. null 2020:1-10.

[36] Ma J, You Z. Energy absorption of thin-walled square tubes with a prefolded origami Pattern—Part I: Geometry and numerical simulation. J Appl Mech 2014 /01/01;81(1).

[37] Gong X, Gong X, Sun Y. Design, manufacture, and experimental analysis of 3D honeycomb textile composites, part II: Experimental analysis - xiaogang chen, ying sun, xiaozhou gong, 2008. Textile Research Journal 2008 November 1,;78(11):1011-1021.

[38] Cetin E, Baykasoglu C. Energy absorption of thin-walled tubes enhanced by lattice structures. International Journal of Mechanical Sciences 2019 /07/01;157-158:471-484.

[39] Westerman B, Stringfellow PM, Eccleston JA. EVA mouthguards: How thick should they be? Dental Traumatology 2002 February 1,;18(1):24-27.

[40] Wu JZ, Pan CS, Wimer BM. Evaluation of the shock absorption performance of construction helmets under repeated top impacts. Engineering failure analysis 2019 Feb;96:330-339.

[41] Ashby MF. Materials selection in mechanical design. 4th ed. Burlington, MA: Butterworth-Heinemann; 2011.

[42] Hierarchy of Controls. 2015; Available from:
https://www.cdc.gov/niosh/topics/hierarchy/default.html. [citedNov 3,2020] .

[43] McEntee D. The Robots are Here. How Do We Work Safely with Them? 2019; Available from:
https://ohsonline.com/articles/2019/11/19/the-robots-are-here-how-do-we-work-safely-with-them.aspx. [citedOct 16,2020] .

[44] 7 Dangerous Jobs That Involve Working with Your Hands. 2019; Available from:
https://cestusline.com/blogs/news/dangerous-jobs-working-with-your-hands. [citedNov 4,2020] .

[45] Why Impact Resistant Gloves are Vital for Oilfield & Oil Rig Workers. 2020; Available from:
https://cestusline.com/blogs/news/impact-gloves-for-oilfield-and-oil-rig-workers. [citedNov 4,2020] .

[46] Fort McMurray, Canada - Detailed climate information and monthly weather forecast. Available from: https://www.weather-ca.com/en/canada/fort-mcmurray-climate. [citedNov 4,2020] .

[47] Fort Mcmurray Alberta Canada Climate Statistics, with Monthly Temperature, Precipitation, & Snowfall, including Fort Mcmurray Extremes. Available from: https://www.eldoradoweather.com/canada/climate2/Fort%20Mcmurray.html. [citedNov 4,2020] .

[48] Oil and Gas Extraction - Safety Hazards Associated with Oil and Gas Extraction Activities. Available from: https://www.osha.gov/SLTC/oilgaswelldrilling/safetyhazards.html. [citedNov 4,2020] .

[49] Loshek D. Classification of adequate impact protection for hands[dissertation]University of Wisconsin-Milwaukee; 2015.

[50] Nielson LE, Landel RF. Mechanical properties of polymers and composites . 2nd ed. 6000 Broken Sound Parkway NW, Suite 300 Boca Raton, FL: Taylor and Francis Group; 1993

Chapter 3 : Materials and Methods

3.1 Materials

Currently, in the glove manufacturing industry, there are three materials primarily used to construct the bumpers for impact resistant gloves: D3O®, a polyvinyl chloride (PVC), and blends of thermoplastic rubber (TPR). Thus, these three materials were chosen to be analyzed for the thesis. In addition, silicone will be analyzed in depth as Superior Glove is developing it as a potential material to create gloves. Other materials were considered for testing, such as halobutyl rubber (HBR); however, through the material selection process outlined in Chapter 4, D3O®, PVC, Silicone and TPR were deemed the most viable materials for the impact glove bumpers at this point in time (refer to Chapter 4 for further information). This section outlines the basic information and properties of each material as well as the specific blends used for experimentation. Table 3.1 summarizes the experimental techniques used in the thesis to meet the objectives and research questions outlined in Chapter 1.

Table 3.1: Summery of the experimental techniques used for the objectives of the research.

Objective	Experimental Technique	Anticipated Outcomes
Find a material currently not used in the industry	• GRANTA EduPack™	• Identify a potential material for the bumpers
Find the most ideal material to create a glove bumper from	• Drop testing at 20°C, -20°C, and -40°C • DMA temperature and frequency sweep • HSV	• Rank the materials used for bumper selection
Identify the effects of geometry and dimension on transmitted force	• Abaqus® model • HSV • Drop testing	• Identify how small a bumper can get before there is an increase in transmitted force • Identify the effects of circle and square geometries with the same surface area have on transmitted force • Identify which dimensional constraint influences transmitted force the greatest

3.1.1 D3O®

D3O® is a non-Newtonian foam like material, which means that it has strain rate dependent properties. For example, if a force was applied at a low strain rate, D3O® will be easily compressed and flow. If the same force was applied at a high strain rate D3O® "locks up" and does not allow for material flow [1] .The non-Newtonian property of D3O® gives it the ability to absorb energy at high strain rates [1] . D3O® is formed through injection molding. The D3O® used for experimentation was the XT set foam manufactured by D3O®. The properties of the XT D3O® supplied by the manufacturer are displayed in Table 3.2 in section 3.5.1.

3.1.2 PVC

Polyvinyl chloride (PVC) is a low-cost polymer that is created by adding chlorine to the base polyethylene chain [2]. In its purist form, PVC is ridged and inflexible with a low tensile strength [2]. To create a flexible PVC, plasticizers are introduced, which gives the PVC rubber-like properties [3].

The PVC used during experimentation was the Vestolit 7021 Ultra B which uses a plasticizer to give it rubber-like properties. According to the manufacturer, this grade of PVC is good for moulding, casting, and dipping, and should be used when there is low moisture and good storage stability. The properties of Vesolit 7021 Ultra B are shown in Table 3.2 in section 3.5.1.

3.1.3 Silicone

Silicone is a synthetic rubber that is made with a silicone-oxygen (Si-O) polymer chain instead of a carbon-carbon (C-C) chain, making it more stable than the C-C backbone [4]. The relevant properties of silicone are high temperature resistance, good flexibility (i.e., low elastic modulus) at low temperatures, good tear resistance and compression set over a wide temperature range, and it has good insulating properties [2].

Two blends of silicone were used for experimentation in this thesis. The first was Bluesil RTV 1556 silicone. This silicone is a two-component silicone that is fast curing as it can cure with heat, ranging from 100-150°C, within 30 minutes or at room temperature in 16-24 hours. The Bluesil silicone is high strength and it has a high tear cut resistance, chemical resistance, and temperature resistance. Bluesil RTV 1556 also does not shrink during curing, making it an ideal material to mold to specific dimensions. The second blend of silicone was Bluesil TCS 7663. This silicone is similar to the RTV 1556 except that it has a lower viscosity, allowing for a more complete deaeration when the

compound was mixed. The specific mechanical properties of the silicones are shown in Table 3.2 of section 3.1.5.

3.1.4 TPR

Thermoplastic rubber (TPR), also known as thermoplastic elastomers (TPE), are a type of elastomer characterized by their resistance to abrasion, cutting, and scratching [2]. TPR also has a high tensile strength and hardness; therefore, it has a high wear resistance [2]. TPR can have a wide range of hardness due to the amount of crosslinking in the bulk material from vulcanization.

All of the TPR used in experimentation were created by Wizi Co. The specific blend of TPR is TR-4025 and the specimens were produced via injection molding. The properties of TR-4025 are outlined in Table 3.2 in section 3.5.1.

3.1.5 Summary of General Properties

Below is a summary of the properties of each of the materials tested. The information was either taken directly from the supplier data sheet or from the information supplied on GRANTA EduPack™ (created by Ansys Inc. in Canonburg, PA), a materials database. If the information was not supplied or found, it was labeled as unavailable.

Table 3.2: A summary of the properties for the materials used for testing.

Material	Specific Blend	Shore Hardness (A)	Tensile Strength (MPa)	Service Temperature Range (°C)	Elongation at break (%)	Density (kg/m³)	Poisson's Ratio
D3O®	XT SF005	60	1.8	Unavailable	200	520	Unavailable
PVC	Vestolit 7021 Ultra B	50	38-46	-18.2 to 62.3 [5]	40-80 [5]	300	0.4 [5]
Silicone	Bluesil RTV 1556	30	7.1	-55 to 249	660	1020-1220 [5]	0.47-0.49 [5]
Silicone	Bluesil TCS 7663	30	3.6	-55 to 249	215	1020-1220 [5]	0.47-0.49 [5]
TPR (Batch 1)	TR-4025	20-50	1.8	-65 to 107 [5]	600-780 [5]	930-970 [5]	0.49-0.51 [5]
TPR (Batch 2)	TR-4025	40	1	-65 to 107 [5]	643.25	930-970 [5]	0.49-0.51 [5]
Halo-butyl rubber	Exxon bromobutyl rubber 2222	Unavailable	9.9	-51 to 120 [5]	905	910-950 [5]	0.5 [5]

3.2 General Specimen Preparation

3.2.1 PVC and Silicone

The specimens for PVC and Silicone were created for experimentation in this thesis by adding a plasticizer to the base material at a specific weight ratio, (specific ratios detailed in sections 3.2.1.1 and 3.2.1.2). The base material was first transferred to a beaker and weighed. Once the desired amount of the base material was added to the beaker, the plasticizer was slowly added and stirred until the adequate weight ratio was achieved. The materials were then stirred until a visually homogeneous compound was formed. The action of stirring induced bubbles into the compound. In order to remove the bubbles, the compound was either left to sit for 30 minutes if it had a low viscosity (PVC) or vacuumed for 15-20 minutes if the compound had a high viscosity (silicone).

When the compounds were adequately mixed and deaerated, they were poured into two molds and leveled off with a putty knife. Figure 3.1 illustrates the set up of one of the molds before the compound was poured. The mold (1) was placed on a lid (2) to allow for ease of removal from the workbench. A plastic sheet (3) was placed on the bench to collect the excess material that was leveled by the putty knife (4). An overview of the specific dimensions and creation of the mold can be found in section 3.2.1.3 below.
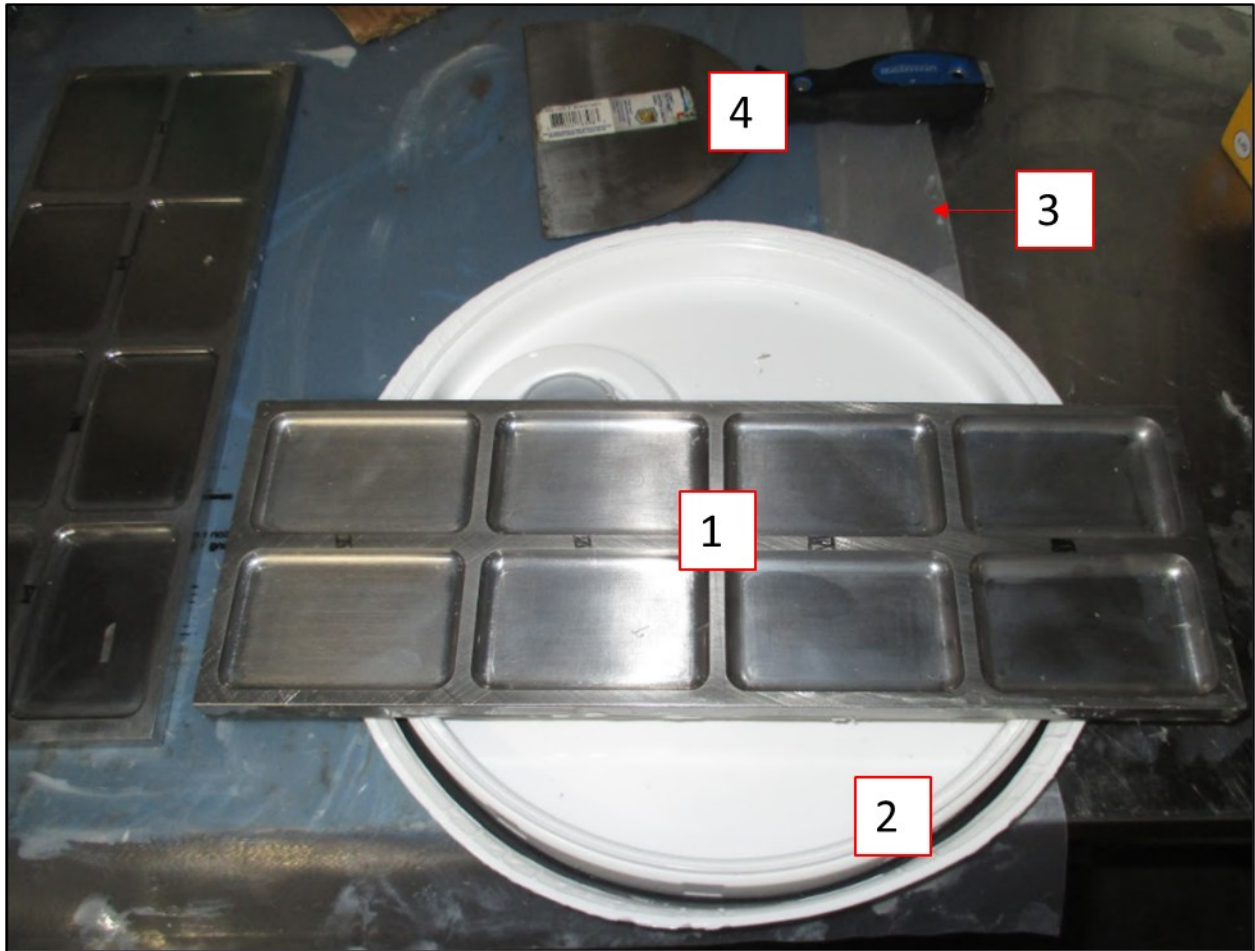
Figure 3.1: The set up for creating the mold. A lid (2) was placed under the mold (1) in order to allow for easy removal. A plastic sheet (3) was placed under the area to prevent contamination and putty knife (4) was used to level the specimens.

Once the compound was poured, it was left in the molds on a flat surface for 30 minutes to allow further deaeration. The molds were then transferred to a pre-heated oven to cure. Washers were used to prop up the corners of the molds in order to keep the specimens' level as the ovens that were used did not have a perfectly level surface.

When the specimens were fully cured, they were removed from the oven and let to cool off in the mold at room temperature for a minimum of 1 hour. The specimens were then labelled with a code identifying the material, batch number, and molded thickness in the upper left corner, defined by the orientation of the mold (see Figure 3.3 of section 3.2.1.4). One batch is defined as a set of specimens created from one compound mixture poured into the molds (the compound was re-created for every batch). Thus, a full batch consisted of 16 specimens with thicknesses increasing in 0.5 mm increments from 0.5-8 mm. In some experiments, only a partial batch was created as the thinner specimens were not needed.

3.2.1.1 PVC

The creation of the PVC used a 1:1 weight ratio of base material to plasticizer. The base material used was Vestolit B 7021 Ultra and the plasticizer was dioctyl adipate (DOA). To create a full batch of PVC specimens, 200 g of each component was used. For curing, the compound was placed into the oven at 175°C for 20 minutes.

3.2.1.2 Silicone

Two separate types of silicone were used. Batch 1 used silicone Bluesil RTV 1556 which comprised of Bluesil RTV 1556 A base material and Bluesil RTV 1556 Clear B plasticizer in a 10:1 weight ratio. This silicone was placed into the oven at 150°C for 15 minutes. The remainder of the batches used Bluesil TCS 7663 as it had a lower viscosity while having similar performance and properties to Bluesil RTV 1556. This Bluesil TCS 7663 silicone used a TCS 7663 base material and TCS 7600 plasticizer in a 10:1 weight ratio and was cured at 110°C for 15 minutes and 120°C for another 15 minutes.

3.2.1.3 Mold Creation and Dimensions

The polished steel mold used to make the PVC and silicone specimens was made by a third-party using dimensions provided. The mold was created from a stainless steel alloy and the surface was polished to allow for a flat surface of the specimens and to prevent the materials from mechanically bonding to the surface. The mold had to be made into two separate plates as the mass and dimensions of the mold would become an ergonomic hazard to the specimen creator if it was one piece.

Figure 3.2 outlines the dimensions of the two plates of the mold. Each tile square measured 84 mm in length and 54 mm in width. The depth of the tiles increased numerically by 0.5 mm, with the 4.5 –

8mm thicknesses on one plate (I) and 0.5 – 4 mm thicknesses on the other plate (II) (Figure 3.2indicates the location of each of the thicknesses). The corners of the molds were rounded with a radius of 10 mm to match the TPR specimens created in the first batch. A fillet at the bottom of each mold was machined in order to allow for easy removal of the specimens.
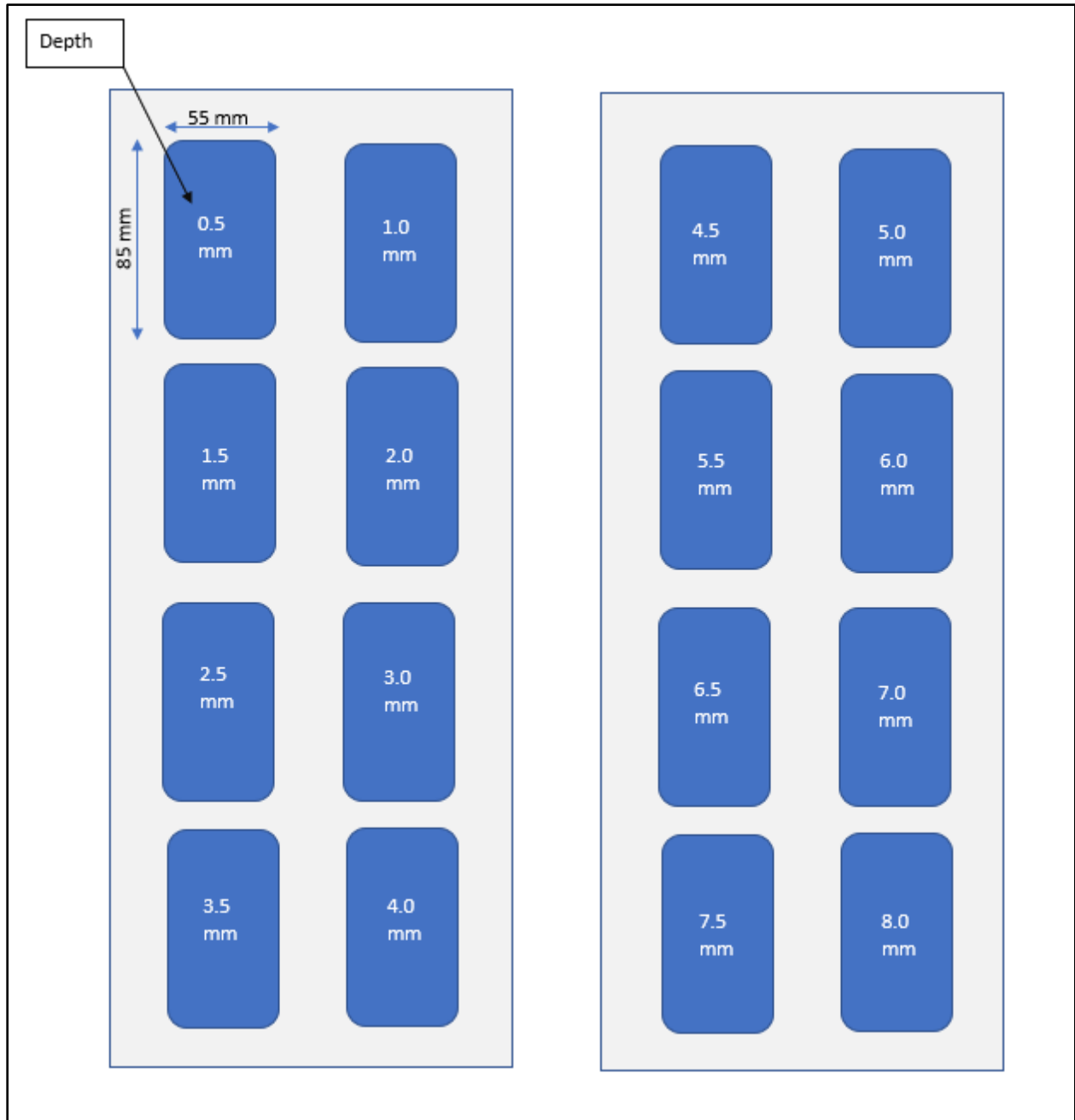
Figure 3.2: A schematic of the mold design that was sent to a third party for manufacturing. The thickness of each mold is given as the depth. The lateral dimensions measured 85 mm x 55 mm (shrinkage caused the actual specimen to be smaller in each dimension by 1 mm). The radius of the fillet and edges were 10 mm, which matched the radius of the first batch of TPR specimens.

3.2.1.4 Measuring Thickness

Due to the warped surface of the oven, the plates were leveled in the oven before curing by eyeballing the top surface at a perpendicular angle (a level was not available to use due to contamination concerns). To level the plates, metallic scrap washers were used to prop up the required corners. As levelling the plates by sight has large margin of errors, the specimens required a particular way to measure the thickness (eyeballing the mold was recognized as inaccurate, which is why multiple measurements of thickness were completed). The margin of error through eyeballing was also compounded by the initial leveling process of scraping the excess material and the shrinkage of the material when it was cured. Thus, each specimen was measured for thickness using an Ames Logic™ Basic Digital Indicator (manufactured by B.C. Ames in Melrose, MA) thickness tester on the left, middle, and right locations of the specimen along the long axis (in the center of the short axis). For the thickness measurements, the specimen label was oriented at the bottom left corner of the specimen, as shown in Figure 3.3.
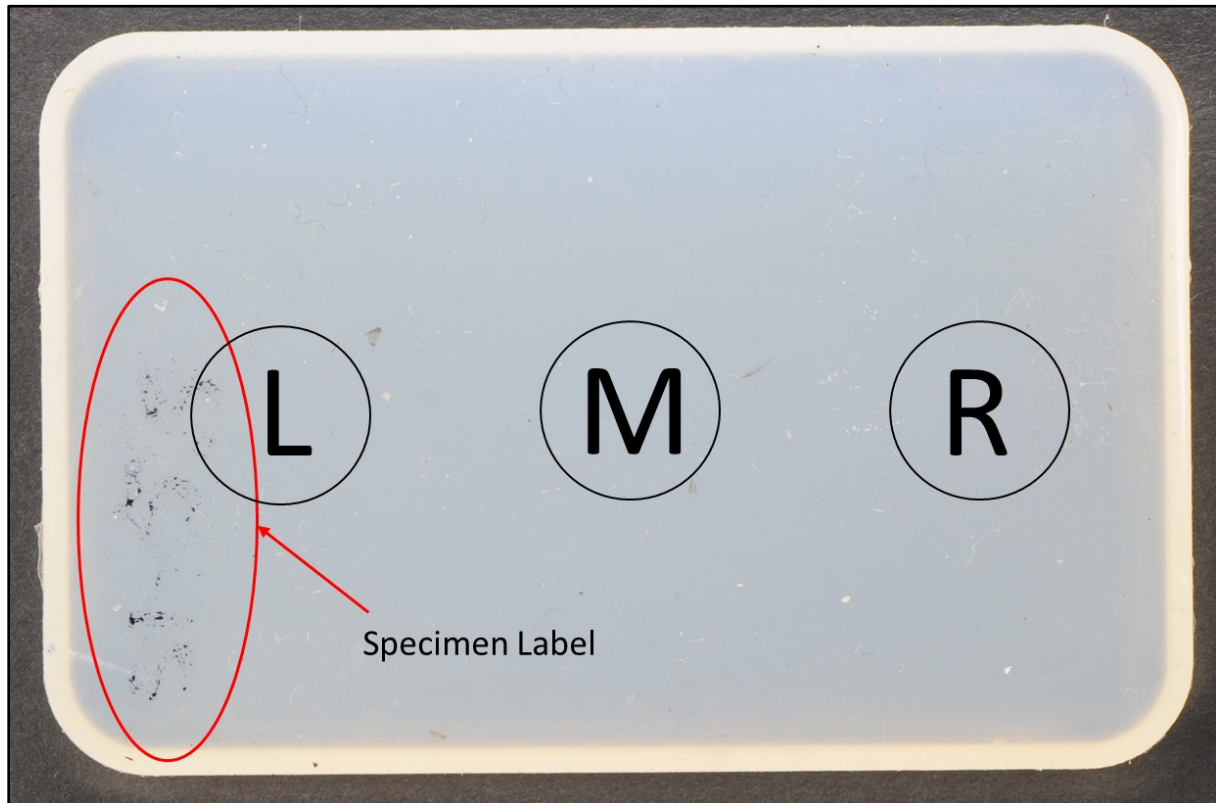
Figure 3.3: The locations for measuring thickness of the 5.5 mm thick silicone specimen for batch 1. When the thickness was measured, the specimen label was placed in the lower left corner (indicated) and a measurement was recorded for the left (L), middle (M), and right (R) side of the specimen.

3.2.2 D3O® and TPR Specimens

Ready-made specimens of D3O® and TPR were provided by the suppliers. For D3O®, the material was supplied as a 6mm thick sheet. The length and width dimensions (84 mm x 54 mm) were measured with a ruler- that had 0.5 mm increments - and cut with a razor blade from the bulk sheet to create the rectangular-shaped specimens.

The TPR specimens were created through injection molding. With injection molding, the TPR is injected into a pre-made mold through a gate. In the first batch of specimens tested (thickness testing and hardness testing), the gate was positioned in the center of the specimen. The first batch of specimens had a thickness range of 4.5 – 8.5 mm, increasing by 0.5 mm and a shore harness range of 20 A to 50 A. The second batch of specimens ordered had the gate placed at the edge, as there was an uncertainty of the effect the gate geometry had on the impact performance of the previous batches. The second set of specimens had a thickness range of 0.5 – 8 mm and a shore hardness of 30 A, to match the silicone and PVC specimens created. All of the specimens measured 84 mm x 54 mm in length and width, respectively. Figure 3.4 illustrates the differences in the placement of the gates of the specimens, (a) is batch one with the gate in the centre; and (b) is batch two with the gate at the side.
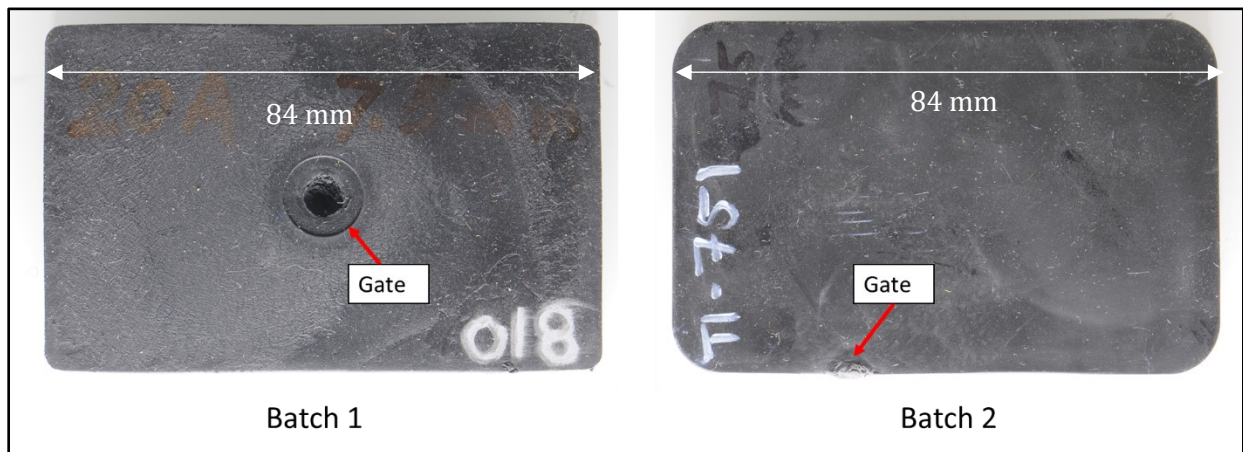
Figure 3.4: A side by side comparison of the gate locations for the two batches of TPR. For batch 1, the gate was located in the center of the specimen (indicated). The effects of the gate on the transmitted force were a concern, so the gate was moved to the edge for batch 2 (indicated).

3.3 Impact Testing Apparatus

All of the drop tests conducted in this thesis used a SB069 Cadex Mini Twin Wire Impact Machine (Cadex Inc., Quebec City). The rating for the testing machine was 110-220 Vac, 50/60 Hz. A

photograph of the machine and set up is shown in Figure 3.5. As discussed in Chapter 2, section 2.2, the machine consists of a striker guided by two wires and an anvil attached to a load sensor. The additional features, that are unique to the machine, a hand-crank (1), to raise and lower the striker, a ruler and guide (2), to measure the drop height of the striker, a locking mechanism to lift and drop the striker (3), and a speed sensor (4) to measure the velocity of the striker at the impact. These features are different than machines that are used by a third-party tester to verify the gloves. The third-party tester uses an automated machine that with a press of a button will guide the striker up to the desired height and calculate the velocity at impact. A custom wooden table was constructed (5) in order to provide more support and minimize movement of the specimens being tested. Without the wooden table, the specimens were prone to falling off the anvil after the initial strike or shifting positions from the initial set up.
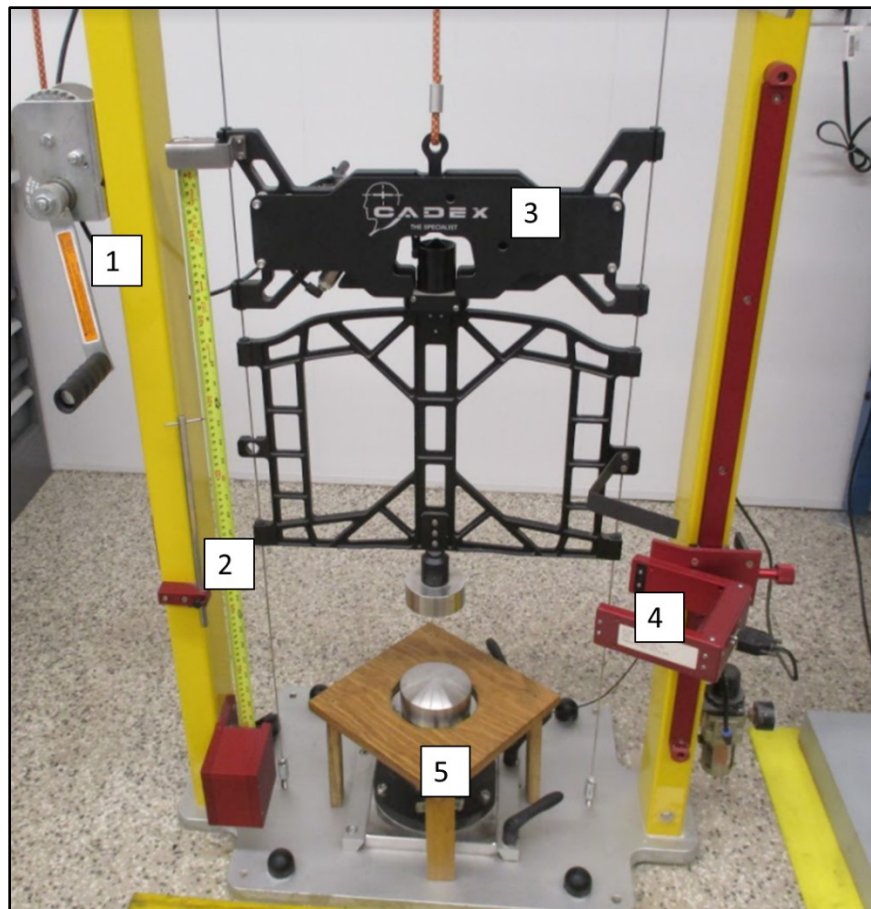
Figure 3.5: The testing apparatus for the impact experiments. (1) Is the hand crank; (2) is the ruler to measure drop height; (3) is the locking mechanism that releases the striker; (4) is the speed sensor to measure the velocity of the striker at the start of the impact; and (5) is the custom wooden table to provide stability to the specimen tested.

The speed sensor is an important feature of the set up. The calculation of the theoretical drop height (20 cm, refer to Chapter 2) does not account for friction. By setting up a speed sensor, the experimenter can be confident that the striker is contacting the specimen with adequate energy. If the energy is too low at impact, the impact performance results for the specimen will be inflated. In the experiments conducted in this research, the actual height of the drops to achieve a 2 ± 0.4 m/s impact velocity was 22 cm. The speed sensor works by calculating the velocity of a metal band attached to the striker guide (the speed sensor 4 in Figure 3.5) when it passes through the speed sensor's time gate. To set up the speed sensor, there is an adjustable knob on the side to move the sensor up and down. The sensor also has a light on it to indicate if the metal band is in the time gate. If the light is on, the metal band is in the time gate; therefore, the sensor is adjusted to a height just after the light is off. The speed sensor is created by Cadex Inc. (Quebec City) and requires a yearly calibration by a Cadex Inc. representative.

There were also two separate load cells for the tests, one for the 1-6 kN transmitted force range and one for the 6-9 kN range. Using the correct load cell was important for the test in order to get accurate results (see Appendix B about accuracy of measurements, in general the margin of uncertainty was 250 N for the drop testing). The machine was not designed to test transmitted forces greater or equal to 10 kN. Thus, a load sensor that had a higher range than 9kN was not required.

3.3.1 Testing Procedure

All tests followed the procedure that is outlined in ANSI 138-2019 [6]. The only exception was the "accelerated repeated impact testing" (ARIT) tests that were conducted modified some of the steps in order to shorten the set-up time as the results of the experiment were intended to show time dependent behaviours of the. The procedure, as per the ANSI standard, is as follows:

1. Mark intended testing area of the specimen;
2. Place specimen on the anvil, lining up the intended testing area with the center of the anvil (which should also be the center of the striker);
3. Using the hand crank, lower the striker so that it is just touching the top surface of the specimen;
4. Adjust the speed sensor so that the indicator light is off when it is just above the metal piece attached to the striker guide;
5. Use ruler and hand crank to raise the striker up 22 cm (to account for friction);

6. Keeping clear of the impact area, turn on machine and hit test on the screen;

7. Press button next to testing screen to drop the striker;

8. Record impact and velocity indicated on the screen.

3.3.2 Load cell output

With every drop test conducted, the load cell records the transmitted force and time information and displays a graph on a connected screen. Figure 3.6 illustrates an example of a typical output from a drop test. In a typical drop test, there is an initial period where no force is recorded (1), this is the time between the depression of the "drop" button and the striker contacting the specimen. Next there will be a large initial force peak (2), followed by multiple oscillations with substantially and sequentially, smaller peaks (3). These oscillations have a negative force due to the anvil moving up and down slightly during the test – this was discovered through high speed videography discussed in section 3.5. The oscillations after the first initial peak are consequently attributed to the anvil moving up and down rather than the specimen bouncing multiple times. Thus, only the initial peak is taken into consideration for the impact performance of the specimen. The maximum transmitted force that is experience by the anvil is recorded on the top right corner of the screen (4). The velocity of the metal strip passing through the timing gate of the speed sensor is displayed on the bottom right portion of the screen (5). It should be noted that the test results displayed in Figure 3.6 are from an initial drop height of 20 cm, showing that friction will reduce the impact speed by 0.07 m/s (in some tests, it reduced it by 0.1m/s).
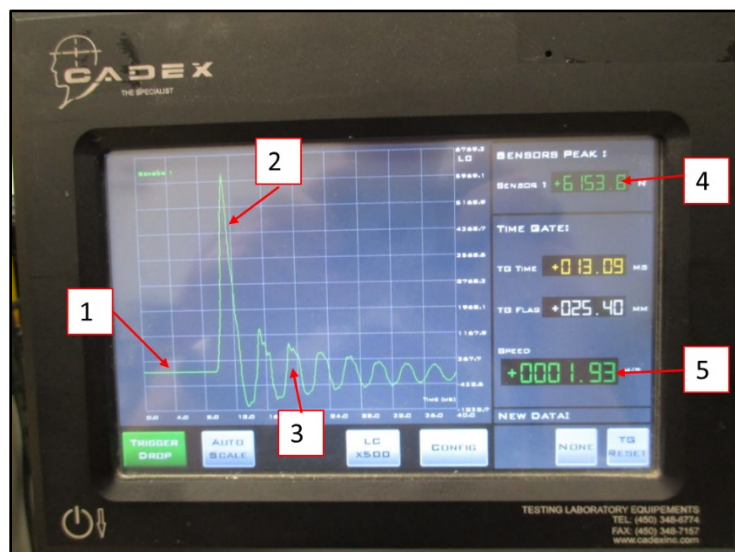
Figure 3.6: An example of a typical output from a drop test. (1) is the time for the striker to drop; (2) is the initial force peak; (3) are the subsequent anvil oscillations; (4) is the peak force output; (5) is the velocity measured of the drop.

Occasionally, the load sensor would give an incorrect reading, which could have been due to an incorrect signal or loose wire. These incorrect readings were identified by either the shape of the impulse graph displayed not fitting the typical large peak and subsequent oscillation pattern or a peak force ±1 kN out of the expected range (expected range based off of pervious testing of the same material and thickness). In addition, the velocity displayed on the screen would commonly be out of the 2 ± 0.1 m/s range for these tests, indicating that the initial strike may not have been recorded. Figure 3.7 displays two examples of incorrect screen recordings; (a) shows an unusual shape of the graph with a force 5 kN out of the expected range and velocity out of range; and (b) illustrates a graph that has a velocity and force within expected range but the impulse curve is randomized indicating that the results cannot be used as the data from the test could be unreliable.

(a)   (b)

Figure 3.7: Examples of incorrect readings. If a test produced a reading shown in the Figure, it was deemed void.

3.3.3 Finding the Impact Zone

One critical unknown from the Cadex Mini Twin Wire Impact Machine set up was the area of contact between the striker and the anvil. Due to the anvil's curvature, the impact area or zone of the two surfaces cannot be easily calculated. It is critical to know this area so that the experiments had a reference point of the immediate impact zone. To find this area, epoxy was placed onto the center of the anvil and the striker was lowered until it was completely resting on the anvil (independent of the locking mechanism). The imprint that was left from the contact is observed in Figure 3.8, with (a) showing the imprint left on the anvil, and (b) showing the imprint left on the striker with a ruler for reference. The imprint on the anvil had a more circular shape that measured 20 mm in diameter. The striker had more of an elliptical shape (possibly due to wetting) that measured 20 mm at the longest

axis. The results from the ARIT impact testing in Appendix B further demonstrated that the immediate impact zone of the anvil and striker is circular with a diameter of approximately 20 mm. Thus, the surface area of the impact zone was determined to be 314 mm².

(a)   (b)
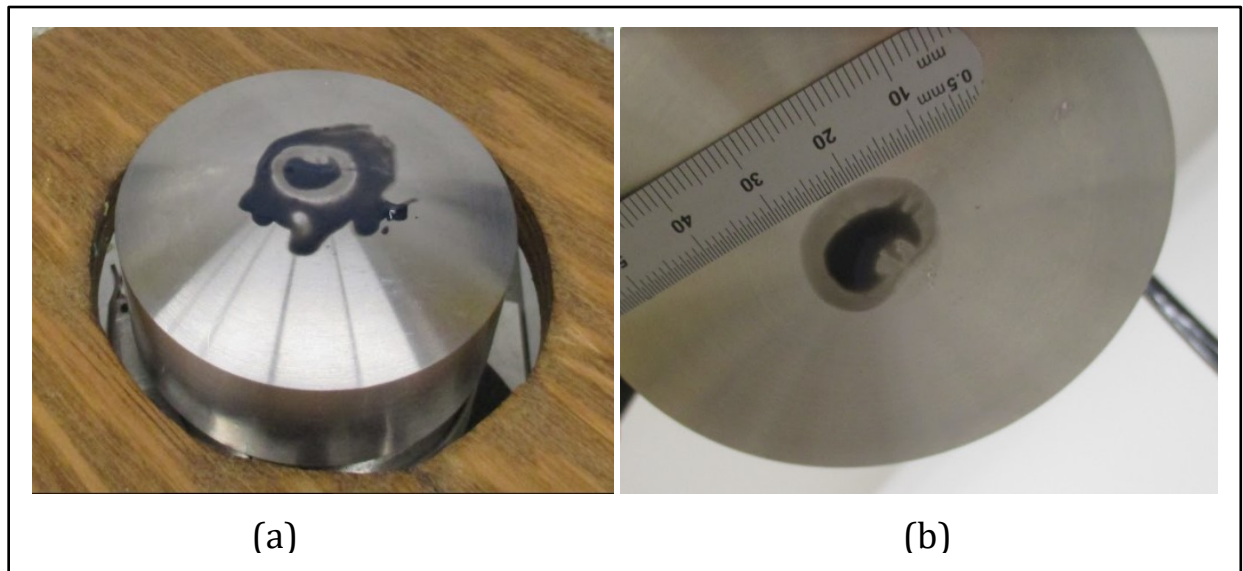
Figure 3.8: The contact surface area of the striker and anvil. The diameter of the circular shape was measured to be 20 mm, corresponding to a surface area of 314 mm².

3.3.4 Securing Specimen

There were three main methods used in the tests conducted to ensure minimal movement of the specimen. The first was the use of the custom wooden board. The wooden board was primarily used for large specimens, such as testing a glove. The problem with the wooden board is that it still allowed for lateral movement of the specimens, especially the 84 mm x 54 mm tile specimens that were created in section 3.2. Thus, the second method for securing the specimen was to use a clip secured to the wooden board out of the line of fire of the striker so that it would not interfere with the tests. For this research, a generic 32 mm black binder clip, a screw, and spare washers from Superior Glove's machine shop were used. The spare washers were added until the desired height was achieved, and a washer was added above the clip in order to secure it (refer to Figure 3.9 in section 3.4 for the clip set up). The method of using a clip required the specimen to be in a slight flexed position before it was tested; however, it did not have an impact on the transmitted force output when the same specimen was tested with and without the clip (specimen was tested on opposite sides to avoid strain hardening effects). The clip was an effective way to secure the specimens when the specimen size remained 84 mm x 54 mm. For any tests completed that the longest dimension was

less than 80 mm, double sided tape was used to secure the specimen. The effects that the tape had on impact performance were conducted by comparing the same specimen tested with tape and without tape (see Appendix B). While the tape did decrease the transmitted force, it was consistently in the 150 N range and that factor could be added to the results of the test to achieve a more accurate result. However, as the testing herein was for comparison purposes—not absolute magnitude—the values of transmitted force were not corrected for force reductions due to tape.

3.4 Impact Tests Conducted

All of the impact tests conducted were performed using the Cadex mini twin wire machine in a temperature and humidity-controlled room (as per the ANSI/ISEA 138-2019 standard). For all of the tests, the temperature of the room was 20-21°C and the humidity was 63-65%.

3.4.1 Accelerated Repeated Impact Testing

Accelerated repeated impact testing (ARIT) testing was conducted to see the effects of the material being impacted multiple times in a short time (time was dependent on the ability for the experimentor to set up for and record each test, which ended up being 20 drops in 5 minutes). This testing was performed to determine if there was a noticeable change to the performance of the specimen, as defined by the transmitted force of each drop, if it were to be impacted subsequent times. The purposed of conducting ARIT is because a possible use-case scenario of the gloves is a worker having their hands repeatedly impacted in a short amount of time. Recall section 2.7 of Chapter 2 for examples of use-case scenarios.

To conduct the ARIT tests, five separate thicknesses of TPR were used: 4.5mm with a hardness of 20A and 50A, 7.5 mm with a hardness of 20 A and 50 A and 8.5mm with a hardness of 30A. These specimens were chosen by the minimum and maximum thickness specimens supplied for 20 A, as the 20 A was not supplied thicker than 7.5 mm. The 8.5 mm and 30A specimen was chosen as it was the thickest specimen with a mid range hardness. The specimens of TPR were secured to the same location by a clip installed onto the wooden board around the anvil, as shown in Figure 3.9. Pieces of tape were placed along the anvil aligning with the length and width of the original position of the specimen. The placement of the tape had a purpose as a visual indicator of the lateral movement of the specimen. Once the specimen was secured, the test was set up as per section 3.3.1, following the ANSI 138-2019 standard. The test was then performed, and the transmitted force was recorded. The striker and striker guide were immediately lifted up to the locking mechanism to repeat the test (total

of 20 separate impacts). In a standardized test, the striker would have to be lowered and remeasured for the drop height; however, this takes over 1 minute to do this, these steps were skipped in favour for the more time efficient step of lifting the striker back up to the locking mechanism. To ensure the drop height was the same for each impact, the height of the striker was checked before each drop. Using this short cut method, 20 drops were able to be conducted within 4 to 5 minutes, depending on if the striker drop height needed to be adjusted.

Figure 3.9: A example of how the ARIT tests were set up. A clip was used to hold the specimen in place and two pieces of tape were aligned along the edges to ensure minimal movement of the specimen.

3.4.2 Effects of Surface Area on Impact

The effects of surface area on impact experiment was designed to address the trade off point of transmitted force and surface area. (i.e., at what surface area size is there diminishing returns on transmitted force?).

With the effects of surface area on impact experiment, one specimen tile was used during the entire round of testing. The tests initially started with the thickest specimens created as they would provide

the lowest transmitted force baseline, as discovered through thickness testing, and thus the highest working range, which is defined as the difference between the 10 kN maximum for testing and the initial transmitted force of the full specimen tile. Additionally, the use of the thickest specimen would minimize the risk of damaging the machine or cause the load sensor to be uncalibrated.

A piece of double-sided tape was used to secure the specimens to the anvil in order to prevent the specimens from moving, especially the specimens with a small surface area, as this could damage the drop tester. From the testing results outlined in Appendix B, the tape had an effect of decreasing the transmitted force by 150 N. For consistency, the same piece of tape was used for the entire specimen tile – from the first full piece test to the smallest surface area test.

To conduct the surface area analysis experiment, a 100 mm piece of double-sided tape was carefully placed over the anvil impact zone, ensuring that there were no wrinkles or deformation in the piece of tape. The specimen was then measured along its initial long side (side A) and its initial short side (side B). For all of the specimens, these original measurements were 84 x 54 mm for side A and B, respectively. The specimen was then placed on the anvil, with the specimen shifted to the left so that the middle of the right side was tested (refer to Appendix B for diagram). The shifted placement of the specimen had the purpose of ensuring that a particular area of the specimen was not repeatedly tested as strain hardening and softening is prevalent in materials, as demonstrated by the results of the ARIT testing. In addition, the ARIT testing showed that the impact-affected area of the specimens extended 40 mm in diameter for the lower hardness specimens; therefore, testing the bulk specimen on one end will return the same results as if it were tested directly in the middle.

The specimen was tested as per the procedure outlined in section 3.3.1, which is further detailed in Appendix B. When the drop was complete, the specimen was removed, and the tape remained on the anvil. The specimen was measured for thickness and then cut in half along side A using a ruler to measure the halfway point (42 mm), a needle and paint to finely mark the halfway point, and a razor blade to cut the specimen. Care was taken when cutting the specimen to ensure that the cut was perpendicular to side A in all directions. Once the specimen was cut in half, the right side (already tested side) was re-measured and placed to the side and the left side was measured for the new side A and B length (42 x 54 mm). The specimen was placed on the anvil with the testing area shifted downward, so the upper portion (from the original orientation) was tested. The specimen was tested again, removed from the anvil, and measured for thickness. The specimen was measured and cut in

half again against side B so that the new specimen size measured 42 mm on side A and 27 mm on side B. Again, the specimen was tested with a shift to the left, removed and cut in half along side A. The direction of the cuts was alternated along side A and B until the test was terminated. Figure 3.10 illustrates the cut order and testing locations. The blue dashed lines are the cuts made along side A and the red dashed lines represent the cuts made along side B. The order of the cuts is denoted with a number in numerical order. The testing locations are indicated with a green X. It should be noted that once the specimen was too small to shift, meaning its surface area was smaller than the impact zone outlined in section 3.3.3, it was tested directly in the middle. The test was terminated when either the subsequent drop was predicted to be greater than 10 kN (i.e., the previous drop was in the 7 kN range), or the sound produced from the drop was recognized as metal on metal contact of the striker and anvil (i.e., potential damage to the machine). The number of cuts completed in the experiment before termination depended on the thickness and material of the specimen being tested. The most a specimen was cut was 7 times with dimensions measuring 5 mm x 6-7mm, depending on the accuracy of the cutting. Refer to Appendix B for further details of the test.
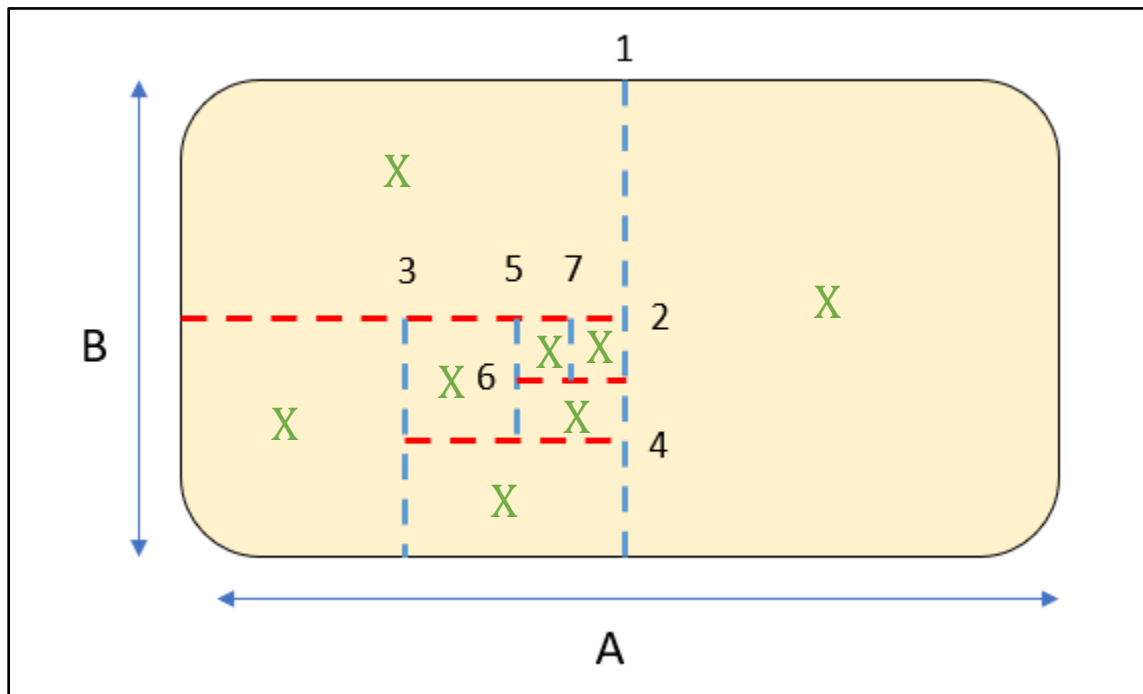
Figure 3.10: A schematic of the cut order for the surface area testing. The blue dashed lines are the cuts made along the "A" direction and the red dashed lines are the cuts made along the "B" direction. The order of the cuts are labeled accordingly and the test sites are indicated with an "X".

The surface area analysis was also conducted on 3 silicone specimens in the opposite cutting order to see if different transmitted force behaviours were observed. (I.e., a change in cut order meant that side B was cut first, followed by side A, and so forth.) The specimens were then compared to the silicone specimens of similar thickness in order to see if there was a difference in results depending on the cut order. The results of these tests can be found in Appendix B.

3.4.3 Thickness

Drop testing where the thickness of the specimen of the same lateral dimensions was changed was conducted in order to see the relationship of thickness and transmitted force. In impulse mechanics, the energy a body absorbs is related to the thickness by:

$$W = F \cdot d \tag{3.1}$$

where all of the work done on the material (W) is the energy absorbed. Assuming the force applied (F) to the material is the same, by increasing the thickness (d) more energy will be absorbed, and the transmitted force will be reduced. From the simple work equation, one might assume that the relationship of thickness and energy absorbed is linear; however, there are many additional factors influencing energy absorption (see Chapter 2) and thus testing for thickness-effects was required.

For the thickness testing, specimens of PVC, Silicone, and TPR were prepared ranging from 0.5 mm-8mm in increasing increments of 0.5 mm. Each specimen set consisted of 16 specimens to be tested. The specimens were then tested using the clip shown in Figure 3.9 to secure the specimen and tested according to the procedure outlined in section 3.3.1.

3.4.4 Hardness

In the first batch of TPR supplied by AQR from China, the specimens had a range of thickness and hardness. For the same thickness, the specimens were created to have 20A, 25A, 30A, 40A, and 50A hardness. As the effects of hardness on transmitted force were unknown, an experiment was conducted to find if hardness had any effect. This experiment coincided with the thickness test for the first batch of TPR, as all of the tiles in the batch were measured for thickness and hardness and then tested for transmitted force. Thus, one impact was required, and the data could be sorted by hardness or thickness for analysis.

3.4.5 Low Temperature

A low temperature drop test were conducted in order to determine any effects on transmitted force of materials that were cooled to -20°C and -40°C. In the test, 6mm specimens of D3O®, PVC, TPR, and silicone were used. The 6 mm thickness was used since D3O® was only supplied as 6 mm thick sheets; therefore, using 6 mm thick specimens allowed for a direct comparison of materials.

To complete the test, the drop tester was pre-set with the striker already raised to a height of 22 cm. The specimens were also prepared using the method outlined in section 3.5 in order to capture the motion effects of temperature through the use of HSV. Each specimen was then put into a Espec EPL-3H freezer (manufactured by ESPEC in Hudsonville) and initially cooled to -20°C. This test required three people in order to be as time efficient as possible to reduce the transfer of heat to the material. The three people required were: one person to open the freezer door when the internal temperature reached exactly -20°C, one person to remove the specimen with the appropriate gloves and place it on the anvil, and one person to conduct the drop test as soon as the specimen was placed on the anvil. This same procedure was repeated for each material specimen. After that, the internal temperature of the freezer was lowered to -40°C and the same procedure was repeated, ensuring that the other side, defined by the length of the specimen, was tested in order to make sure that strain hardening from repeated impacts did not occur.

3.5 High Speed Videography

The purpose of the high speed videography (HSV) was to be able to visualize the and discern the dynamic nature of a material's behaviour at each stage of the impact, and to permit the measure of velocities at each stage, how much the material compressed, and the strain of the material. This information was also used to verify the ABAQUS model outlined in section 3.7 and Appendix C.

For the HSV, a Fast Cam SA5 camera (Photron, Tokyo) was set up so that the frame was level with the anvil, as shown in Figure 3.11. This was to ensure that the "X" and "Y" axis of the camera frame were congruent to the axis of the physical anvil to ensure minimal uncertainty in the strain calculations due to the frame being angled. The specimens used in the HSV were 6 mm specimens of D3O®, PVC, TPR, and Silicone. One set of the materials was prepared for room temperature drop testing and one set of the materials was prepared for the cold temperature testing.

Figure 3.11: A photograph of the HSV set up for the drop testing.

3.5.1 Specimen Preparation for High-Speed Videography Drop Testing

In order to create fiducial markings for strain measurements, the specimens were prepared by cutting 1-2 mm deep notches 10 mm apart into the face parallel to the camera frame. The notches were cut using a razor blade and a ruler was used to measure the locations of the notches. The face that was cut was also colored by a black sharpy for the light-colored materials (D3O®, PVC, and Silicone) and a white paint pen was used to color the edge of the TPR. The purpose of coloring the

material was to provide contrast so that the propagation of the strain and structural bending in the material could be visually identified with ease. It should be noted that the PVC and Silicone specimens required an extra step before the notches were added: the edge that the notches were going to be cut into required the removal of the fillet in order to have a flat surface of the entire thickness. The removal of the fillet was completed by cutting parallel to the fillet edge at the point where the fillet started.

3.6 DMA

The purpose of the DMA experimentation was to identify and compare the temperature and frequency properties of D3O®, PVC, TPR (20A and 50A), and Silicone. Conducing DMA experimentation assisted in the understanding of why some materials would perform better at lower temperatures than others during the cold weather testing. In addition, the physical properties of D3O® are relatively unknown as they are a trade secret; therefore, the DMA analysis would be able to show why D3O® behaves as it does.

Dynamic mechanical analysis (DMA) is used to measure and characterize the bulk properties of a material that affect performance, more specifically the viscoelastic response of a material to oscillations [7]. DMA is also used to find the major transition temperatures of a material, as discussed in section 2.4 of Chapter 2. A DMA machine applies an oscillating force to the specimen and measures the material's response to the force [7]. Depending on the experimentation, the force can be a compressive force, a bending force, torsional, or a tension force. When the oscillating force is applied, a sinusoidal strain is generated in the material from the applied stress. The lag between the stress applied and stain generated allows for properties such as the elastic modulus to be calculated [7]. DMA machines have the ability to change the frequency of the oscillations and the temperature during the test.

3.6.1 DMA Specimen Preparation

DMA machines require a specific geometry and specimen depending on the testing mode. For compression testing, the required geometry was a cylindrical disc measuring less than 10 mm in diameter and greater than 3 mm in thickness. To create the specimens, a 1mm thick tubular metal die with the approximate inner diameter of 8 mm was placed into a drill press and used to cut holes into 6 mm specimens of each material. The specimens that were used for the low temperature testing, outlined in section 3.4.5 above, were used for the temperature sweep tests. A water bath (plastic tub

filled with water) and wooden board were used when cutting the specimens. The water bath was used to immerse the specimen in water while cutting in order to keep it cool. This step mitigated the risk of changing the specimen properties due to heat from the friction generated by the rotating tube. The wooden board was used as a backing layer for when the cut was finished.

The use of the drill press created a specimen with a uniform cylindrical surface, which was critical as variations in surface dimensions can affect the results of the DMA testing. Due to their low stiffness, elastomers can be challenging to cut at slow rates as they will compress when a load is applied, causing the material beneath the surface layer to be stretched out. Once the cut is made, the resulting specimen will have an hourglass profile (see Figure 3.12). The use of the drill press created a more uniform shape due to the high cut rate (the material does not have time to compress). Figure 3.12 shows the results of the specimens being hand cut (far left) and cut with the drill press without a water bath (middle), and with a water bath (far right)

Figure 3.12: the results of the specimens being hand cut (far left) and cut with the drill press without a water bath (middle) and with a water bath (far right). The specimen that was cut with a drill press and water bath was used in DMA testing due to the uniform profile.

3.6.2 Equipment Set Up

The DMA testing was conducted with a Perkin Elmer DMA 8000 Dynamic Mechanical Analyzer (manufactured by PerkinElmer in Waltham, MA). The machine was set up and calibrated according to the instructions provided with the machine. This step was completed every time the machine was turned on. Figure 3.13 shows a schematic of the DMA machine in the position it was calibrated in.

The testing area is contained within the cover (indicated) and the tubes on the cover are used to cool or heat the testing area. The temperature of the testing area is indicated on the right tower.
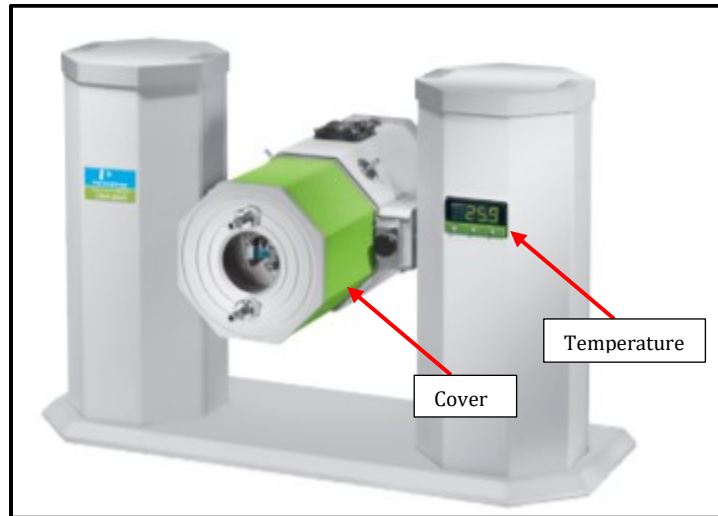
Figure 3.13: Calibration position for the DMA machine. The cover for the temperature testing is indicated. The temperature within the cover is displayed on the right tower (indicated).

Once it was calibrated, the body of the machine was rotated so that the testing area pointed upwards (i.e., the cover was upwards). To secure the specimen for compression testing, one plate and eight screws were used (four above the plate and four below), as shown in Figure 3.14. These parts were attached to the machine when it was calibrated and were removed in order to place the specimen in the aparatus. Before the specimen was placed onto the machine, it was measured three times for thickness and diameter using a digital calliper with 0.01 mm precision. The average of these measurements was added into the machine's testing software under measurements for a cylindrical specimen. Once the specimen was placed on the testing platform, the screws and plate were assembled and adjusted so that the plate just touched the top surface of the specimen. Ensuring that the plate was in a correct position was an essential step as if it were not placed correctly it risked either over compressing the specimen, rendering the results of the experiment invalid, or not compressing or contacting the specimen at all, resulting in absence of data.
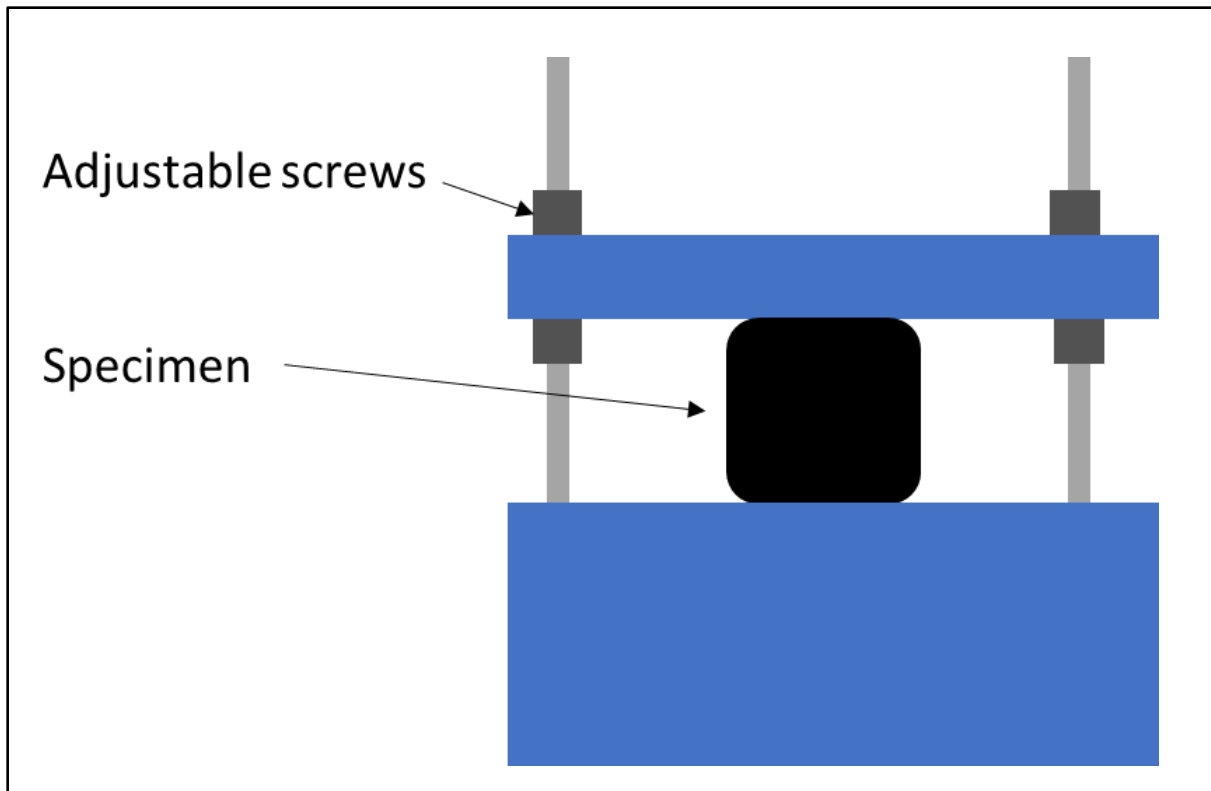
Figure 3.14: A schematic of the specimen set up in the DMA testing machine. The plate on top of the specimen was adjusted by screws (indicated). The screws were placed above and below the plate to ensure that there was not excessive compression placed on the specimen.

When the specimen, screws, and plate were correctly adjusted, the desired testing variables of frequency, rate of change in temperature, and compression depth were input into the testing software. For all of the specimens, a compression depth of 0.05 mm was used as a smaller depth did not produce results. The test was then run by hitting the run button on the test software. It should be noted that temperature sweeps had the additional step of hooking up a tank of liquid nitrogen to the cover and cooling the testing chamber to the desired temperature.

3.6.2.1 Temperature Sweep

The temperature sweep function of the DMA testing was used to determine the behaviours of each material for temperatures of -80°C to 80°C. These temperatures were chosen as they encompass the use-case temperatures (-40°C to 40°C), as well as provide a large margin of error to see what would happen if the temperatures fell out of the use-case range.

To conduct the temperature sweep tests, liquid nitrogen was used to cool the testing area to just above -80°C. The frequency of the machine was held constant at 1 Hz, meaning that the 0.05 mm compression of the specimen would occur once per second. The change in temperature was set to decrease at a rate of 1°C/minute.

3.6.2.2 Frequency Sweep

The purpose of the frequency sweep tests for each material was to see if there were changes to the absorption properties of the material, defined as the tan delta, which is a measure of the ratio of storage modulus to the loss modulus. From a use-case standpoint, it is useful in determining how frequent and repeated impacts affect the material response.

For the frequency test set up, the temperature was held constant at the temperature of the room (22-23°C). Through trial and error, the frequency range was set to be between 0.01 and 50 Hz; the machine could only support frequencies up to 100 Hz, however, when the machine would approach 100 Hz, the testing software would terminate the test due to "sensor and vibration failure", as indicated by a pop up on the screen. Thus, 50 Hz was selected as the top range in order to minimize the risk of damaging the machine.

Chapter 3 References

[1]D3O® Impact Protection | Nothing protects better than D3O®. Available from: https://www.d3o.com/. [citedJan 7,2021] .

[2]Harper CA. Handbook of plastics, elastomers, and composites. 4th ed. New York: McGraw-Hill; 2002.

[3]Ashby MF, Shercliff H, Cebon D. Materials: Engineering, science, processing and design. Oxford, UNITED KINGDOM: Elsevier Science & Technology; 2007.

[4]Askeland DR, Wright WJ. The science and engineering of materials. 7. ed., SI ed. Boston, Mass: Cengage Learning; 2016.

[5]Granta Design Limited. Granta edupack . Level 3 2020;20.1.1.

[6]American national standard for performance and classification for impact resistant hand protection. . International Safety Equipment Association 2019 February.

[7]Menard KP. Dynamic mechanical analysis. first edition ed. Boca Raton, FL [u.a.]: CRC Press; 1999.

Chapter 4 : Materials Selection

4.1 Introduction

This chapter details the materials selection process for glove bumpers, which is part of the embodiment stage of the Ashby design process (see Chapters 1 and 2). The chapter will also examine ranking the selected materials based on their performance, defined as having a low transmitted force during a drop test or high tan delta (tanδ) during DMA testing, for different temperatures and frequencies. A detailed look into temperature and frequency was dictated by the use case scenario of the gloves: they will be used in a variety of temperatures and there are instances the gloves will be subjected to impacts multiple times.

The research questions from section 1.3 of Chapter 1 that Chapter 4 attempts to address are:

(1) Is there a material currently not used by the glove industry that can enhance the impact performance of gloves?

(2) What material should be used for the glove bumpers based on the use case of the gloves? (This question will also be examined in Chapter 5).

4.1.1 Overview of the Ashby Materials Selection Process

In the materials selection process, a desired attribute profile for the unknown material is identified by defining the function, constraints, objectives, and free variables of the design. The Ashby design process describes this materials selection step as the translation [1]. In the translation step, an equation for each performance objective, such as minimizing mass, is established and a material index for the objective is identified. A material index is the "property or property group that maximizes the performance for a given design" [1, pg. 104]. For example, if the objective of the design is to minimize the mass while keeping the stiffness above a certain threshold, the material index would attempt to maximize the minimum mass, or in other words, identify the lowest density material for the specified stiffness.

To identify an index, the equation of the performance objective (P) of the design is rearranged and grouped in terms of the functional requirements (F), geometric parameters (G), and material properties (M) to have a performance function equation of the form:

$$P = \left[\left(\begin{array}{c}Functional \\ requirements, F\end{array}\right), \left(\begin{array}{c}Geometric \\ parameters, G\end{array}\right), \left(\begin{array}{c}Materials \\ properties, M\end{array}\right)\right] = f(\mathrm{F}, \mathrm{G}, \mathrm{M}) \qquad (4.1)$$

The material index is derived from the material's properties (M) and can be inversed depending on whether or not the objective is to be minimized or maximized.

Once the translation step is completed and a material index is identified, the next step of the Ashby design process is to plot the materials indices using a materials selection software, GRANTA EduPack™, and apply attribute limits to the data (e.g., minimum service temperature). This step is known as screening (which identifies materials for further analysis). The last two steps of the Ashby design process are ranking and documentation. In the ranking step, the aim is to seek out a list of the top materials that will maximize the performance of the design. The final step of documentation is to deeply explore the shortlist of materials to identify the best material for the design. The documentation step is performed because the list of constraints cannot always be listed as attribute limits (e.g., how a material is processed), and there is rarely a single material that meets all design criteria—there are often trade-offs and documentation that allow for better comparison and contrast to arrive at a final selection.

4.2 Materials Selection for Impact Resistant Glove Bumper

4.2.1 Translation

As outlined in Chapter 2, an impact resistant glove is a specific concept that will protect the hands of workers employed in the oil and gas, construction, forestry, and mining industries from blunt force trauma. The impact resistant gloves use a bumper on the back of the glove as the primary way to absorb the impact energy from the blunt force. A bumper for back of the hand protection in its most basic form is a tile of material with a specified surface area (A) and a thickness (h). Figure 4.1 illustrates the simplest shape for the tile, a rectangular surface area with a length (L) and width (w). In an ideal scenario, when the bumper is impacted, a force (F) will be applied to the bumper parallel with the thickness, as shown in Figure 4.1.
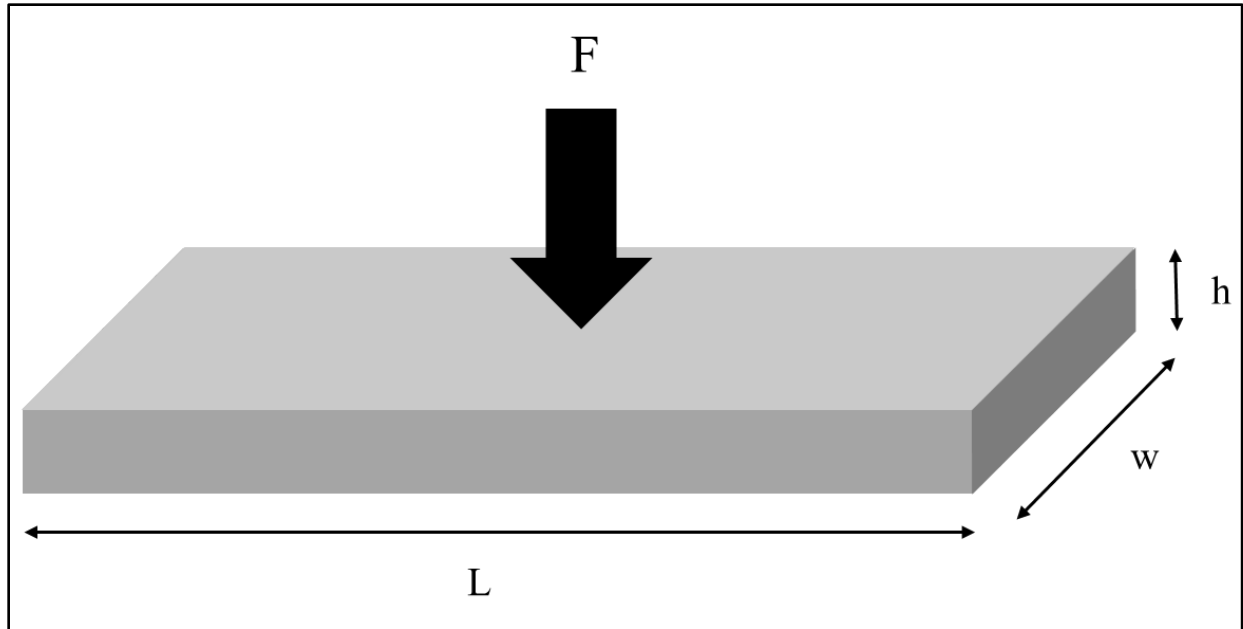
Figure 4.1: The dimensions of the simplest form of a bumper used for material selection. (h) is the thickness, (L) is the length, and (w) is the width. The direction of the impact force (F) is indicated.

The bumpers can come in many shapes and forms other than what is shown in Figure 4.1; however, to be able to easily compare and contrast different materials, the shape of the bumper was chosen to be a rectangle tile with a specified length (L) and width (w).

A simplified version of Table 1.2 in Chapter 1 for the design requirements of the bumper is shown in Table 4.1 below. For the simplified version of the bumper design requirements (Table 4.1), the area of the tile impacted is specified and the thickness (h) becomes a free variable. The objectives of the bumper remain the same: minimize the thickness, minimize the mass, and maximize the loss coefficient (tan delta). In Table 4.1, the applied constraints are that the bumper's stiffness must allow for adequate dexterity (defined as S*), the material must be able to perform in temperatures ranging from -40°C to 80°C, and the cost of the materials, including processing and manufacturing, must be less than $9 CAD, as specified by Superior Glove Works Ltd (Superior Glove). Superior Glove has the ability to slush mold onsite; however, injection molding requires outsourcing to a third party which adds to the processing costs. Thus, the type of molding required was considered in the $9 CAD cost of the material. (A full cost analysis was not completed in this thesis; Superior Glove was to do one if a successful material was found).

Table 4.1: The design requirements for a bumper defined by the function, constraints, objective, and free variables

Design Requirements for a Bumper on an Impact Resistant Glove *Simplified*	
Function	• Protect vulnerable areas of the hand from blunt force trauma
Constraints	• Must reduce the transmitted force to values outlined in ANSI/ISEA 138-2019 • Stiffness: must be low enough to allow for adequate dexterity, defined as S* • Length (L) and width (w) of bumper is specified as 84 mm x 54 mm • Service temperature: must be able to function in temperatures ranging from -40°C to 80°C • Cost: less than $9 CAD in total materials cost
Objective	• Minimize thickness • Minimize mass • Maximize loss coefficient (tan delta)
Free Variables	• Choice of material • Thickness of bumper

4.2.1.1 Material Indices

For the bumper of an impact resistant glove, the bending stiffness of the material must be below a value of S* to allow for dexterity of the hand when bending the fingers. Thus, the stiffness of a rectangular bumper is defined as:

$$S = \frac{C_1 E I_m}{L^3} \leq S^* \tag{4.2}$$

where C_1 is a material constant that depends on the distribution of the loads, E is the Young's modulus of elasticity of the material, and L is the length of the rectangular bumper (refer to Figure 4.1). I_m is the second moment of area, which for a rectangular cross section is defined as:

$$I_m = \frac{wh^3}{12} \tag{4.3}$$

where w is the width of the bumper and h is the thickness (refer to Figure 4.1). One of the objective functions for the bumpers is to minimize the thickness (h). By substituting equation (4.3) into (4.2),

and rearranging the variables to solve for thickness, a performance function for the bumper thickness is:

$$h \leq \left(\frac{12S^*}{C_1 w}\right)^{1/3} (L) \left(\frac{1}{E^{1/3}}\right) \tag{4.4}$$

where S*, C1, and w are the functional constraints, L is the geometric constraint, and the Young's modulus is the only material property. Since the functional and geometric constraints are all specified, the only freedom left is the material properties. Thus, the first material index, correlating to the minimum thickness objective is:

$$M_1 = \left(\frac{1}{E^{1/3}}\right) \tag{4.5}$$

The second objective of the bumper design is to minimize the mass. The mass of the bumper is defined as the surface area (A) multiplied by the thickness (h) and density (ρ). For the rectangular bumper, the surface area is defined as the length (L) multiplied by the width (w). Thus, the equation for the mass of the bumper is:

$$m = Ah\rho = Lwh\rho \tag{4.6}$$

Substituting equation (4.4) in for the thickness (h) and rearranging the variables for a performance function gives:

$$m \leq \left(\frac{12S^*}{C_1 w}\right)^{1/3} (L^2 w) \left(\frac{\rho}{E^{1/3}}\right) \tag{4.7}$$

where the material's properties are again grouped together in the last pair of brackets. The objective to minimize the mass is to minimize the last group of brackets or maximize the inverse of the brackets. Thus, as it is easier to deal with specific properties when the maximum is sought [1], the minimum mass of the bumper is one that gives the greatest value of the second material index, defined as:

$$M_2 = \left(\frac{E^{1/3}}{\rho} \right) \tag{4.8}$$

The last objective of the bumper for impact resistant gloves is to maximize the tan delta (tanδ). The tan delta is the material property measured through DMA testing (see Chapter 3) and is defined as the loss modulus (E'') divided by the modulus (E'):

$$tan\delta = \frac{E''}{E'} \tag{4.9}$$

The value of tan delta is a material property itself that needs to be maximized. Thus, the third material index is:

$$M_3 = tan\delta \tag{4.10}$$

A summary of each material index and the objective from which it was derived is shown in Table 4.2:

Table 4.2: A summary of the material indicies required for each design objective for impact resistant gloves.

Design Objective	Corresponding Material Index
Minimize thickness	$M_1 = \left(\dfrac{1}{E^{1/3}} \right)$
Minimize mass	$M_2 = \left(\dfrac{E^{1/3}}{\rho} \right)$
Maximize loss coefficient	$M_3 = tan\delta$

4.2.2 Screening

To select a material, there are multiple ways to screen the vast array of materials (e.g., setting limits on desired material characteristics or plotting the material indices). One way of screening for a material is to seek the subset of materials that can meet the design objectives by plotting the corresponding material indices and determining which materials could work. Another method to screen materials is to use a material that is already used in the design to be a reference point and compare and contrast the materials based on that reference point. Both of these methods are outlined below.

4.2.2.1 Screening Via Indices

A subset of materials that have a low value of $E^{1/3}/\rho$ while having a maximized value of tan delta is sought. Using the GRANTA EduPack™ software [2], the material index for minimizing mass (M_2) is plotted against the material index for maximizing the loss coefficient (M_3). Figure 4.2 shows the result of the output plot with the materials grouped in their family envelopes (note: not all of the family envelopes are labeled). For example, all of the foams are colored green, the metals and alloys are red, plastics are blue, and the elastomers are cyan. It can be seen in Figure 4.2, that composites, foams, plastics, and elastomers have a high tan delta relative to the other material families. In addition, elastomers, plastics, metals and alloys, and foams have a low M_2 value, as observed in Figure 4.2.
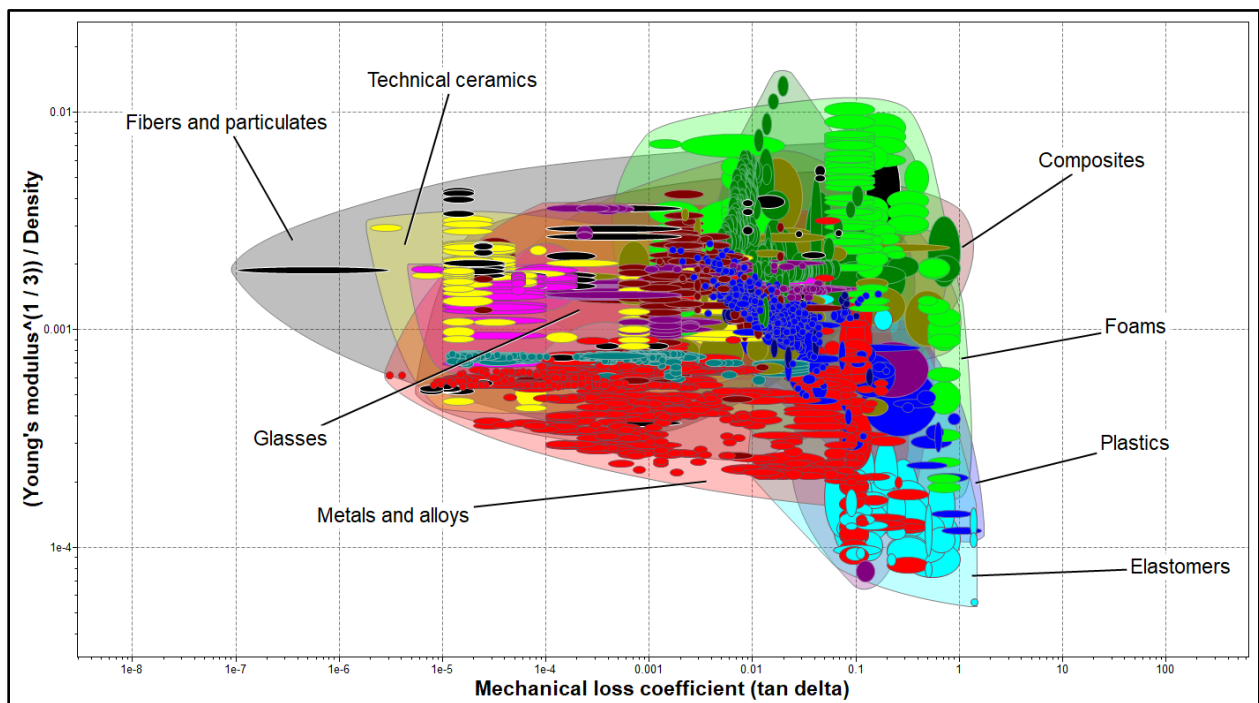
Figure 4.2: GRANTA EduPack™ plot of M$_2$ vs M$_3$. The groups of material familes are indicated. The search region for high performing bumper materials is the bottom right area of the graph.

To help select the best materials, two guidelines are drawn on the diagram, as illustrated in Figure 4.3, and the search region defined. The first is a M_2/M_3 guideline with a slope of 1 (indicated with a 1 in Figure 4.3). The slope represents the ratio of the indices. Because the indices are equally important, the value of the slope is 1. This guideline can be moved across the field of materials, however, the goal is to find the highest tan delta with the lowest value of M_2. Thus, any materials not meeting the guidelines are eliminated (eliminated materials are colored grey in Figure 4.3). The guideline was

positioned in such a way to have 20 materials remaining in order to eliminate most materials but still have enough materials remaining for the filtering stage. The second guideline is a vertical line (indicated with a 2) stating that the tan delta must be at least 0.3 for the material to be considered for the design. Normally, a definite attribute of the design would be specified in the filtering stage of the Granta EduPack™ software; however, the tan delta values are not listed as one of the variables that can be filtered within the software and must therefore be filtered in the graphing stage. Figure 4.3 shows the materials that are remaining after the guidelines were positioned with notable materials highlighted, such as silicone, PVC, acrylic rubber, halobutyl rubber, and foams.
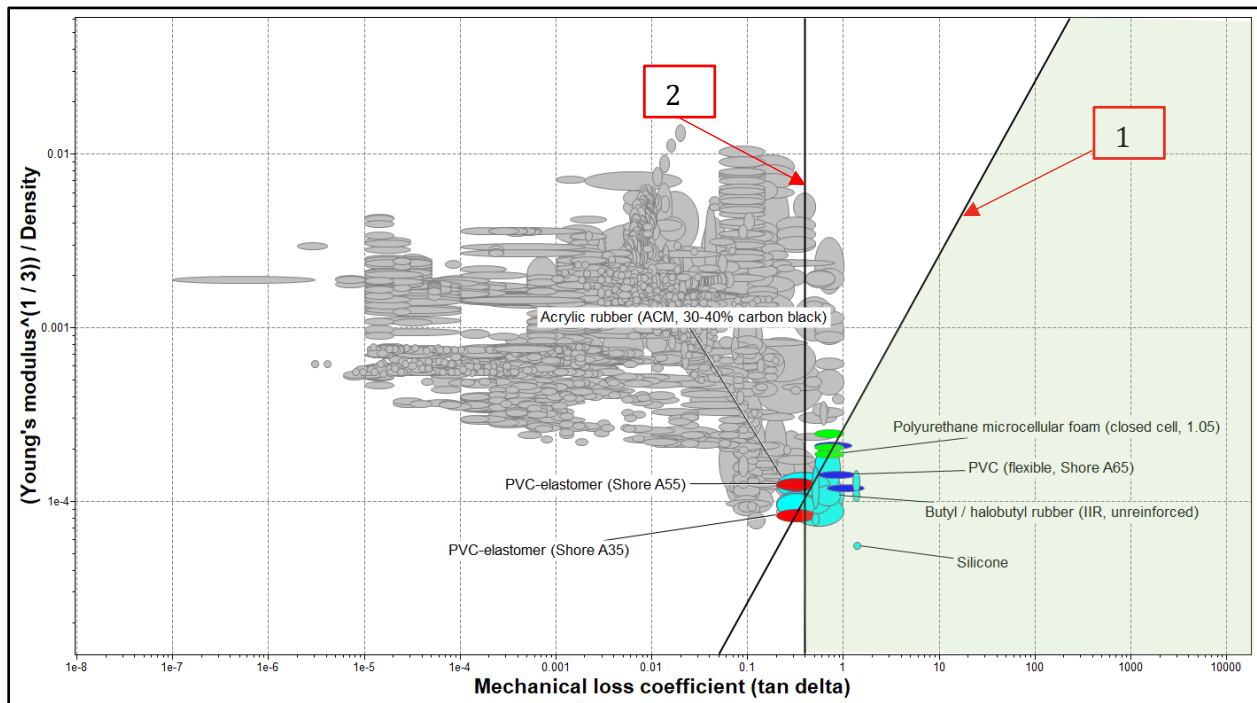
Figure 4.3: The initial stage of material selection for the M_2 vs M_3 plot. In the first stage, two guidelines are used to filter materials. (1) Is the M2/M3 guideline with a slope of 1 as both indices have equal importance. (2) Is a vertical M_3 guideline stating that the tan delta must be above 0.3. The search region for the initial stage is shaded green.

The next stage of the materials selection process is to apply filters to the search results based on the desired attributes of the design. For the gloves, filtering comprised defining the minimum service temperature as -40°C or less, and the maximum service temperature as at least 80°C into the filtering stage of the GRANTA EduPack™ software. The result of the service temperature filter is shown in Figure 4.4 below. In Figure 4.4, the materials that have not passed each stage are removed (as opposed to being colored grey) and the axes of the plot have been adjusted to zoom in on the materials that have passed multiple stages.
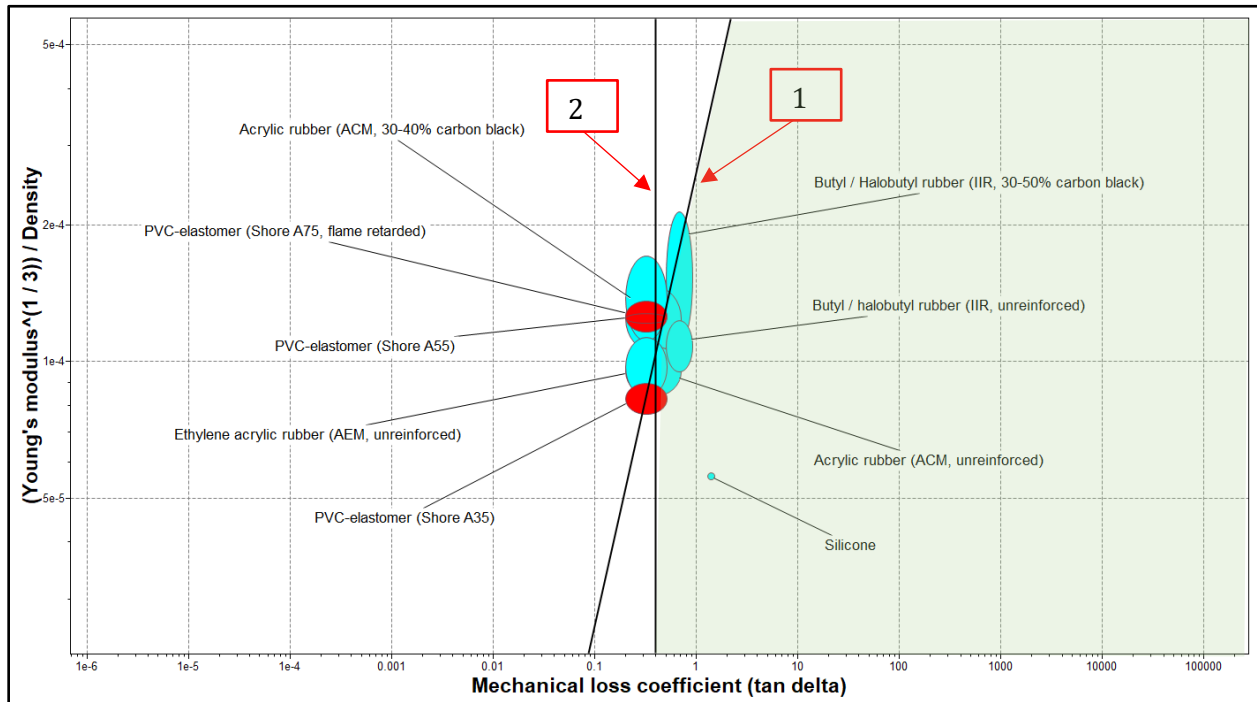
Figure 4.4: The remaining materials of the M₂ vs M₃ plot after the second filter for service temperatures had been applied. Guidelines (1) and (2) are the same as Figure 4.3 above and the search region is shaded green.

As shown in Figure 4.4, the materials that function in -40°C to 80°C while having a low mass and high mechanical loss coefficient are acrylic rubbers, butyl/halobutyl rubbers, PVCs, and silicones (labeled in Figure 4.4).

4.2.2.2 Screening Via Reference Material

Since there are many designs and materials already used in the impact glove industry, another way to screen for a material is to use a pre-existing reference material to compare against all of the other materials (such as a material that is state-of-the-art, or an industry standard). The most common material used in modern impact resistant gloves is TPR. Since the objective is to find a material that can be made thinner than TPR and have a higher tan delta, TPR will be used as a trade off point with a Young's modulus of elasticity defined as E_0 and a tan delta defined as $\tan\delta_0$. According to equation (4.4) above, a bumper made of any material will have a relative thickness to that of TPR given by:

$$\frac{h}{h_0} = \left(\frac{E_0}{E}\right)^{1/3} \tag{4.11}$$

and a relative tan delta of:

$$\frac{tan\delta}{tan\delta_0}$$

(4.12)

where $tan\delta_0$ is the tan delta of TPR and $tan\delta$ is the tan delta of the material selected.

In this screening process, there is a trade off, and the trade-off between (4.11) and (4.12) is desired. The trade off means that a penalty function (Z*) must be derived:

$$Z^* = a_h{}^* \left(\frac{h}{h_0}\right) - a_d{}^* \left(\frac{tan\delta}{tan\delta_0}\right)$$

(4.13)

where a_h* is an exchange constant that measures the decrease in penalty for a decrease in the material thickness and a_d* measures the fractional increase in tan delta. If both the exchange constants are of equal value, meaning that they have the same weighted importance, then the penalty function contour that is plotted on the graph is:

$$\frac{Z^*}{a_h{}^*} = \left(\frac{h}{h_0}\right) - \left(\frac{tan\delta}{tan\delta_0}\right)$$

(4.14)

Changing the weighting of the exchanging constants will change the shape of the penalty function contour depending on if thickness or tan delta is more desired.

Figure 4.5 shows the plot of material thickness relative to TPR against the tan delta of a material relative to TPR. The Young's modulus of elasticity of TPR used for the ratio was 1.8 MPa, which was given by the material supplier, and the value of tan delta was 0.5. In Figure 4.5, the origin point, or location of the TPR, is where both ratios have a value of 1, as shown by the solid black lines. The solid black lines serve as a way to divide the plot into quadrants: materials that can be made thinner than TPR and have a higher tan delta are displayed in the bottom right quadrant.
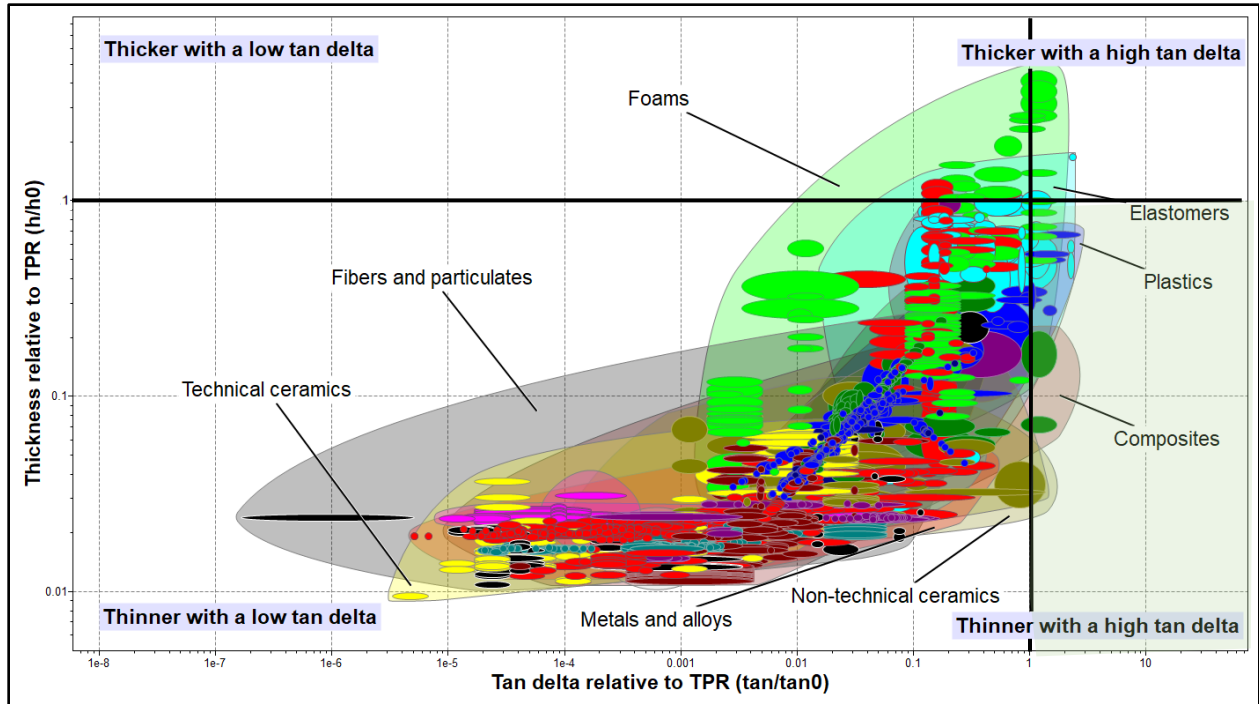
Figure 4.5: A plot of the material thickness and tan delta relative to TPR. Guide lines are used to indicate the baselne of TPR, and the location of TPR on the plot is the blackdot where the guidelines meet. Materials that are thinner than TPR with a higher tan delta are in the lower right corner (green shaded area).

The next step of the screening process is to apply the same filters based on the desired attributes as before (service temperature range), while also specifying that the bending stiffness must be below 500 MPa to allow for adequate dexterity. The result of the filter is displayed in Figure 4.6.
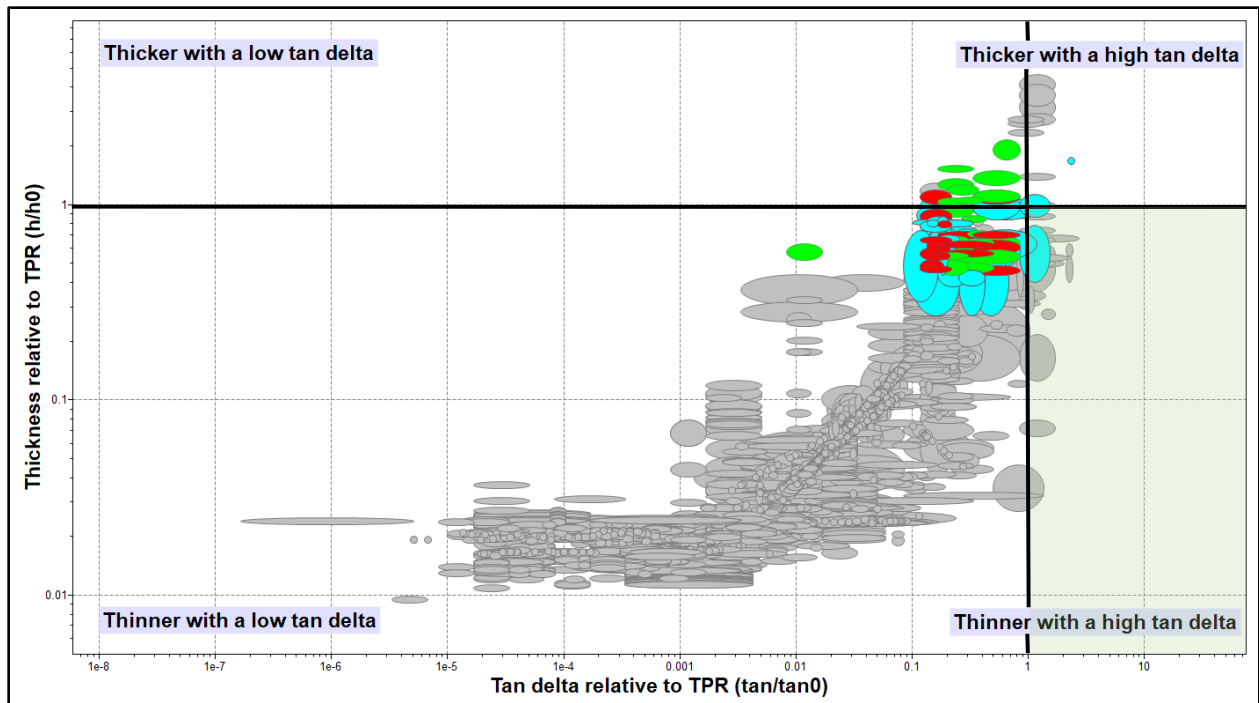
Figure 4.6: The resulting materials from the first screening process. Grey materials indicate they did not pass the first screen.

Figure 4.7 is a zoomed in version of Figure 4.6 with the labels identifying some of the materials of interest such as acrylic rubber, butyl rubber, foam, PVC, and silicone.
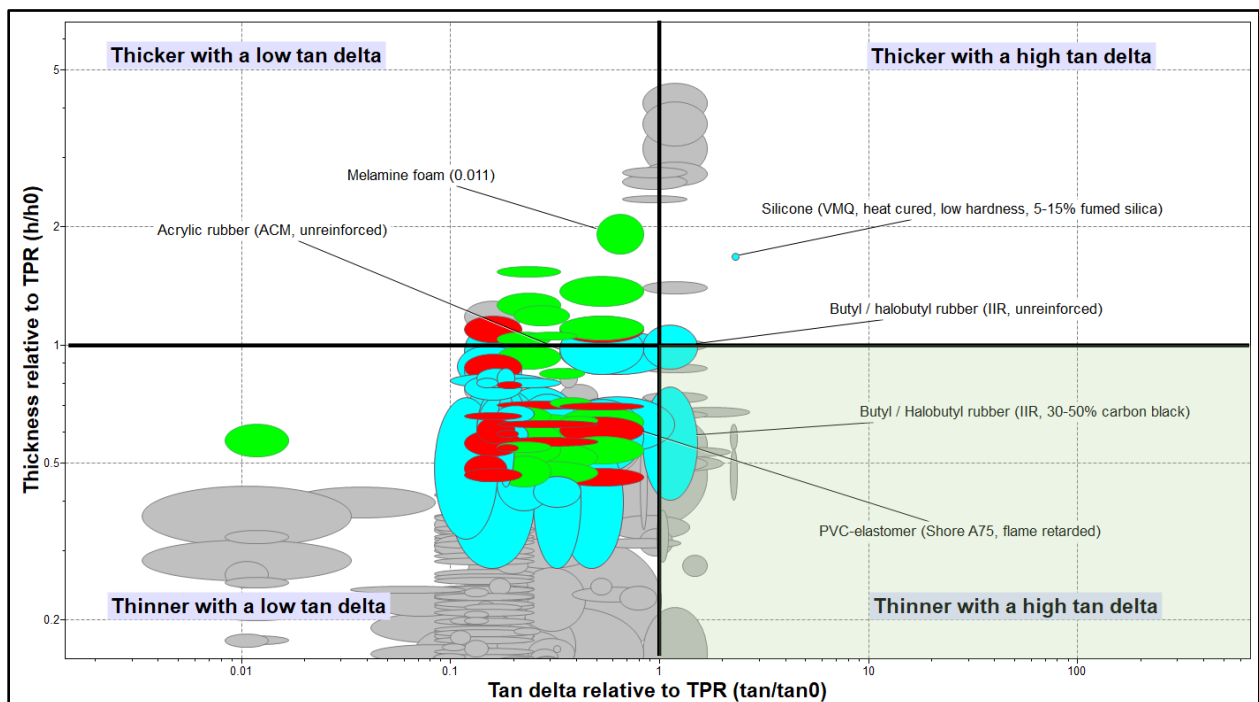
Figure 4.7: A zoomed in verion of Figure 4.6. The location of some materials of interest are labelled.

98

Since the purpose of the material selection is to find a material that absorbs more energy than TPR, a vertical guideline can be placed on the graph at the TPR origin point (1). Any material that does not meet a tan delta ratio of at least 1 was eliminated, as illustrated in Figure 4.8.
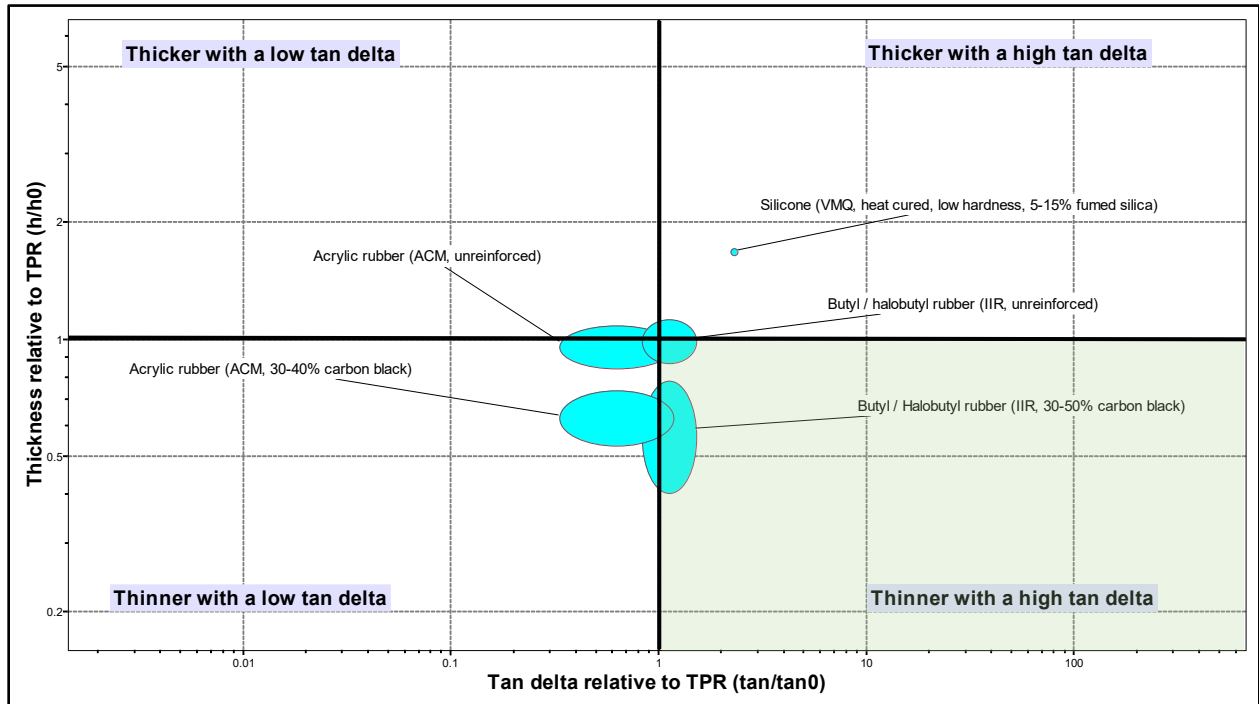
Figure 4.8: The result of eliminating materials that do not have a tan delta that is higher than TPR.

Through screening using TPR as a reference material, three types of materials were identified for the impact bumpers: acrylic rubber, butyl rubber, and silicone.

4.2.3 Ranking

Two types of materials that are not currently used in the impact protection glove industry were identified in the screening step: acrylic rubber and butyl/halobutyl rubber. Silicone was also identified as a good bumper material and it is currently being used in gloves produced by Superior Glove.

Table 4.3 below compares and contrasts the materials identified through the materials selection with the already existing materials based on the desired materials indices, with 1 being the best and 6 being the worst. The rankings were based on the locations of the materials in the GRANTA EduPack™ plots. For example, in Figure 4.8, the halobutyl rubber envelope extended further than the acrylic

rubber along the x-axis (correlating to tan delta), and thus, it was given a higher ranking. D3O®
ranked higher in tan delta due to its performance in DMA testing, discussed in section 4.4 below.

Table 4.3: A ranking of each material for glove bumpers for each material index, with 1 being the best and 6 being the worst.

Material	M_1 $(1/GPa^{1/3})$	M_2 $(GPa^{1/3} *m^3/kg)$	M_3 (GPa/GPa)	Overall Rank
Acrylic Rubber	3	2	4	**3**
Butyl Rubber	2	3	3	**2**
D3O®	unknown	unknown	1	**NR***
PVC	1	5	6	**5**
TPR	4	4	5	**4**
Silicone	5	1	2	**1**

*D3O® was not given a rank due to unknown values of two material indices.

As is shown in Table 4.3, there is no single material that outperforms all of the others for each
material index. Both of the newly identified materials, acrylic rubber and butyl rubber theoretically
rank in the middle for all indices when compared to the existing materials and thus should be
considered when creating bumpers for impact resistant gloves. The indices, however, do not express
the processing abilities and whether or not they are oil or water resistant. The details of the two
identified materials will be further explored in the following documentation section.

4.2.4 Documentation

The use of impact resistant gloves in oil and gas, construction, mining, and forestry industries exposes
the exterior of the bumper to oil, flames, and water. Thus, the bumper must be oil resistant and water
resistant. In terms of processing, Superior Glove uses slush molds to mold the bumpers and
outsources materials that require injection molding to a third party (adding to the processing costs).
To fasten the bumpers to the gloves, sewing or thermal adhesion is used. In order to meet the
processing demands, the bumper must be able to be molded and sewn on. All of the aforementioned
constraints were considered when looking into the material characteristics as potential ways to
eliminate the material (e.g., if the material was not able to be molded, the material was eliminated).

Based on data within GRANTA EduPack™, acrylic rubber was identified to have poor water-resistant
characteristics and butyl rubber was identified to have poor oil-resistant characteristics (GRANTA

EduPack ranks characteristics as poor, ok, and good) [2]. These characteristics make both materials poor choices as bulk materials and would need a cover or coating to be used as a bumper. Acrylic rubber also has high-water absorption, defined by % weight gained in 24 hours and was more expensive than silicone per kg ($7.06 CAD/kg compared to $4.79CAD/kg) [2]. Superior Glove disclosed that the material cost of silicone was already close to their maximum materials budget; therefore, acrylic rubber was eliminated as a possible material for a bumper. Superior Glove, however, was interested in exploring the possibility of using halobutyl rubber (HBR) as a material for the bumper as HBR was less expensive than silicone.

4.2.4.1 Eliminating HBR

To evaluate HBR, Superior Glove procured Exxon™ bromobutyl rubber grade 2222 which required it to be sent to a third party, Infinity Rubber, to mix the dry rubber compound together as Superior Glove did not have the ability to do this in their own facilities. Once it was mixed by Infinity Rubber, the dry rubber compound was heat pressed at 140°C into the stainless-steel mold outlined in section 3.2 in chapter 3. The result of the heat pressed halobutyl rubber is displayed in Figure 4.9. As is shown, the halobutyl rubber specimens had major flaws in the form of voids in the specimen (indicated). The specimens also were not able to be made with a precise thickness, and were 1-2mm thicker than the mold, which can be seen from the flashing that developed on the specimen (indicated).

Figure 4.9: The result of the heat pressed halobutyl rubber. The specimen displayed large voids and a lack of thickness precision, as seen from the flashing that developed on the specimen (indicated).

In terms of impact testing, halobutyl rubber had analogous transmitted forces when compared to TPR and PVC (the existing materials for bumper protection) at similar thicknesses.

After such initial tests, halobutyl rubber was eliminated as a possibility to be used as a material for the bumpers of impact resistant gloves. The elimination was due to the difficult processing (third party manufacture), the poor forming (voids), and the impact performance (similar to existing materials).

4.2.4.2 Remaining Materials

The elimination of acrylic rubber and butyl rubber left four materials for analysis in the remainder of the experiment. These materials were: D3O®, PVC, TPR, and silicone, which are all currently being used as materials in the impact glove industry. The impact performance of each material under different temperatures and frequencies was assessed and then compared and contrasted with the other materials.

4.3 Comparison of Materials to be Used for the Bumpers

From the materials selection process, four materials emerged as candidates for the experimental materials for the thesis: D3O®, PVC, TPR, and silicone. The TPR was supplied in a range of hardness, so to save time, the hardest (50A) TPR and softest (20A) TPR were selected for the experimentations, as all of the other hardness specimens yield transmitted force results between the 50A and 20A specimens (see section 4.3.3). The following section addresses the performance of each of these materials, in terms of transmitted force, when the temperature and frequency are changed. In addition, the section will explore the effects of hardness on transmitted force.

4.3.1 Varying Temperature

It is important to know the effects of varying temperature on the performance (defined by peak transmitted force) on each of the materials. Two methods were used to find the effects of temperature. The first method was to cool specimen tiles in a freezer and perform drop tests on them. The force-time data from the drop test output was analyzed for peak transmitted force and impulse. The second method was to perform a temperature sweep using DMA.

4.3.1.1 Peak Force

Table 4.4 below displays the peak transmitted force recorded from the drop testing at temperatures of 20°C, -20°C, and -40°C for each 6mm thick specimen. The hardness of each specimen could not be controlled; therefore, it is listed in the table to illustrate the possible effects of hardness on peak transmitted force. At 20°C, D3O® was the best performing material; however, at the colder temperatures D3O® was the worst performing of the five materials tested. Both of the softest materials, silicone and TPR 20A, had a transmitted force close to 5800 N at room temperature and outperformed all of the other materials when the temperature was decreased. Both PVC and TPR 50A had a hardness of 50A and saw their peak force decrease more than 1200 N when the temperature was dropped to -20°C, and increase by more than 600 N when the temperature was decreased again to -40°C.

Table 4.4: The peak transmitted force for drop testing at 20°C, -20°C, -40°C for each 6mm thick specimen. The hardness and force columns are heat colored to indicate high (red) and low (green) values of each column.

Temperature	Material	Hardness (A)	Transmitted Force (N)
20°C	D3O	60	5440
	PVC	50	6919
	Silicone	30	5771
	TPR	20	5824
		50	5897
-20°C	D3O	60	8224
	PVC	50	5308
	Silicone	30	3299
	TPR	20	3503
		50	4623
-40°C	D3O	60	9281
	PVC	50	5924
	Silicone	30	2861
	TPR	20	3749
		50	5222

Figure 4.10 illustrates the effects of the temperature on transmitted force using the data from Table 4.4. The different levels of the ANSI/ISEA 138-2019 standard are shaded grey and the region that does not meet any level is shaded yellow. The data points are shape coded by shore hardness, where the inverted triangle is 60A, the squares are 50A, the right triangle 30A, and the circle is 20A. As observed in Figure 4.10, low hardness materials at low temperatures performed the best (had the lowest transmitted force), and D3O® at low temperatures performed the worst (had the highest transmitted force).
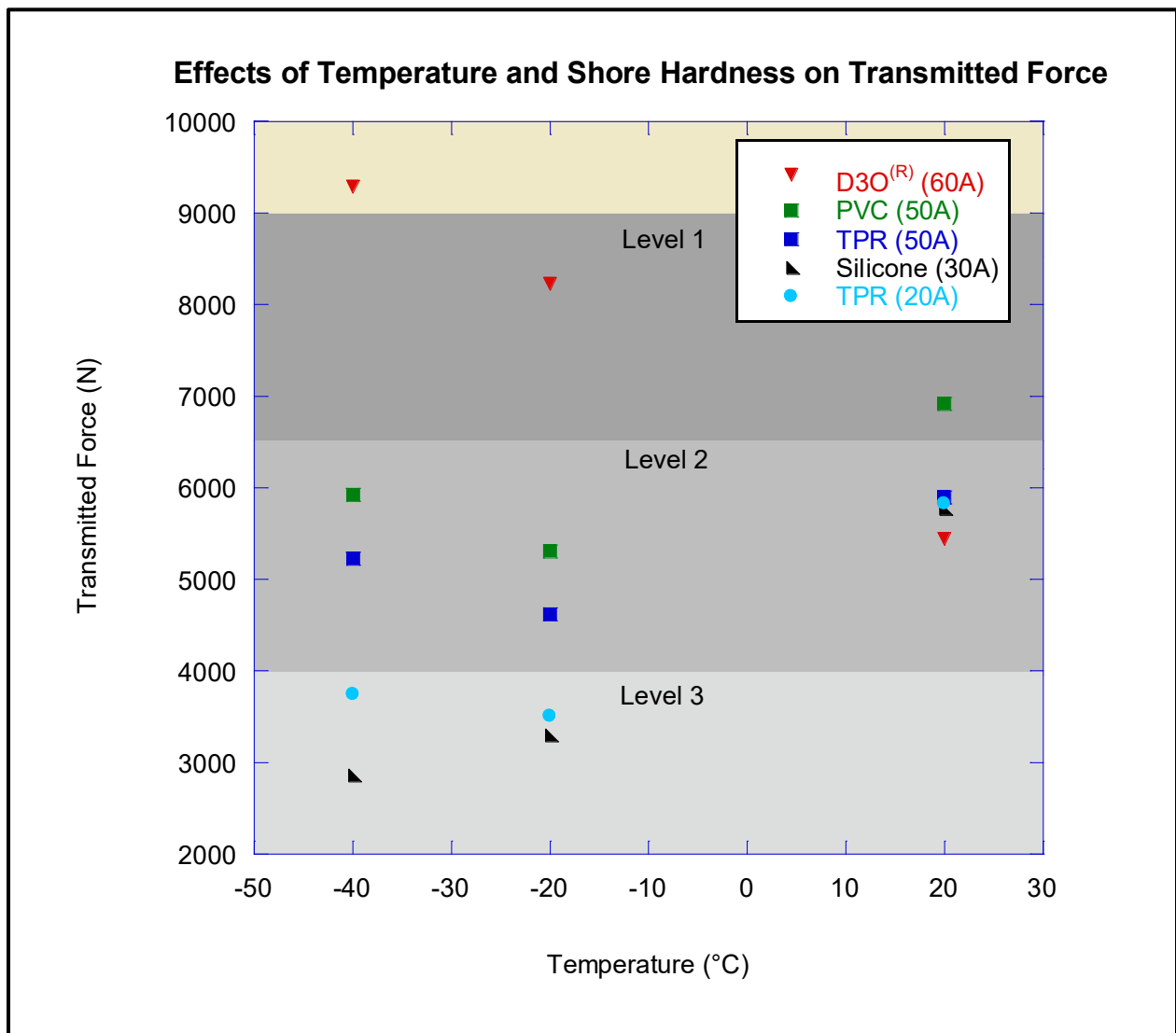
Figure 4.10: A plot showing the effects of hardness on transmitted force using the data from Table 4.4. The data points are shape coded by shore hardness, where the inverted triangle is 60A, the squares are 50A, the right triangle 30A, and the circle is 20A. Each specimen was 6 mm thick and measured 84 mm x 54 mm in length and width.

4.3.1.2 Impulse

The impulse of each material is the product of the total force by the time over which the force is applied. A specimen can have the same impulse but a lower transmitted force if the force acting on the specimen was for a longer duration. In a force-time graph, the area under the force-time curve is equal to the specimen's impulse. Figure 4.11 and Figure 4.12 below display the results of each of the force-time data collected for the initial force peak during the 20°C testing and -20°C testing, respectively.

In Figure 4.11, the room temperature data for TPR 50A was incorrect as the load cell gave the exact same points as the previous silicone test; therefore, the results of the TPR 50A specimen were omitted. D3O® (red) shows an initial increase in transmitted force before the other materials (or a higher initial impulse) and reaches its peak force close to the same time as PVC and before silicone and TPR 20A. Silicone (black), TPR 20A (light blue), and TPR 50A (dark blue) have a similar shaped curve; however, silicone, which outperformed both TPR specimens at room temperature, comes to a peak slightly before the TPR 20A specimen and slightly after the TPR 50A specimen. The PVC curve (green) displays a sharper peak than the other materials, illustrating that it was subjected to a large force over a smaller time. Thus, through observation the impulse of each material is not the same. Using the Gaussian method to calculate impulse, the impulse of each material was (in increasing order): 7.8 N·s for D3O®, 9.2 N·s for silicone, 9.4 N·S for TPR 50A, 10.2 N·s for TPR 20A, and 10.9 N·s for PVC. Consequently, materials with lower impulse had a lower peak force, with the exception of TPR 50A, which had a lower impulse than TPR 20A.
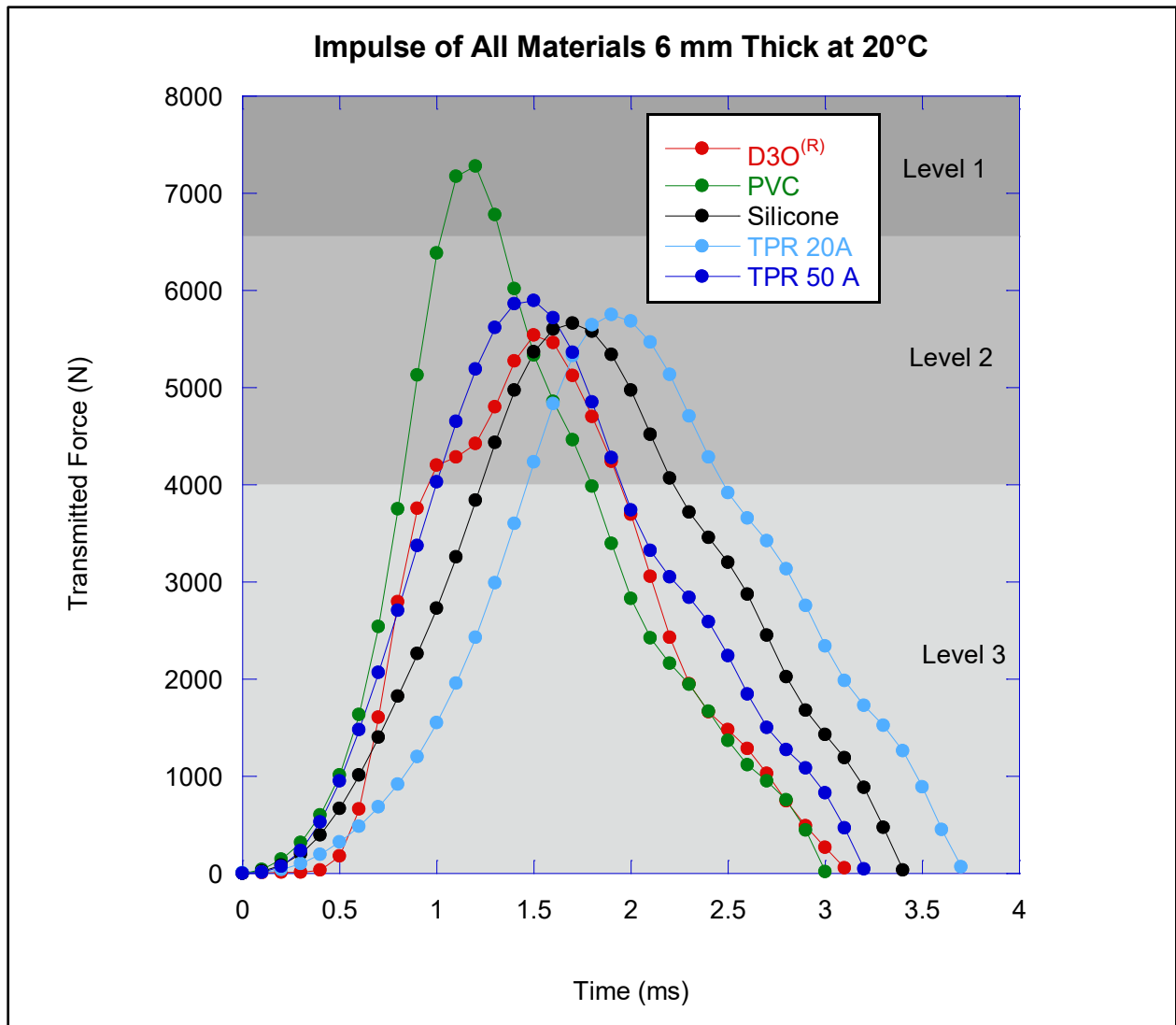
Figure 4.11: The impulse curve for each material tested at room temperature. Data was truncated so that the onset of the impulse started at time 0 (drop testing starts time at 0 for when the mass is released). Each specimen measured 84 mm x 54 mm laterally.

Figure 4.12 illustrates the impulse curves of each material at -20°C. When comparing the shape of each material curve to the room temperature curve the following observations are made: the curve for D3O® (red) starts and finishes at the same time but has a larger peak; the curves for PVC (green), silicone (black), and TPR (shades of blue), all flatten and shift to the right. The impulse of each material is: 7.9 N·s for both hardnesses of TPR, 8.0 N·s for D3O®, 8.6 Ns for silicone, and 10.7Ns for PVC. One observation that should be noted that the impulse decreased for every material except for D3O®, which increased by 0.2 N·s. This observation shows that there are two objectives when

dealing with the impulse of a material: to change the shape of the impulse curve (make it flatter while keeping the impulse the same) or decreasing the total impulse.
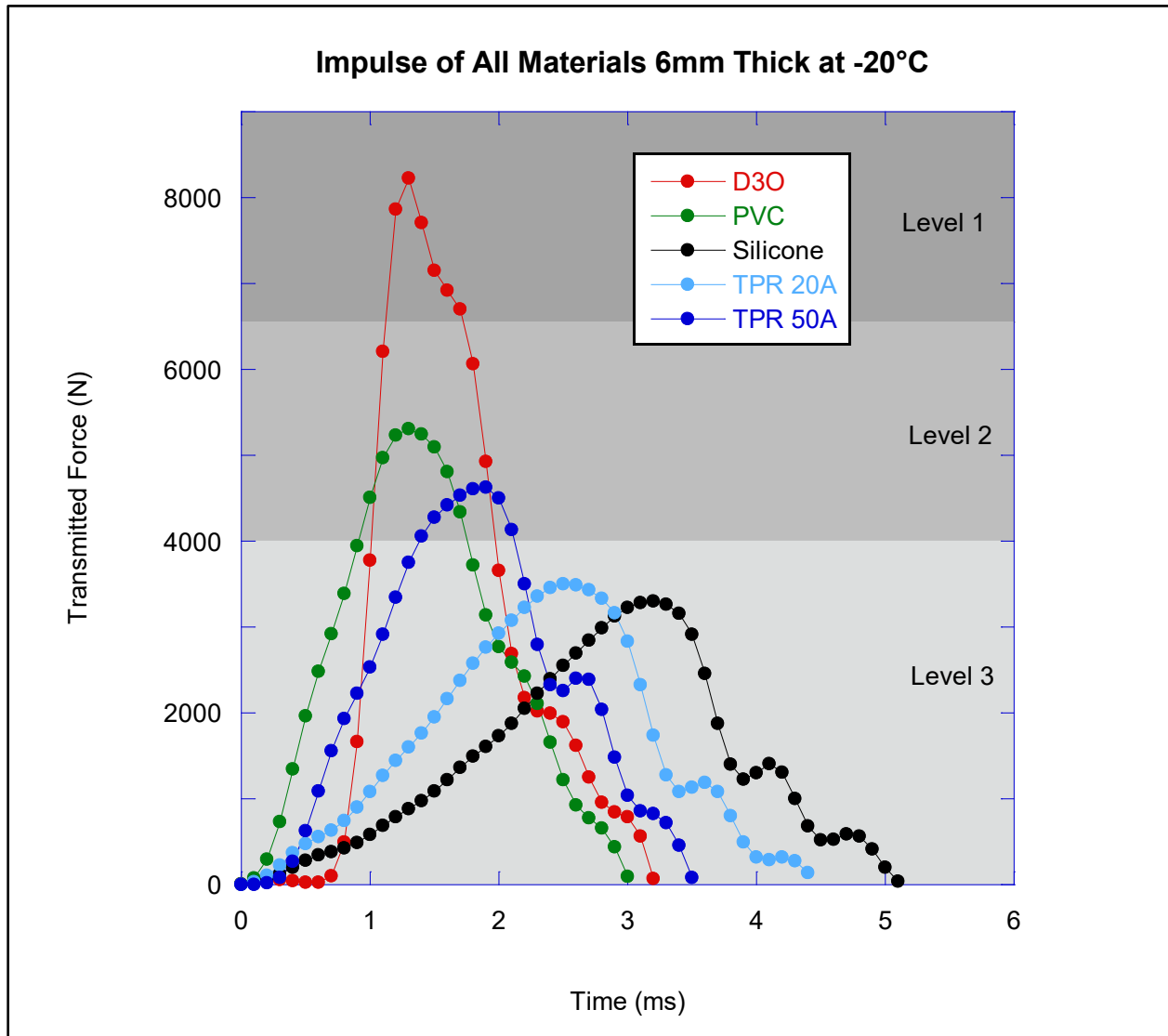
Figure 4.12: The impulse curves of each material at -20°C. Data was truncated so that the onset of the impulse started at time 0 (drop testing starts time at 0 for when the mass is released). Each specimen measured 84 mm x 54 mm laterally.

4.3.1.3 DMA Temperature Sweep

The results of the drop tests and impulse data show that it is difficult to predict the behaviour of each material with limited temperature data. A DMA temperature sweep of each of the specimens was conducted in order to analyze the behaviour of each material for the entire intended service temperature for the design (-40°C to 40°C) as well as to see where the glass transition temperature occurred in each material.

The storage modulus of each specimen over a range of temperatures from DMA testing is shown in Figure 4.13. All of the tests were conducted at a frequency of 1 Hz (meaning one compression every second) and the specimens were cooled to -70°C in order to locate the glass transition temperature. The location where each curve has a significant drop (highly negative slope) in Figure 4.13 indicates where the material's glass transition temperature initiates (where the material goes from behaving like a glass to behaving like a rubber). For TPR 20A and 50A (light and dark blue), the glass transition temperature, defined by the peak in tan delta when these drops in temperature occur (peaks found in Figure 4.14 below), occurs at -60°C; for silicone (black) the transition occurs at -40°C; for PVC (green) the glass transition temperature is -30°C, and for D3O® (red) the glass transition temperature is 30°C. The locations and shapes of the glass transition temperatures offer insights to why each material performed the way it did under testing at 20°C, -20°C, and -40°C. At room temperature, all of the materials are in the rubber regime; however, when the temperature is decreased to -20°C D3O® is no longer in the rubber regime and has a high storage modulus. As a result, D3O® performs the worst of the materials at lower temperatures because it becomes glassy, and unable to absorb impact. When the temperature is further decreased to -40°C, TPR 20A and silicone have not met their glass transition temperatures, but are close to the transition temperatures, which correlates to a higher tan delta (see Figure 4.13 below) which results in a lower transmitted force than at -20°C. At -40°C, TPR 50A and PVC are in the process of transitioning from the rubbery regime to the glassy regime and consequently have a higher transmitted force than at -20°C.

DMA Temperature Sweep - Storage Modulus E'
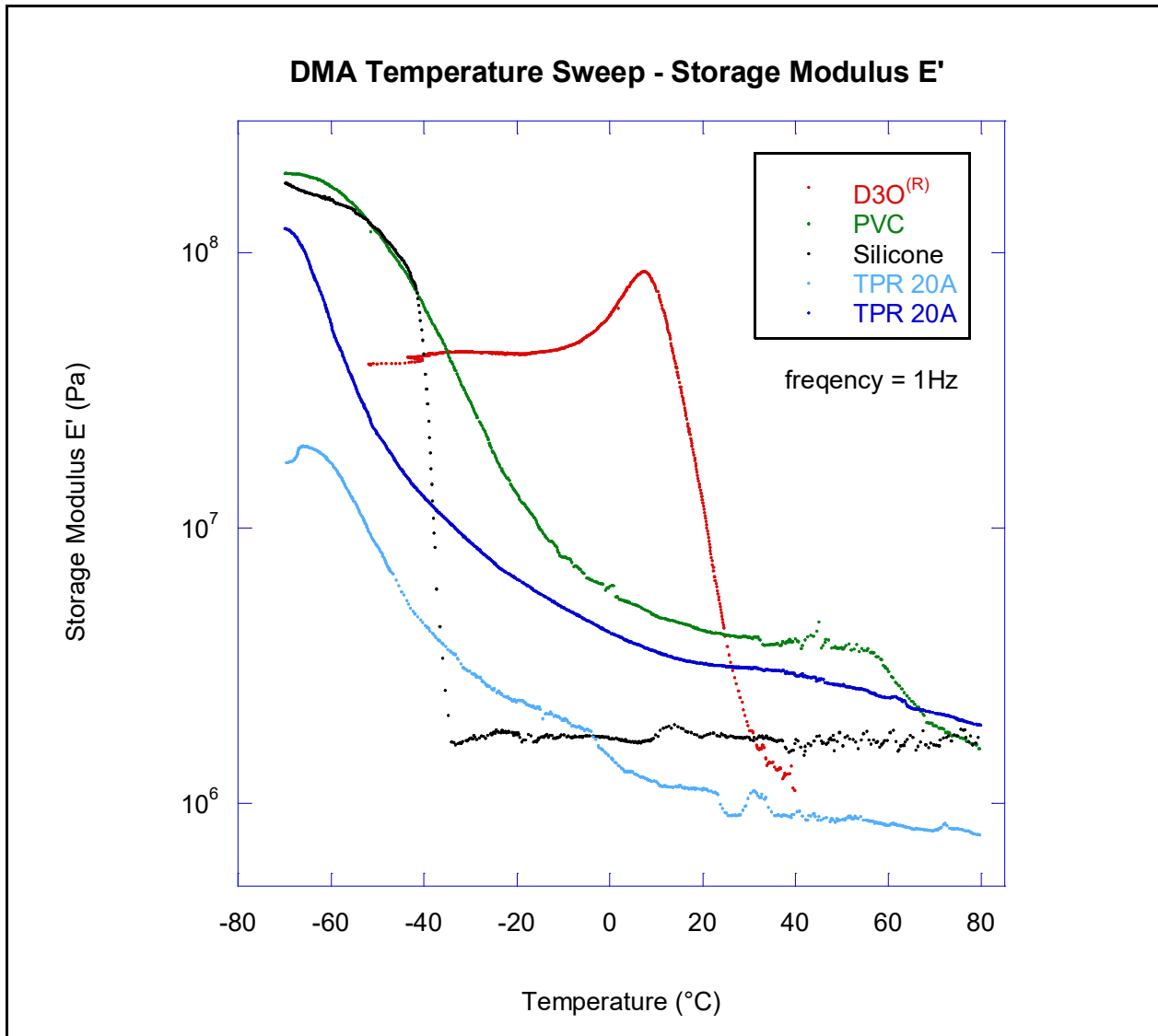
Figure 4.13: The results of the DMA temperature sweep testing completed for each material. D3O®(black) had the highest glass transition temperature, defined as the onset of the drop in the curve at 15°C.

Figure 4.13 above cannot answer why D3O® has a lower transmitted force at room temperature. Why D3O® performs better at room temperature is shown in Figure 4.14 below. In Figure 4.14, the tan delta of each material is plotted against the temperature. As discussed in Chapter 2, the tan delta is a measurement of the loss modulus and the storage modulus. The higher the tan delta, the better the material is at absorbing energy. In addition, the tan delta peaks identify the glass transition temperature for each material. Figure 4.14 shows that D3O®'s tan delta is 2-3 times higher than the other materials at room temperature, which is why it is better at reducing the transmitted force at this temperature. Through the observations of the tan delta, a hypothesis can be made that D3O® was specifically designed to reduce transmitted force at room temperature conditions (in contact

with human skin and tissues). The hypothesis cannot be confirmed as information related to the creation of D3O® is a trade secret.
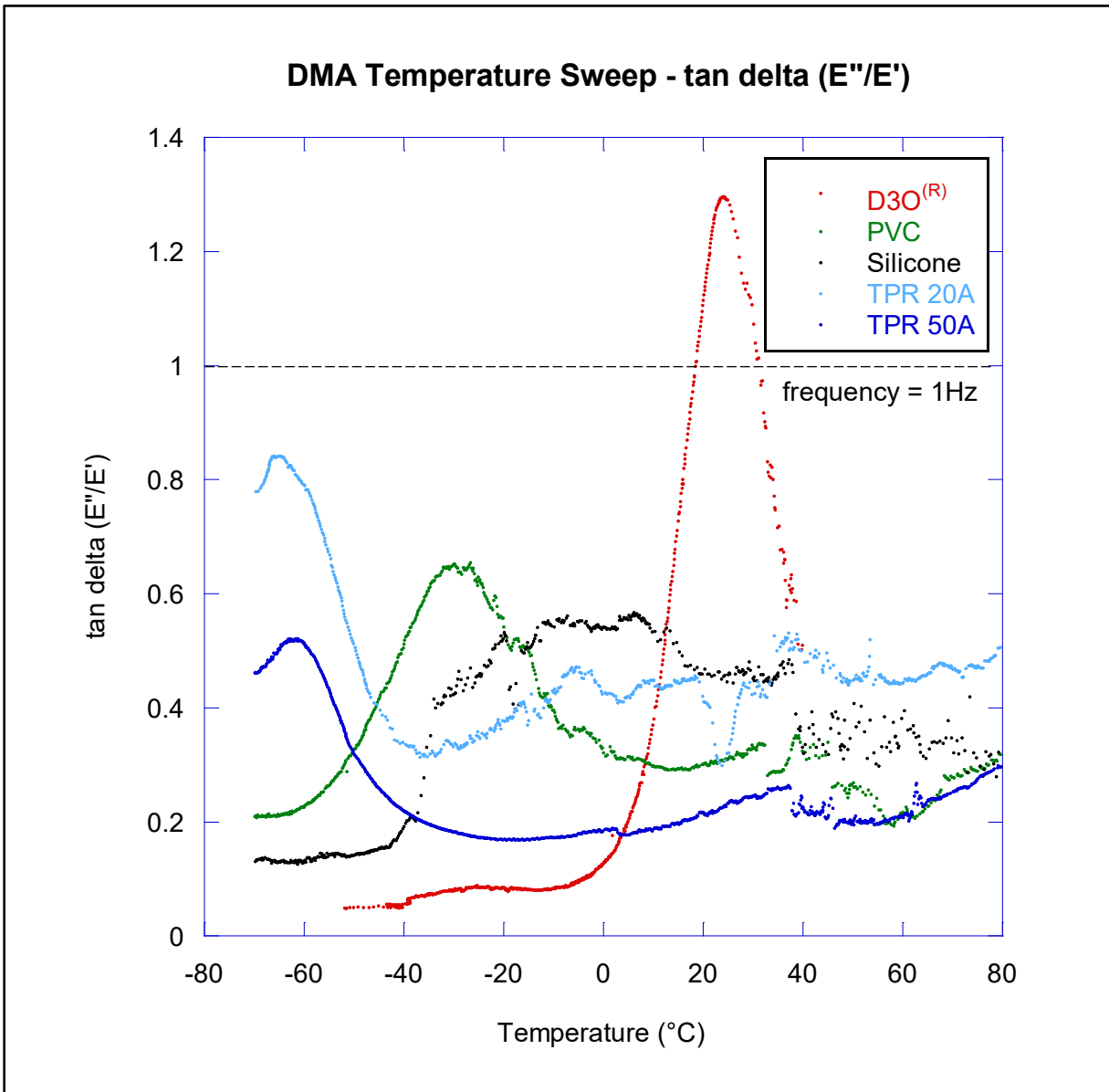
Figure 4.14: The tan delta of each material vs temperature.

Figure 4.15 shows the results of each drop test for each temperature series plotted against the tan delta. Each level of protection region, defined per the ANSI/ISEA 138-2019 standard, is shaded with the lightest being the highest level of protection and the darkest being the lowest. Any reading that is in the pink section would fail to meet any level of protection within the standard. As shown by Figure 4.15, tan delta is not an absolute way to show if the material will offer better impact protection

and the magnitude of tan delta is material dependent; therefore, tan delta should not be the only factor considered for reducing transmitted force. For example, four tests with a lower tan delta than D3O® at room temperature (1.1 - dot indicated), were able to achieve the criterion for level 3 while the D3O® at room temperature achieved a level 2.
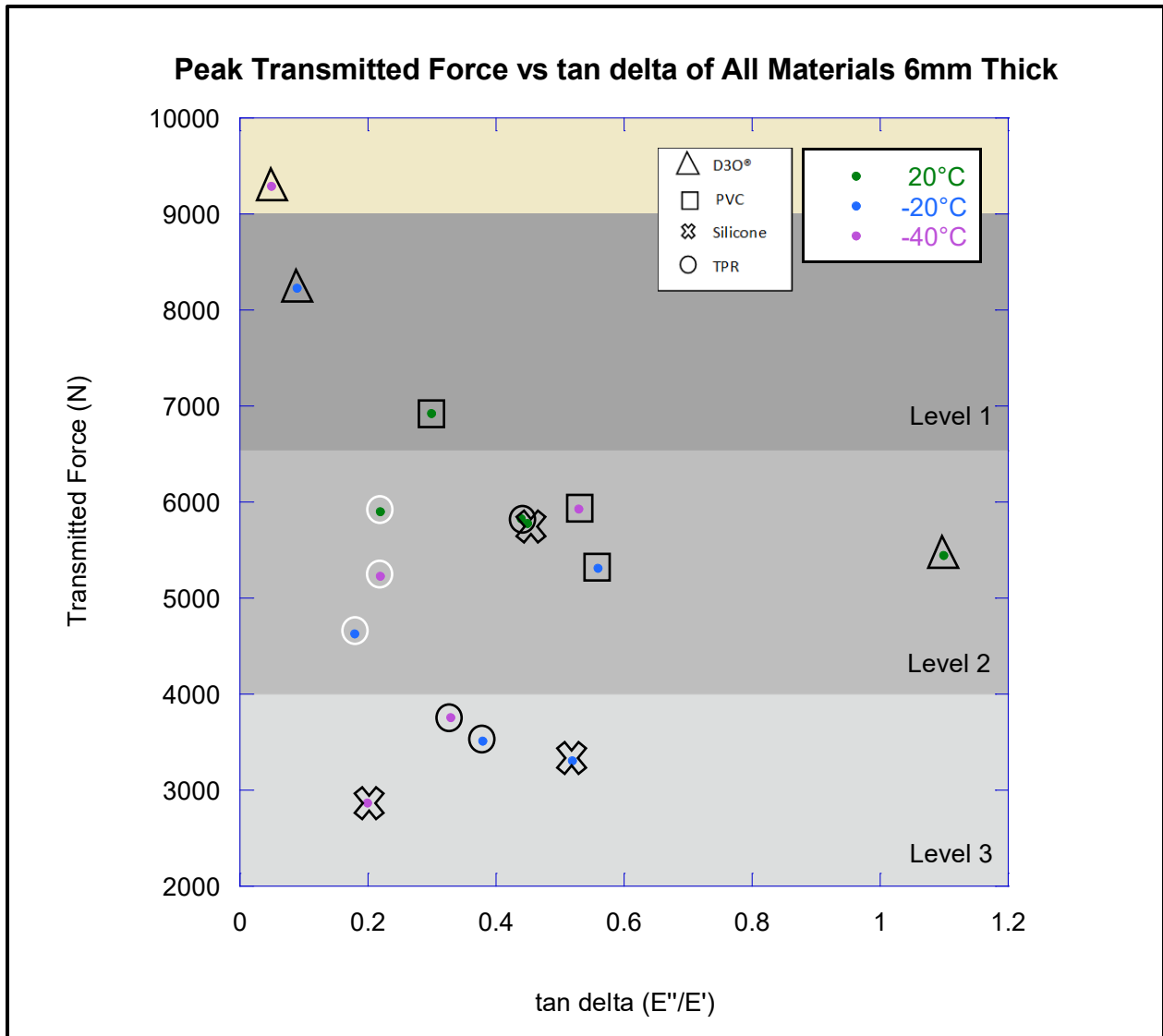
Figure 4.15: The effects of tan delta on transmitted force for three temperatures: 20°C (green), -20°C (blue), and -40°C (purple). Each material was given a unique shape on the plot: triangles are D3O®, squares are PVC, crosses are silicone, and circles are TPR. The TPR hardness is differentiated by color, with the black circles identified as TPR with a shore hardness of 20A and the white circles identified as TPR with a shore hardness of 50A.

4.3.2 Varying Frequency

Knowing the behaviour of each material under different frequencies is important as the use case of the gloves could result in the glove being subjected to multiple impacts over a short period of time.

For example, a construction worker using a hand grinder in a confined space could result in the knuckles being impacted frequently. Thus, based on equipment limitations, a frequency sweep was conducted on all of the materials at room temperature from 0.1 Hz to 100 Hz with 10 test points per frequency decade.

Figure 4.16 shows a composite of all the different materials' tan delta values at for the DMA frequency sweep. As displayed, D3O® (red) has a higher tan delta at low frequencies compared to the other materials. Thus, D3O® will absorb more energy, correlating to a lower transmitted force, out of all the materials at a frequency range of 0.1- 70 Hz at room temperature. At the higher frequencies of 70 Hz -100 Hz, silicone has the highest tan delta and will absorb the most energy compared to the other materials. Although D3O® does not perform as well at higher frequencies compared to the other material, the tan delta is still high at 0.6, which demonstrates that D3O® still has a high energy absorption capability at higher frequencies.
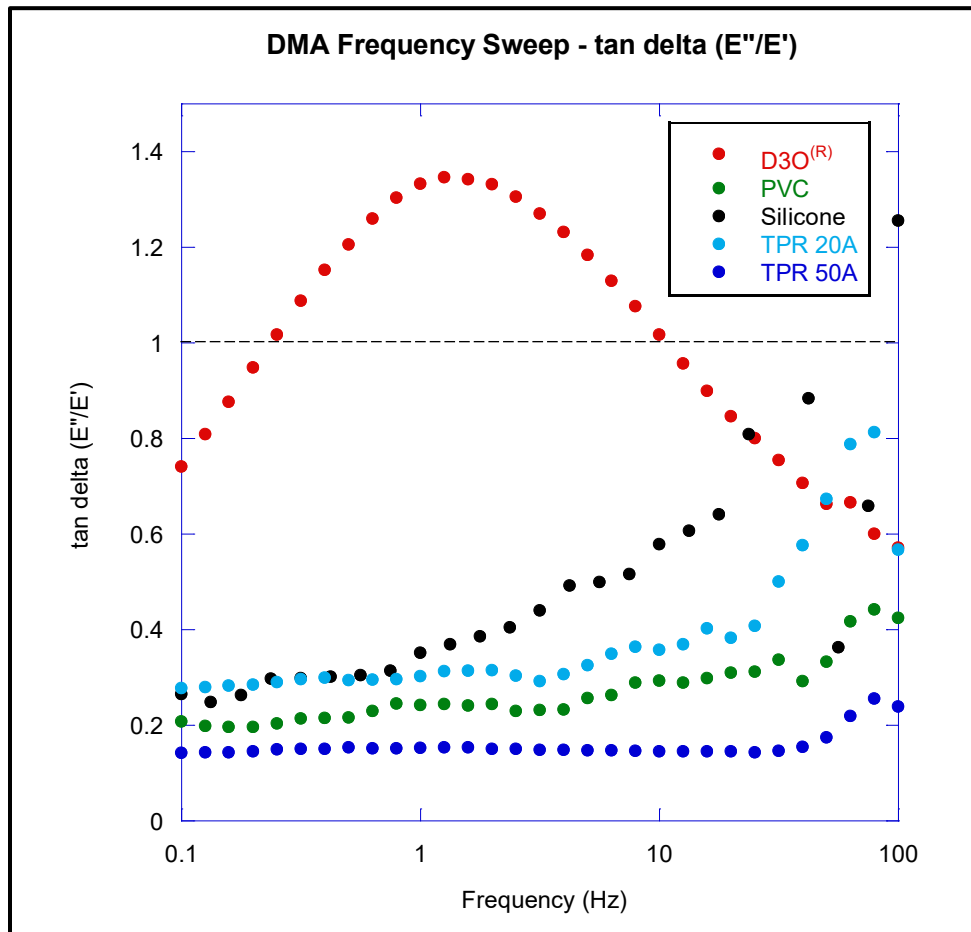
Figure 4.16: The tan delta of each material tested through DMA across different frequencies. At lower frequencies, D3O® (red) had the higher tan delta. At higher frequencies silicone (black) and TPR 20A (light blue) had the higher tan delta.

4.3.3 Varying Hardness

As demonstrated in the drop tests conducted in section 4.3.1, there is an observed correlation between hardness and transmitted force. This correlation is such that specimens of the same material with a lower hardness have a decreased transmitted force when the specimen dimensions are the same (i.e., TPR 20A has a lower transmitted force than the TPR 50A for the same specimen thickness and surface area). In general, the softer the specimen, the better it performed at room temperature (with the exception of D3O®); however, the type of material also played a role in the transmitted force (e.g., silicone has a hardness of 30A, but had a lower transmitted force than TPR 20A).

TPR was the only material that was created to have varying hardness for experimentation as it was made by a third party who had the ability to control the hardness of the blend. Figure 4.17 illustrates the effect of hardness on transmitted force for TPR specimens with 6 mm, 7 mm, and 8 mm thicknesses. These thicknesses were chosen as they were the specimens supplied with a full range (20A, 25A, 30A, 40A, 50A) of hardness. The equation for each thickness is given as a linear function of the effects of hardness on transmitted force. At room temperature, the general trend of the graph is that when hardness is increased, the transmitted force is increased as well. In addition, there is an observed correlation between thickness and transmitted force (the thinner the material, the higher the transmitted force), which will be discussed in Chapter 5. Thus, hardness is another variable that affects transmitted force.

Effects of Hardness on Transmitted Force for TPR

$F_t = 4.59e+3 + 19.2x(H)$ $R^2 = 0.838$

$F_t = 4.17e+3 + 16.6(H)$ $R^2 = 0.811$

$F_t = 4.00e+3 + 9.46(H)$ $R^2 = 0.546$

6 mm
7 mm
8 mm

Level 2
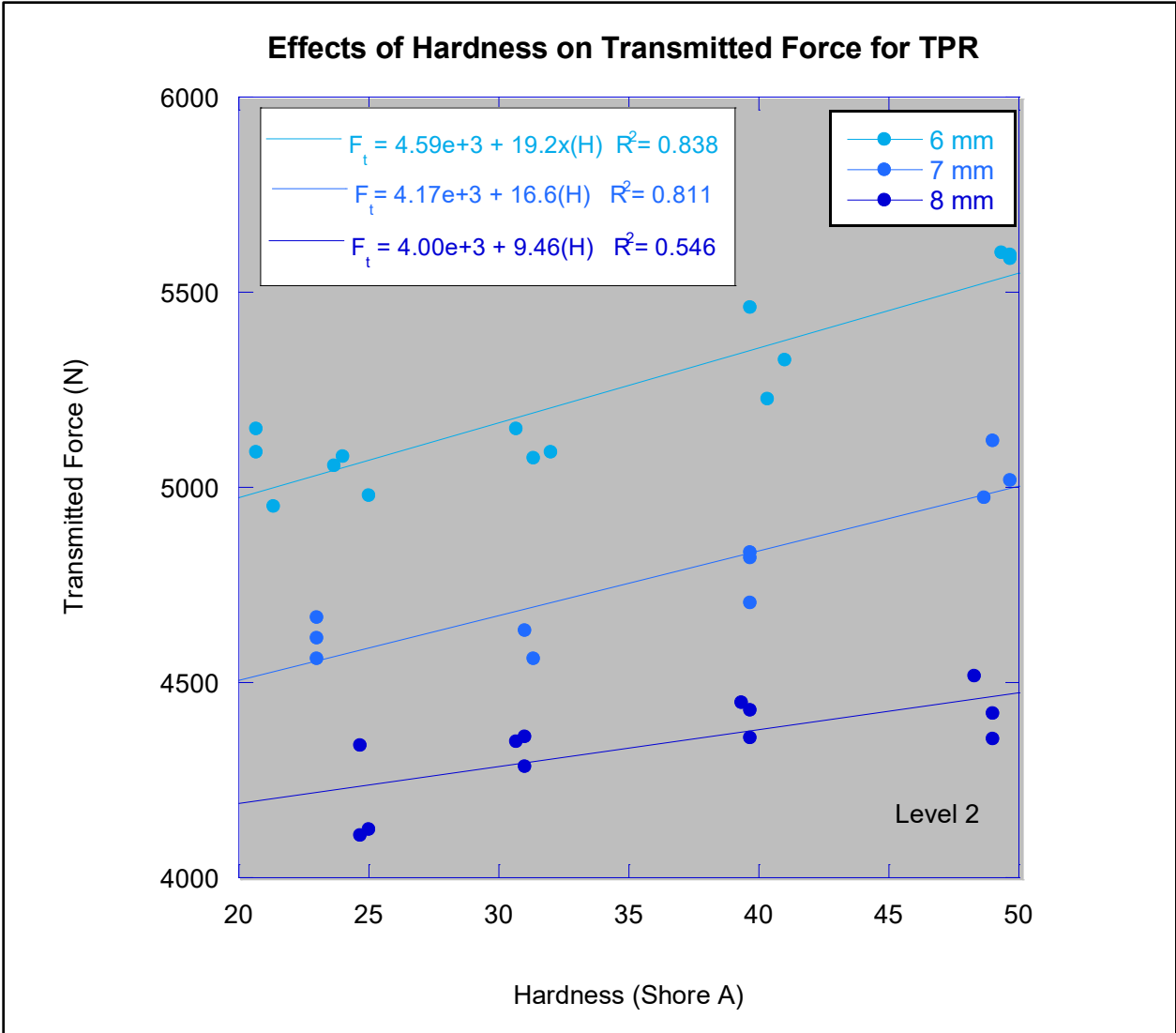
Figure 4.17: The effect of shore hardness on transmitted force for 6 mm, 7 mm, and 8 mm thick specimens of TPR. Each shore hardness specified had 3-5 TPR specimens tested. The specimens had lateral dimensions of 84 mm x 54 mm.

4.3.3.1 Hardness with Repeated Impacts

In the accelerated repeated impact testing conducted there was an observable difference in the material specimen for TPR 20A and TPR 50A of the same thickness after all 20 drops were completed. When the experiment was completed, each specimen had noticeable rings of plastic deformation radiating out from the impact test site. There were two major rings to note: the smallest ring and the largest ring. The smallest ring measured 20 mm in diameter, which correlated to the contact surface area of the anvil and striker. This ring was observed on the bottom face of the specimen and was caused by the residue of the double-sided tape adhering to the specimen during each test. The larger ring was observed on both sides of the specimen and varied in diameter depending on the hardness

of the specimen. The outer ring measured 40 mm for the 20A specimens, 30 mm for the 50A specimens and 38 mm for the 30A specimens. The outer ring demonstrated the extent of the plastic deformation, or the outward edge of the damage front caused by the impact.

Figure 4.18 illustrates a 4.5 mm 20A specimen after the repeated impact testing. The smaller circle is indicated with a red arrow and the larger circle that was observed on both sides is indicated with a blue arrow. For the 20A specimen, other rings were observed between the small and large ring and can be attributed to the softer material having a lower stiffness and coming into contact with more of the adhesive of the double-sided tape. These rings in the middle were not observed on the harder specimens, which were stiffer and did not contour to the anvil in the same way the 20A specimens did when they were impacted.
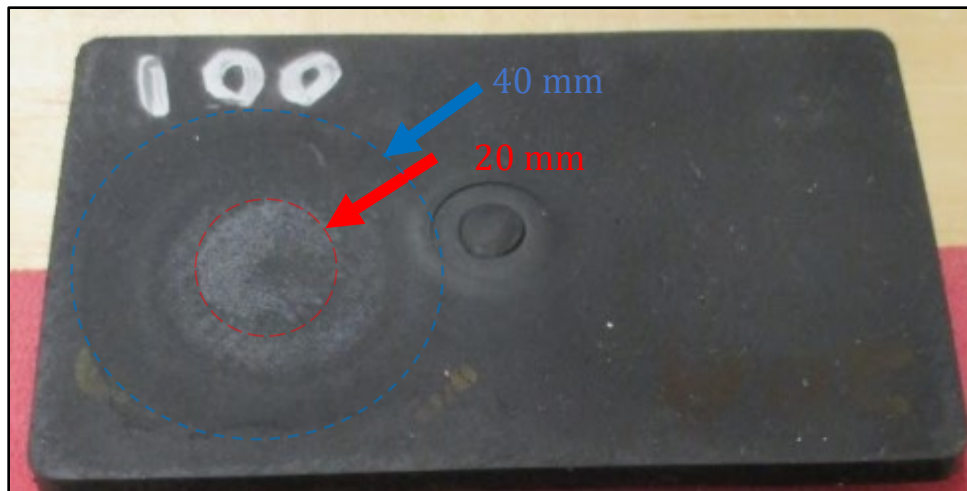
Figure 4.18: An example of the rings produced during the repeated impact testing on a standard 84 mm x 54 mm TPR 20A specimen 4.5 mm thick. The smaller ring (red) measured 20 mm in diameter and the larger ring (blue) measured 40 mm in diameter.

The observations made during the accelerated impact testing indicate that the outer ring of the softer specimen was larger than the outer ring observed on the harder specimen. As it was on both sides, the outer ring was concluded to be a visual indicator of the plastic deformation of the specimen. Thus, the damage from the stress wave was greater in the softer specimen and could be a factor in understanding why a lower hardness reduces the transmitted force—the amount of material involved that plastically deformed decreased the transmitted force as the impact energy was able to be absorbed by the increased number of broken interatomic bonds.

4.3.4 Rankings of the Materials to be Used

Table 4.5 below shows a ranked summary (with 1 being the best and 5 being the worst) of the performance of each material for different temperatures and frequencies. In addition, the performance rank for the hardness of TPR is provided. The ranking is based on the transmitted force for the temperature readings, the tan delta for frequency, and the transmitted force for hardness. Materials with a low transmitted force or higher tan delta were ranked higher (assigned a 1). Note: the hardness and frequency rankings are based off of room temperature data. The overall ranking was assigned by using both the temperature and frequency rankings, with a higher weighting given to the temperature ranking.

Table 4.5: The ranking of each material for different temperatures, frequencies, and hardness. The best materials were assigned a 1, and the worst a 5. For the temperature and hardness rankings, 1 was assigned to the specimen that had the lowest transmitted force. For the frequency rankings, 1 was assigned to the material with the highest tan delta and 5 was the lowest tan delta. The overall ranking was assigned by using both the frequency and temperature rankings, giving a higher weighting to the temperature ranking.

Material	Room Temperature Ranking	Cold Temperature Ranking	Low Frequency Ranking	High Frequency Ranking	Hardness Ranking	Overall Ranking
D3O®	1	5	1	3	---	3
PVC	5	4	4	4	---	5
Silicone	2	1	2	1	---	1
TPR 20A	3	2	3	2	1	2
TPR 50A	4	3	5	5	2	4

Based on the overall rankings shown in Table 4.5, silicone and TPR 20A would be the better materials to use for impact resistant bumpers as they are the top performers for various temperature and frequency ranges.

4.4 Summary

Table 4.6 below provides a summary of Chapter 4 and how it answered the desired research question.

Table 4.6: A summary of the research questions addressed in Chapter 4 and how they were evaluated.

Research Question	Method Used to Evaluate the Question	What was Learned
(1) Is there a material currently not used by the glove industry that can enhance the impact performance of gloves?	• Ashby design method for materials selection • GRANTA EduPack	• There are additional materials, such as HBR, that could be used for glove bumpers in order to meet the design objectives; however, HBR and other materials did not perform well when the materials selection scope was broadened (e.g., defining that the glove must be oil resistant) • The method used to process the material and how easily it can be processed matters (at least as much as the material itself).
(2) What material should be used for the glove bumpers based on the use case of the gloves?	• Drop testing at different temperatures • DMA frequency sweep • DMA temperature sweep	For the materials tested: • At room temperature D3O® should be used • At cold temperatures (-20°C and -40°C) silicone or TPR 20A should be used • If a wide range of service temperature is required, silicone should be used • At low frequencies (0.1-1 Hz) D3O® should be used • At high frequencies silicone should be used • For the same material, such as TPR, the lower hardness should be used

Chapter 4 References

[1]Ashby MF. Materials selection in mechanical design. 4th ed. Burlington, MA: Butterworth-Heinemann; 2011.

[2]Granta Design Limited. Granta edupack . Level 3 2020;20.1.1.

Chapter 5 : Dimension-Dependent Impact Response

5.1 Dimension Overview

When designing impact resistant gloves, it is important to understand how the thickness of the bumper and its dimensions affect the performance of the glove. For example, a designer may want to know how changing the thickness of the bumper by 1 mm affects the performance of the bumper, or how thin the bumper can be made in order to achieve the desired performance level outlined in ANSI/ISEA 138-2019 standard [1]. In addition, human hands have a limited surface area on the dorsal side of the hand, and the dimensions of a finger are drastically different than the dimensions of the back of the hand [2]; therefore, a designer would most likely want to know how changing the length and width of the bumper would affect the transmitted force.

The research questions from section 1.3 of Chapter 1 that Chapter 5 attempts to address are:

(2) What material should be used for the glove bumpers based on the use case of the gloves? (The question was also examined in Chapter 4).

(3) What are the effects of thickness, surface area, and volume on reducing transmitted force?

(4) When keeping thickness consistent, when does the lateral size (surface area) of the bulk material stop affecting impact performance?

5.1.1 Thought Experiment of Keeping Volume Constant

One thought experiment that reveals that the dimensions of the bumper matter, and are an independent factor from volume, is the geometries presented in Figure 5.1 below. Assuming both geometries have the same volume of material, the transmitted force is predicted to be different for both geometries as the long rectangle (a) is thicker than the square (b) in the direction of impact (indicated by the arrow); however, the long rectangle is more likely to develop stress concentrations and buckle due to the lack of material in the directions perpendicular to the impact. Increasing the height or thickness of the rectangle while keeping the volume constant would exaggerate the effect of the lack of material in the perpendicular direction. Thus, the dimensions of the geometry influence the manner in which the bumper absorbs impact by changing the mechanism of deformation.
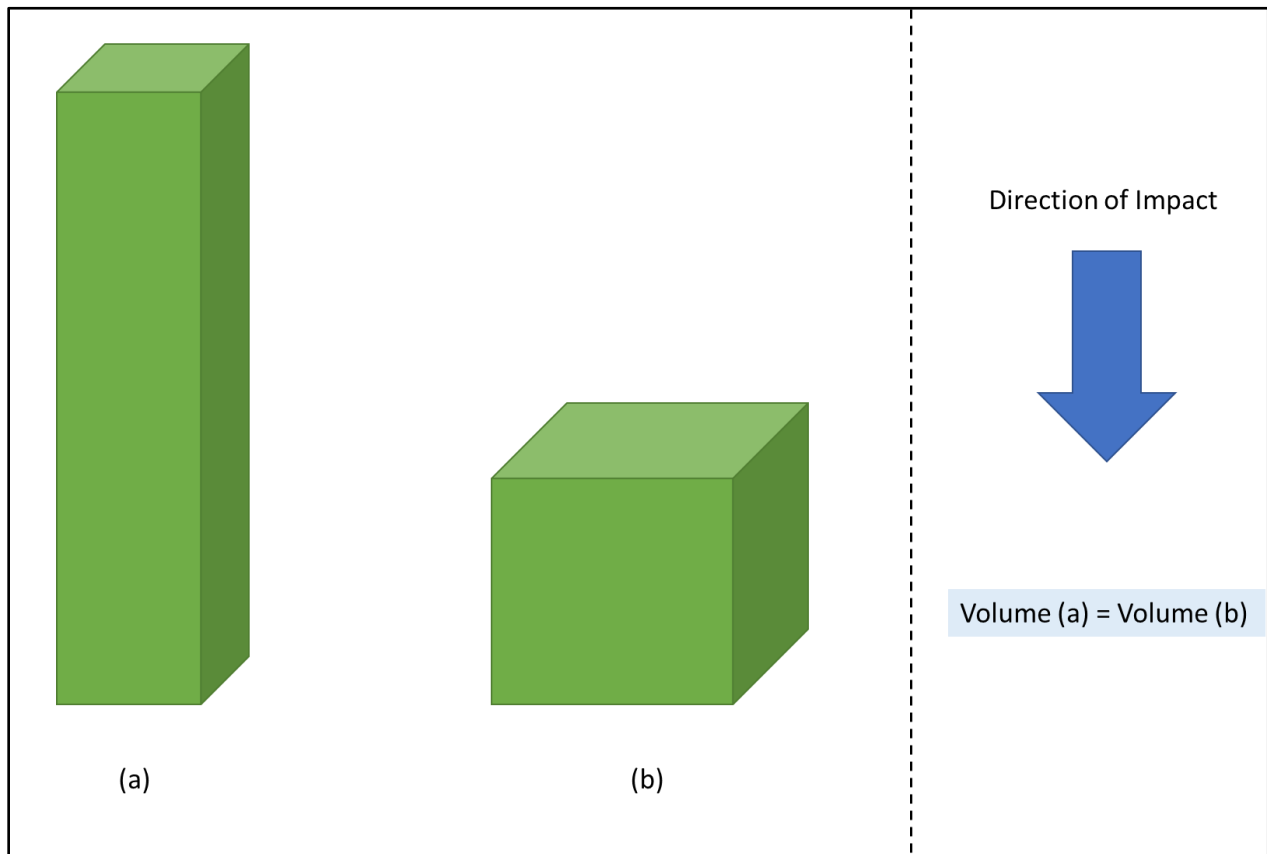
Figure 5.1: A visual thought experiment of how dimensions can influence transmitted force. In the Figure, both geometry (a) and (b) have the same volume; however, it is unlikely they will have the same transmitted force due to the influence dimensions have on how the material deforms under impact.

5.2 Thickness

The effect of thickness on energy absorption and transmitted force is in general described as: the thicker the energy absorber is, the lower the transmitted force. For example, a person jumping off a platform onto a mat will have a "softer" landing, or lower contact force with the ground (transmitted force) when the mat is thicker. Since the conditions of the jumper are assumed to be constant, (i.e., mass, jump height, and velocity), the softer landing can be attributed to the work-energy principle. The work done to an object is equal to the change in kinetic energy. Assuming that the kinetic energy at the time the person initially contacts the mat is the same and that the person comes to a full stop, the change in kinetic energy, or work, is equal to the kinetic energy at contact. Work (W), in its most basic form, is equal to a force (F_1) applied over a distance (d):

$$W = F_1 \cdot d \tag{5.1}$$

Thus, if work is kept *constant* for each jump off the platform (constant kinetic energy), the increasing of the thickness of the mat (increasing (d) in (5.1)) would consequently make the force applied to the mat and the force on the person smaller.

For the specimen tiles used in the experimentation, the work done on the material is 5 J from the time it comes into contact with the material to the bottom of the impact. Plugging this number into (5.1) and rearranging for the force gives:

$$F_1 = \frac{5(J)}{h^*} \tag{5.2}$$

where (h^*) is the distance the mass traveled in the direction of the thickness. Equation (5.2) cannot be used to solve for the transmitted force, however, because it is too general and omits other influences, such as the material properties of the specimens. If equation (5.2) were used, in order to get 1 N of transmitted force, the distance the mass would have to travel after impact is 5 m – which is too high of a value and the distance the mass would have to travel would become exponentially larger in order to reduce the transmitted force further as (F) and (h^*) are inversely proportional in equation (5.2). Thus, there are more factors influencing the force of the impact.

One of the possible factors influencing the force of the drop is the fact that materials have spring energy due to their atomic bonds [3]. Thus, when the mass is dropped onto the material, a spring force (F_s) will act against the mass in the form of:

$$F_s = -kh^* \tag{5.3}$$

where (k) is the spring constant of the material, measured in N/m and (h^*) is the distance the mass travelled, or by how much the material compressed. Thus, using the new work equation is (using the work-energy principle) is:

$$W = F_1 \cdot h^* - \frac{1}{2}k(h^*)^2 \tag{5.4}$$

Rearranging for transmitted force (in this case, F_1) and substituting 5 J into the work term gives:

$$F_t = \frac{5 + \frac{1}{2}k(h^*)^2}{h^*} \tag{5.5}$$

Figure 5.2 below illustrates the effect of thickness on the transmitted force of three of the materials used during testing: PVC, TPR, and silicone. The Figure is shaded grey for performance levels as per the ANSI/ISEA 138-2019 standard, with the yellow shaded area tests that do not meet any performance level. The TPR (blue) used for the data was the TPR from the second batch, which had a hardness of 30 A. The silicone (black) used the testing results from the first batch, and the PVC (green) includes all of the manufactured batches. For each specimen, the thickness experiment was terminated when the transmitted force was above 9 kN as the machine can only register forces up to 9.9 kN, as discussed in Chapter 3. All of the materials display the same trend: the thicker the material the lower the transmitted force. The value of the transmitted force for a certain thickness is also dependent on the type of material. For example, the 8 mm thick specimens of TPR and silicone have a lower transmitted force than the same thickness of PVC. For the data that is displayed, each material's transmitted force appears to have a logarithmic or linear relationship with thickness; however, as discussed above, the relationship is not linear and is likely exponential due to the inverse relationship of transmitted force and thickness in equation (5.2) above.
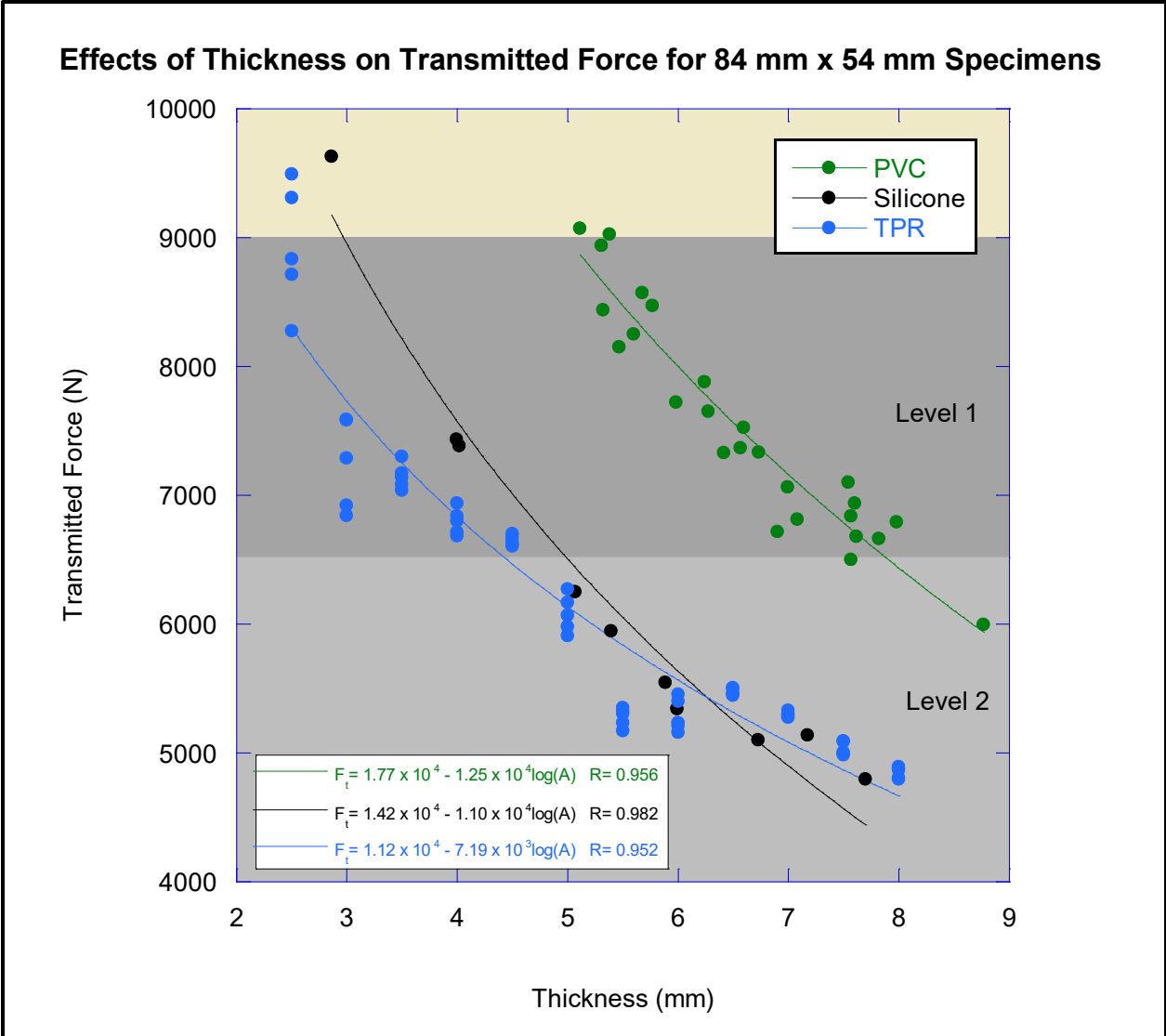
Figure 5.2: The effects of thickness on transmitted force of an 84 mm x 54 mm specimen tile. The data for PVC (green), Silicone (black), and TPR (blue) are given and logarithmically curve fitted. Due to equation (5.2) above, the relationship of thickness to transmitted force is likely to be exponential; however, the logarithmic curve fit all of the data better.

5.2.1 Hardness and Thickness

A main observation from Chapter 4 was that hardness affects transmitted force: the softer the material the lower the transmitted force. This conclusion, however, arose from observing the behaviour of specimens of the same thickness. Figure 5.3 contains a plot of thickness vs. transmitted force for different material hardness of the first batch of TPR. Each hardness was designated its own shade of blue, with the harder specimens having a darker shade of blue and the softer specimens having a lighter shade of blue. From Figure 5.3, the observation that the softer the specimen, the lower the transmitted force, is still valid across multiple thicknesses. The different hardness

specimen groups also display the same trend as shown in Figure 5.2 above: the thicker the specimen the lower the transmitted force. In addition, the trend of the graph appears to be linear; however, the trend is likely an exponential function as well due to the relationship of force and thickness of equation (5.2) above. One note about Figure 5.3 is that the 6.5 mm TPR specimens used in the testing had an actual thickness closer to 6 mm, which explains the data gap on the graph. Another note is that the one 50A data point at 7.5 mm measuring 5400 N is an outlier and was attributed to uncertainty in testing.
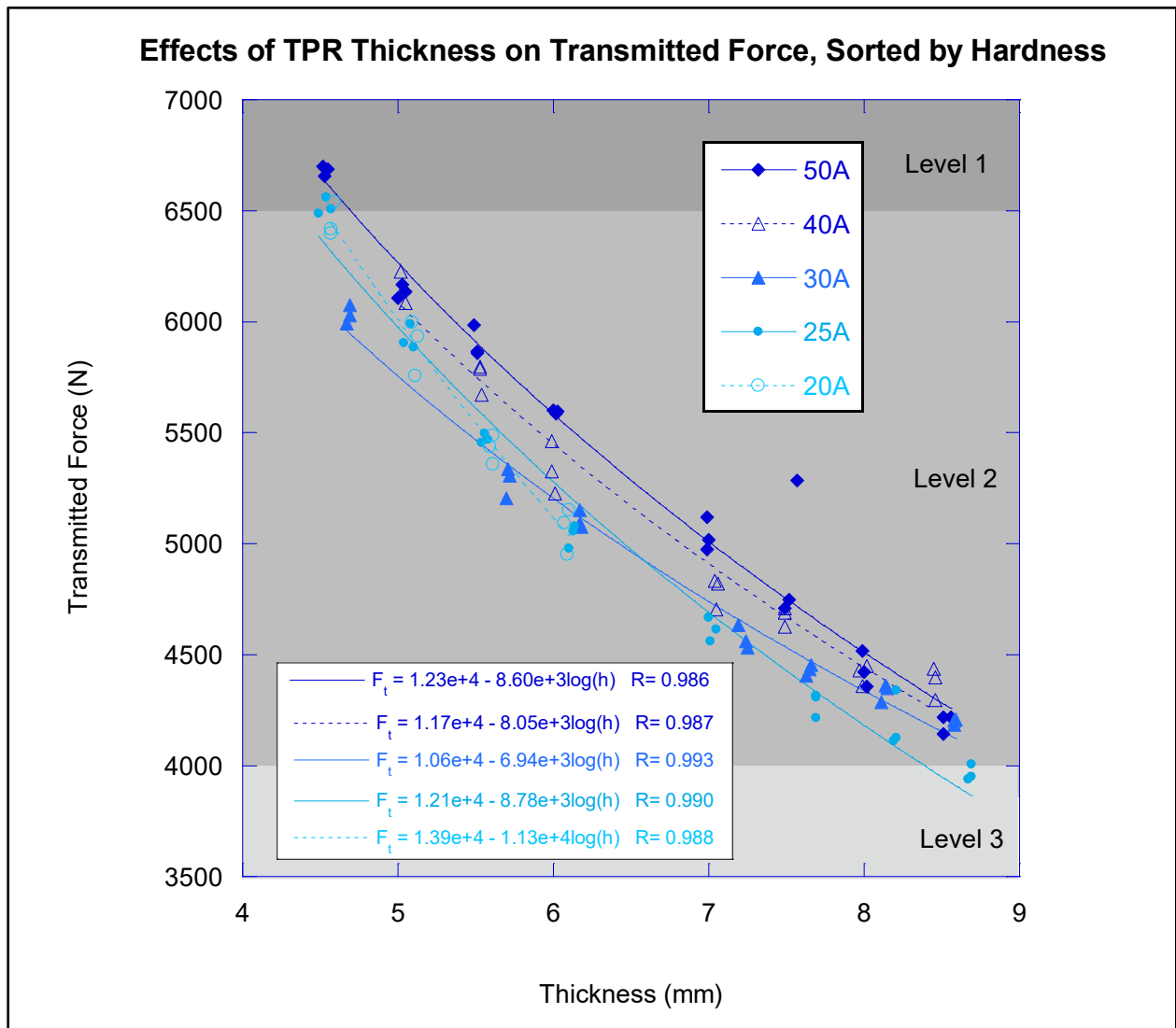
Figure 5.3: The effects of thickness on transmitted force, sorted by hardness. The harder specimens of TPR were assigned a darker blue and the softer specimens a lighter blue in order to visually display the effects of hardness on transmitted force. The 50A, 40A, 30A, 25A had 20-23 specimens tested and the 20A had 12 specimens tested. The specimens measured 84 mm x 54 mm laterally.

124

As displayed in Figure 5.3, thickness has a larger impact on transmitted force than hardness, as shown by the changes to the data points when thickness is changed compared to hardness. Hardness, however, does play a role in changing the transmitted force. For example, a softer (20A) specimen only has to be 6 mm thick to have the same 5 kN of transmitted force as a harder 50A specimen that is 7 mm thick.

5.3 Surface Area

When designing a bumper for an impact resistant glove, it is important to understand how the dimensional constraints, imposed by the surface area of the hand, affect the performance of the glove. For example, does a bumper with the same thickness perform the same on the fingers when compared to the back of the hand? The surface area of one finger is significantly smaller than the back of the hand. Due to the smaller surface area, a hypothesis can be generated that the bumpers on the fingers will not perform (reduce transmitted force) as well as a bumper on the back of the hand for the same thickness. This hypothesis arises from the prediction that a reduction in the bumper volume will decrease the specimen's ability to absorb impact; therefore, increasing the transmitted force. In fact, there should be an expected trade off point where increasing the surface area of a bumper with the same thickness does not substantially improve the impact performance.

The next section attempts to test the hypothesis. The surface area experiments were primarily conducted on silicone and it will be the material of focus for the section. Silicone was chosen for in depth experimentation due to its ability to be easily molded into any shape, the promise it showed from preliminary impact experiments, and it was the material that Superior Glove was most interested in developing.

5.3.1 Surface Area Analysis of Silicone

To find the effects of surface area, an 84 mm x 54 mm specimen tile of uniform thickness was used. The specimen was initially impact tested, cut in half along its length (reducing the surface area by half) and tested again. This procedure was repeated, alternating the directions of the cut in a perpendicular fashion, until the surface area was so small that the next cut would generate a transmitted force over 10 kN. For further details of the procedure see Section 3.4.2 of Chapter 3 and Appendix B.

Figure 5.4 shows a 7.5 mm silicone specimen after it had been tested for surface area (the top face, defined by the face with the label, is face down). Each cut was identified and the order of the cut is indicated with the commensurate number. Due to the lack of precision when cutting, each pieces' dimensions were measured after it was cut; the size of each piece was not assumed to be half of the surface area of the test before. Visually, there was no deformation or change in structure observed on the four larger pieces. The smaller pieces displayed a decrease in thickness, which was more prominent as the pieces became smaller.
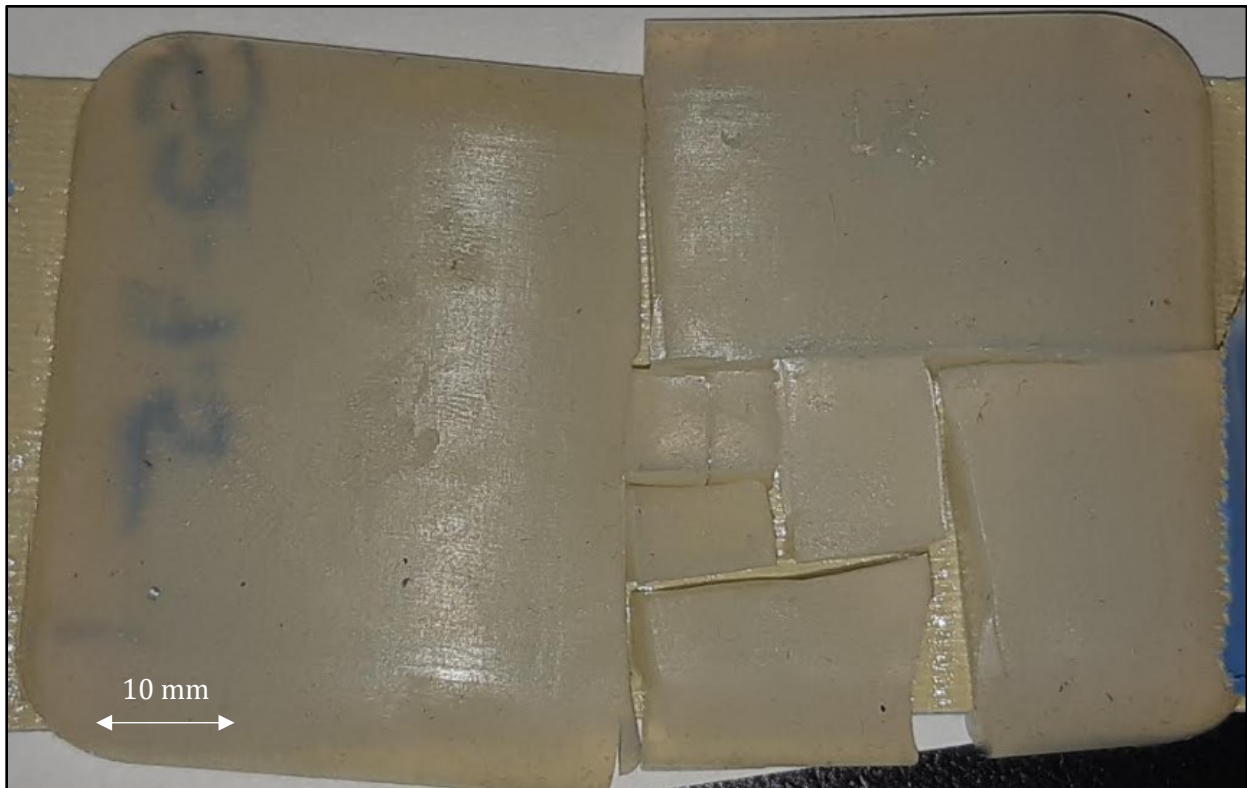
Figure 5.4: The 7.5 mm thick silicone specimen from batch 2 after the surface area analysis testing was conducted. The specimen surface that came into direct contact with the striker is shown in the Figure. The inconsistencies of the cuts were attributed to the tools available. The cut inconsistencies did not change the transmitted force more than 250 N (the range of uncertainty) as found from multiple surface area reduction testing.

Figure 5.5 illustrates the locations of the drop testing (red circles) conducted on the specimens. Recall from Chapter 3 that the impact contact surface of the anvil and striker was circular with a 20 mm diameter. The overlap of the circles show that the four smallest pieces were subjected to impact multiple times.
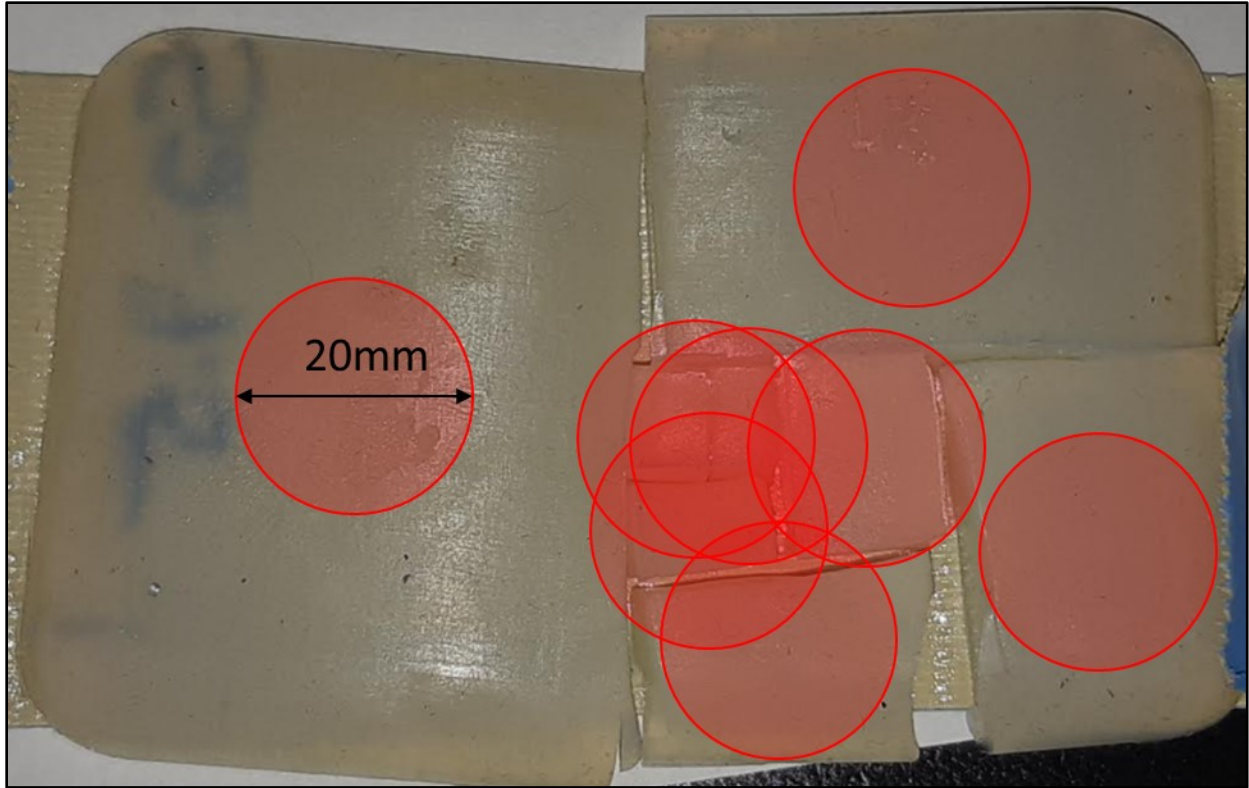
Figure 5.5: The locations of the drop testing (red circles) overlayed onto the specimen tested. The red circles are a visual indicator of the areas of the specimen that were in direct contact with the anvil-striker contact zone.

Figure 5.6 displays photographs of the two smallest pieces and the largest piece. The smallest pieces have a significant decrease in thickness compared to the largest piece and appear to have a convex, or bulging, shape in the other directions. In addition, the top surface of the smallest pieces, which were the ones that came into direct contact with the anvil, have a slight negative camber (concave down) form to them. The change of shape of the smaller pieces was attributed to plastic deformation which occurred when the load applied to the specimen exceeded the material's yield strength [3] (i.e., the material has permanently deformed and will not return to its original form on its own). An attempt to find all of the material's yield strength was made; however, the tensile tester available could not reach loads large enough to reach the yield strength of the material.
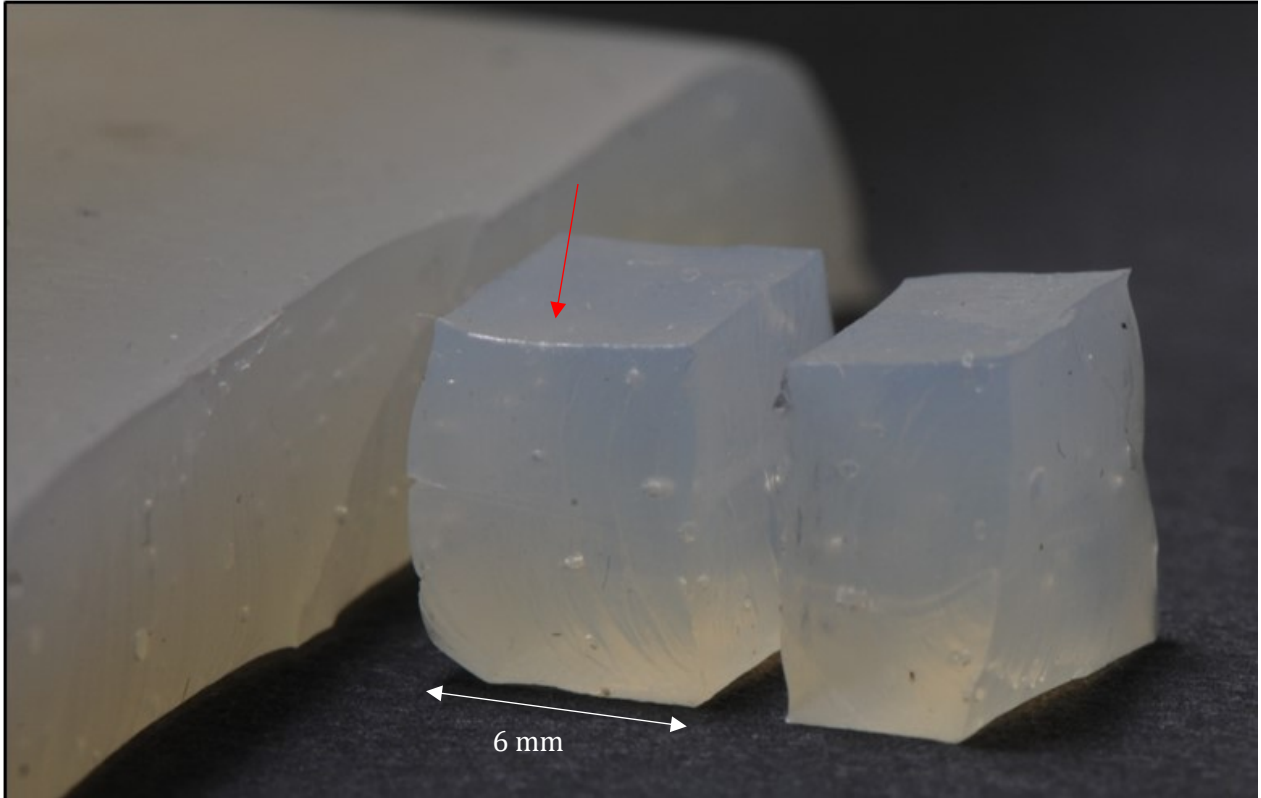
Figure 5.6: The deformation observed on the two smallest pieces after the surface area testing was completed. The pieces had a noticeable reduction in thickness and a slight negative camber on the surface that came into contact with the striker (indicated).

The test results of the reduction of surface area are shown in Figure 5.7. Figure 5.7 displays data from the 8 mm specimen of silicone of on a semi-logarithmic scale, and the grey shaded regions represents the corresponding levels of the ANSI/ISEA 138-2019 impact standard. The dependence of transmitted force on surface area was similar for all of the silicone specimens and did not reflect the trend that was hypothesized. When each silicone specimen was tested the same phenomena occurred: as the specimen was tested then cut into a smaller piece the transmitted force decreased as the surface area was reduced up until a certain point. At this point (approximated by the red dashed line), the transmitted force increased when the surface area was significantly reduced. Figure 5.7 below illustrates the point of inflection. On the right side of the graph, the transmitted force was measured to be 3985 N for the initial 84 mm x 54 mm specimen. When this specimen was reduced in size by half, the transmitted force only slightly decreased (3952 N). The next two reductions in surface area were accompanied by a 500 N reduction in transmitted force. When the specimen's surface area was reduced from 21 mm x 27 mm (567mm^2) to 21 mm x 13.5 mm (283.5mm^2) the transmitted force increased and every subsequent cut the transmitted force increased rapidly. Thus,

the graph can be observed to have two distinct regions, one being the area to the left of the inflection point (left of the red dashed line) where the data forms a vertical asymptote, and the other being to the right of the inflection point (right of the red dashed line), where the data forms a horizontal asymptote.
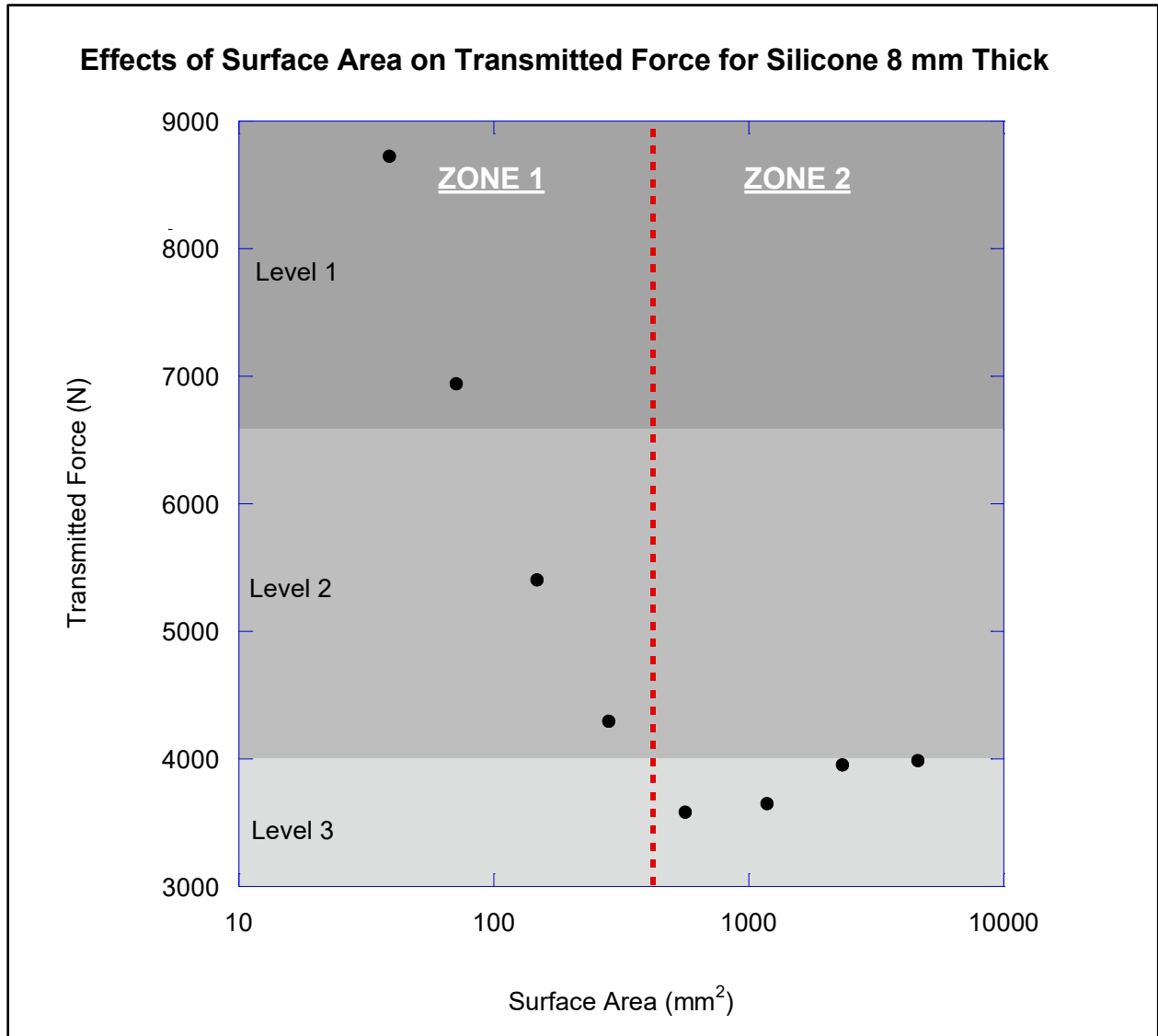
Figure 5.7: The transmitted force vs surface area plot for 8 mm silicone. Zone 1 contains the surface areas smaller than the inflection point (red line), and zone 2 contains the surface areas above the inflection point

There is a correlation to the pieces that had observable plastic deformation (the smallest four) and the regions of the graph in Figure 5.7 above. The smallest four pieces are all located in the region to the left of the inflection point (zone 1), which indicates that the inflection could be due to plastic

deformation occurring in the material (i.e., the behaviour of the left region is dictated, in part, or wholly, by plastic deformation); however, normalizing the transmitted force with the volume, as shown in Figure 5.8, illustrates that the behaviour of zone one is more likely due to the interaction volume of the material (i.e., the transmitted force increases exponentially due to the decrease in volume available for energy absorption). At small surface areas, the amount of normalized force-volume is higher in contrast to the curve fit, suggesting that the energy absorption is not as effective at small surface areas, likely due to permanent deformation. For the right-side region (zone 2) in Figure 5.7, the transmitted force increases as the surface area increases. One hypothesis for this phenomenon is that due to the inherit length scale of the specimen, there is minimal plastic deformation occurring. Plastic deformation reduces the transmitted force as more energy is absorbed due to the bonds breaking [3].
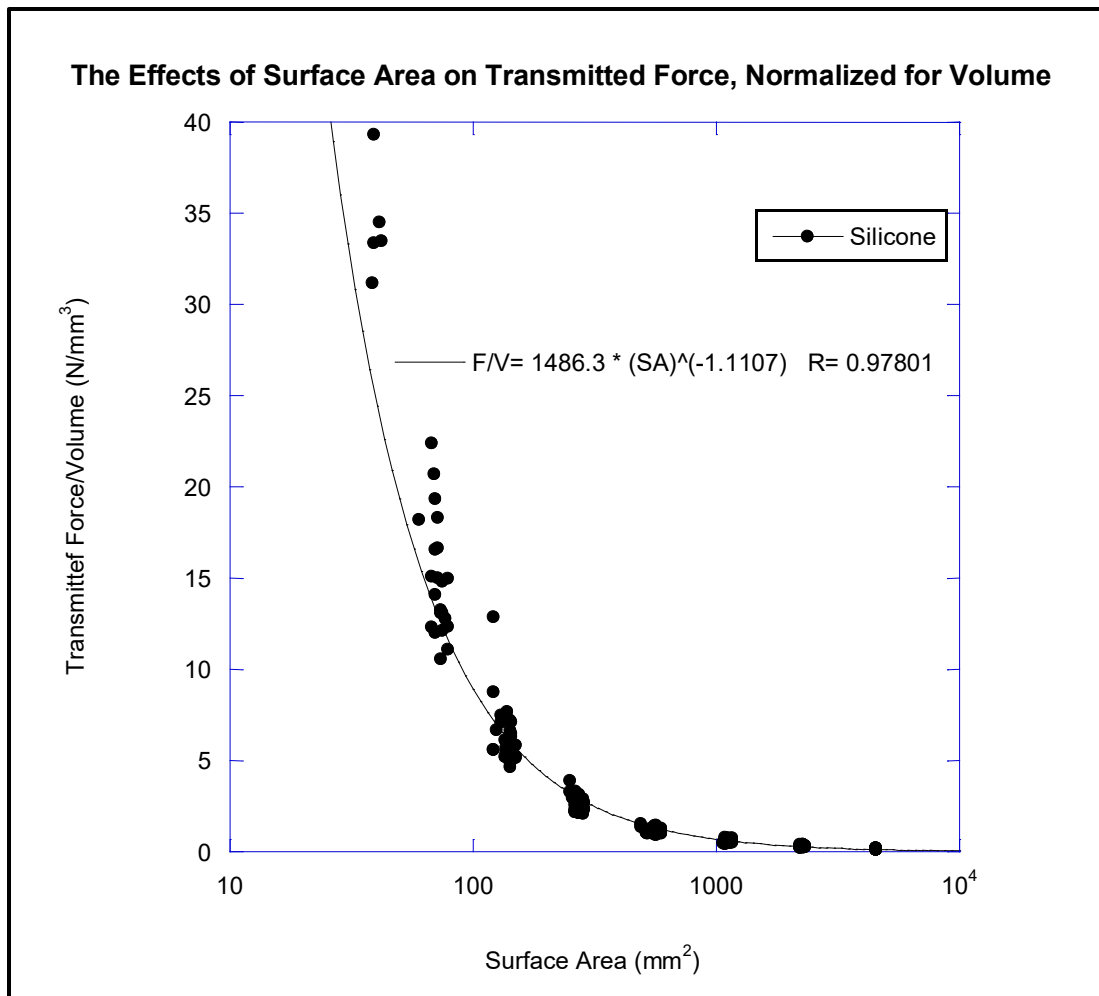
Figure 5.8: The surface area analysis with transmitted force normalized for volume. With small surface areas, the amount of normalized force-volume is higher in contrast to the curve fit, suggesting that the energy absorption is not as effective on small surface areas, likely due to permanent deformation.

130

To further show the two surface area regions, Figure 5.15 below displays all of the silicone specimens that were tested. In Figure 5.15, the thicker specimens in the 8-9 mm range are blue, the specimens in the 7-8 mm range are green, and the specimens in the 6-7 mm range are yellow. In addition, the darker the shade of the color, the thicker the specimens. The thicker specimens had an overall lower transmitted force when considering similar surface areas. When all of the thicknesses are compared, the data points appear to converge on both zones the closer they get to the inflection point (dashed red line), creating a bow-tie shape to the graph (highlighted by solid red lines). The area of convergence occurs close to the surface area 314 mm², which is the contact surface area between the striker and anvil (see Chapter 3). This observation alludes to the fact that there is a characteristic length scale for material behvaiour and the dimensions of the testing apparatus have an influence over the end of zone 1 (where the bumper performance is more sensitive to the amount of plastic deformation in the material) and the start of zone 2 (where the bumper performance is most sensitive to the thickness).
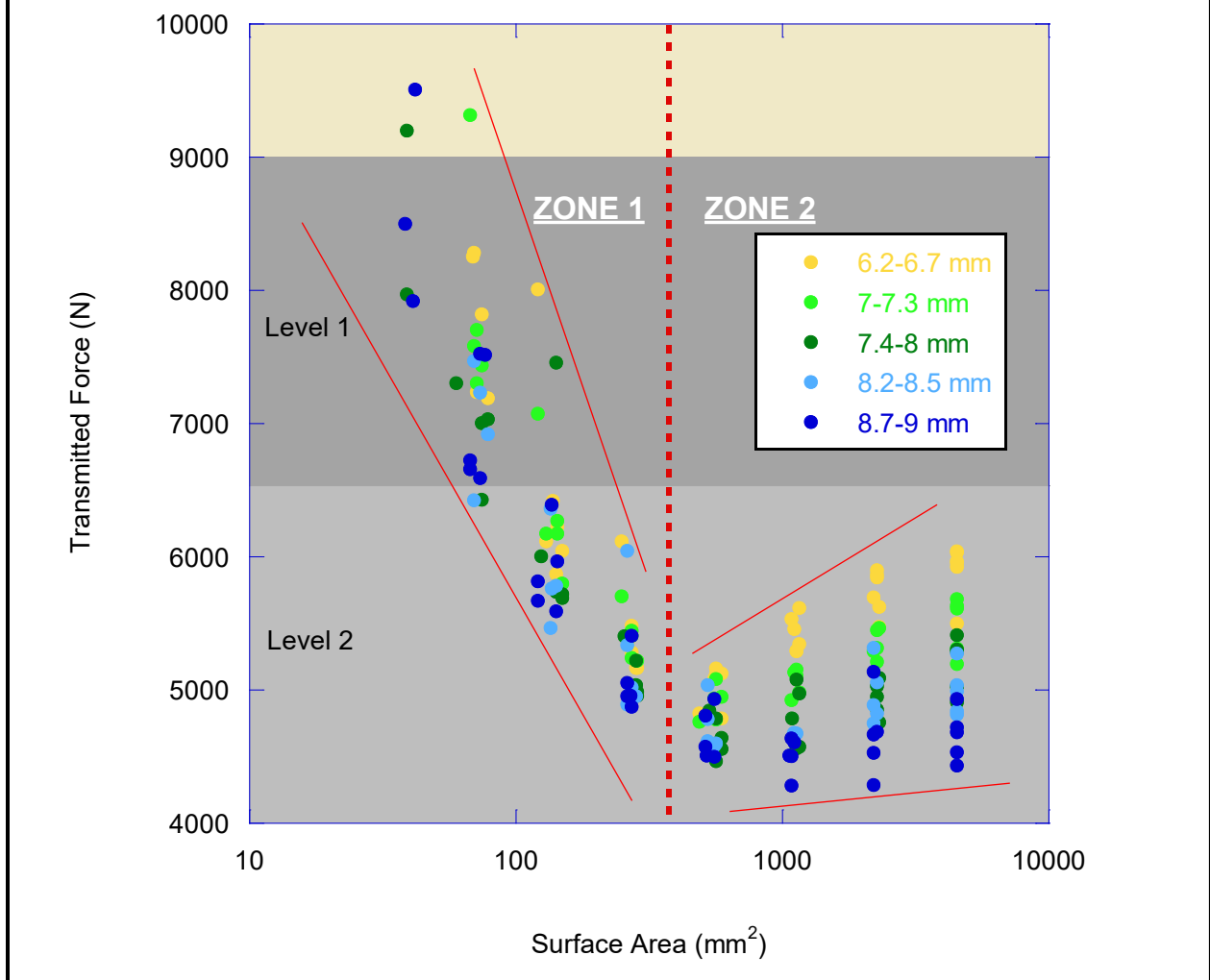
Figure 5.9: All of the silicone specimens tested for the effect of surface area on transmitted force. The thickness of the specimens are indicated in the legend on a rainbow scale: thinner specimens were assigned a color closer to yellow and thicker specimens were assigned a color closer to blue.

5.3.1.1 Changing the Cut Order of Experiment

Changing the cut order (cutting side B first instead of side A) of the surface area experiment was explored for silicone, and the results are detailed in Appendix B. The results of changing the cut order showed that the lateral dimensions are more important than surface area when interrogating transmitted force. For example, a 40 mm x 20 mm piece from a specimen produced similar transmitted force results as a 20 mm x 20 mm piece. Once one lateral dimension was less than 20 mm, the cut order did not matter suggesting that the 20 mm dimension was more important than the total surface area. The 20 mm dimension was also the diameter size of the striker-anvil contact

surface, which demonstrates that the surface area behaviour of the silicone is influenced by the dimensions of the testing apparatus.

5.3.1.2 Impulse of Decreasing Surface Area

The impulse data for the silicone surface area analysis experiment was collected. Figure 5.10 shows the impulse data for each surface area piece of the S11-8 silicone specimen (silicone from batch 10 with a thickness of 8 mm). The data is color coded by zones: surface areas that are plotted in zone 1 are purple and surface areas that are plotted in zone 2 are blue. The larger surface areas were assigned a darker shade of the respective color. All of the data was reassigned to have an initial time of 0 s for comparison, which was 25 ms into the drop (testing apparatus assigns initial time as when the weight is released). For the impulse data, the initial drop (full 84 mm x 54 mm specimen tile) produced a bell-shaped curve. The next three subsequent tests (blue data), which all have surface areas in the zone 2 range, had a similar shape and shifted the impulse curve to the right. The next drop, defined as the fifth largest surface area (263 mm^2 in Figure 5.10), was the first curve to shift in the opposite direction. The fifth largest surface area drop was the first test with a surface area in zone 1. The shape of the fifth curve displayed a similar shape to the previous curves; however, it had a slightly larger peak and the peak occurred before the other curves. The last three tests (purple data) displayed a significant change to the impulse curve: the curve shifted further to the left (indicating that the transmitted force occurred earlier), the curve peaked at a higher magnitude for each drop, and the tail of the curve had multiple peaks before the transmitted force reached zero. Thus, the behaviour of the impulse curves confirms that there are two separate behaviour zones for which surface area affects transmitted force.
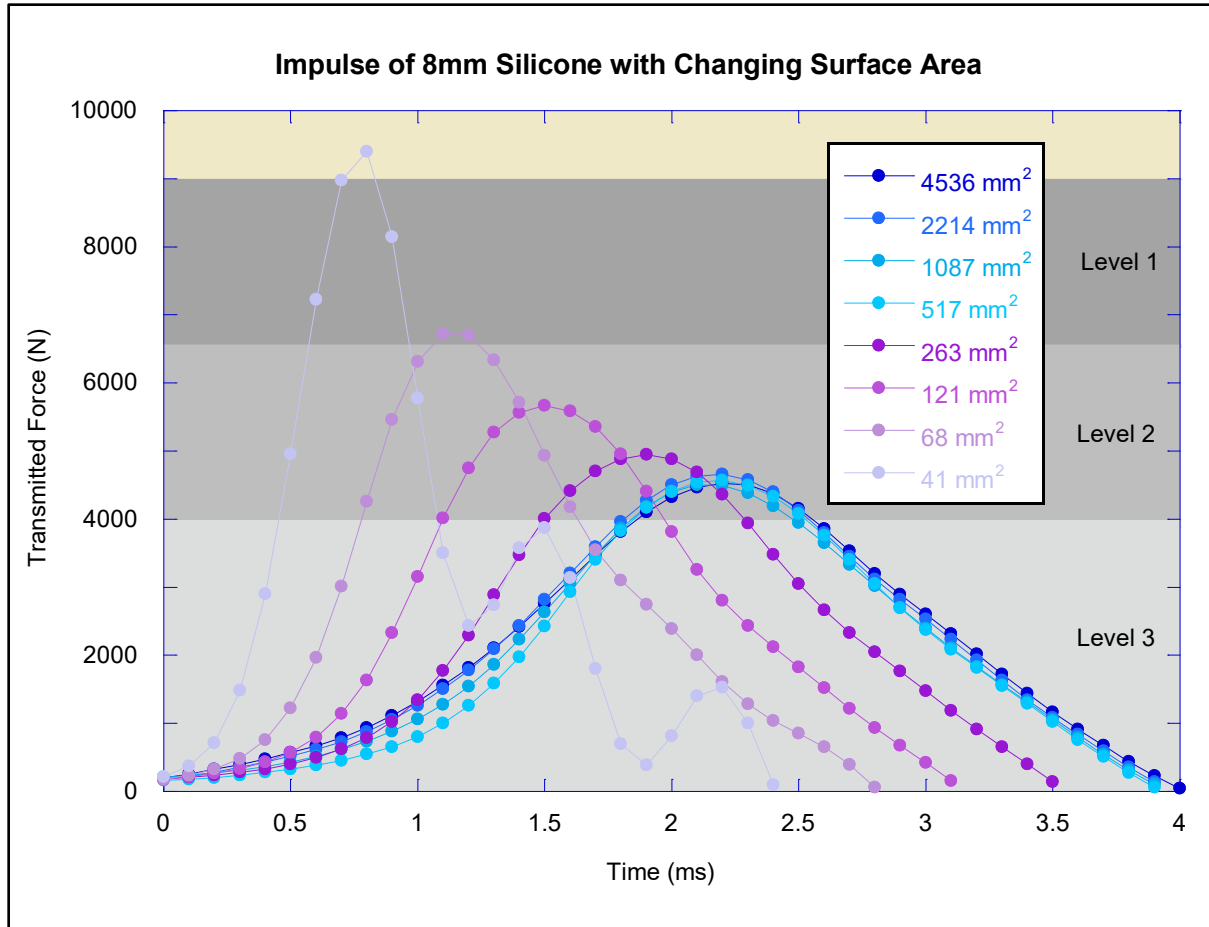
Figure 5.10: The impulse curves for each piece of the 8 mm specimen of silicone tested. The purple surface areas are found in Zone 1 and the blue surface areas are found in Zone 2.

The impulse of each curve was calculated and is presented in Table 5.1. The impulse was calculated using the Gaussian method. Further impulse curves were analyzed for other tested silicone specimens and can be found in Appendix B. The other silicone specimens had similar behaviour of their impulse curves.

Table 5.1: The calculated impulse from the impulse curve of each piece from the 8 mm silicone specimen

Cut Number	Corresponding Surface Area (mm²)	Impulse (N·s)
0 (full specimen)	4536	86.3
1	2214	85.4
2	1087	82.1
3	517	79.0
4	263	77.8
5	121	79.9
6	68	79.4
7	41	76.9

5.3.2 Comparing and contrasting materials

The same experiments for surface area discussed above were completed for all of the materials with the specimens with the largest thickness. For PVC and TPR, the thickness was 8 mm and 8.5 mm, respectively. D3O® was completed using 6 mm thickness as that was the *only* available thickness. The specimens of PVC and TPR also had visible plastic deformation at the four smallest specimens, as shown by the TPR 50A specimen in Figure 5.11 (arrows indicate the four smallest pieces). Note: this was the first specimen used in the surface area experiment and the locations of the cuts were changed to accommodate for the outer-edge fillet of the PVC and silicone specimens.
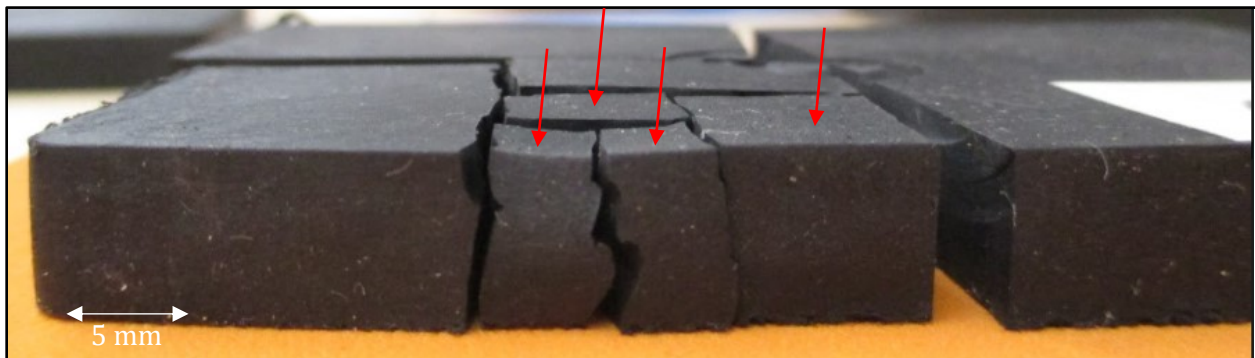
Figure 5.11: A specimen of 84 mm x 54 mm TPR 50A after the specimen was tested for impact. The smallest pieces are indicated with an arrow. This TPR specimen was one of the first tested and had imprecise cuts due to tools available. Superior Glove requested minimal destructive testing of their specimens, so the test was not repeated. The cut inconsistencies did not change the transmitted force more than 250 N (the range of uncertainty) as found from multiple surface area reduction testing.

Figure 5.12 illustrates the results of the tests conducted for PVC and TPR compared to silicone specimens of similar thickness. D3O® was omitted from the graph as it did not have a similar thickness and behaved in a different manner than the other materials (see Section 5.3.2.1 below). A similar phenomenon was observed for all the materials in the 8 mm range; however, the point of inflection varied between each material as shown in Figure 5.12. PVC (green) showed an inflection point at the smallest surface area, approximately 130 mm². The other inflection points can be observed on Figure 5.12. In addition to the varying deflection points, each material produced different hockey-stick shaped performance envelopes (indicated by dashed lines, color congruent to specimen material type). The curves all share the same general pattern, but the rate of the horizontal and vertical asymptotes for the left and right tails varied greatly between the materials and the hardness. Thickness did not change the shape of the curve, only shifted it vertically downwards as the material became thicker, commensurate to what was previously observed.
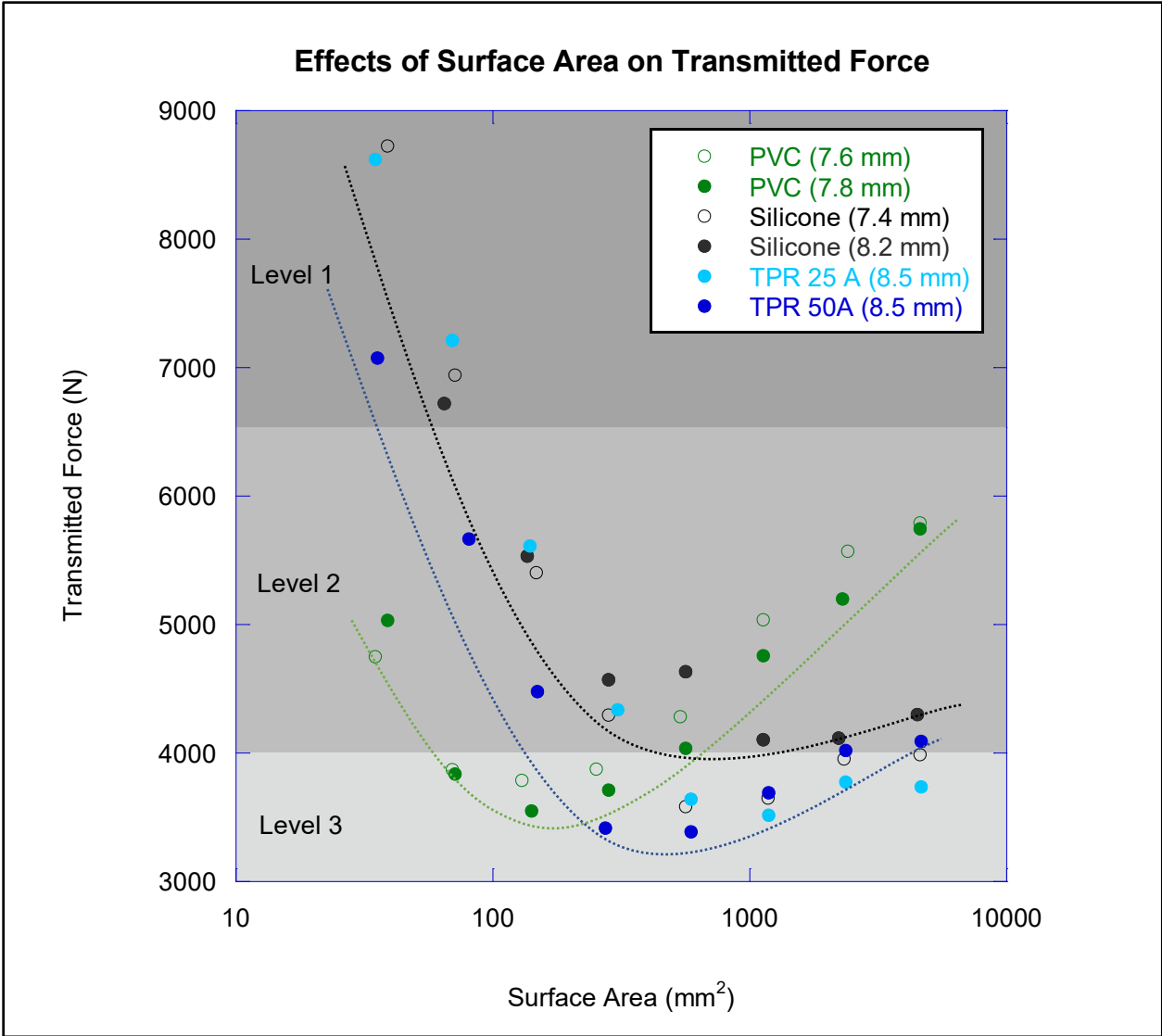
Figure 5.12: A comparison of the PVC, silicone, and TPR specimens on the effects of surface area on transmitted force. All the specimens measured 84 mm x 54 mm laterally, the thickness of each specimen is indicated in the legend. The dashed lines are to illustrate the check mark shape performance envelope of each material (color corresponds to the material type).

The data displayed in Figure 5.12 above suggest that for smaller surface areas, PVC would perform better than TPR and silicone. Thus, PVC would be a better material to use for the bumpers on the fingers of gloves, and other regions requiring a bumper with a small surface area, compared to TPR and silicone. For larger surface areas, both silicone and TPR 20A would perform better than PVC and a harder TPR; therefore, silicone and TPR 20A would be a better choice than TPR 50A and PVC for bumpers placed on the back of the hand. This idea of placing different materials in different locations on the glove is currently not used in the glove industry.

The results of comparing and contrasting the tested materials revealed many factors that influence the transmitted force. Hardness, thickness, the material selected, and surface area all have the ability to influence the specimen's impact performance. To provide further evidence that thickness and material alone do not influence the transmitted force, Figure 5.13 presents the data shown in Figure 5.12 above with D3O® added, with the x-axis changed for thickness of the specimen instead of surface area. The thickness of the material remained relatively the same for all of the drops; however, the transmitted force increased for each material. Thus, thickness and material are not the only factor influencing transmitted force: the surface area of the specimen can significantly influence the transmitted force as well.
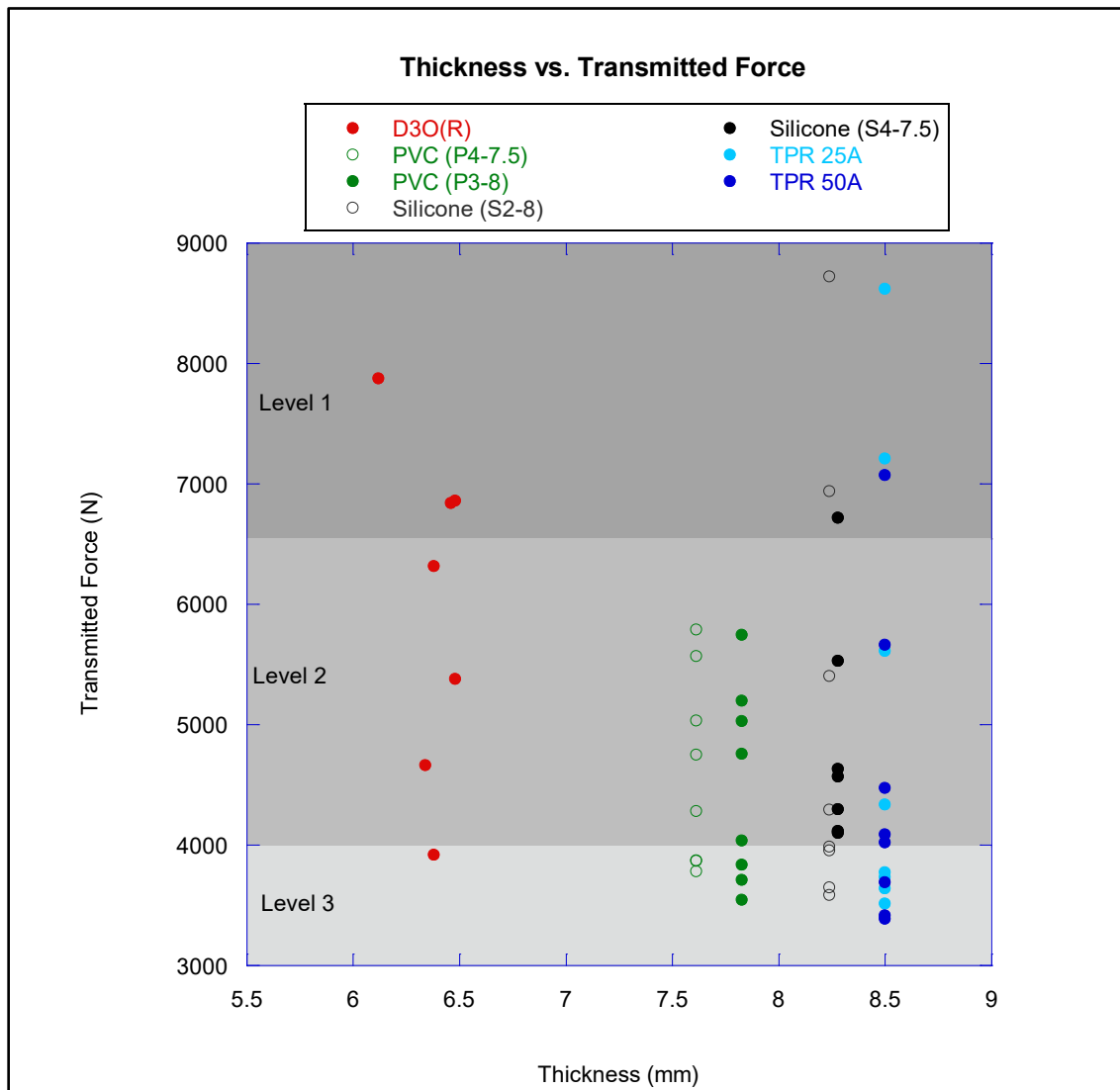
Figure 5.13: A plot of the thickness vs transmitted force for the surface area analysis specimens. The data presented show that thickness is not the only factor when reducing the transmitted force. All specimens had lateral dimensions of 84 mm x 54 mm.

5.3.2.1 Behaviour of D3O®

Figure 5.14 below presents the results of reducing the surface area of D3O®. Due to the limited supply of D3O® specimens, only one test was conducted (N=1); therefore, the intention of Figure 5.14 is to show the relative behaviour of the transmitted force of D3O® when the surface area was reduced. For D3O®, as the surface area decreased the transmitted force increased in an exponential manner (the behaviour appears to be linear in Figure 5.14 due to the semi-logarithmic scale). When the surface area was reduced from 283 mm^2 to 142 mm^2, there was a decrease in transmitted force by 500 N. This decrease in force could be due to the material behaviour or it could be a result of a testing uncertainty, as these uncertainties were found to vary the results by up to 500 N (see Appendix B). If the decrease is assumed to be a testing uncertainty, then the decrease in surface area for D3O® results in a higher transmitted force. The drastically different behaviour of D3O® compared to the other materials tested (see Figure 5.12) is likely due to the material nature of D3O®: where D3O® exhibits exaggerated non-Newtonian characteristics when compared to the other materials. The overall performance envelope of D3O® appears to be straight on a semi-logarithmic scale if the one data point mentioned above is considered an outlier (performance envelope illustrated by red dashed line)
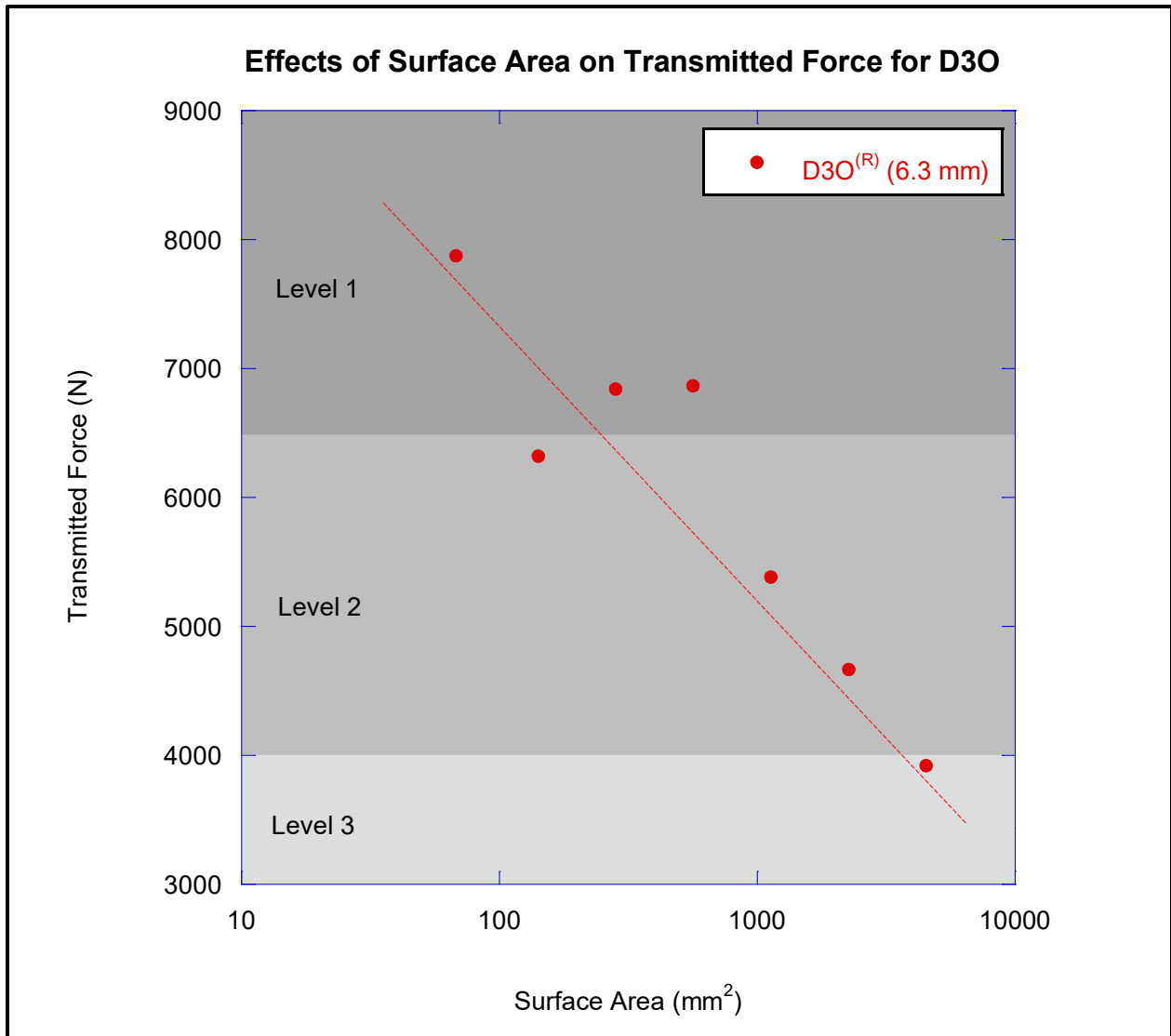
Figure 5.14: The effect of surface area on transmitted force for D3O®. Only one specimen was tested; therefore, the shape of the curve is inconclusive. The lateral dimensions of the D3O® specimen measured 84 mm x 54 mm. The performance envelope of D3O® (discounting the data outlier) is indicated with a dashed line.

5.4 Deriving an Equation to Predict the Surface Area Effects on Impact Performance

The next section attempts to derive an equation to predict the effects of surface area. Deriving an equation to predict the effects of surface area on transmitted force would be a useful tool for a designer as they would be able to mathematically determine what thickness and surface area their design needs to be in order to achieve the intended performance metric (transmitted force). In addition, the data collected in the thesis thus far indicate that there is a mathematical relationship between thickness, surface area, material type, and hardness.

139

Using the curve fitting software TableCurve® 2D v5.01.02, the following best fit equation was derived for the transmitted force-surface area behaviour of TPR, PVC, and Silicone:

$$F_t = a + b(lnx) + c(lnx^2) + d(lnx^3) \tag{5.5}$$

where F_t is the transmitted force, a, b, c, and d are unknown constants that influence the shape of the graph, and x is the surface area. The equation was selected from over 8000 equations in the program. The equation was selected as it was the only equation that adequately matched all of the data for each thickness of silicone (i.e., some equations were a good fit for one thickness but did not transfer well to another thickness). In addition, the surface area curves of PVC, TPR, and silicone show two separate minima and maxima peaks in the function with asymptote limits.

Figure 5.15 below presents the output from the TableCurve® software for the P3-7.5 specimen (PVC with a 7.5 mm thickness from batch 3). The x-axis, which is not labeled, is the surface area and the y-axis is the transmitted force. As shown in Figure 5.15, the chosen equation (5.5) provides a similar trend to the data points. The a, b, c, and d constants for the P3-7.5 specimen's equation are provided at the top of the graph along with the adjusted r^2 value (0.996).
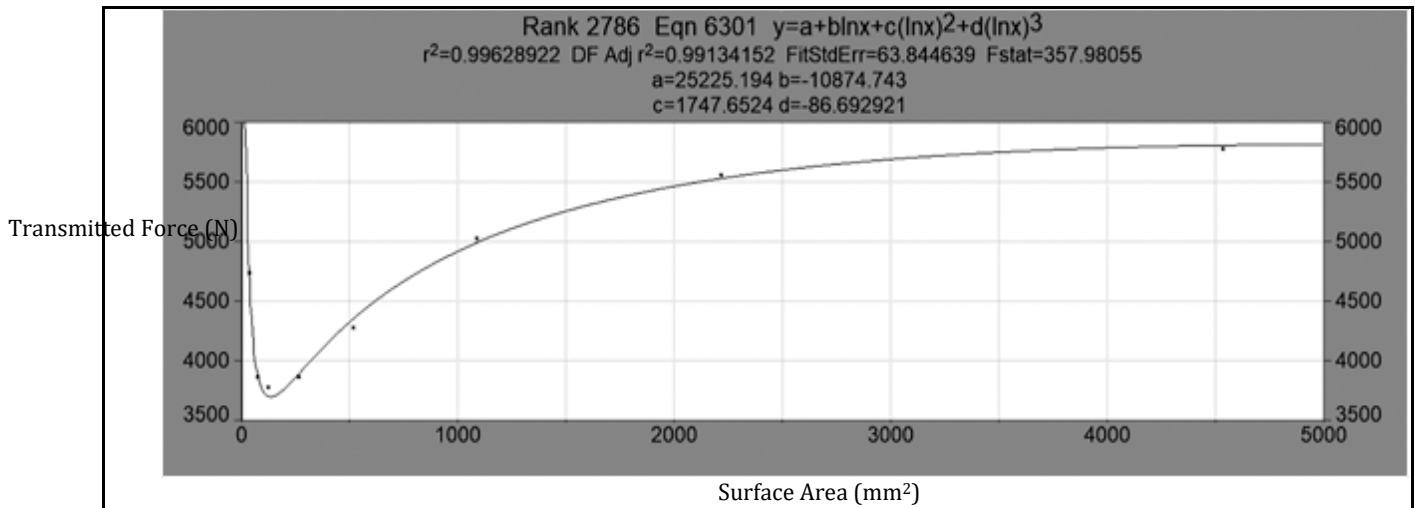
Figure 5.15: A screenshot of the output from the TableCurve® software for the best fit equation for the data. The x axis is the surface area and the y axis is the transmitted force, which were added in after as the software does not label axis.

5.4.1 Parameter Definition and Sensitivity Analysis

To derive the parameters a, b, c, and d, of equation (5.5) another graphing software, Desmos, was used [4]. This graphing software enables the user to enter in their equation and assign each parameter a sliding bar of values. For example, a sliding bar for the "a" parameter (defined by the TableCurve® software [5]) was added with the values of $10000 \leq a \leq 40000$. The upper and lower limits of the sliding bar were based on the data collected for the term during the curve fitting (e.g., the "a" parameter had an average value of 25000 and did not exceed 35000 or go below 15000 for any of the data collected).

To provide a reference point, the initial values of a, b, c, and d were arbitrarily chosen as the values that TableCurve® assigned to the silicone specimen S8-7 (7mm thick, from batch 8). These assigned values were a=32000 ; b=-10800; c=1410; and d=-60. The original reference point equation was assigned to be black and two more identical equations were added: one with a blue color to show a positive increase in the parameter and one with a red color to display a decrease in the parameter. The following subsections detail the results of a sensitivity analysis of the curve fitting parameters.

5.4.1.1 Parameter "a"

Figure 5.1 shows the results of changing parameter "a" of the transmitted force vs. surface area curve. The black line is the original equation used. The blue line is the result of increasing the value of "a" by 500 to 32500. The red line is the result of decreasing the value of "a" by 500 to 31500. As illustrated in Figure 5.16, changing the value of "a" shifts the graph up or down, which is a logical result as "a" is the point at which the curve intercepts the y-axis (the y-intercept). The parameter of "a" is most likely a function of thickness as the testing result data showed that changing the thickness of the graph shifts the curve up or down.
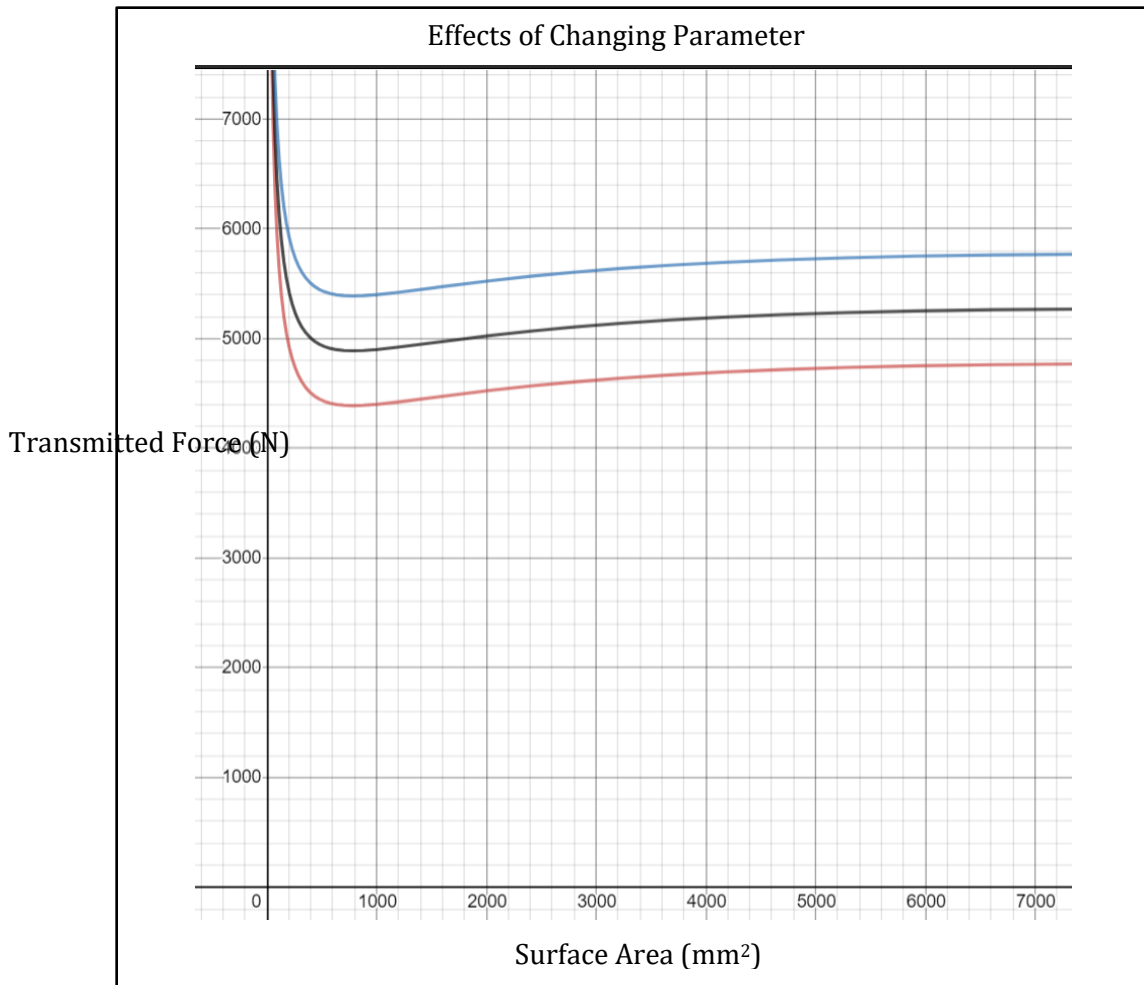
Figure 5.16: A screenshot of the output from the Desmos graphing calculator. The original value of "a" is 3200 and is indicated with the black line. The blue and red lines are the effects of increasing (blue) or decreasing (red) "a" by 500 (units unknown).

5.4.1.2 Parameters "b" and "c"

Both parameters "b" and "c" had similar effects on the curve: they shifted the entire curve up or down as well as changed the tail angle of the curve. Since both results were similar, Table 5.2 was created to show a side-by-side comparison of the parameters. Based on the data displayed in the table, parameter "b" had a higher influence on shifting the graph up or down than parameter "c". In contrast, parameter "c" appeared to have a greater influence of the magnitude of the minima peak. Based on the sensitivity analysis, a hypothesis can be made that both "b" and "c" parameters are a function of the material and the thickness; however, parameter "c" is more likely a function of the material.

Table 5.2: A comparison of parameter "b" and "c" from the TableCuve® equation using Desmos. For each chart shown, the x-axis is the surface area and the y-axis is the transmitted force.

Parameter "b"	Parameter "c"
Value Change: ±200 (initial value of -10,800)	Value change: ±20 (initial value of 1,400)

Transmitted Force (N)

Surface Area (mm²)

Transmitted Force (N)

Surface Area (mm²)

Value Change: ±500 (initial value of -10,800)	Value change: ±50 (initial value of 1,400)

Transmitted Force (N)

Surface Area (mm²)

Transmitted Force (N)

Surface Area (mm²)
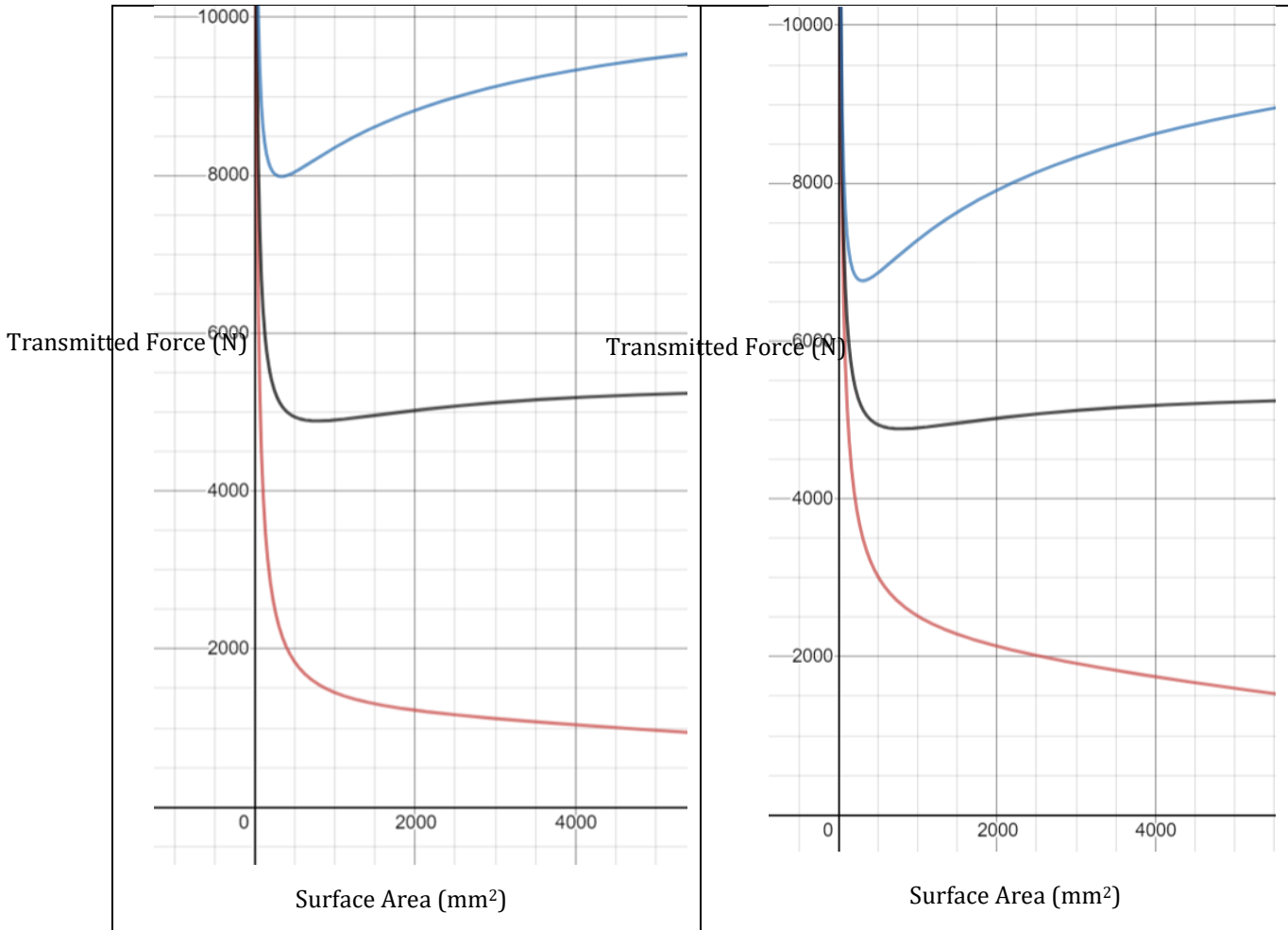
5.4.1.3 Parameter "d"

Figure 5.17and Figure 5.18 below display the results of changing parameter "d" by ±0.5 and ±2, respectively. The small range of magnitude change was selected as parameter "d" had little variance across all of the specimens when curve fitting. Changing the value of parameter "d" primarily resulted in changing the angle of the tail of the curve (or the angle of "zone 2"). Since parameter "d" had little variance but changes the angle of the tail, parameter "d" is likely a function of the surface area of the material and its thickness – which would make it a function of the volume of the material.

144
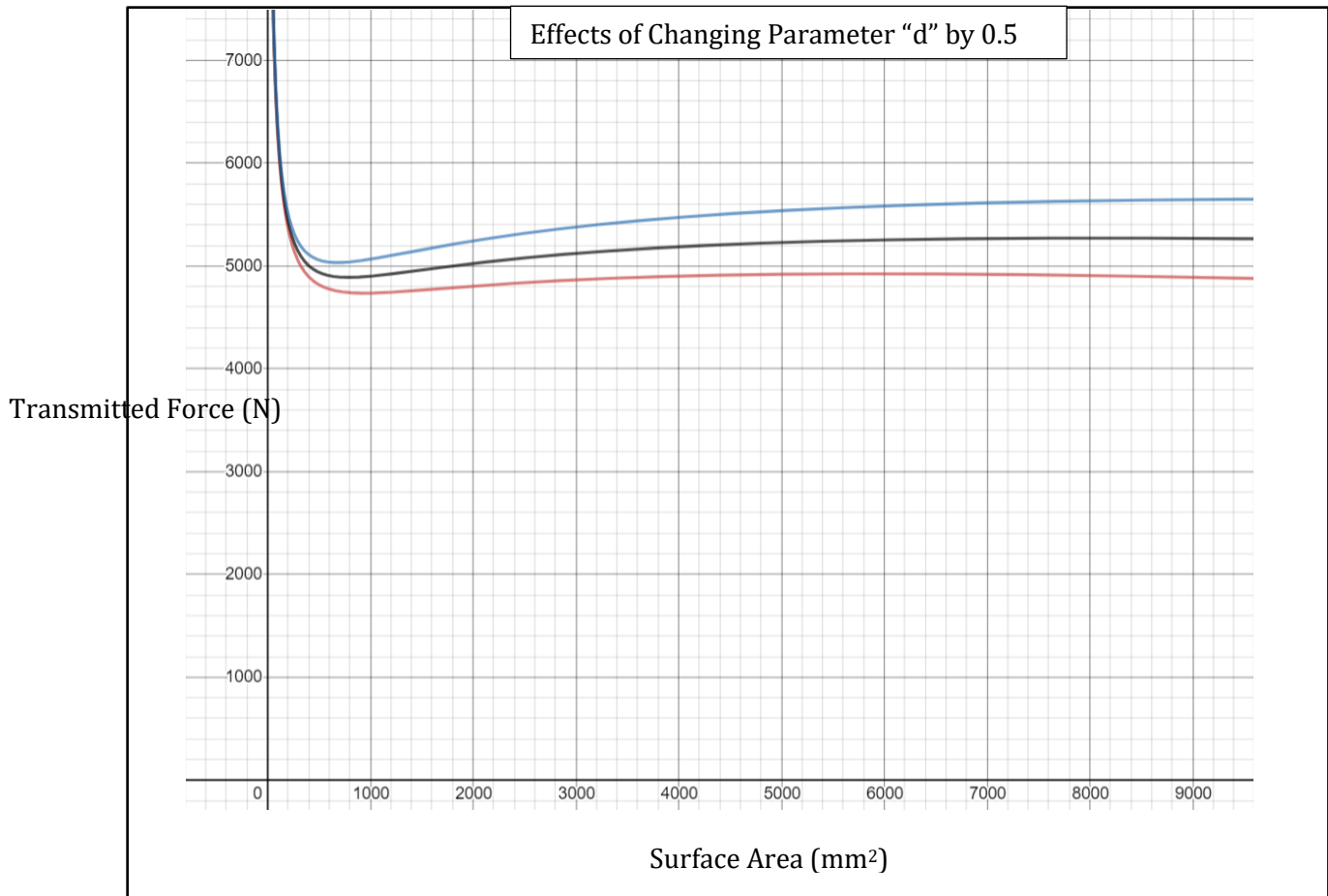
Figure 5.17: A screenshot of changing parameter "d" by 0.5. The black line is the original and the red line is reducing the parameter by 0.5 and the blue line is increasing the parameter by 0.5

145
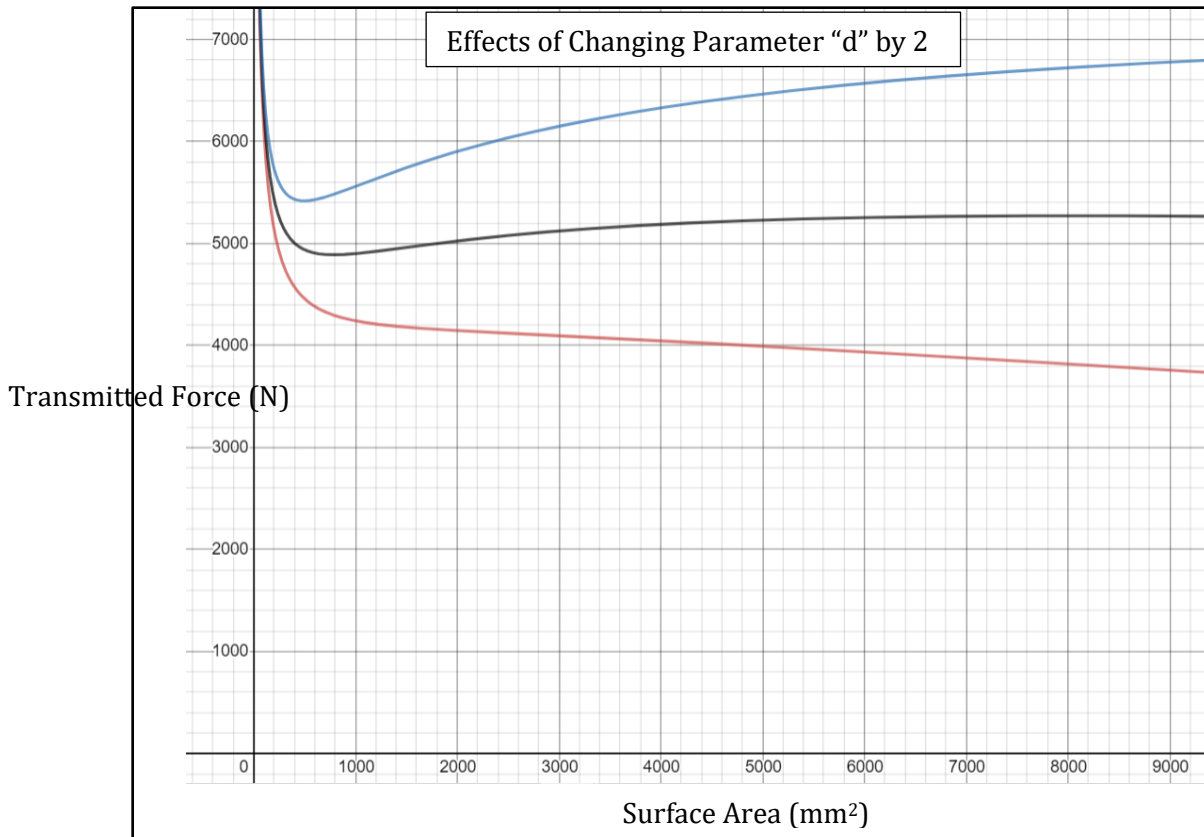
Figure 5.18: A screenshot of changing parameter "d" by 2. The black line is the original and the red line is reducing the parameter by 2 and the blue line is increasing the parameter by 2.

5.5 Summary

Table 4.6 below provides a summary of Chapter 5 and how it answered the desired research questions.

Table 5.3: A summary of the research questions addressed in Chapter 5 and how they were evaluated.

Research Question	Method Used to Evaluate the Question	What was Learned
(2) What material should be used for the glove bumpers based on the use case of the gloves?	• Drop testing for surface area	• Different materials should be used on different parts of the hand • Smaller surface areas of the hand, such as the fingers, should use PVC • Larger surface areas should use D3O® or silicone

(3) What are the effects of thickness, surface area, and volume on reducing transmitted force?	• Drop testing with different thicknesses, keeping lateral dimensions constant • Drop testing for surface area	• Increasing the bumper thickness, without changing the surface area, reduces the transmitted force • Changing the surface area, while keeping the thickness constant, caused two unique transmitted force performance zones for PVC, silicone, and TPR. Zone 1 was where plastic deformation was suspected to be the main influence on transmitted force and zone 2 is where the bulk material was suspected to be the main influence • Changing the cut order of the surface area experiment for silicone showed that the lateral dimensions are more important than surface area when interrogating transmitted force
(4) When keeping thickness consistent, when does the lateral size (surface area) of the bulk material stop affecting impact performance?	• Drop testing for surface area	There is a critical surface area unique to each material where the mechanism for energy absorption changes • For silicone and TPR this occurred at 314 mm^2 • For PVC this occurred at 150 mm^2 • Not enough data was collected for D3O® to identify the critical surface area • The surface area of the contact between the anvil and the specimen, and the specimen and the striker was 314 mm^2

Chapter 5 References

[1]American national standard for performance and classification for impact resistant hand protection. . International Safety Equipment Association 2019 February.

[2]Tilley AR. The measure of man and woman. 1. publ. ed. New York: Whitney Libr. of Design; 1993.

[3]Lu G, Yu TX. Energy absorption of structures and materials. Cambridge: Elsevier Science & Technology; 2003.

[4]Desmos | Graphing Calculator. Available from: https://www.desmos.com/calculator. [citedJan 7,2021] .

[5]Systat Software. TableCurve2D.

Chapter 6 : Conclusions and Future Work

6.1 Conclusions

Designing bumpers for impact resistant gloves is a complicated undertaking with many interacting variables. For example, to have a glove that provides adequate dexterity for the user, the bumper must be thin and flexible (have a low elastic modulus); however, a thin bumper does not necessarily absorb energy and reduce transmitted force as well as a thick bumper, as demonstrated in Chapter 5. Finding the thinnest bumper that can reduce the transmitted force to achieve any level outlined in the ANSI/ISEA 138-2019 standard for impact resistant gloves is just one of the unique challenges to the bumper design—and accomplishing that particular goal does not guarantee hand protection in all use cases or contexts. Other challenges arise from understanding the use-case scenarios for the gloves, such as the criterion that the gloves will be used in extreme temperatures that range from -40°C to 40°C. The high variation in use temperature is a challenge because many material properties are temperature dependent, such as the elastic modulus, and the afforded impact protection by bumper will change depending on the external temperature.

Once a material is selected for the bumper there is also the additional challenge of knowing where to place the bumpers and selecting the geometry each bumper should have. Figure 6.1, for example, shows a glove that meets the ANSI/ISEA 138-2019 standard. This glove has bumpers placed on the testing locations, which will meet the standard; however, from the hand anatomy and injury statistics review conducted in Chapter 2, the locations of the bumpers do not protect the areas of the hand that are more likely to get injured, such as the first and fifth metacarpal (indicated with red in Figure 6.1). Design should never be to a standard, rather, the design should be checked against the standard.
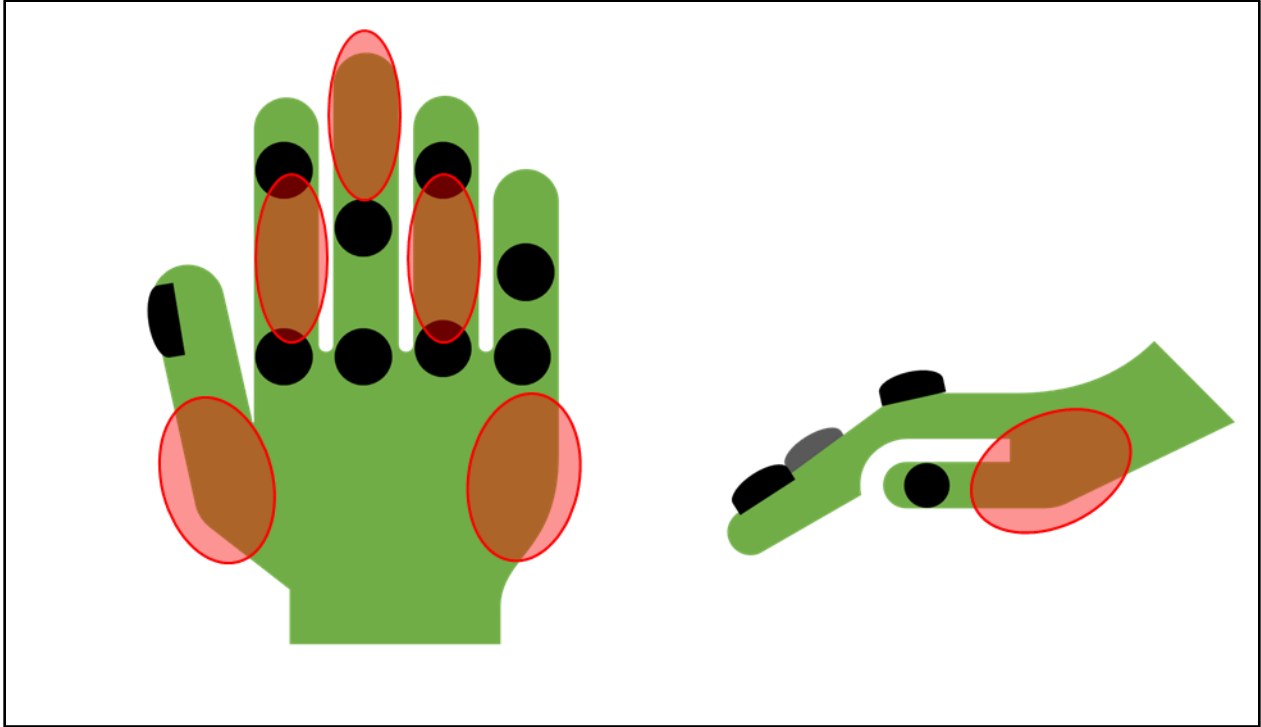
Figure 6.1: An example of an impact resistant glove that will pass the ANSI/ISEA 138-2019 standard based on testing locations. The bumpers of the glove (black dots) are placed on the testing locations outlined in the standard [1]. The locations of the bumper do not protect most of the areas of the hand that are likely to be injured from impact (shown in red).

The purpose of this thesis, however, was not to create a design that can meet all of the interacting and conflicting objectives for bumper design detailed above. Instead, the purpose of the thesis was to develop further understanding and knowledge of how different materials, dimensions, and geometries affect the transmitted force in order to provide knowledge for improving bumper design. For example, there is little published knowledge of how reducing lateral dimensions of polymers can reduce the transmitted force. The results and conclusions of the research conducted for materials, dimensions, and geometric effects are detailed below. In addition, the secondary objective of the research was to develop a method to predictively model impact testing in order to reduce the time and materials required to create physical bumper prototypes.

6.1.1 Materials for Gloves

The results of the material selection and testing in Chapter 4 and Chapter 5 indicated that there is no single "ideal" material from which to create glove bumpers. The design requirements to meet the use-case scenario for the glove, as well as the processing and cost requirements of the manufacturer, create too broad of a scope for one material to meet. If the scope is narrowed, then some materials

become more promising than do others. Specifically, the research conducted in this thesis showed that:

- Based on the materials selection criteria in Chapter 4, the current materials used for bumpers in the impact resistant glove industry (D3O®, polyvinyl chloride (PVC), silicone, and thermoplastic rubber (TPR)) are good materials to use for bumper design at the present time. There are other materials that exist, such as halobutyl rubber (HBR), that are effective in meeting the design objectives: minimizing mass, maximizing tan delta, and minimizing the thickness; however, HBR did not perform well when the materials selection scope was broadened (see Section 4.2.4.1). Broadening the scope involved examining whether or not the material is easily processed (does not require extra equipment to be produced or long production periods), water resistant, oil resistant, flame resistant, and low in cost (materials cost and production cost).

- How the material is processed and how easily it can be processed matters. HBR is a material that was identified in Chapter 4 as theoretically possessing better impact properties than the materials currently used. When the specimens of HBR were created, the creation required a multi-step process involving third parties to compound the rubber. After the mixing, the HBR was molded on site. When the HBR was molded, the specimens were extremely porous, and the accuracy of the thickness was poor- the specimens did not have a uniform thickness and were more than 2 mm thicker than intended. In addition, the HBR performed slightly better, defined as less than a 500 N reduction in transmitted force, as 8 mm thick silicone at room temperature (thickness of HBR was more than 8 mm). Thus, the performance of the HBR specimen did not surpass the effects of the additional processing required and the lack of precision of the HBR bumper when it was produced to be considered an ideal material for the glove design.

- At room temperature, D3O® is the best material amoung the materials tested for a glove bumper if cost is not factored in. The dynamic mechanical analysis (DMA) temperature sweep testing and cold temperature drop testing conducted in Chapter 4 showed that D3O® outperformed PVC, silicone, and TPR at room temperature (performance defined as the ability to reduce the transmitted force). In temperatures below 0°C, silicone and TPR 25A (low hardness TPR) performed the best and D3O® performed the worst. Thus, D3O® should

be utilized for the design if the glove is used in a place that the bumper can remain at a temperature close to 20°C, and where cost is not a hard constraint. If the glove is to be used across the entire -40°C to 40°C temperature range, silicone is the best choice material due to its better performance at high and low temperatures when compared to the other materials tested.

- At room temperature, testing frequencies close to 1 Hz (equivalent to one impact per second), D3O® has a higher tan delta. Tan delta measures the elastic modulus against the loss modulus. A higher tan delta suggests that the material will be able to absorb more energy, thereby reducing the transmitted force. At higher frequencies (10-100 Hz), silicone had a higher tan delta. Thus, in use-cases where there is a high frequency of impacts (e.g., a construction worker using a jackhammer close to a wall where the knuckles could be impacted), silicone is the best choice material – at least for some design criteria. At lower frequencies, D3O® is the best choice.

- The hardness of the material matters. For materials of the same type (e.g., TPR) decreasing the hardness results in reductions in transmitted force . The high speed video observations of the TPR specimen tiles in Chapter 4 demonstrated that the lower hardness specimens allow for the strain waves generated by the impact to propagate farther from the impact site. As a result, the global strain was increased and the volume of material involved in absorbing energy was increased, thereby reducing the transmitted force.

- A non-linear relationship was observed for transmitted force as a function of surface area and material; PVC exhibited reduced transmitted forces at smaller surface areas when compared to the other materials, as shown by the surface area analysis in Chapter 5. PVC at smaller surface areas exhibited the most observable damage (plastic deformation) to the material. At larger surface areas (defined as above 314 mm^2), D3O® and silicone had a lower transmitted force. Thus, PVC should be considered as a bumper material of choice for locations with small surface area, such as the fingers, and D3O® and silicone would be a better material selection for the back of the hand, where there is a large surface area with a limited requirement for flexibility. The idea of placing different materials in different locations on the glove is currently not used in industry.

6.1.2 Dimensional Effects

The dimensions of the bumper, defined as the thickness, and surface area (length and width), as well as the volume of the bumper, were discovered to affect transmitted force in Chapter 5. The main findings of the dimensional effects of the bumper were:

- Increasing the bumper thickness, without changing the surface area, reduces the transmitted force. The relationship between thickness and transmitted force appeared to be linear; however, due to the inverse relationship that force and thickness have for work, the relationship is more likely an exponential relationship (i.e., as the bumper becomes thinner the transmitted force increases exponentially). This interpretation could not be tested as the machine used for testing could not record a transmitted force over 10 kN and the thinnest specimens that could be tested under the 10 kN limit were 2.5 mm thick.

- Changing the surface area, while keeping the thickness constant, caused two unique transmitted force performance zones for PVC, silicone, and TPR. For each of these materials, these zones were defined at the point where the transmitted force vs. surface area curve inflected. The surface area inflection for each material was close to a characteristic length of 314 mm^2, with PVC's inflection point happening at a smaller surface area (150 mm^2).
  - When the surface area was smaller than the inflection point defined in Figure 5.7, the transmitted force increased as the surface area was reduced in an exponential fashion, appearing to asymptote the vertical axis at surface area equal to zero. In this small surface area zone, referred to as zone 1 in Chapter 5, the pieces that were tested exhibited signs of plastic deformation: there was permanent deformation to the dimensions of the pieces and a color change was observed in the PVC specimens (internal damage). Thus, the primary mechanism affecting the transmitted force is plastic deformation.
  - When the surface area was larger than the inflection point (zone 2), the transmitted force increased as the surface area increased. The increase in transmitted force can be explained by the lack of plastic deformation occurring when the material is larger. The plastic deformation in the material assists in decreasing transmitted force as the breaking of interatomic bonds absorbs some of the impact energy.

- Changing the cut order of the surface area experiment for silicone showed that the lateral dimensions are more important than surface area when interrogating transmitted force. For example, a 40 mm x 20 mm piece from a specimen produced similar transmitted force results as a 20 mm x 20 mm piece. Once one lateral dimension was less than 20 mm, the cut order did not matter suggesting that the 20 mm dimension was more important than the total surface area. Note that 20 mm was the diameter of the striker-anvil contact surface, which also shows that the dimensions of the testing apparatus have an influence on the transmitted force results.

- When different harnesses of TPR (TPR 25A and TPR 50A) were compared in the surface area analysis, TPR 50A outperformed TPR 25A in zone 1, and TPR 25A performed better in zone 2. TPR 25A exhibited a larger radius of plastic deformation compared to TPR 50A (40 mm vs 30 mm). The larger amount of plastic deformation caused the transmitted force to be reduced due to the increase in energy absorbed from interatomic bonds breaking.

- The behaviour of D3O® was different than the other materials in the surface area experimentation. Instead of having two distinct zones with one inflection point causing a "banana shape", the transmitted force of D3O® kept increasing as the surface area decreased. There was a reduction in transmitted force at the 100 mm^2 mark; however, D3O® was only tested once due to the number of specimens available, so the data is inconclusive as the reduction could be attributed to testing uncertainty. The drastically different behaviour of D3O® compared to the other materials tested is likely due to the material nature of D3O®: D3O® exhibits exaggerated non-Newtonian characteristics when compared to the other materials.

- The surface area of the contact between the anvil and the specimen, and the specimen and the striker was 314 mm^2, with a 20 mm diameter (as illustrated in Chapter 3). As aforementioned, the inflection point of the silicone, PVC, and TPR was close to 314 mm^2 in the surface area analysis and the transmitted force increased when the lateral dimensions were reduced below 20 mm. The similarities in the surface areas and lateral dimensions suggest that the testing apparatus has an influence on the surface area vs. transmitted force curve (i.e., a characteristic length scale). Further analysis is required to confirm this

154

hypothesis; however, since the ANSI/ISEA 138-2019 standard specifies the exact dimensions of the anvil, this concept was not explored further in this thesis.

- All dimensions matter and have an influence on transmitted force. For example, for the surface area testing, the thickness was kept constant, yet the transmitted force changed as the surface area changed.

6.1.3 Geometric Effects

The change in the bumper geometry was examined using Finite Element Analysis in Appendix C. More specifically, square and circle surface area shapes with the same thickness and surface area were examined. In addition, creating a hole in the center of the specimen shape was also analyzed as a literature review of crush testing steel rods suggested that adding a hole increased the energy absorption. The testing was conducted using an Abaqus® model and the preliminary results were:

- Adding a hole in the center of the specimen decreased transmitted force. Analyzing the stress and strain contour plots of the specimens showed that the decrease in transmitted force was due to the additional strain that could be achieved by the additional material deformation caused by the creation of the hole (e.g., buckling). This decrease in transmitted force caused by the addition of a hole was hypothesized to only occur as long as there is enough material volume for the impact. An attempt was made to find the volume-transmitted force trade off point; however, the Abaqus® model was limited and did not have a failure criterion, thus, the results of adding a hole are inconclusive, were not validated, and further testing and analysis are required.

- The square geometry reduced transmitted force more than a circle of the same surface area in the simulations. This result contradicted the results of the crush testing of axial tubes reviewed in the literature. One reason for the difference could be the difference in testing conditions: impact vs. static crushing, dimensions, and types of materials (polymers vs. metals). Another explanation could be the limitations of the Abaqus® model, as discussed in Appendix C. Examining the stress strain contour plots of the model, however, showed that the square geometry had a larger overall universal strain (i.e., more cells in the model exhibited strain).

6.1.4 Effectiveness of Preliminary Abaqus® Modelling

A preliminary model was created to simulate the impact testing outlined in the ANSI/ISEA 138-2019 standard. The preliminary model was able to visually simulate the impact for the 84 mm x 54 mm tile specimens of silicone and TPR. The preliminary model was not as accurate, or became invalid, when the specimen geometry was drastically changed. The results of the model are as follows:

- The model was able to accurately simulate the visual appearance of deflections of a 6 mm thick TPR specimen tile measuring 84 mm x 54mm, when compared to the high speed videography.

- The failure criterion for each material was not modelled. The lack of failure criterion was due to the lack of failure data available for the specific blend of materials tested. An attempt was made to collect this data by tensile testing the specimens; however, the tensile tester available did not have the range to reach the loads required for the specimens to reach failure. The absence of the failure criterion caused the cells created by the mesh in the Abaqus® model to infinitely deform instead of failing. The lack of failure in the simulation resulted in the inaccuracy of the model for specimens that did not measure 84 mm x 54 mm in lateral dimensions.

- Despite the lack of failure criterion, the model was able to predict the visual effects of the deformation for the specimen tested. More specifically, the locations of the stress and strain concentrations within the specimen are able to be modelled, yet the quantities of the stress and strain can not be deemed accurate.

6.2 Applications of Learning

Based on the information detailed above, design guidelines can be made for designers to use when creating bumpers for impact resistant gloves:

(1) Different materials should be used on different parts of the glove to protect the hand. (i.e., one material for the finger bumpers and another for the back of the hand).

(2) Areas vulnerable to injury should have a thicker bumper (i.e, the first and fifth metacarpals, knuckles, and proximal phalanges).

(3) The geometry of the design should attempt to produce the most global strain in order to increase energy absorption.

(4) Damage to the bumper is acceptable, and moreover, necessary to achieve full energy absorption; therefore, the glove should be designed to be a consumable.

(5) Caution should be applied when using testing standards to measure design success, as the performance results are dictated by the testing conditions and might not align with the actual use of the gloves.

6.2.2 Superior Glove Prototypes

Using the information discovered by the effects of reducing the surface area on transmitted force, Superior Glove is creating prototypes with bumper pieces that have a surface area in the lower end of zone 2. The prototypes are still in development; however, they illustrate that the information obtained and knowledge developed through completion of this study have a practical use for industry.

6.3 Future Work

The results of the thesis show promise for reducing the transmitted force by changing the geometry and the possibility of predicting the transmitted force through an Abaqus® model simulation. Potential areas of future research include further experimentation to explore other ways to absorb energy through dimensions and geometry, enhancing the model created to account for failure, and developing a better bumper material than the materials that are currently in use.

6.3.1 Experiments

Some of the potential experimental areas to explore include:

- Layering different materials on top of each other. The hypothesis for layering is that if a harder layer is placed in direct contact with the striker during impact with a low hardness material underneath, the harder top layer will not readily deform causing a larger volume of

the lower hardness material to be involved in the impact. Increasing the interaction volume of the low hardness layer would increase the energy absorbed. There was a brief experiment conducted to see if changing the order of the layers of TPR (i.e., putting a harder TPR in direct contact with a striker vs. putting a softer TPR in direct contact with the striker) would change the transmitted force for the same layer composition. The results indicated that there was no significant difference with order of the layers for TPR (see Appendix B); however, the layers used might not have had a significant enough hardness difference to see significant results. Future drop tests should examine the use of materials with increased hardness, such as hard metals, to evaluate the effects of layering.

- Creating a composite specimen where the internal composition of the material is a non-Newtonian fluid with a polymer shell. Non-Newtonian fluids are strain rate sensitive and behave in a similar manner as D3O®. The hypothesis is that placing a non-Newtonian fluid inside of a bumper will decrease the transmitted force compared to a solid bumper of the same geometry.

- Changing the internal geometry of the specimen to induce more strain in the material. For example, instead of having a solid specimen, creating a specimen that is openly porous or has a honeycomb structure on the inside. The voids created by the structure would allow for more strain as the material is not inhibited by its bulk.

- A more complete analysis on the surface area geometry. In this thesis, only circular and square cross sections of a flat surface were examined. Future analysis could be completed on other shapes such as triangles. In addition, changing the topography of the specimen is another area to explore to examine if irregular topography can induce strain, thereby reducing transmitted force, compared to a flat surface. The trade off between the size of a hole and volume of material involved in the impact should also be analyzed further, starting with the circular and square geometries.

6.3.2 Modelling

The model created in the thesis is a promising start; however, the following adjustments need to be made for the model to encompass a wide range of specimen geometries and sizes:

- A failure criterion, and temperature and strain rate effects for each material, must be established. The first step to obtaining the data would be to conduct tensile testing on each material or use a split-Hopkinson pressure bar (SPB) at the lower 2 m/s velocity to achieve a stress-strain curve for the material. Adding a failure criterion will enhance the model by defining when the cells in the mesh will fail due to an overload in stress.

- The model requires verification and validation through further drop testing. In addition, a mesh size analysis must be performed before the model can be validated.

6.3.3 Development of new material

As the understanding of reducing transmitted force improves, new materials for impact resistant gloves can be developed. For example, developing a new material similar to D3O® that has a service temperature for -40°C to 40°C should be examined in the future.

Bibliography

Chapter 1 : Introduction

[1] Canada, Employment and Social Development. Our Hands at Work! 2013; Available from: https://www.canada.ca/en/employment-social-development/services/health-safety/reports/hands.html. [cited Dec 2,2019].

[2] TED: The Economics Daily. Type of injury or illness and body parts affected by nonfatal injuries and illnesses in 2014 : The Economics Daily: U.S. Bureau of Labor Statistics. Available from: https://www.bls.gov/opub/ted/2015/type-of-injury-or-illness-and-body-parts-affected-by-nonfatal-injuries-and-illnesses-in-2014.htm. [cited Nov 29,2019].

[3] 7 Dangerous Jobs That Involve Working with Your Hands. 2019; Available from: https://cestusline.com/blogs/news/dangerous-jobs-working-with-your-hands. [cited Nov 4,2020].

[4] Here are the most common work-related hand injuries. 2018; Available from: https://www.ishn.com/articles/108061-here-are-the-most-common-work-related-hand-injuries?v=preview. [cited Dec 2,2019].

[5] Olson A. Dorsal defense: Guard against impact & abrasion injuries. 2015; Available from: https://www.ishn.com/articles/100623-dorsal-defense-guard-against-impact-abarsion-injuries?v=preview. [cited Nov 3, 2020].

[6] Geng J. Everything You Need To Know About ANSI/ISEA 138 – The New Impact Standard. 2019; Available from: https://www.superiorglove.com/blog/everything-you-need-to-know-about-ansi-isea-138-the-new-impact-standard. [cited Oct 8, 2020].

[7] American national standard for performance and classification for impact resistant hand protection. . International Safety Equipment Association 2019 February.

[8] Carpanen D, Kedgley AE, Shah DS, Edwards DS, Plant DJ, Masouros SD. Injury risk of interphalangeal and metacarpophalangeal joints under impact loading. Journal of the Mechanical Behavior of Biomedical Materials 2019 September; 97:306-311.

[9] Ashby MF. Materials selection in mechanical design. 4th ed. Burlington, MA: Butterworth-Heinemann; 2011.

[10] Nielson LE, Landel RF. Mechanical properties of polymers and composites . 2nd ed. 6000 Broken Sound Parkway NW, Suite 300 Boca Raton, FL: Taylor and Francis Group; 1993

Chapter 2 : Literature Review

[1] American national standard for performance and classification for impact resistant hand protection. . International Safety Equipment Association 2019 February.

[2] Doyle JR, Botte MJ, Roselius E, Krames C. Surgical anatomy of the hand and upper extremity. Philadelphia, Pennsylvania: Lippincott Williams & Wilkins; 2003.

[3] Hand anatomy. 2015 July 8,.

[4] Human Hand Bones Anatomy N2 image. Available from: https://pixy.org/1356057/. [cited Nov 5,2020].

[5] Carter HV, Gray H, Book St. Metacarpophalangeal articulation and articulations of digit. ulnar aspect. 1858 before date QS:P,+-00-00T00:00:00Z/7,P1326,+-00-00T00:00:00Z/9.

[6] Shahid S. Anatomy of grip. Available from: https://www.kenhub.com/en/library/anatomy/anatomy-of-grip. [cited Nov 4,2020] .

[7] English: Based off: 2015 14 October.

[8] Skin Feeling of the Hand. Available from: https://myhealth.alberta.ca:443/Health/pages/conditions.aspx?hwid=zm6309. [cited Dec 9,2020] .

[9] Tilley AR. The measure of man and woman. 1. publ. ed. New York: Whitney Libr. of Design; 1993.

[10] Galloway A. Broken bones. Springfield, Ill: Charles C Thomas; 1999.

[11] Carpanen D, Kedgley AE, Shah DS, Edwards DS, Plant DJ, Masouros SD. Injury risk of interphalangeal and metacarpophalangeal joints under impact loading. Journal of the Mechanical Behavior of Biomedical Materials 2019 September; 97:306-311.

[12] Choi CQ. Brute Force: Humans Can Sure Take a Punch. 2010; Available from: https://www.livescience.com/6040-brute-force-humans-punch.html. [cite dOct 20,2020] .

[13] What Is a Contusion? Bone Contusions, Muscle Contusions, and Causes. 2018; Available from: https://www.healthline.com/health/what-is-a-contusion. [cited Nov 9,2020] .

[14] Flexor and Extensor Tendon Laceration. Available from: http://www.rushortho.com/body-part/hand/flexor-extensor-tendon-laceration. [cited Nov 10,2020] .

[15] Heller JL. Laceration versus puncture wound: MedlinePlus Medical Encyclopedia Image. 2019; Available from: https://medlineplus.gov/ency/imagepages/19616.htm. [cited Nov 10,2020] .

[16] TREATING NERVE DAMAGE IN THE HAND & WRIST. Available from: https://www.muirortho.com/treatments/hand-wrist/treating-nerve-damage-in-the-hand-

wrist/#:~:text=Damage%20to%20the%20nerves%20that,problems%20positioning%20the%20hand%20correctly. [citedNov 4,2020] .

[17] Ashby MF, Shercliff H, Cebon D. Materials: Engineering, science, processing and design. Oxford, UNITED KINGDOM: Elsevier Science & Technology; 2007.

[18] Askeland DR, Wright WJ. The science and engineering of materials. 7. ed., SI ed. Boston, Mass: Cengage Learning; 2016.

[19] Thermoset vs. Thermoplastics - A Comparison of Materials, Advantages and Disadvantages. Available from: https://www.thomasnet.com/articles/plastics-rubber/thermoset-vs-thermoplastics. [citedDec 10,2020] .

[20] Granta Design Limited. Granta edupack . Level 3 2020;20.1.1.

[21] Menard KP. Dynamic mechanical analysis. first edition ed. Boca Raton, FL [u.a.]: CRC Press; 1999.

[22] Callister WD. Materials science and engineering. 7. ed. ed. New York, NY: Wiley; 2007.

[23] Harper CA. Handbook of plastics, elastomers, and composites. 4th ed. New York: McGraw-Hill; 2002.

[24] Xia Z, Alphonse VD, Trigg DB, Harrigan TP, Paulson JM, Luong QT, et al. 'Seeing' strain in soft materials. Molecules 2019 Feb 1,;24(3).

[25] Lu G, Yu TX. Energy absorption of structures and materials. Cambridge: Elsevier Science & Technology; 2003.

[26] Jones N. Energy-absorbing effectiveness factor. International Journal for Impact Engineering 2010 June;37(6):754-765.

[27] Zhang Z, Sun W, Zhao Y, Hou S. Crashworthiness of different composite tubes by experiments and simulations. Composites Part B: Engineering 2018;143:86-95.

[28] Bambach MR, Elchalakani M, Zhao XL. Composite steel–CFRP SHS tubes under axial impact. Composite Structures 2009;87(3):282-292.

[29] Salehghaffari S, Tajdari M, Panahi M, Mokhtarnezhad F. Attempts to improve energy absorption characteristics of circular metal tubes subjected to axial loading. Thin-Walled Structures 2010;48(6):379-390.

[30] Alavi Nia A, Haddad Hamedani J. Comparative analysis of energy absorption and deformations of thin walled tubes with various section geometries. Thin-Walled Structures 2010;48(12):946-954.

[31] Niknejad A, Abdolzadeh Y, Rouzegar J, Abbasi M. Experimental study on the energy absorption capability of circular corrugated tubes under lateral loading and axial loading. Proceedings of the

Institution of Mechanical Engineers, Part D: Journal of Automobile Engineering 2015 February 2,;229(13):1739-1761.

[32] Othman A, Abdullah S, Ariffin AK, Mohamed NAN. Investigating the quasi-static axial crushing behavior of polymeric foam-filled composite pultrusion square tubes. Mater Des 2014;63:446-459.

[33] Guler MA, Cerit ME, Bayram B, Gerçeker B, Karakaya E. The effect of geometrical parameters on the energy absorption characteristics of thin-walled structures under axial impact loading. null 2010;15(4):377-390.

[34] Zahran MS, Xue P, Esa MS, Abdelwahab MM, Lu G. A new configuration of circular stepped tubes
reinforced with external stiffeners to improve energy
absorption characteristics under axial impact . Latin American Journal of Solids and Structures 2017 Feb;14(2):292-311.

[35] Sulaiman S, AlHajji M, Jaafar CNA, Aziz FA, Zuhair T. Effect of composite material distribution and shape on energy absorption systems. null 2020:1-10.

[36] Ma J, You Z. Energy absorption of thin-walled square tubes with a prefolded origami Pattern—Part I: Geometry and numerical simulation. J Appl Mech 2014 /01/01;81(1).

[37] Gong X, Gong X, Sun Y. Design, manufacture, and experimental analysis of 3D honeycomb textile composites, part II: Experimental analysis - xiaogang chen, ying sun, xiaozhou gong, 2008. Textile Research Journal 2008 November 1,;78(11):1011-1021.

[38] Cetin E, Baykasoglu C. Energy absorption of thin-walled tubes enhanced by lattice structures. International Journal of Mechanical Sciences 2019 /07/01;157-158:471-484.

[39] Westerman B, Stringfellow PM, Eccleston JA. EVA mouthguards: How thick should they be? Dental Traumatology 2002 February 1,;18(1):24-27.

[40] Wu JZ, Pan CS, Wimer BM. Evaluation of the shock absorption performance of construction helmets under repeated top impacts. Engineering failure analysis 2019 Feb;96:330-339.

[41] Ashby MF. Materials selection in mechanical design. 4th ed. Burlington, MA: Butterworth-Heinemann; 2011.

[42] Hierarchy of Controls. 2015; Available from: https://www.cdc.gov/niosh/topics/hierarchy/default.html. [citedNov 3,2020] .

[43] McEntee D. The Robots are Here. How Do We Work Safely with Them? 2019; Available from: https://ohsonline.com/articles/2019/11/19/the-robots-are-here-how-do-we-work-safely-with-them.aspx. [citedOct 16,2020] .

[44] 7 Dangerous Jobs That Involve Working with Your Hands. 2019; Available from: https://cestusline.com/blogs/news/dangerous-jobs-working-with-your-hands. [citedNov 4,2020] .

[45] Why Impact Resistant Gloves are Vital for Oilfield & Oil Rig Workers. 2020; Available from: https://cestusline.com/blogs/news/impact-gloves-for-oilfield-and-oil-rig-workers. [citedNov 4,2020] .

[46] Fort McMurray, Canada - Detailed climate information and monthly weather forecast. Available from: https://www.weather-ca.com/en/canada/fort-mcmurray-climate. [citedNov 4,2020] .

[47] Fort Mcmurray Alberta Canada Climate Statistics, with Monthly Temperature, Precipitation, & Snowfall, including Fort Mcmurray Extremes. Available from: https://www.eldoradoweather.com/canada/climate2/Fort%20Mcmurray.html. [citedNov 4,2020] .

[48] Oil and Gas Extraction - Safety Hazards Associated with Oil and Gas Extraction Activities. Available from: https://www.osha.gov/SLTC/oilgaswelldrilling/safetyhazards.html. [citedNov 4,2020] .

[49] Loshek D. Classification of adequate impact protection for hands[dissertation]University of Wisconsin-Milwaukee; 2015.

[50] Nielson LE, Landel RF. Mechanical properties of polymers and composites . 2nd ed. 6000 Broken Sound Parkway NW, Suite 300 Boca Raton, FL: Taylor and Francis Group; 1993

Chapter 3 : Materials and Methods

[1]D3O® Impact Protection | Nothing protects better than D3O®. Available from: https://www.d3o.com/. [citedJan 7,2021] .

[2]Harper CA. Handbook of plastics, elastomers, and composites. 4th ed. New York: McGraw-Hill; 2002.

[3]Ashby MF, Shercliff H, Cebon D. Materials: Engineering, science, processing and design. Oxford, UNITED KINGDOM: Elsevier Science & Technology; 2007.

[4]Askeland DR, Wright WJ. The science and engineering of materials. 7. ed., SI ed. Boston, Mass: Cengage Learning; 2016.

[5]Granta Design Limited. Granta edupack . Level 3 2020;20.1.1.

[6]American national standard for performance and classification for impact resistant hand protection. . International Safety Equipment Association 2019 February.

[7]Menard KP. Dynamic mechanical analysis. first edition ed. Boca Raton, FL [u.a.]: CRC Press; 1999.

Chapter 4 : Materials Selection

[1]Ashby MF. Materials selection in mechanical design. 4th ed. Burlington, MA: Butterworth-Heinemann; 2011.

[2]Granta Design Limited. Granta edupack . Level 3 2020;20.1.1.

Chapter 5 : Dimension-Dependent Impact Response

[1]American national standard for performance and classification for impact resistant hand protection. . International Safety Equipment Association 2019 February.

[2]Tilley AR. The measure of man and woman. 1. publ. ed. New York: Whitney Libr. of Design; 1993.

[3]Lu G, Yu TX. Energy absorption of structures and materials. Cambridge: Elsevier Science & Technology; 2003.

[4]Desmos | Graphing Calculator. Available from: https://www.desmos.com/calculator. [citedJan 7,2021] .

[5]Systat Software. TableCurve2D.

Appendices

[1]Qiao P, Yang M, Bobaru F. Impact mechanics and high-energy absorbing materials: Review. Journal of Aerospace Engineering 2008 Oct 1,;21(4):235-248.

[2]Cetin E, Baykasoglu C. Energy absorption of thin-walled tubes enhanced by lattice structures. International Journal of Mechanical Sciences 2019 /07/01;157-158:471-484.

[3]Jones N. Energy-absorbing effectiveness factor. International Journal for Impact Engineering 2010 June;37(6):754-765.

[4]Guler MA, Cerit ME, Bayram B, Gerçeker B, Karakaya E. The effect of geometrical parameters on the energy absorption characteristics of thin-walled structures under axial impact loading. null 2010;15(4):377-390.

[5]Alavi Nia A, Haddad Hamedani J. Comparative analysis of energy absorption and deformations of thin walled tubes with various section geometries. Thin-Walled Structures 2010;48(12):946-954.

[6]Sulaiman S, AlHajji M, Jaafar CNA, Aziz FA, Zuhair T. Effect of composite material distribution and shape on energy absorption systems. null 2020:1-10.

[7]Zhang Z, Sun W, Zhao Y, Hou S. Crashworthiness of different composite tubes by experiments and simulations. Composites Part B: Engineering 2018;143:86-95.

[8]American national standard for performance and classification for impact resistant hand protection. . International Safety Equipment Association 2019 February.

[9]Granta Design Limited. Granta edupack . Level 3 2020;20.1.1.

[10]Harper CA. Handbook of plastics, elastomers, and composites. 4th ed. New York: McGraw-Hill; 2002.

[11]Friction and Friction Coefficients. Available from: https://www.engineeringtoolbox.com/friction-coefficients-d_778.html. [citedNov 6,2020] .

Appendix A : Experimental Conditions

A.1 Temperature and Drop Testing Equipment

A.1.1 Temperature and Humidity

All tests, unless stated, were tested at room temperature, 20 ± 2°C, with a humidity of 65 ± 2%.

A.1.2 Machine Information

Machine Used: SB069 Cadex Mini Twin Wire Impact Machine

The serial number for the speed sensor used: HVTG120150328-1

Certification number of speed sensor: CERT-CAL-506-7.584.

A.1.3 Camera Specifications

Camera Used: FASTCAM SA5-1000K-M1 (Photron, Japan)

Camera Lense: Carl Zeiss 100 mm F2 ZF.2 Makro Planar T* (Germany)

Lights Used: AOS-A-LED-W150 lights (x2; 1500 lumens each) AOS Technologies AG (Switzerland)

Frame Rate: 60,000 frames per second

Resolution: 320 pixels by 192 pixels

Shutter: 16.42 microseconds

A.2 Uncertainty of Experimental Conditions

The Cadex mini twin wire machine used during the drop testing experiments had many possible sources of uncertainty:

- The machine was hand cranked and the height was measured by a ruler with 1mm increments. This lack of precision to set up the test could result in different transmitted force results.
- The load sensor calibration
- Load sensor readings
- Temperature and humidity of the room
- The composition of the specimens

As a result, the transmitted force values are not precise and there is a margin of uncertainty of approximately ± 250 N. Thus, any test that was completed could not be confirmed to reduce

transmitted force better than another if the difference between the tests were less than 250 N and more impact tests were required.

Table A.1 below illustrates an example of the wide range of transmitted force with five separate 6 mm TPR 20A specimens from the same batch tested within 10 minutes of each other. The five specimens with the same thickness and hardness produced a variance of 535 N (the difference of the lowest value to the highest value).

Table A.1: The transmitted force of five separate specimens of 20A TPR 6mm thick from batch 1. The room conditions were constant for the testing and all of the tests were completed in under 10 minutes. The results of the transmitted force show a wide margin of uncertainty for transmitted force.

6 mm TPR 20A Specimen Number	Transmitted Force (N)
10	5487
11	5438
12	4952
13	5091
14	5150

Appendix B : Additional Drop Testing Experiments

Appendix B presents the additional drop testing experiments conducted in the research. The majority of the tests in Appendix B were not completed fully or did not have enough correct readings to be included in the body of the thesis.

B.1 Tape vs. No Tape

The effect of using double sided adhesive tape on transmitted force to secure the specimens was examined during the ARIT analysis. As there was no way to properly secure the specimen without interfering with the path of the striker when the specimen size was less than 80 mm in dimension, double sided tape was used. The tape was identified to as having the potential to change the results of the drop testing by aiding the energy absorption. Thus, multiple tests were completed where the specimen was held with tape and with the clip (without tape) for multiple drops in a 3-minute time frame. Figure B.1 below displays the data from the tests. The red data points are the drops completed with tape and the blue data points are the drops completed without tape. The results of Figure B.1 show that the tape reduced the transmitted force; however, the reduction in transmitted force was on average 150 N, with specimen (b) having the highest variance average of 300N.
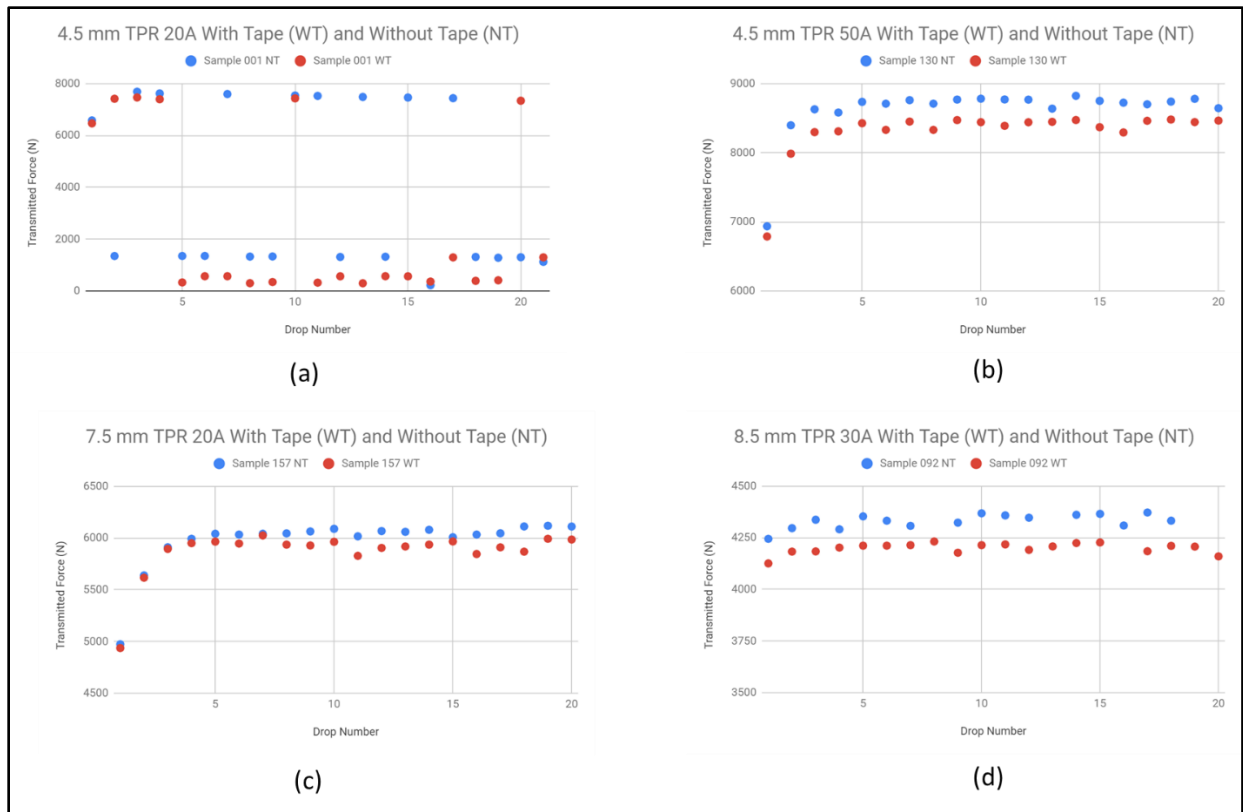
Figure B.1: A comparison of the drop testing completed with tape (red data) and without tape (blue data). For all of the charts, the drop number is on the x-axis and the transmitted force is on the y-axis. The TPR specimens tested in order were (a) 4.5 mm 20A, (b) 4.5 mm 50A, (c) 7.5 mm 20A, 8.5mm 30A. For each test, the tape reduced the transmitted force of all the specimens on average by 150 N, with the highest average variance recorded of approximately 300 N for specimen (b).

B.2 Accelerated Repeated Impact Testing (ARIT)

The purpose of the ARIT testing was to examine what happens when a specimen was impacted multiple times as quickly as possible. For each ARIT test specimen, a drop test was completed 20 times on day 1 and then repeated again on day 2 exactly 24 hours later, to see if there was a difference between the days. The purpose of completing the test again 24 hours later was to see if there was plastic deformation occurring in the specimen or if it recovered to its original state.

B.2.1 Specimens Used

Table B.1: Overview of the thickness and hardness specimens used for the ARIT testing. All of the specimens were comprised of TPR from batch 1. There were no 8.5mm 20A or 8mm 20A specimens available; therefore 7.5 was used. The specimens were picked according to their extremes and one specimen (specimen 091) was picked at random to be tested.

Specimen Number	Thickness (mm)	Hardness (A)
002	4.5	20
129	4.5	50
016	7.5	20
159	7.5	50
091	8.5	30

B.2.2 Results and Observations

A plot of the transmitted force for Specimen 129 on day 1 is shown in Figure B.2. On day 1, no tape was used to secure the specimen to the anvil. Overall, the first three drops were significantly lower than the remaining drops. The remaining drops appeared to have a consistent transmitted force in the 7.7-8.2kN range; however, the data points varied significantly from each drop. On data point five, the specimen remained in the same position for the next two drops (indicated). The transmitted force for each of these drops was similar to the fifth drop.
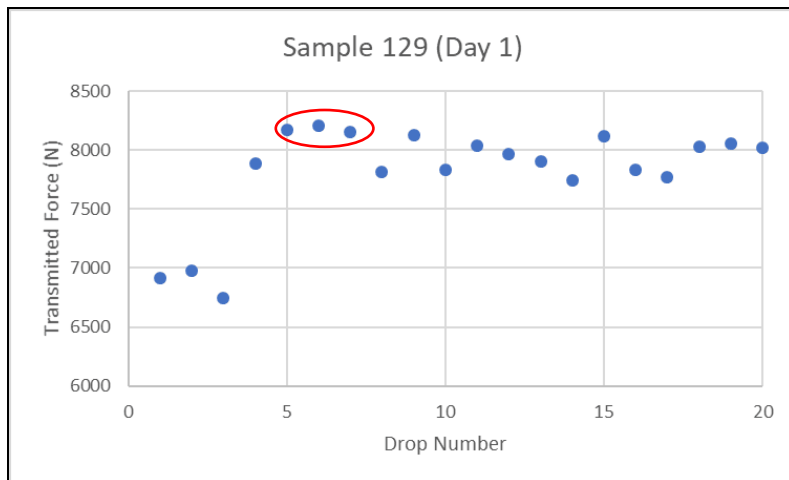
Figure B.2: The results of ARIT testing on specimen 129 day 1. The data shows that the transmitted force increases after the first 3 drops and appears to remain at a constant transmitted force.

On day 2, Specimen 129 was held down with tape and checked after every five subsequent drops. Similar to day 1, day 2 showed that the initial drop had a lower transmitted force than the remaining drops (Figure B.3). The remaining drops also appeared to plateau within a 200N force range. In addition, the data points show a vague wave-like trend every five drops, which correlates to the repositioning of the specimen every five drops.
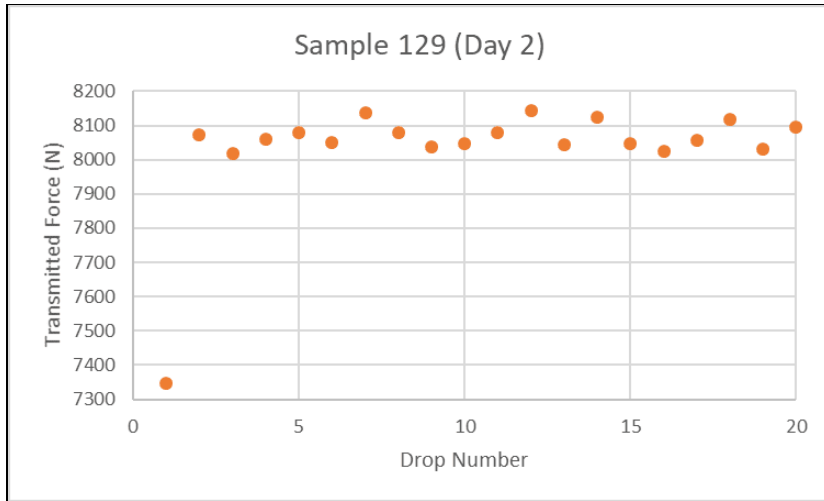
Figure B.3: The same specimen as Figure B.2 tested 24 hours later.

Figure B.4 shows a comparison of day 1 and day 2 results for Specimen 129. The initial transmitted force for day 2 was higher than day 1. The subsequent drops for day 2 stabilized in a smaller range than day 1.
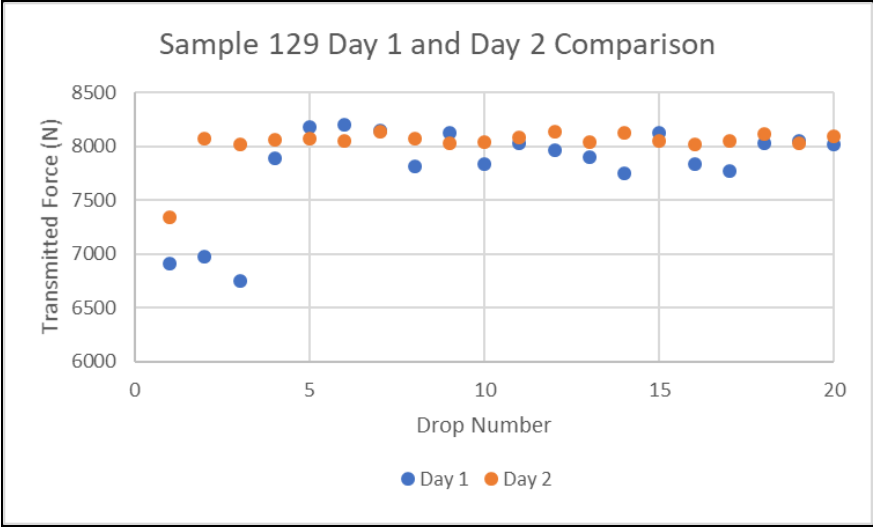
Figure B.4: A comparison of the day 1 and day 2 results of specimen 129.

When comparing specimens of the same thickness and different hardness, the softer specimens showed a decrease in transmitted force on day 2 and the harder specimens showed an increase in transmitted force on day 2. Figure B.5 illustrates the results of the two 7.5 mm specimens. The difference in behaviour of the transmitted force between the days was similar for all tests.
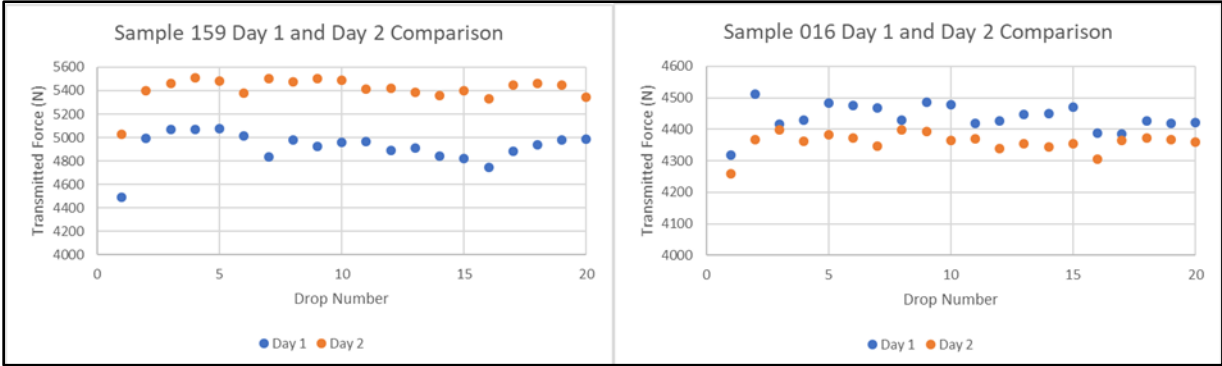
Figure B.5: The ARIT test results for 7.5 mm specimens.

B.3 Testing Additional Locations of the Specimen Tiles

Different locations of the same specimen tile were tested to see if there was an effect on transmitted force. The locations are shown in Figure B.6 and the corresponding transmitted force is presented in Table A.1. Two specimens of 5 mm TPR from batch 1 with a shore hardness of 40A were used in the

testing. The testing locations chosen were the gate, the long edge (side 1), the short edge (side 2), and the corner.
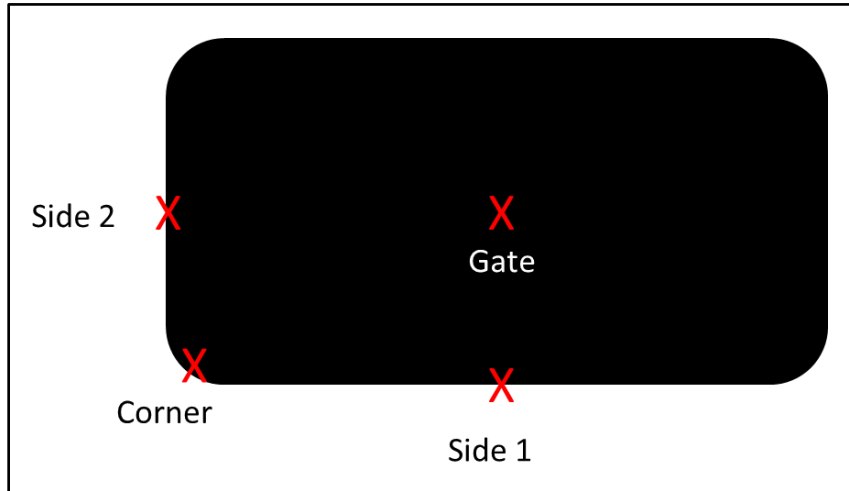
Figure B.6: The location of the four drops completed, indicated with an X.

Table B.2: The transmitted force for the two specimens tested. Both the specimens were 5 mm TPR 40A from batch 1. In both tests, the gate had a large effect on transmitted force compared to the other testing locations.

Drop Location:	TPR Specimen 1 (094) Transmitted Force (N)	TPR Specimen 2 (097) Transmitted Force (N)
Corner	5292	5025
Gate	6214	6310
Side 1	5301	5284
Side 2	5530	5480

B.4 Surface Area

B.4.1 Procedure

1. The specimens were prepared accordingly (see Chapter 3). Specimens that were created in the mold were assigned a top face (face that was exposed to the air during curing) and a

bottom face. For the measurements when cutting the top face was oriented upward as the face was flat and did not have a fillet.

2. The bottom face was the surface that came into contact with the striker. Figure B.7 below illustrates the set up of the specimen for testing. The specimen was offset to one side to avoid overlap in the impact site. The offset was not possible when the lateral dimensions of the specimen were smaller than 40 mm. Double sided tape was used to hold the specimen in place and the same piece of tape was used for the entire specimen (8 tests total).
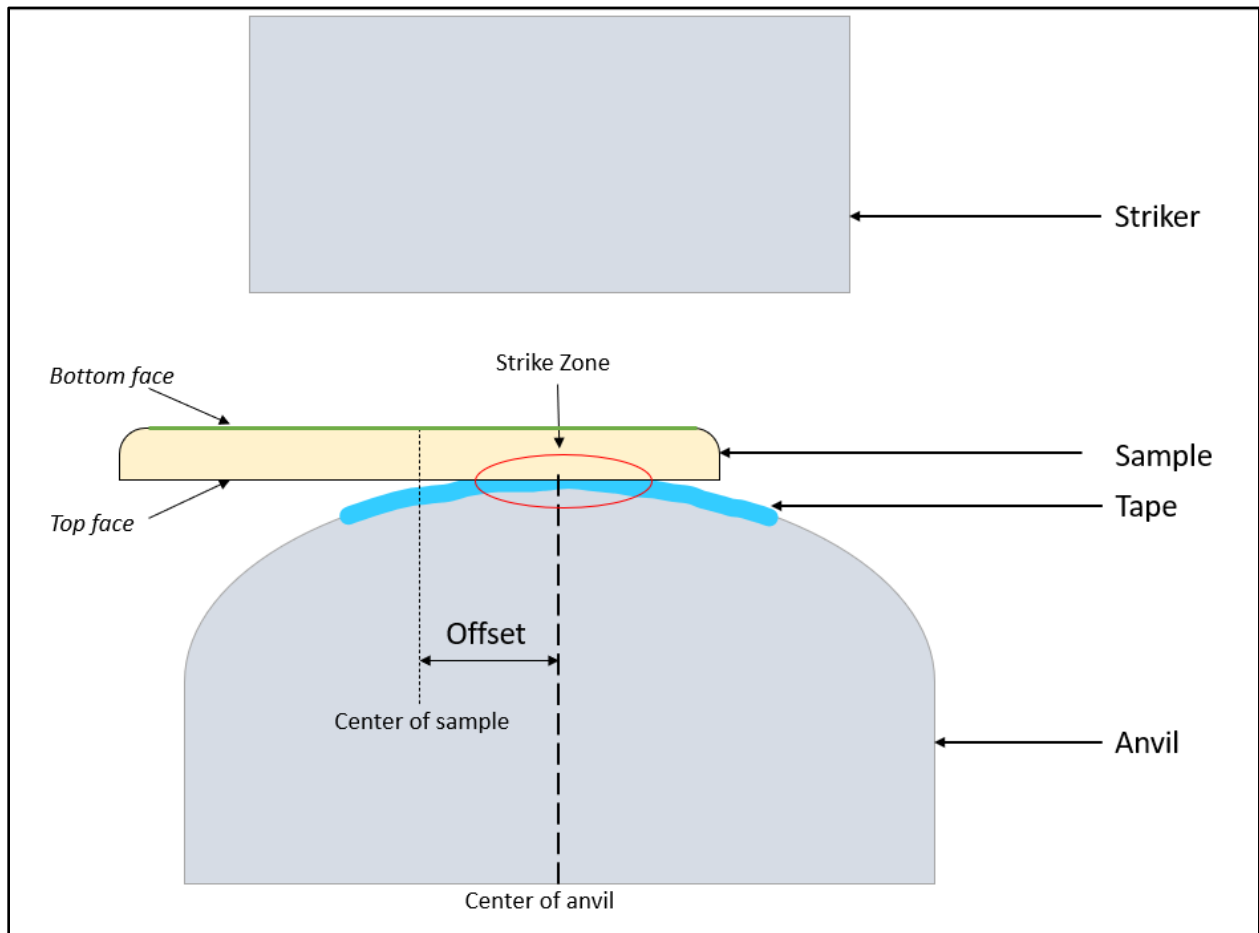
Figure B.7: A schematic of the first test conducted on a specimen for the surface area analysis. For specimens of PVC and silicone that were created in the mold, the bottom face, defined as the surface flush to the mold during curing, was placed upwards (i.e., the bottom face came into contact with the striker during testing). The purpose of placing the bottom face upwards was to ensure that the fillet created from the bold was not in the strike zone.

3. The specimen was tested according to the ANSI/ISEA 138-2019 standard; with the striker raised to 22 cm to account for the loss of kinetic energy to friction.

4. The drop test result, velocity, and any observations about the drop were recorded (i.e. unusual sound, specimen fell off tester, etc.)

5. Specimen was removed from the apparatus and measured for thickness and all physical observations, such as color change, were recorded.

6. A needle and paint pen were used to mark half the length (42 mm) at the top and bottom edges for the first cut (side A).

7. A razor blade was used to cut the specimen in half along side A, as shown in Figure B.8.
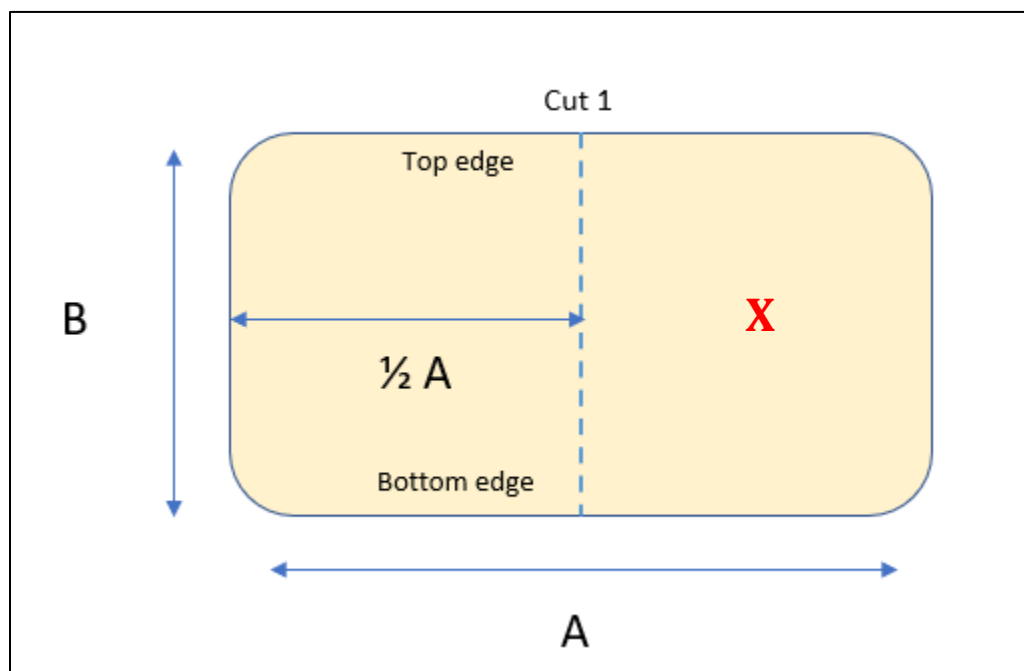
Figure B.8: First cut to be made is denoted with the blue dashed line. "X" is where the specimen was tested on the first drop.

8. The right side was removed in Figure B.8 and the piece that remained was tested again with an offset.

9. The next cut was made by cutting side B in half.

10. Steps 2-9 were repeated until the specimen was reduced to the point that the transmitted force would be over 10 kN for the next drop (the Cadex sensor can only record forces up to 9999 N), or there was risk to damaging the machine (indicated by the sound of the striker contacting the anvil). Figure B.9 illustrates a step by step procedure for the surface area testing. The X in Figure B.9 indicate the test site, and the dashed lines represent the subsequent cut.
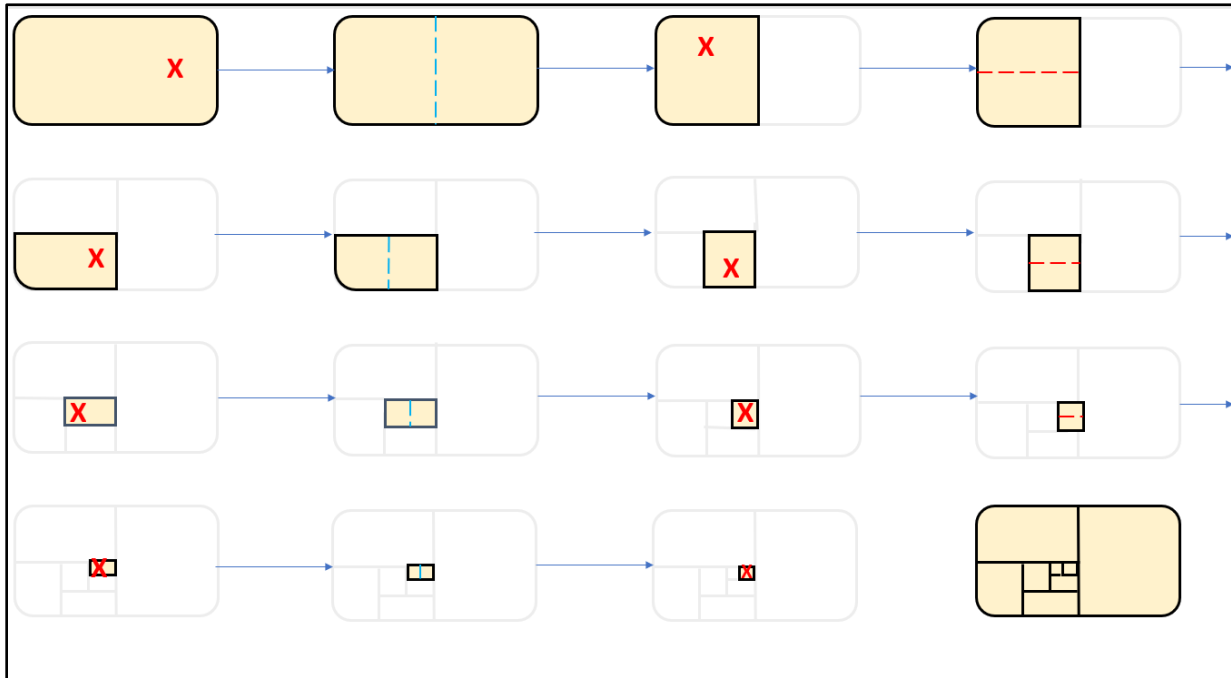
Figure B.9: Step-by-step procedure of where to test. All tests drops are indicated by an "x" and all cuts are indicated by the dashed line. All cuts are to be made with the top face up.

B.4.2 Cut Order

The effects of cut order were examined by changing the order to the cuts made by the "A" and "B" sides (i.e., B was cut in half first). Tiles that were long and skinny (large A dimension and small B dimension) had a similar transmitted force as the next test, when A was reduced in half. This shows that the lateral dimensions could be more important than the surface area when interrogating transmitted force. Once one lateral dimension was less than 20 mm, the cut order did not matter suggesting that the 20 mm dimension was more important than the total surface area.

A plot of the cut order comparison is shown in Figure B.10. Specimens comparable thicknesses were given the same shape. The original cut order data is black, and the new cut order are colored red an

blue. The cuts that had similar transmitted forces are circled. The inset diagram shows a visual representation of the change in tile dimensions A and B.
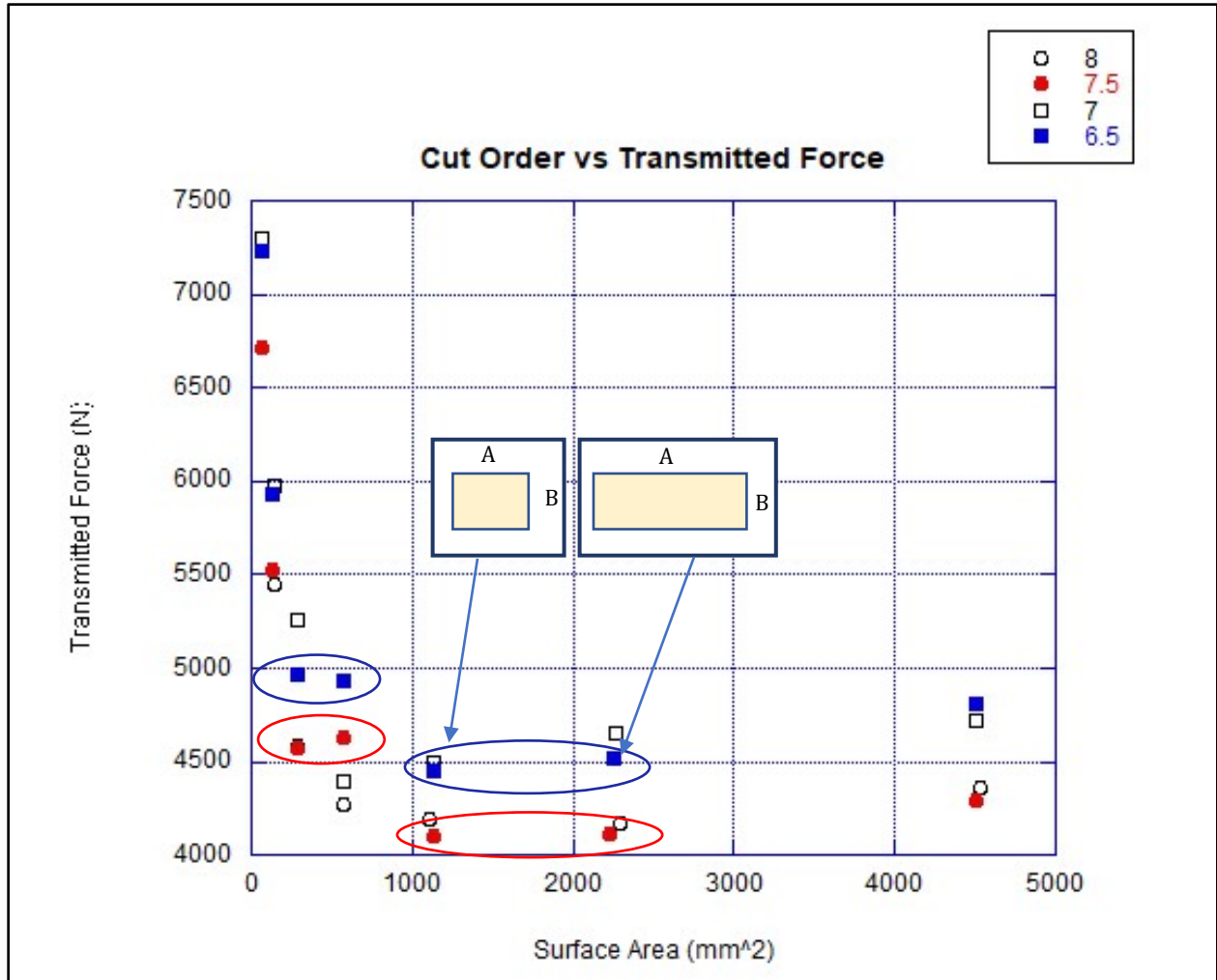
Figure B.10: An example of a comparison of the different cut orders. Specimens comparable thicknesses were given the same shape. The original cut order data is black and the new cut order are colored red an blue. The cuts that had similar transmitted forces are circled. The inset diagram shows a visual representation of the change in tile dimensions A and B.

B.4.3 Surface Area Zone Transition Point

The observations made in the surface area reduction showed that there were two distinct zones for the behaviour of transmitted force for each specimen. The point of the transition between the zones was attempted to be found for silicone, as it was the most abundant material available. For the silicone specimens, the surface area between 300 – 400 mm^2 appeared to be the transition point (see Chapter 5). In order to find the exact transition point, specimens with square lateral dimensions were

180

created. The initial dimensions were 15 mm, 17.5 mm, 20 mm, and 22.5 mm. From the initial testing, the transition zone appeared to be between 20 mm and 22.5 mm. Thus, multiple square specimens were created and tested in these dimension ranges. More 20 mm specimens were made as one hypothesis that arose during the surface area testing was that the lateral dimension of the specimen mattered more than the surface area. The lateral dimension of 20 mm corresponded to the diameter of the contact area of the anvil and striker.

Figure B.11 below shows the results for the attempt to find the transition point. As shown in Figure B.11, the exact transition point could not be found as there was a wide spread of transmitted force for square specimens with dimensions ranging from 20 mm to 22.5 mm. The wide spread of data is due to the uncertainty when conducting the experiments (see Appendix A).
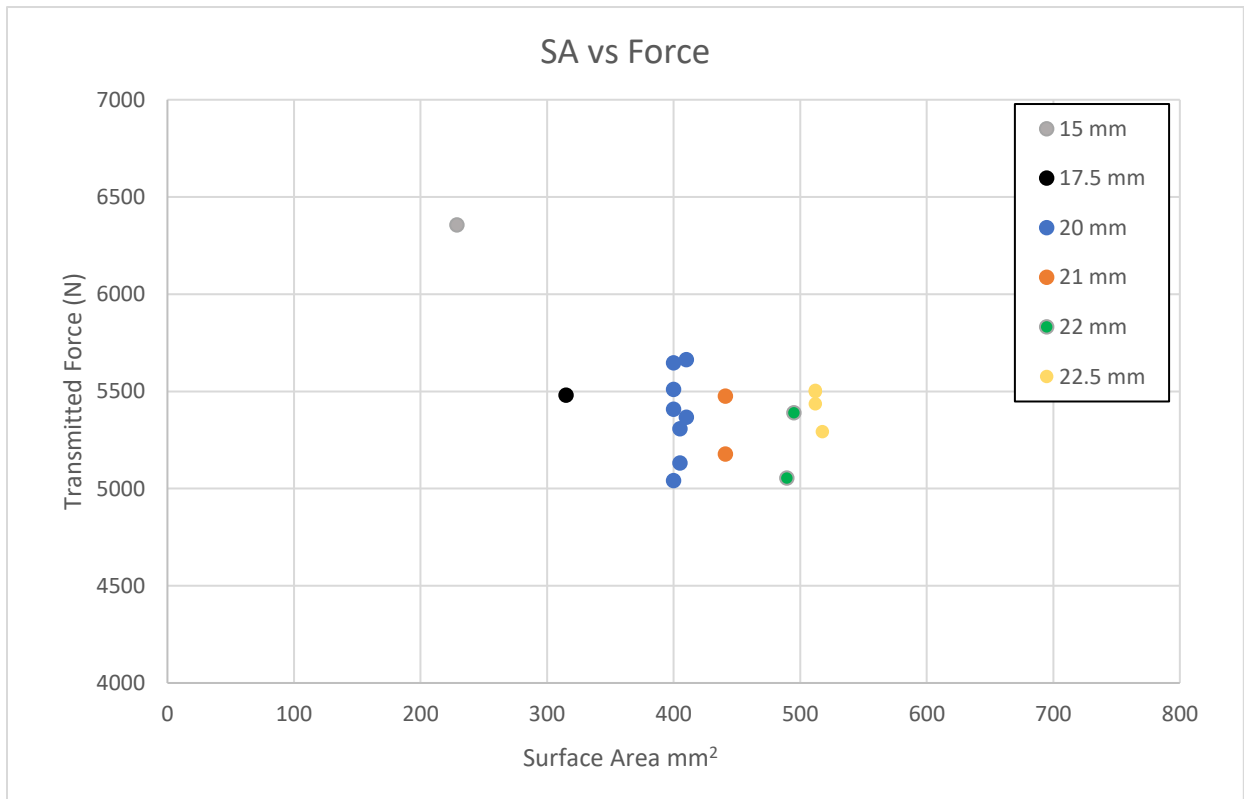
Figure B.11: The results of attempting to find the transition point for silicone 6 mm thick. Each specimen was a square shape, and the outer edge length is given in the legend.

B.4.4 Impulse Curves For Original Cut Order

The following section shows graphical outputs the impulse curves of various silicone specimens and one of the single D3O® surface area analysis – original cut order (Figure B.12). Each cut was given its own color. Cut 0 represents the first test with no cuts made (i.e., the original specimen lateral geometry of 84 mm x 54 mm). All of the other cuts correlate to the cuts described in Figure B.9 above.
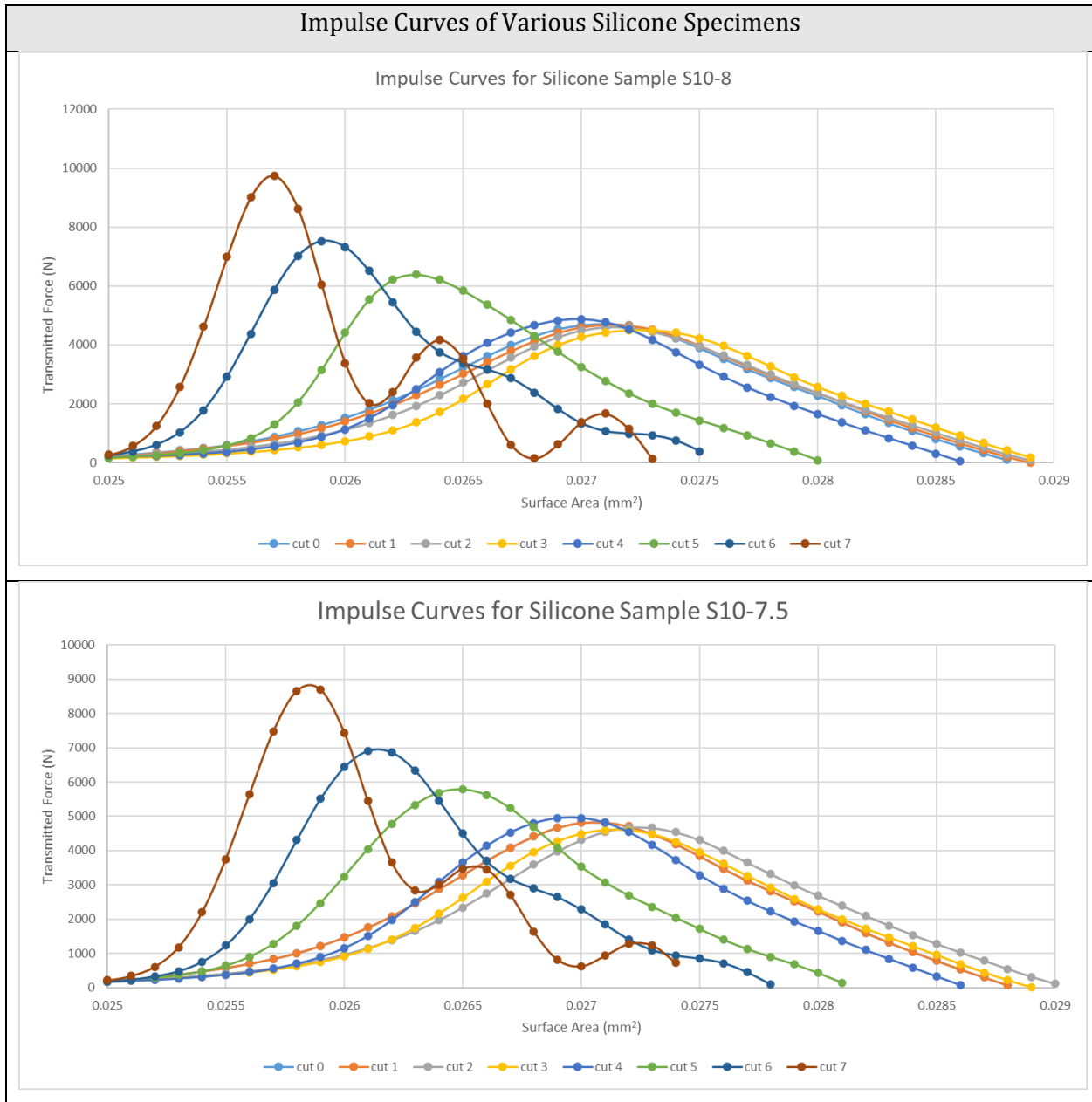
Impulse Curves for Silicone Sample S9-8
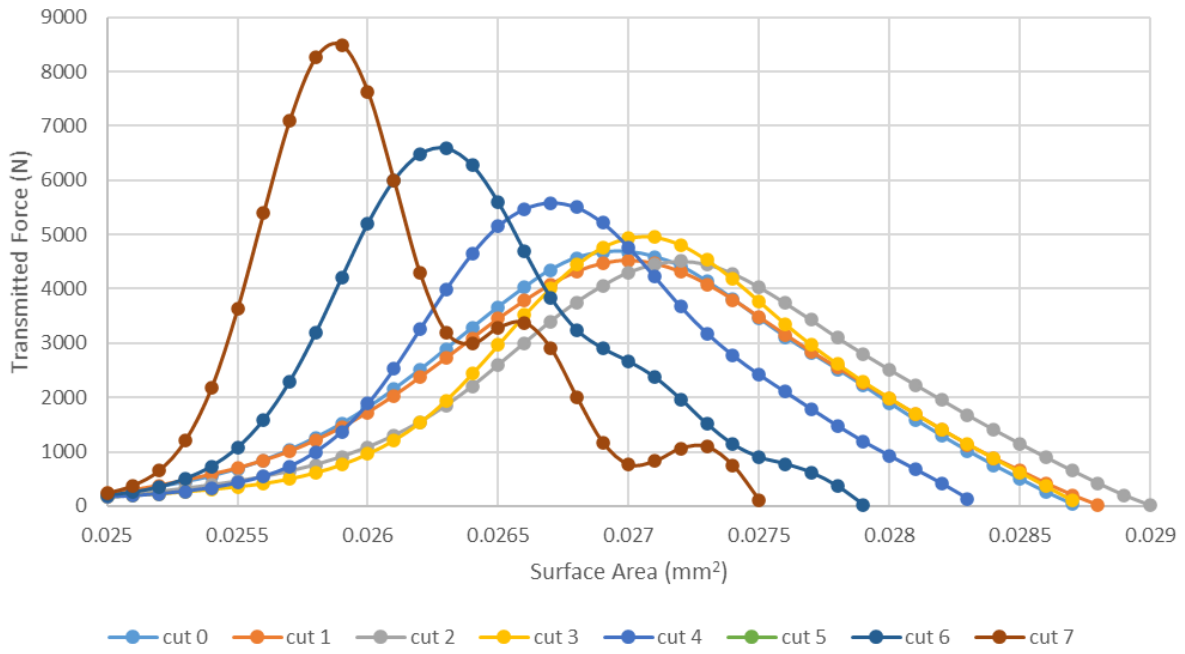
Impulse Curves for Silicone Sample S9-7.5
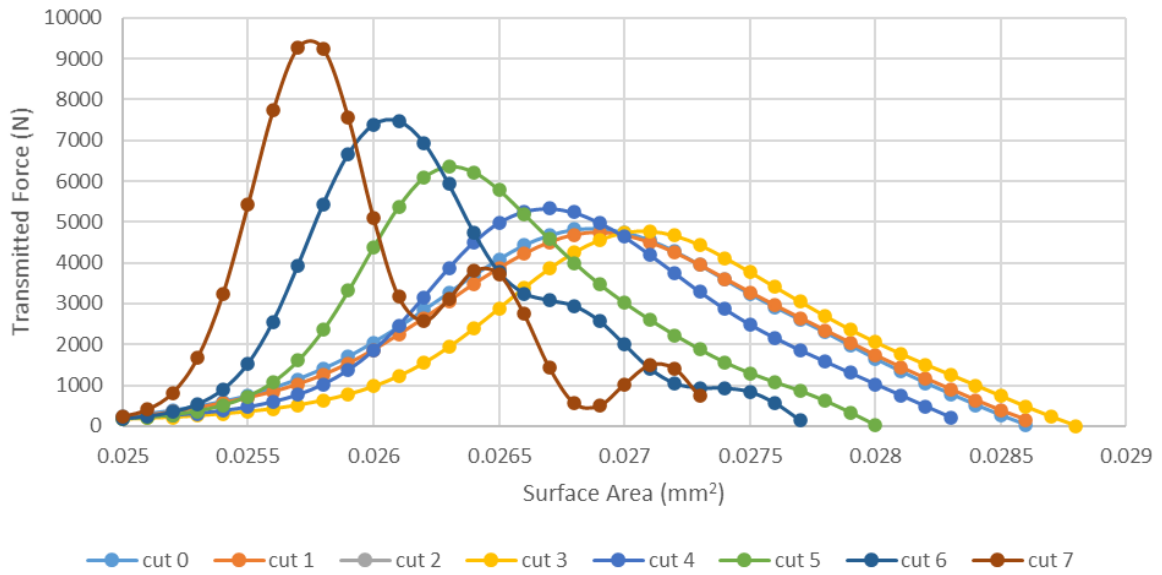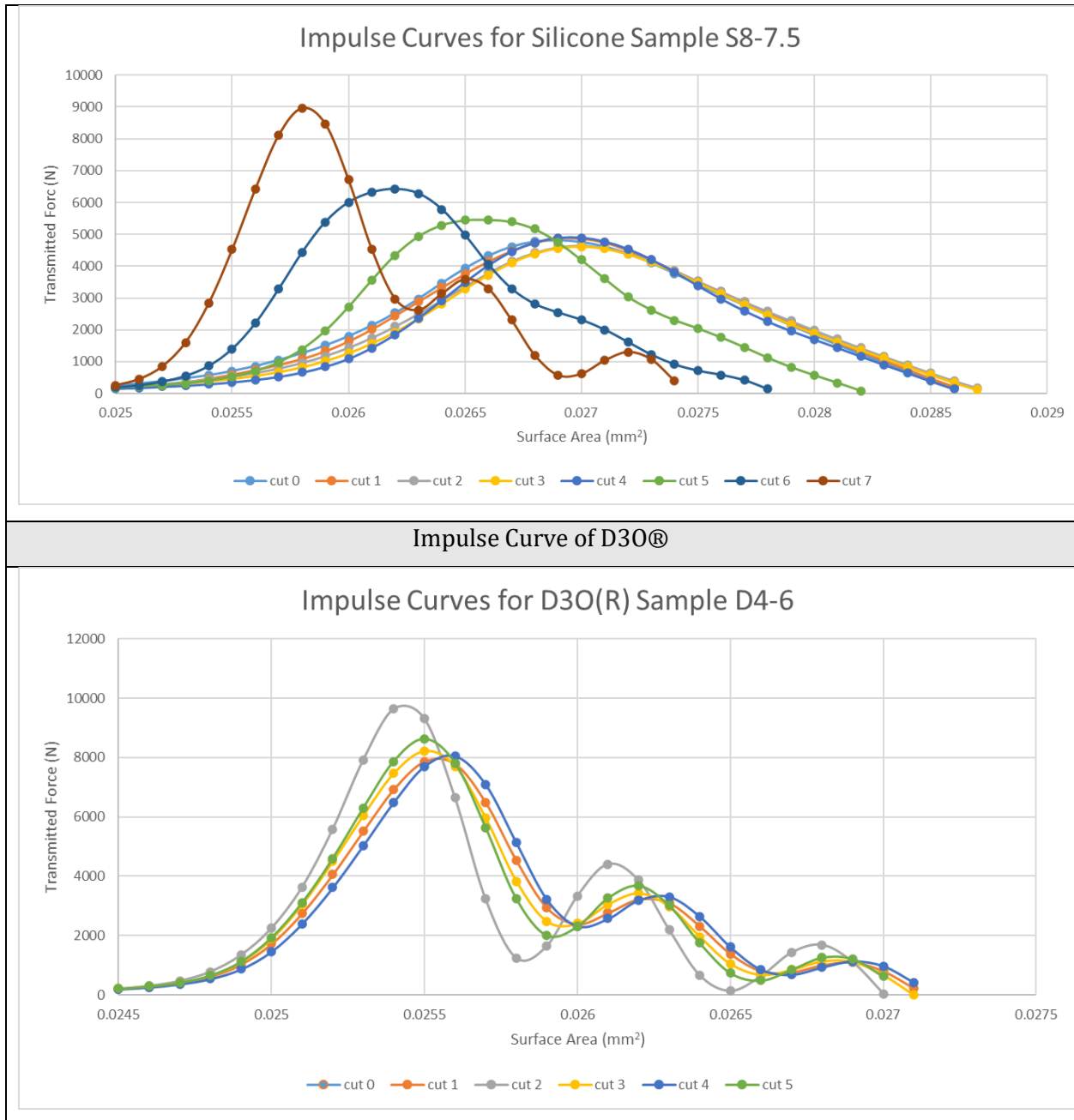
Figure B.12: Impulse curves for silicone and D3O® specimens in the surface area analysis. Each specimen was given a label of (Material Prefix)(Batch Number)-(Thickness). For example, S10-8 means a silicone specimen from batch 10 that was 8 mm thick. All specimens had original lateral dimensions of 84 mm x 54 mm. Note: If a cut does not show up on the graph, the reading was incorrect (i.e., the outputs matched the curve before it or no output was recorded).

B.5 Geometries

An attempt was made to provide physical testing data for the geometry analysis completed in Appendix C. The dimensions of the circle specimens, however, were created to have a diameter of 10

mm and the corresponding square dimension was 8.6 mm (to have the same surface area). These dimensions were chosen as they were small enough to be placed on the finger.

Figure B.13 below presents the specimens that were created for testing. (a) displayes the square geometries created; (b) shows the no hole to 75% hole geometries for the squares; and (c) shows the circle geometries created. When the specimens were tested, they all exhibited signs of plastic deformation, as illustrated in Figure B.14. The results of the transmitted force showed that there was not enough material to see an effect of adding a hole, which was the purpose of the experiment (i.e., all of the specimens were loaded way beyond their yield strength). Thus, the experiment was terminated. Due to the termination of the experiment after testing the square geometries, holes were not cut into the circle geometries. Additional testing with larger specimen dimensions was planned; however, unforeseen circumstances prohibited the testing to be completed.
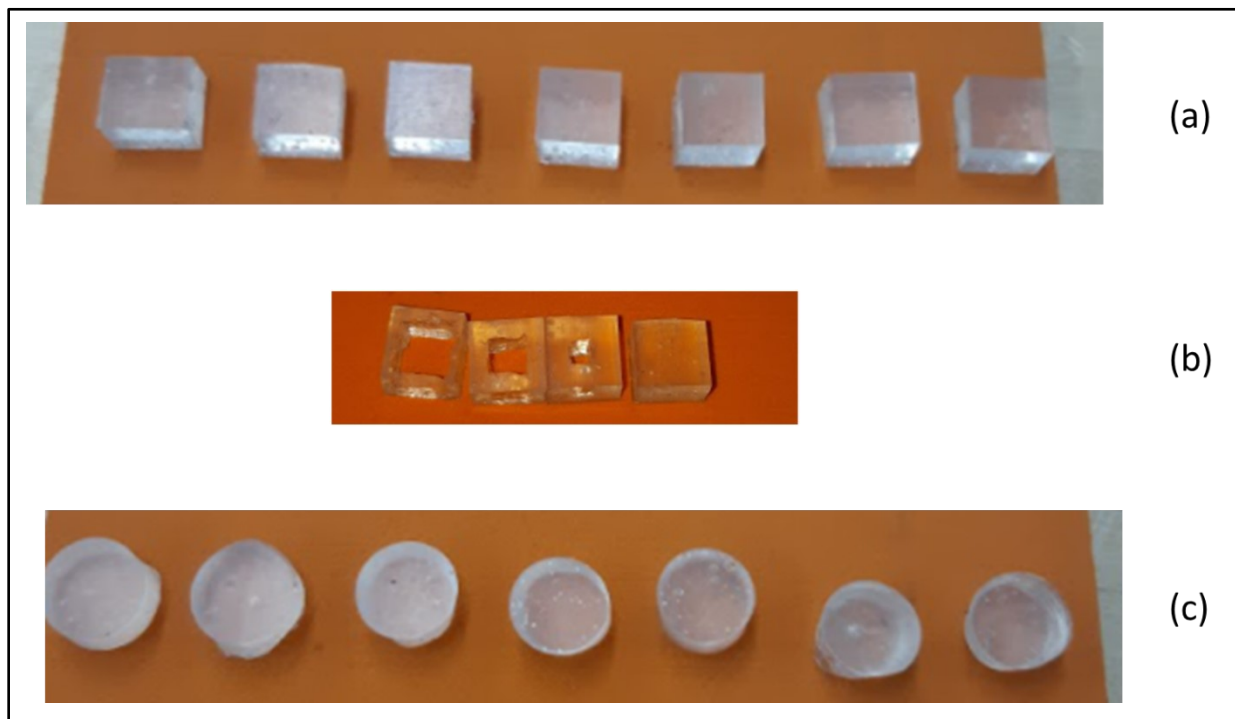
Figure B.13: The 6 mm thick specimens used for geometrical testing. (a) are the square specimens with a side length of 8.6 mm; (b) are the square specimens with holes cut that had a side dimension 25%, 50% and 75% of the outer dimension; and (c) are the circle specimens with a diameter of 10 mm.
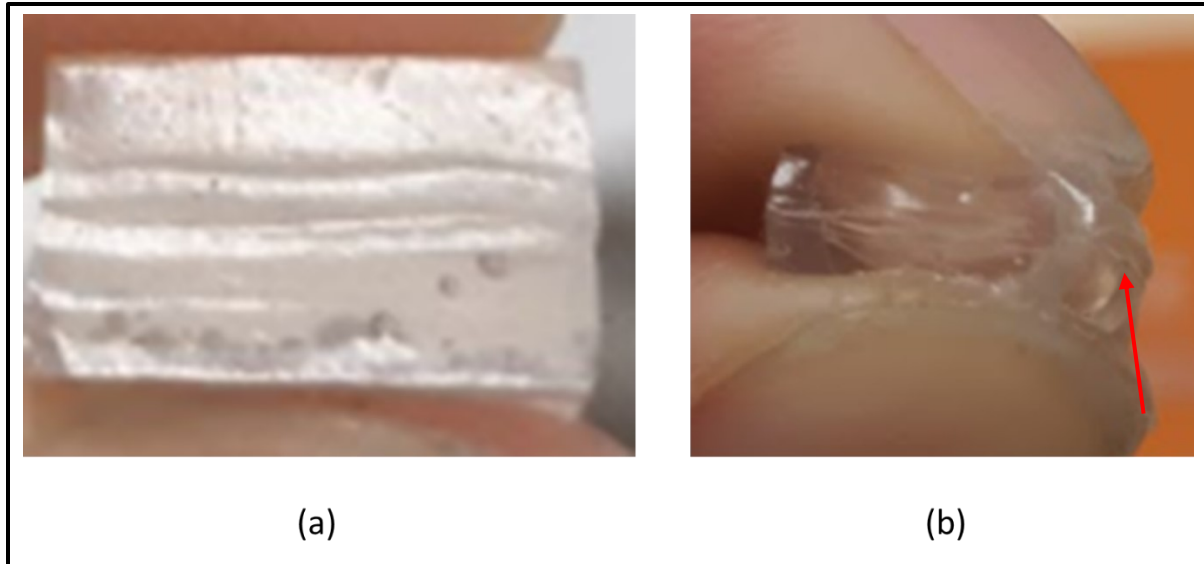
Figure B.14: The damage observed in the square specimens. (a) is the side view of a specimen with no hole, which observed plastic deformation through the formation of stress waves; and (b) is the side view of a 75% hole specimen where the material ruptured (indicated) halfway through the thickness of the specimen.

B.6 Layering

The effects of layering specimen tiles were examined. The purpose of the layering testing was to see if the order of the layer mattered when two specimens were placed together. For the layering experiment, tiles of TPR with 5mm thickness and varying harnesses (25A to 50A) were layered together. Due to the limited number of specimens, similar combinations were prioritized in order to compare them (i.e., 40A on the top and 30A on the bottom and vise versa were prioritized). The data from the layering is presented in Table B.3. The top layer (layer that came into contact with the striker) is on the top row, and the bottom layer (layer closest to the anvil) is on the far-left column. The transmitted force results are presented in the aligning column and row. For example, the 40A top with a 30A bottom produced a transmitted force of 3662 N; reversing the order produced a transmitted force of 3529 N. Comparing the results of the inverse showed that the order of the layer did not matter; however, the composition of the layers mattered (i.e., a 25A/30A performed better than a 40A/50A due to the lower hardness of the layers).

Table B.3: The results of differing the layers of a two-piece 10 mm thick TPR composite. Each layer was 5 mm thick. The top layer was defined as the one that comes into contact with the striker.

Top / Bottom	25A	30A	40A	50A
25A	3374 N			
30A	3512 N		3662 N	3771 N
40A	3698 N	3529 N		3912 N
50A	1611 N*	3771 N	3805 N	

B.7 Composites

A brief experiment was conducted to see if cutting two plugs from 20A and 50A specimens of 6 mm thick TPR would have an effect on transmitted force. The results of the testing completed were 5723 N and 5778 N. Thus, there was no significant difference in transmitted force when swapping the plugs in the materials. Figure B.15 below illustrates the swapping of plugs between the two harnesses. A line was drawn on the specimens to ensure that they remained in the same position as the original bulk specimen.

Figure B.15: The specimens used for swapping plugs. The top specimen is a 20 A TPR 6 mm thick and the bottom specimen is a 50 A TPR 6mm thick. The plugs were marked with a paint pen to ensure the same orientation was kept when they were swapped.

B.8 Kevlar® Meshes

Silicone specimens with 30/3 Kevlar® fibre meshes inserted into the specimens were tested. The theory behind the experiment was to try to induce more energy absorption of the specimens by deforming the Kevlar® fibres. To create the specimens, a Kevlar® weave was created with a wire frame cut from a scrap chicken wire. Two separate weaves were created: one with 5 stitches per wire tab and one with 10 stitches per wire tab. The weave was hand woven with a needle, as shown in (a) of Figure B.16. When the weave was complete, the fame was placed in the mold and the silicon was poured over top. Pouring the silicone after the weave was placed into the molds proved to be an error

as the silicone did not seep through the mesh entirely for both specimens, leaving large voids in the specimens (voids are shown in Figure B.16(b)). The specimens then were cut from the wire frame, measured for their new lateral dimensions, and tested. (c) illustrates the specimen when it was cut from the frame. The results of the test showed that the addition of the Kevlar® mesh did not affect transmitted force when compared to the bulk specimen of silicone for the same thickness. The lack of difference was likely due to the fact that the Kevlar® mesh did not deform (Figure B.16(d)).
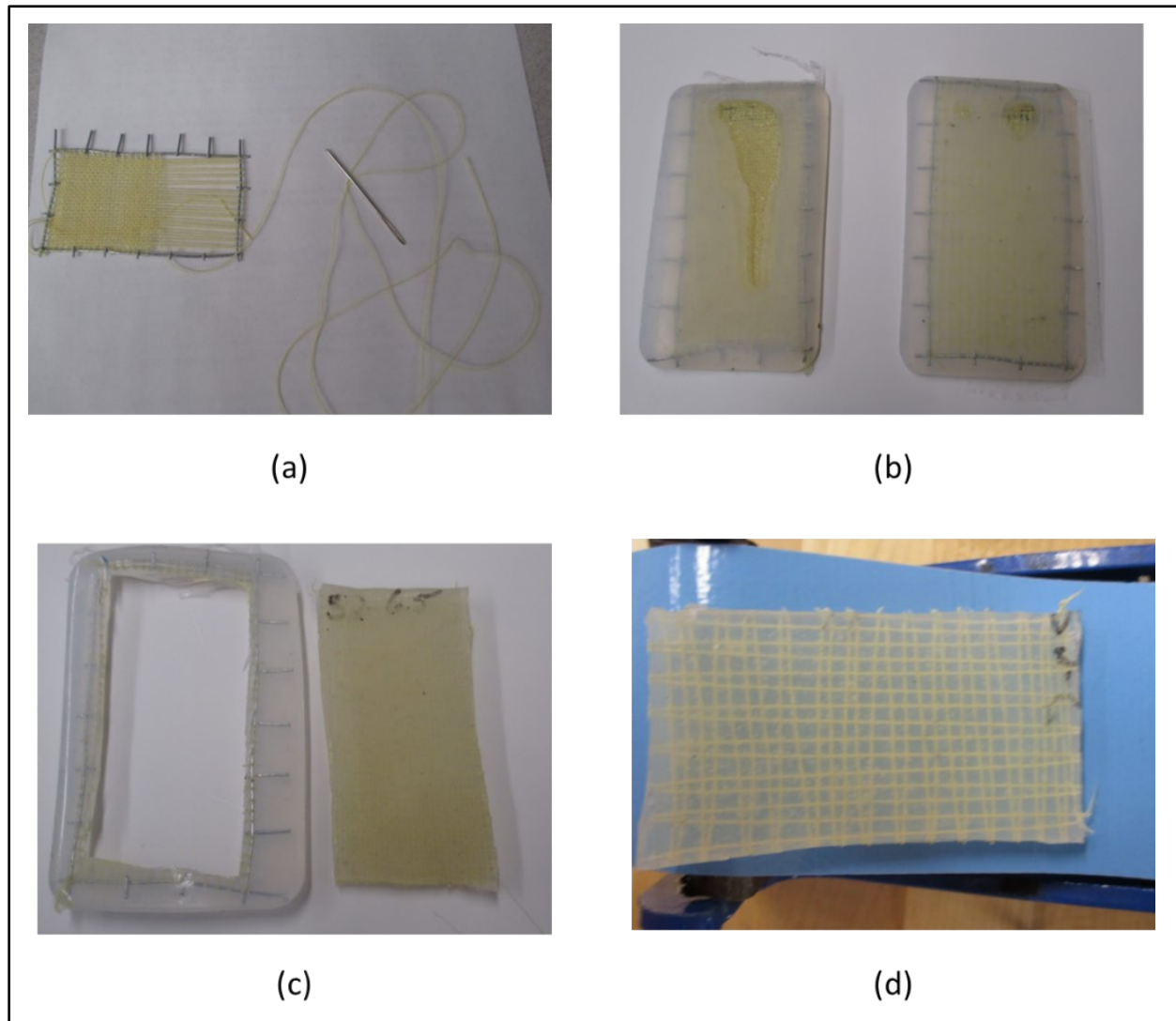
Figure B.16: The process of creating specimens with a Kevlar® mesh. (a) is the creation of the Kevlar® weave; (b) is the specimens after curing, where the weave was discovered to be too fine for the silicone to fully penetrate, resulting in large voids; (c) is the specimen cut for testing; and (d) is the specimen after testing where no deformation to the Kevlar® fibers was observed.

Appendix C Geometric Effects and Preliminary Abaqus® Model

C.1 Importance of Geometry

The following appendix examines the geometric effects of impact resistant bumpers. More specifically, if one geometry of the same thickness and surface area footprint (defined as the area of the bumper that contacts or is adhered to the glove) reduces the transmitted force more than another geometry. For example, does a square reduce the transmitted force better than a circle footprint of the same surface area and thickness; therefore, same volume? In addition, what would happen if a hole is added to the geometry – would the transmitted force decrease? Understanding the geometric effects of the bumper is important in glove design as it allows the designer to be able to potentially achieve a better impact performance (low transmitted force) without changing the material or the amount of material used. Appendix C will use visual and numerical modelling via Abaqus® software and high speed videography (HSV), to attempt to find the geometric effects of various specimens. Due to the inaccurate results of the model, the following information in Appendix C was omitted from the main body of the thesis.

The research questions from section 1.3 of Chapter 1 that Appendix C attempts to address are:

(5) What is the effect of geometry on transmitted force?

(6) How can modelling be used to accurately predict a design's ability to reduce transmitted force?

C.1.1 Review of Axial Crush Testing Experiments

As discussed in Section 2.5 of Chapter 2, there have been many experiments conducted for axial compression testing steel rods of various cross-sectional geometries such as rods and tubes with a circular, square, or hexagonal cross-section [1] [2] [3] [4] [5]. The objective of the axial compression testing experiments was to see which tube absorbed the most energy, as defined by the area under the force-displacement curve. The tube that performed the best was deemed to be the design that could withstand high forces and deform the most (i.e., the design that could maximize the area of the force-displacement curve). The consensus from the axial compression testing was that tubes were able to absorb more energy than rods and that circular cross-sections were better than the other geometries [3] [4] [5] [6] [7]. One reason that the hollow tubes absorbed more energy is that the tubes were able to achieve a more global deformation than the solid rods, meaning that more material

was able to be used for energy absorption as the hollow tubes buckled at multiple locations, as shown in Figure C.1(b) below. The global deformation of the tube keeps the stress concentration low which allows for more deformation before failure. In contrast, the solid rods would withstand more force at first and then bend at one location where the stress would become concentrated at. The stress concentration caused the rod to fail by collapsing on itself leading to minimal displacement when compared to the hollow rods of the same cross-section (Figure C.1(a)).
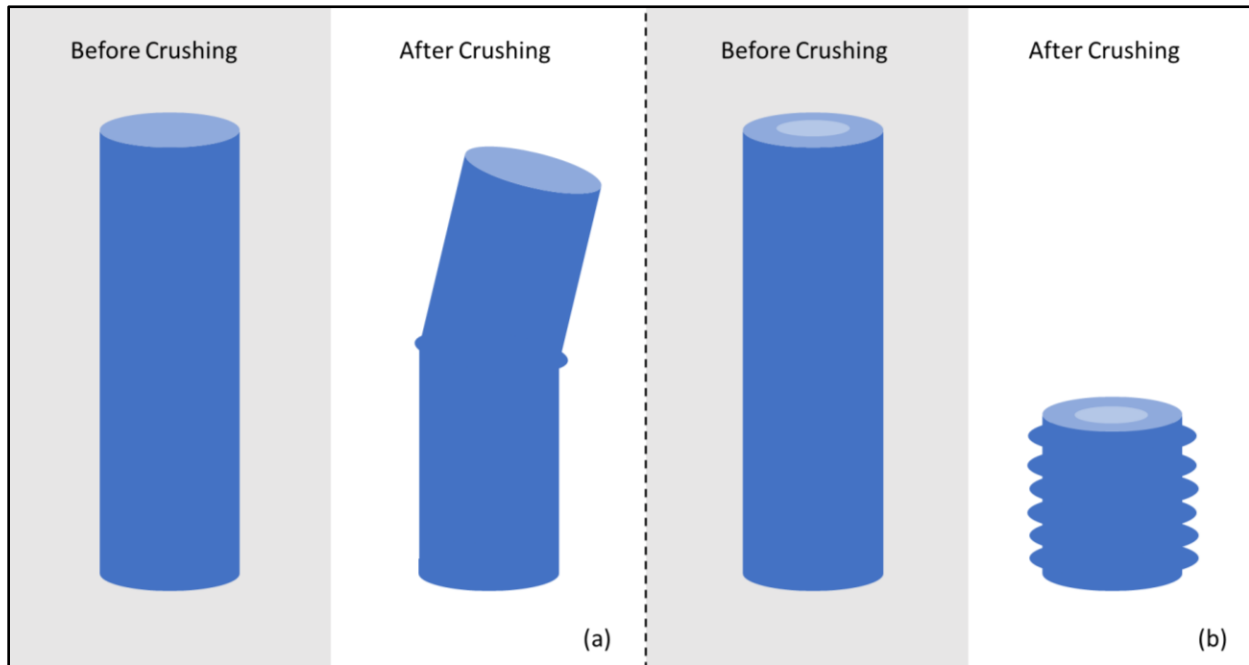
Figure C.1: A schematic of the deformation of a solid rod (a) and hollow cylinder (b) under axial compression. When the solid rod is crushed, it will bend at one location instead of multiple causing a high stress concentration in the one area. The hollow cylinder of the same length will buckle and bend at multiple locations causing multiple stress points with a lower stress concentration than the solid rod. The global buckling of the hollow cylinder allows it to absorb more energy as it achieves more strain.

All of the test runs completed during the axial crush testing were performed on steel specimens that were crushed, not impacted at relatively low velocities; therefore, the results of the testing can give an idea of what to expect if the geometry of a glove bumper were to change and demonstrate that the more deformation or strain a specimen can undergo, the more energy it can absorb. However, the results of the axial crush testing cannot be extrapolated for the geometry of the glove bumper as the loading condition is different (static crushing versus low-velocity impact), the scale of the specimens

are different, and the material used for the bumpers are polymers which are microstructurally different than metals.

C.2 Modelling (Preliminary)

The preliminary model was created to be a simplified version of the ASNI/ISEA 138-2019 standard, consisting of an anvil, striker, and an 8 mm thick specimen measuring 84 mm x 54 mm. The striker was created as a discrete ridged part to have a mass of 2.5 kg. The anvil and specimen tile were created to be deformable bodies for the collision. Abaqus® software requires that each part be assigned a mesh for calculation. The mesh assigned to the parts were 5 mm for the striker and anvil, and 10 mm for the specimen. The specimen had a larger mesh size due to the elastic properties assigned to it. Reducing the mesh size of the elastic specimen caused error in the calculations and the Abaqus® program aborted the simulation. The equation used for the calculations in the model was the linear elastic model, where the elastic properties were found by using the data supplied by the suppliers (see Chapter 3).

To simulate transmitted force, a history output was created and assigned to the bottom surface of the anvil. The history output created involved selecting the reaction forces on the surface in the direction of impact. The result of adding a history output to the bottom surface of the anvil was that each node (intersection point of the mesh) on the bottom surface had a calculated impact force. To find the total transmitted force, all of the nodes were summed and plotted.

To find the effects of geometry on reducing transmitted force when a bumper comprised of a polymer is subjected to low impact velocities, a preliminary Abaqus® model was created. The impact preliminary model consisted of a striker, specimen, and anvil. The striker and anvil of the preliminary model was dimensioned to mimic the ANSI/ISEA 138-2019 standard [8]. The striker was raised 2 mm above the top surface of the specimen and given a mass of 2.5 kg and a constant velocity of 2 m/s so that the specimen was struck with 5 J of energy. The specimen was created to form the desired geometry for analysis. Initially, this geometry was the standard 84 mm x 54 mm tile used in the experiments in Chapter 4 and Chapter 5. Figure C.2 illustrates a screenshot of the preliminary model that was created; the anvil, striker, and specimen are indicated, as well as the boundary conditions applies to the model. The Abaqus® preliminary model was designed to be a simplified version of the drop tests in order to reduce computing time and the complexity of the calculations. In every

simulation, the anvil and striker remained constant (i.e., constant size, mesh, material, and boundary conditions) and the specimen was changed for the simulation.
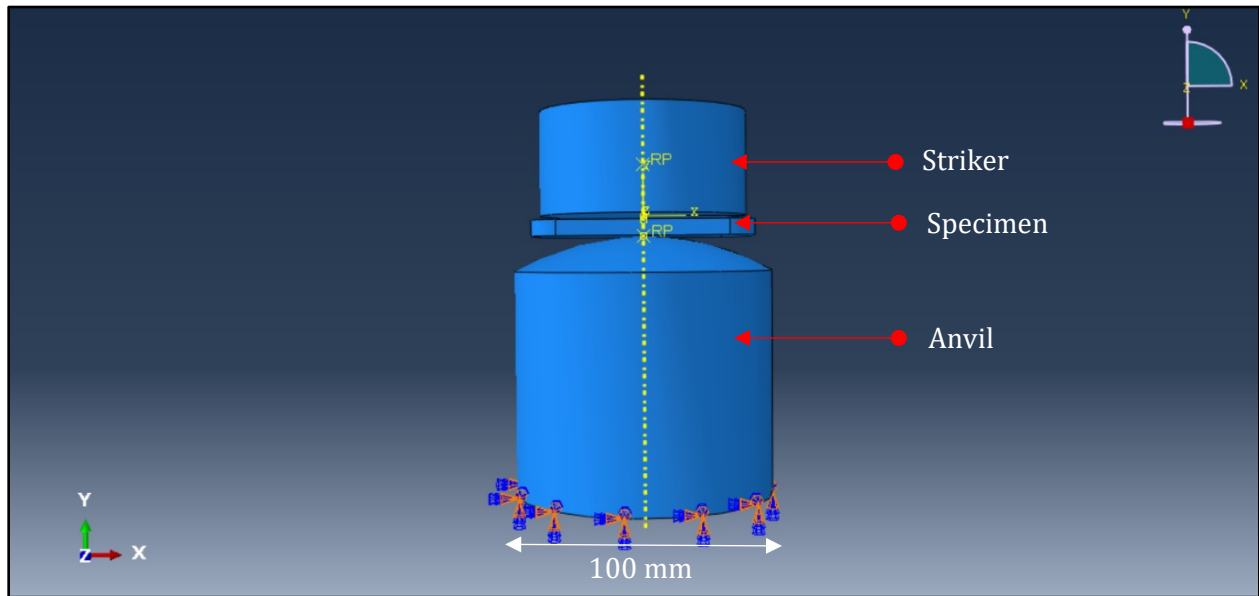
Figure C.2: The final iteration of the Abaqus® model created for simulation, as viewed in the "job" screen of the Abaqus® program. The model was simplified to a striker, specimen, and anvil (indicated) to reduce computational time. The "RP" and yellow guidelines in the figure are the references created to assemble the model. The upper right and lower left corners of the screen show the orientational axis for the model, with the impact motion occurring in the y-direction. The boundary conditions applied to the model are shown by the blue and orange arrows at the bottom surface of the anvil.

C.2.1 Preliminary Abaqus® Model Outputs

The primary objective of the preliminary model was to be able to predict the transmitted force of a bumper design. The preliminary model, however, was also able to visually demonstrate how the specimen deforms under impact as well as where the stress and force concentrations are on the specimen during impact. In addition, Abaqus® has the ability to calculate and create outputs for the different energies in the whole model, such as the kinetic energy and strain energy of the model. The following subsections overview the outputs from the impact simulation using Abaqus®.

C.2.1.1 Visual Outputs

When the simulation was run in Abaqus® the initial output screen given is the preliminary model at the starting time (i.e., when time is zero and no movement has occurred). The initial output is shown in Figure C.3, which is similar to the preliminary model from the "job" screen in Figure C.2 above,

except the output screen has the details of the mesh and is colored green by default. In the output screen, two direction vectors are given, one to show the orientation of the assembly (bottom left corner) and one to select the desired perspective (top right corner). The time step of the frame, fame number (increment), file name, and the time the simulation was ran is presented on the bottom of the screen. The time step increments for every simulation were selected to be 0.001 s.
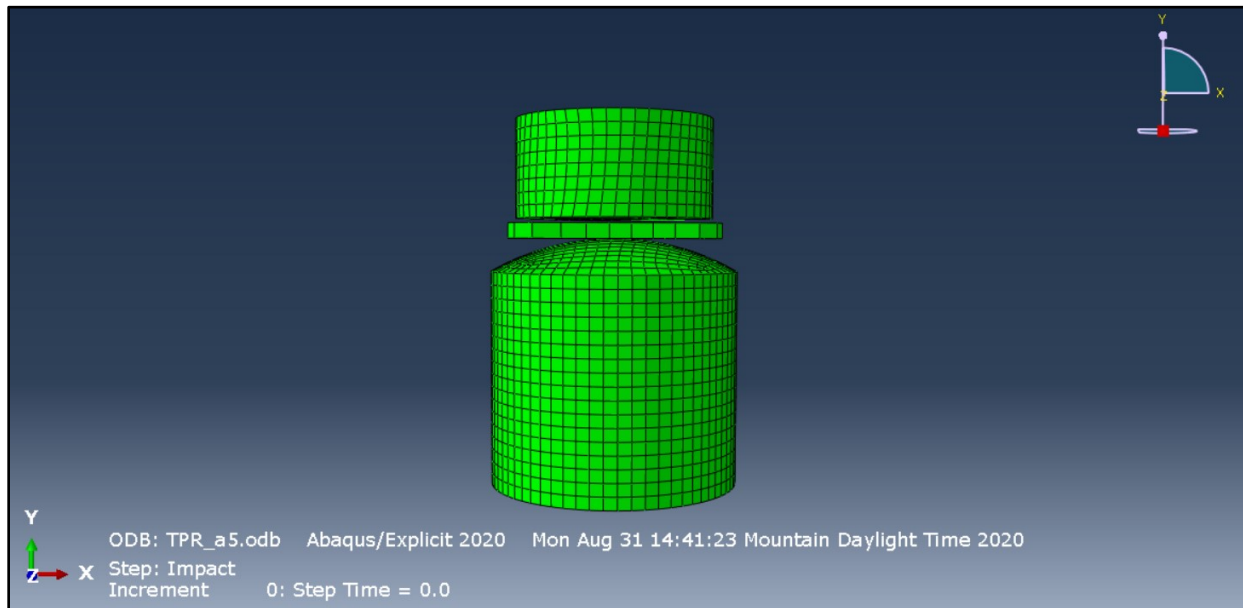
Figure C.3: The initial output screen after the simulation was ran in Abaqus®. The mesh of the parts is shown and the directional axis are displayed in the upper right and lower left corner. The details of the simulation, such as the file name, step, increment, time, and time of the simulation was ran are presented at the bottom of the screen.

From the initial stage, the visual results of the simulation can be observed by isolating every individual 0.001 s frame of the preliminary model or by animating the entire time history of the preliminary model. By animating the entire time history of the preliminary model, a visual indication of the result of the impact on the specimen can be observed. The Abaqus® program also has the ability to isolate each individual part as well as show the same time history with contour plots for many outputs such as deformation, contact force, shear forces, and stresses and strains. For the analysis of the bumpers, the deformation, strain stresses, strain on the specimen, and contact forces of the specimen were primarily examined. Figure C.4 below shows the bottom of the impact (when the kinetic energy of the striker is zero and the maximum transmitted force is reached) contour plots for the von misses stress, strain, contact force, and deformation of the TPR 25A specimen. In each plot, the red color represents the highest magnitude of each output and the blue represents the

lowest magnitude. For example, the deformation contour plot (labeled as magnitude of deflection) shows that at the bottom of the impact, the regions at the long ends of the specimen exhibit the most deformation (U). These contour plots can be isolated for every stage of the simulation.
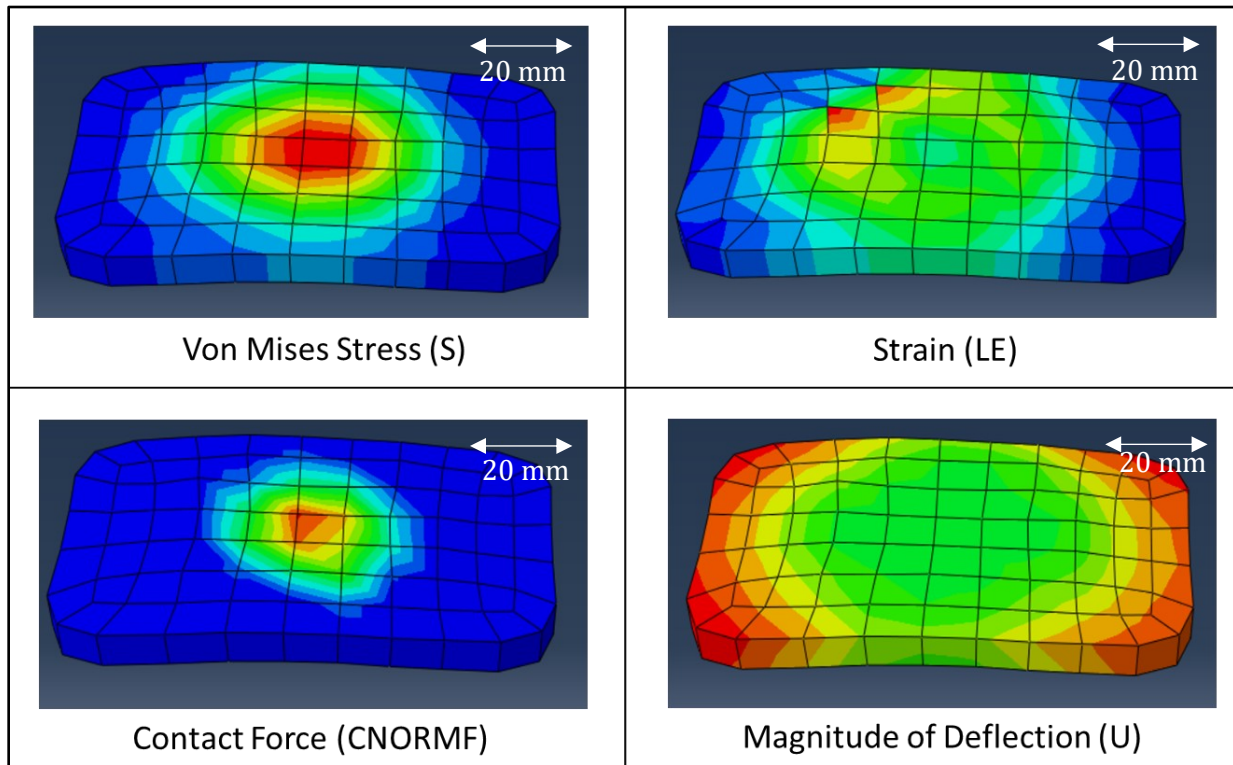
Figure C.4: The stress, strain, contact force, and deformation contour plots for the 6mm TPR 25A specimen at the bottom of the impact. The symbol that is displayed in the Abaqus® drop-down menu is shown in the brackets. For each contour plot, red represents the largest value of the plot and blue is the smallest. For example, in the deformation plot (U) the edges along the width of the specimen are red, indicating that they were subjected to the most deflection (the bending of the mesh can also be observed).

C.2.1.2 Force Outputs

In the preliminary model, the anvil was set up so that it was encastred (does not move or rotate). To simulate the transmitted force, a history output for the reaction forces on the bottom face of the anvil was created. The reaction force history output produces a force-time data for each individual node on the surface selected. Thus, the number of data points for the reaction forces depend on the mesh size. Once the boundary conditions and steps were applied, the simulation was run. In the output screen of Abaqus®, a force-time graph of the sum of the data produced by each node created by the mesh was generated (i.e., every node was added together), as shown in Figure C.5. Figure C.5 shows the results of a drop test simulating a 6 mm thick tile of 25A TPR. Abaqus® is a unitless software;

therefore, the axis in the plots do not have unit labels and are given a magnitude from the specified inputs. The inputs for the simulation were given as standard metric units, so the force is measured in newtons and the time in seconds. As observed in Figure C.5, the result of adding all of the nodes together produce a shape similar to the impulse curves from the experimental testing conducted in Chapters 4 and Chapters 5; however, a lot of chatter was produced on the graph, so the data required additional curve fitting to find the peak transmitted force. The summation of the nodes might not be the correct method for calculating transmitted force – the nodes could be averaged or a single node could be created for the force. The summation method was chosen as the transmitted force results were in similar range to the physical testing (averaging the nodes produced a transmitted force of 40 – 50 N).
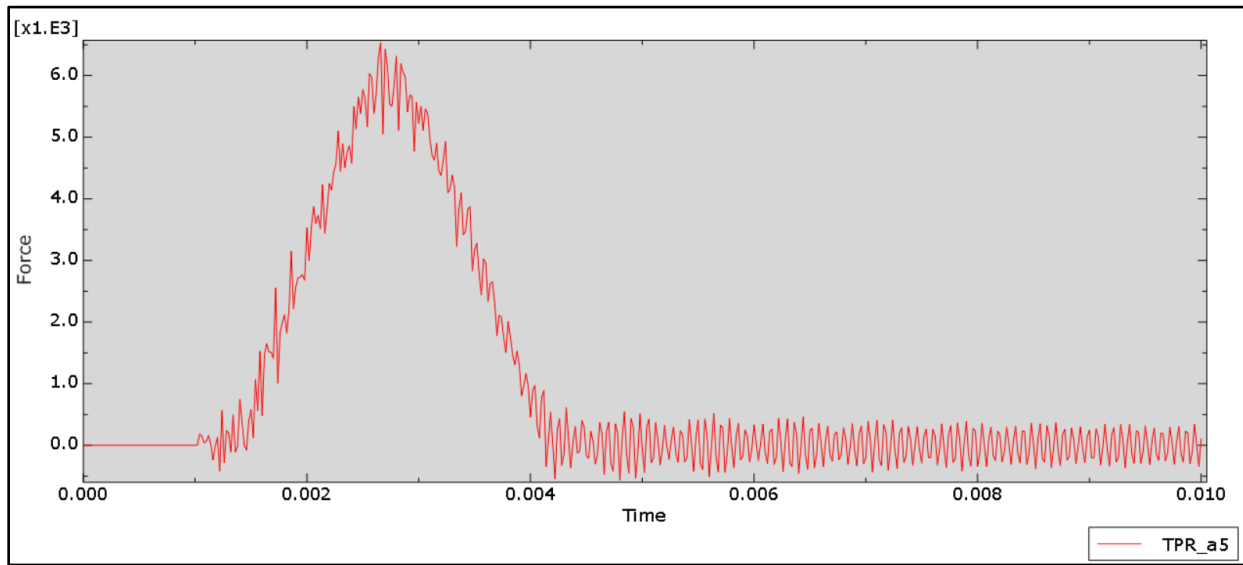
Figure C.5: A force-time output for the 6mm TPR 25A simulation. The graph is a output of all of the nodes summed on the bottom face of the anvil produced by Abaqus®. The transmitted force is measured in Newtons and the time is measured in seconds. The name of the simulation is displayed by Abaqus® in the lower right corner. The shape of the graph shows a peak at the 6000N range approximately 0.0029s into the simulation. Further curve fitting is required to achieve the exact values of force and time due to the chatter of the graph.

To find the peak transmitted force, the Gaussian normal distribution method was used as the curve produced resembled a bell-curve. Thus, the Gaussian function was used to find the best fit curve for the force-time data:

$$f(x) = (F)e^{-\frac{1}{2}\left(\frac{x-\mu}{\sigma}\right)^2} \tag{6.1}$$

196

where f(x) is the expected transmitted force for the time of the step x. µ is the time to reach the peak fore, σ is the slope of the curve, and F is the maximum transmitted force for the entire data range.

For equation 6.1, the peak force (F), time of peak force (µ), and standard deviation are unknown. To find the unknown variables, such as peak force, the chi-square was added to each force-time data point and summed. Chi-square is a method that is used to estimate how closely the distribution matches the data. Thus, the unknown variables of peak force, peak force time, and pulse width can be found by minimizing the chi-square. Using the solver function in excel, the data exported from Figure C.5 resulted in a best fit curve displayed in Figure C.6 using the chi-square method. The data was truncated to only include the positive values of the impact in order to get a more accurate curve fit (i.e. the data used was only the impulse curve). The values produced by the chi square method for peak force, peak force time, and the slope of the standard deviation is shown in the corner.
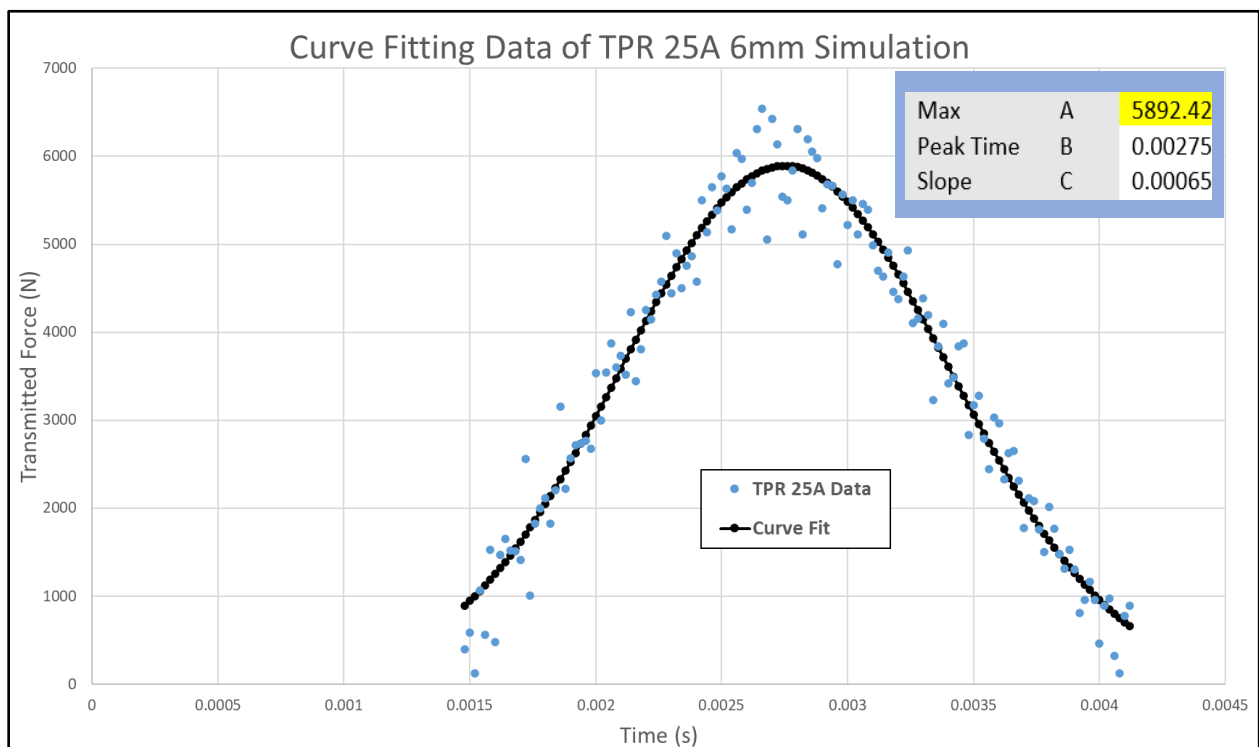
Figure C.6: An excel graph used to curve fit the Abaqus® data in Figure 6.5. The original data are the blue dots, and the result of the curve fit is shown by the black dots. The curve fitting method used was the Gaussian distribution with Chi-square, where the objective is to minimize the Chi-square. Using the solver function in excel to minimize the sum of the Chi-square value, the maximum force, peak time, and slope of the curve can be obtained. The values of the solver output are displayed on the inset of the graph.

The peak transmitted force was determined by running the simulation five times, one with 100, 200, 300, 400, and 500 force data points spaced out evenly over the entire preliminary model. This range was chosen as under 100 data points did not produce enough points to generate an accurate curve and over 500 did not enhance the accuracy of the curve and caused the simulation to have a longer processing time. See Appendix C for further details of the curve fitting analysis. Each of the five simulations were curve fit and the average of the peak transmitted forces was calculated and determined to be the specimen's peak transmitted force. The average of the peak transmitted force was used as the peak transmitted force of each of the five drops for the specimen had a 100 N variance and there was no correlation to the number of data points to the peak force (i.e., increasing the number of data points could not predict if the transmitted force would increase or decrease).

C.2.1.3 Energy Outputs

For the energy outputs, the kinetic energy and total energy of the system were primarily analyzed. The kinetic energy was analyzed as it showed the time for the striker to reach the bottom of the impact (when the kinetic energy reached zero), and the rebounding kinetic energy of the striker. The difference between the initial energy (5 J) and the rebounding energy is used to determine the energy absorbed by the impact. For example, Figure C.7 illustrates the kinetic energy output for the TPR 25A specimen, where the striker rebounded with a maximum kinetic energy of 3.73 J. Thus, the impact absorbed 1.27 J of energy. This energy absorption calculation can only be calculated if a local maximum is achieved after the drop. If the local maximum was not reached, the striker was assumed to be still increasing in kinetic energy after the bottom of the drop.
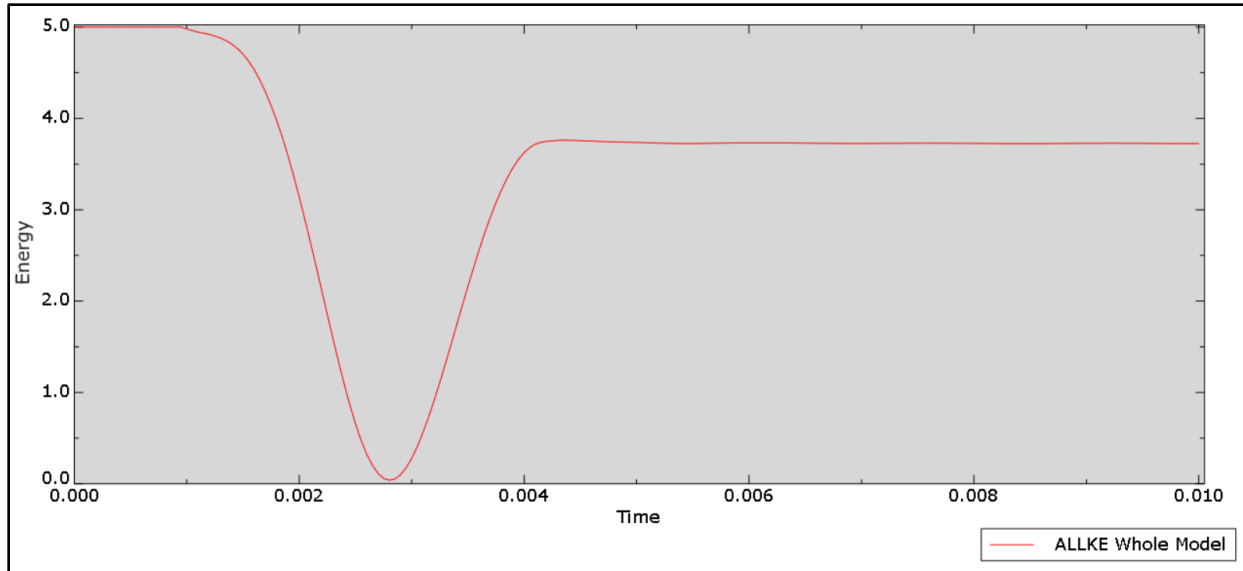
Figure C.7: The kinetic energy (in joules) of the 6 mm TPR 25A simulation for the entire preliminary model in Abaqus. Initially, the striker has 5 J of energy. At the bottom of the impact, where time is 0.0028s, there is no kinetic energy. The striker returns with a peak kinetic energy of 3.73 J.

The total energy of the system output was used to ensure that the total energy of the system remained at 5 J to comply with the law of conservation of energy. Figure C.8 below displays the total energy output for the entire preliminary model. As shown, the energy of the system remains at 5 J (Figure C.8). The values of the total energy were also able to be viewed in the "monitor" tab when the simulation was being run in order to ensure the simulation was behaving correctly (i.e., the energy was not increasing above 5 J).
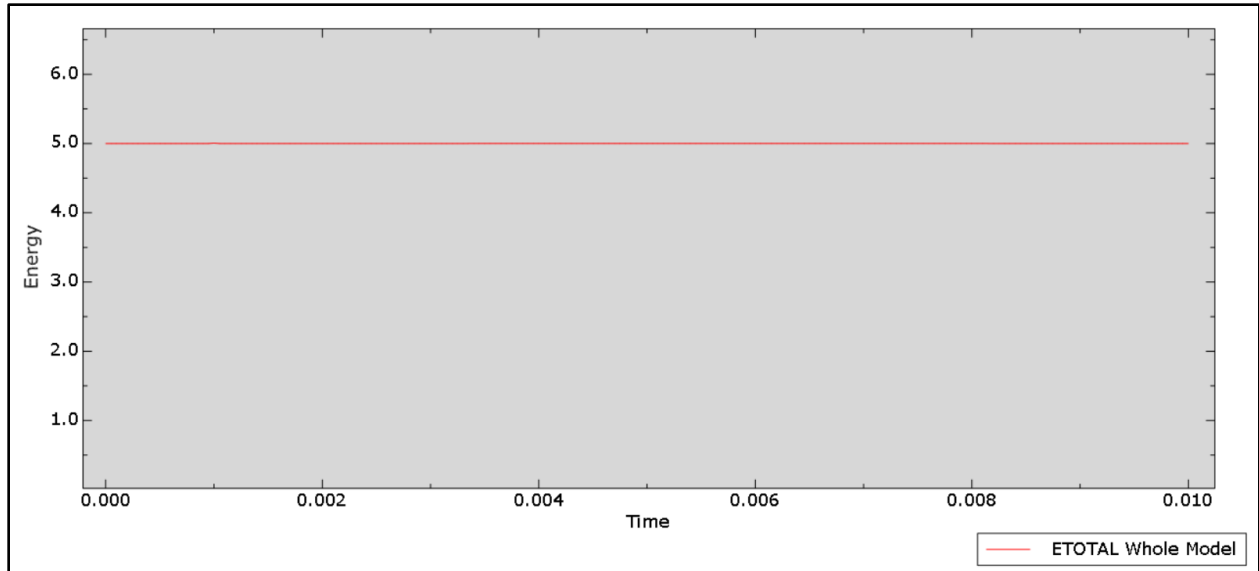
Figure C.8: The correct total energy output for the Abaqus® preliminary model, as exemplified by the 6 mm TPR 25A impact. For this graph output, the energy should remain constant at 5 J of energy to be correct as energy cannot be created or destroyed.

The other energy graph outputs that were used for analysis were the strain energy for the whole preliminary model and the frictional energy for the whole preliminary model. Figure C.9 illustrates the strain energy for the whole preliminary model for the TPR 25A simulation. The maximum strain energy correlates to the time of the bottom of the drop, and the overall shape of the curve correlates to when the striker contacts the specimen, indicating that the primary strain energy of the drop is generated from the striker. The tail of the drop (after 0.005 s) does not flatten to zero, and thus is likely the strain energy of the specimen movement (i.e., when the specimen stretches and contracts after impact causing a "wobble" effect).
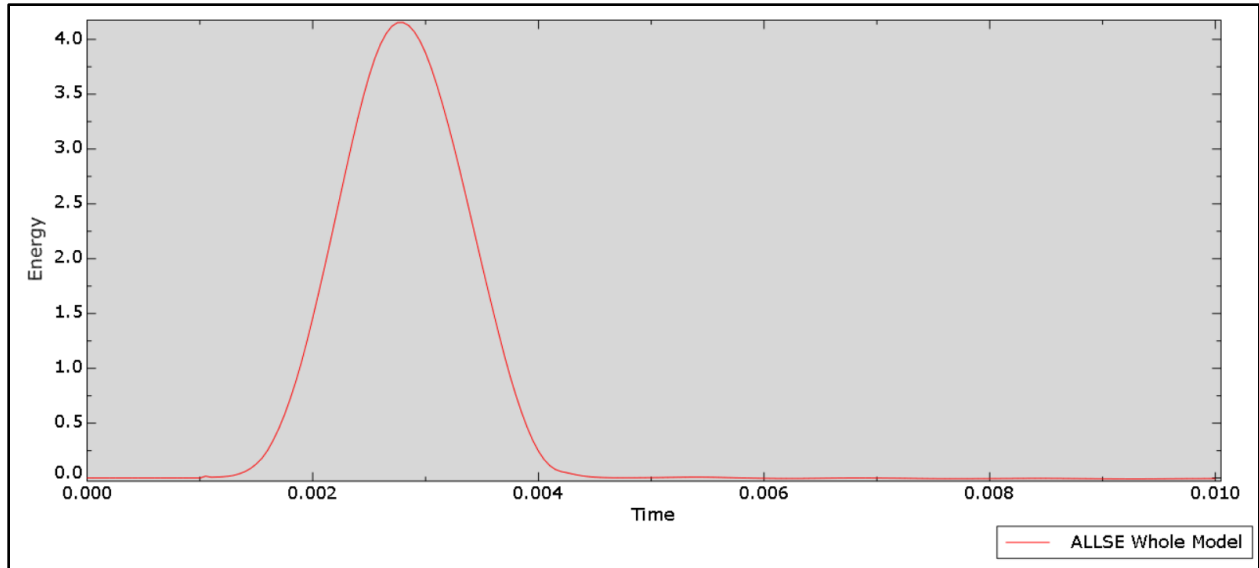
Figure C.9: The strain energy for the whole preliminary model of the 6mm TPR 25A simulation. The strain energy peaks at the same time as the peak transmitted force, which correlates to the bottom of the drop.

The frictional energy of the system for the TPR 25A simulation is presented in Figure C.10. The Figure shows an increasing frictional energy as the drop is completed and appears to arrive at an asymptote at the 0.006 s mark, which correlates to when the specimen leaves the anvil during the simulation. Thus, Figure C.10 illustrates the energy that is lost due to friction during the impact, which is approximately 0.5 J for the TPR 25A simulation. Subtracting this energy from the kinetic energy difference of 1.27 J suggests that the specimen only absorbed 0.77 J of energy for the impact.
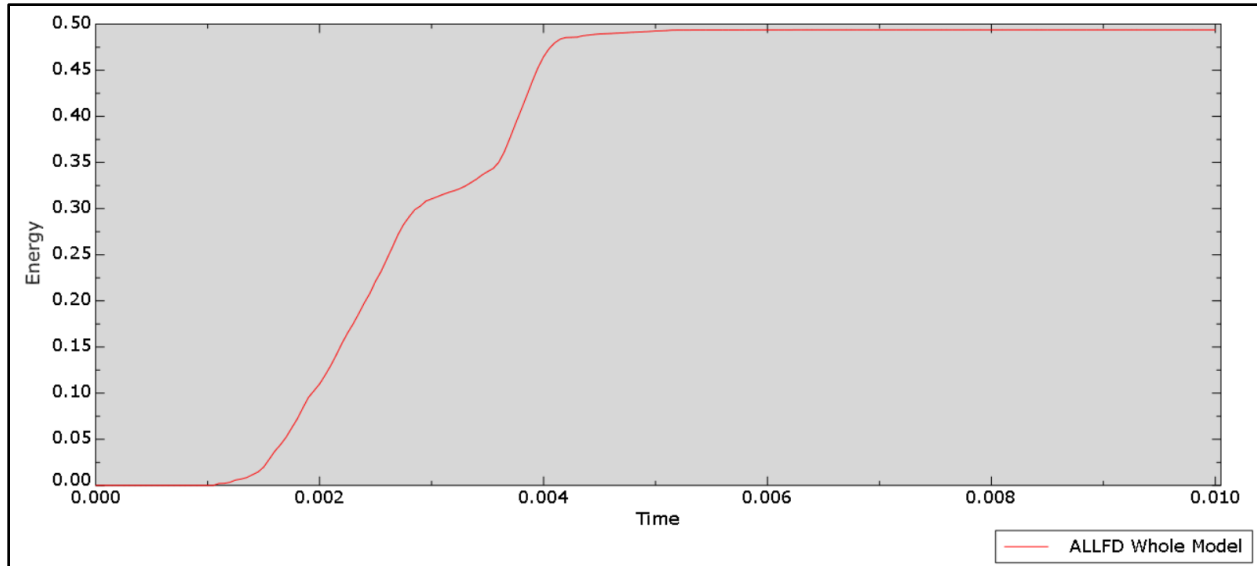
Figure C.10: The frictional energy of the 6mm TPR 25A simulation. As the frictional energy only increases, it is assumed that this is the energy lost due to friction during impact.
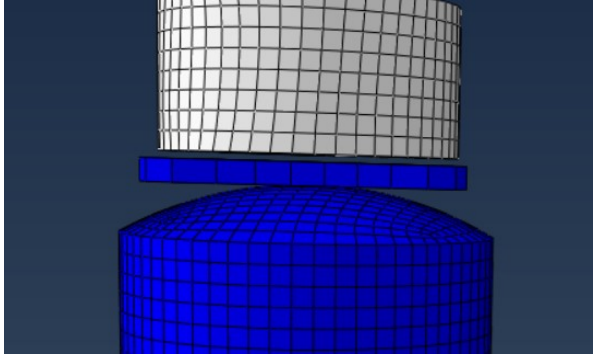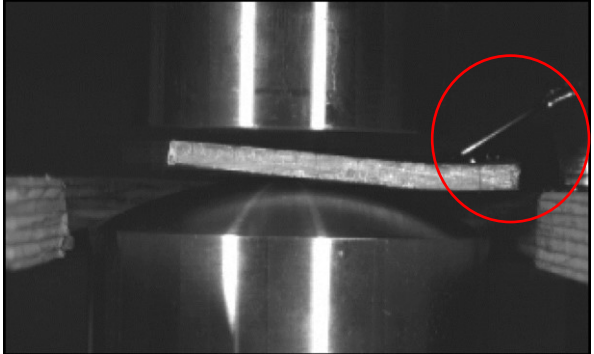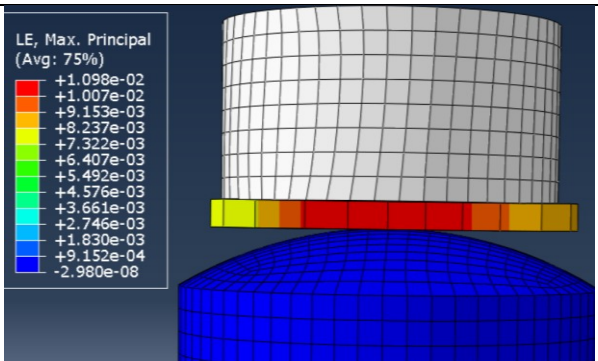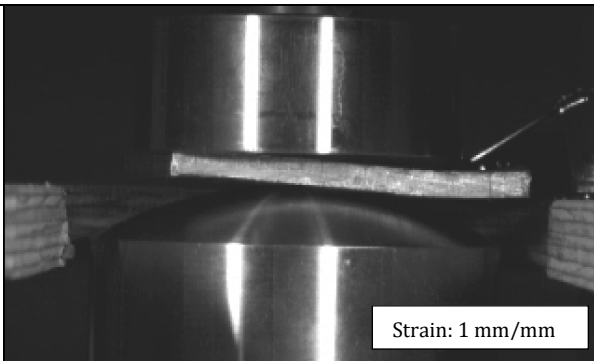
C.2.2 Comparison of Outputs

A comparison of the preliminary model was completed against the visual analysis and calculations from the HSV were used as well as the impulse curves from the experimental data. By comparing the movement of the simulation, more specifically the specimen, to the corresponding drop test in the HSV, the Abaqus® preliminary model could be validated. For example, if the movement patterns of the specimen produced by the simulation were similar for the experimental impact for each stage the preliminary model was confirmed to be adequate. If the preliminary model did not behave similarly to the experimental impact (i.e., no elastic movement or strain in the specimen), the preliminary model was deemed unreliable. Slow motion videography was also used to verify the time of the steps as well as the kinetic energy of the striker on the return on the bounce. The various stages of the drop from the time the striker contacted the specimen to when it was released was compared to the simulation for elapsed time to see if each stage occurred at the same rate. The velocity of the striker on the recovery after the impact was measured and converted to kinetic energy using $KE = \frac{1}{2}mv^2$.

C.2.2.1 Comparison Through HSV

Figure C.11 below shows the side-by-side comparison of the 6 mm TPR 25A impact at various stages with screenshots from the preliminary model shown on the left and the corresponding frame from the HSV displayed on the right. The screenshots of the strain from the Abaqus® preliminary model were chosen as strain could be visually identified in both the Abaqus® preliminary model and the

HSV. In Figure C.11, (1) is the starting point of the simulation and corresponding video frame; (2) is the initial contact between the striker and specimen; (3) is the compression and deformation of the specimen before bottom of the drop is reached; (4) is the bottom of the drop (when the kinetic energy is zero); (5) is at the end of the impulse, when the striker no longer contacts the specimen; and (6) and (7) are the resulting behaviours of the specimen after the impact.

Abaqus® Simulation	HSV
(1) Striker positioned 2mm above the contact point of the specimen. In the HSV drop, a clip (indicated) was used to hold the specimen in place causing the specimen to lie at a slight angle before contact.	
(2) Striker contacts the specimen. The Abaqus® simulation shows the strains that are initiated at contact (colour contour). The striker was created as a rigid body; therefore, the striker does not have a strain output (see code of Appendix D).	

Strain: 1.003
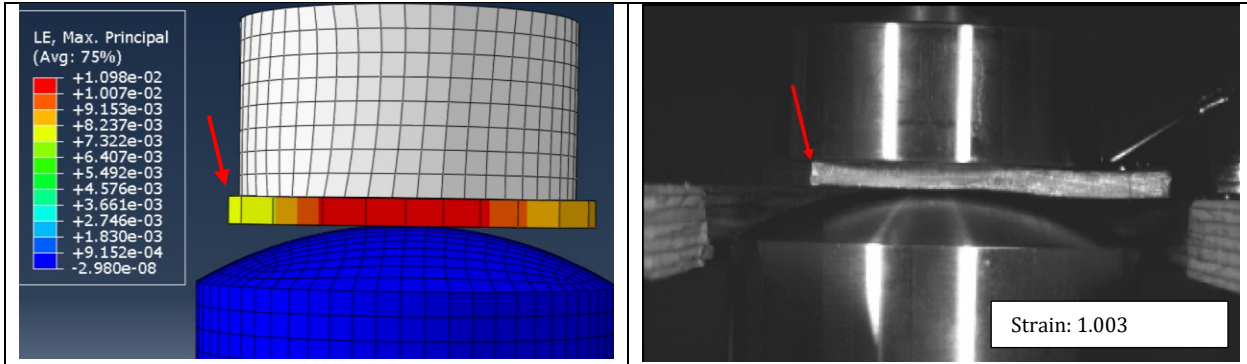
(3) The simulation and frame from the slow-motion 0.8 ms after initial contact. At this stage, the specimen starts to curve with the anvil and striker, causing the end of the specimen to point up (indicated by the arrow).

Strain: 1.077
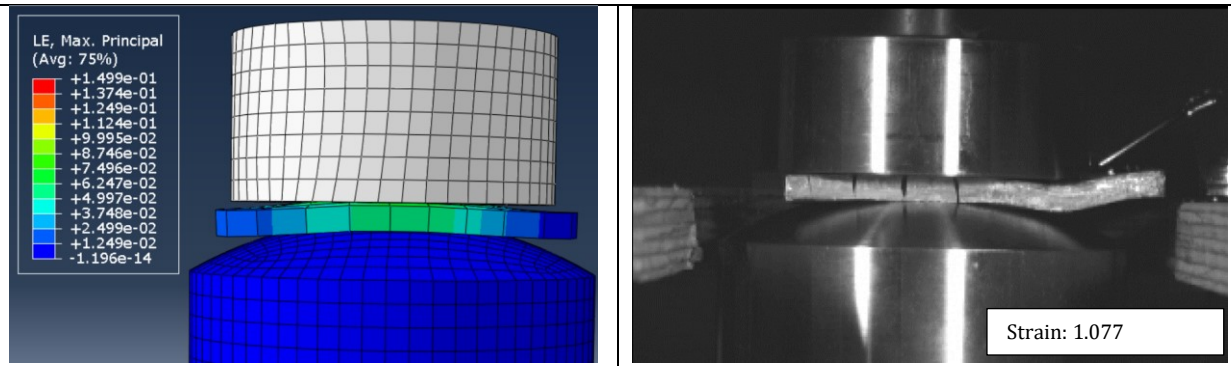
(4) The bottom of the impact, where kinetic energy is zero. In both impacts, the specimen has increased in length due to strain on the outer edges of the specimen, as shown by the increase in cell length on the outer cells the Abaqus® simulation, and spaces that form in the slits on the video analysis. The Abaqus® preliminary model was not created with slits as the slits were used as a visual indication of deformation in the video analysis. In addition, the specimen in both impacts has curved with the shape of the anvil.

Strain: 1.094
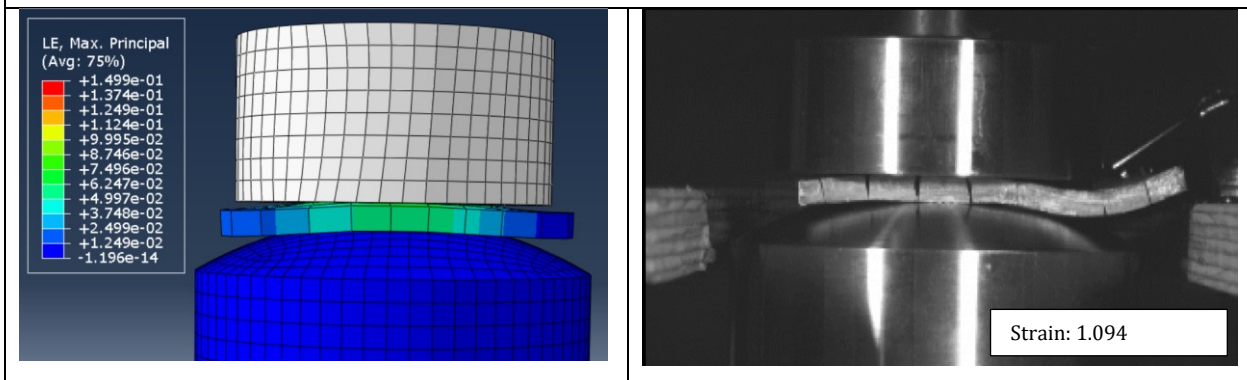
(5) The point at which the striker begins to move upward after the kinetic energy reached zero. In both impacts, the strain on the edges of the specimen and curvature with the anvil increases compared to when the kinetic energy was zero.

Strain: 1.052
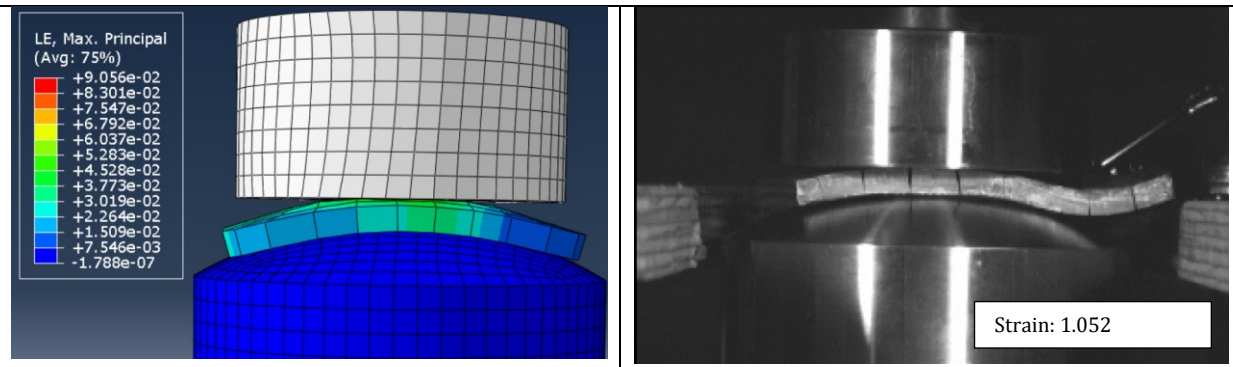
(6) 1ms after the striker started to move upwards. In both impacts, the specimen has completely flattened out against the anvil.

Strain: 1.002
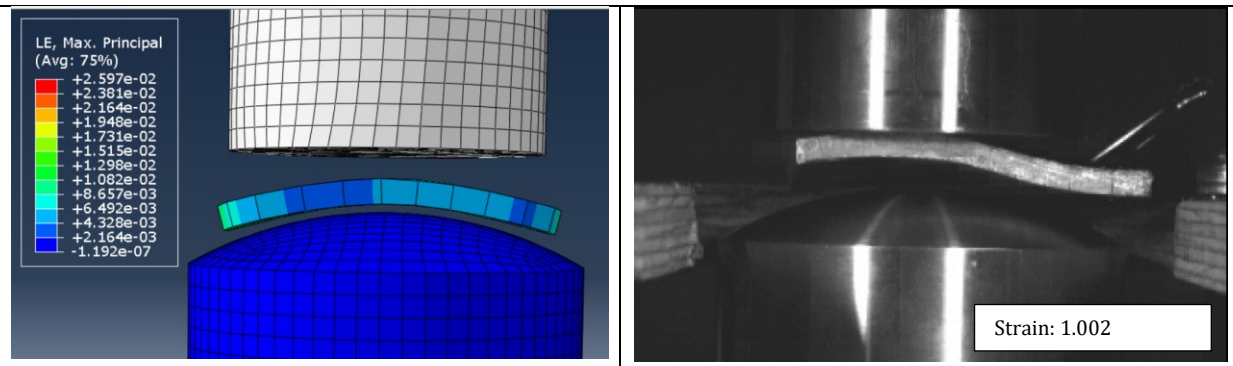
(7) 7ms after the anvil movement, which was the ending of the Abaqus® simulation. In both impacts, the specimen moves off of the anvil with the same contour shape of the anvil. In the video frame, the specimen moved with the striker more than the Abaqus® simulation. The movement with the striker could be due to the clip causing the rebound movement to inflect up more.

Figure C.11: A side-by-side comparison of the Abaqus® simulation (left) and the corresponding highspeed videography frame (right) of the 6 mm TPR 25A impact test. The values of the strain on each cell in the Abaqus® plot are given and the total strain of the specimen for the HSV are indicated.

As shown in Figure C.11, the simulation and experimental drop test have similar deformation mechanics visually, even with the presence of a clip to hold the specimen in place in the HSV drop. In addition, each key point in the impact from initial contact, to the bottom of the drop, to the release of the striker all have a similar elapsed time. Thus, the Abaqus® simulation behaves as it should for an 84 mm x 54 mm tile. To further verify that the simulation is accurate, the velocity of the striker in the HSV was estimated by measuring the distance and time between the frame where the striker just passes the initial contact height (determined by the original thickness of the specimen) after the

impact to the frame where the specimen moved 10 mm. The distance travelled during the points was 10 mm and the time elapsed was 7.42 ms; therefore, the velocity was 1.348 m/s. Calculating the kinetic energy from the rebound velocity of the striker gives a kinetic energy of 2.27 J, which is 1.46 J off of what was calculated by the Abaqus® simulation. Comparing the results of Figure C.11 and the calculated values of the kinetic energy show that the Abaqus® preliminary model is a valid way to visually simulate an impact for the 84 mm x 54 mm tile; however, further tuning of the preliminary model to improve the simulated characteristics of the material is required to get the correct kinetic energy output for the simulation.

C.2.2.2 Comparison with Impulse Graphs

The impulse graphs were used to verify the preliminary model by comparing them to the force output graphs. More specifically, the pulse width (time of the impact), the time for the pulse to reach the maximum, the maximum transmitted force, and the overall shape of the graph. Figure C.12 shows a side-by-side comparison of the Abaqus® (left) and the force output data from experimental impulse data (right) for the TPR 25A specimen.
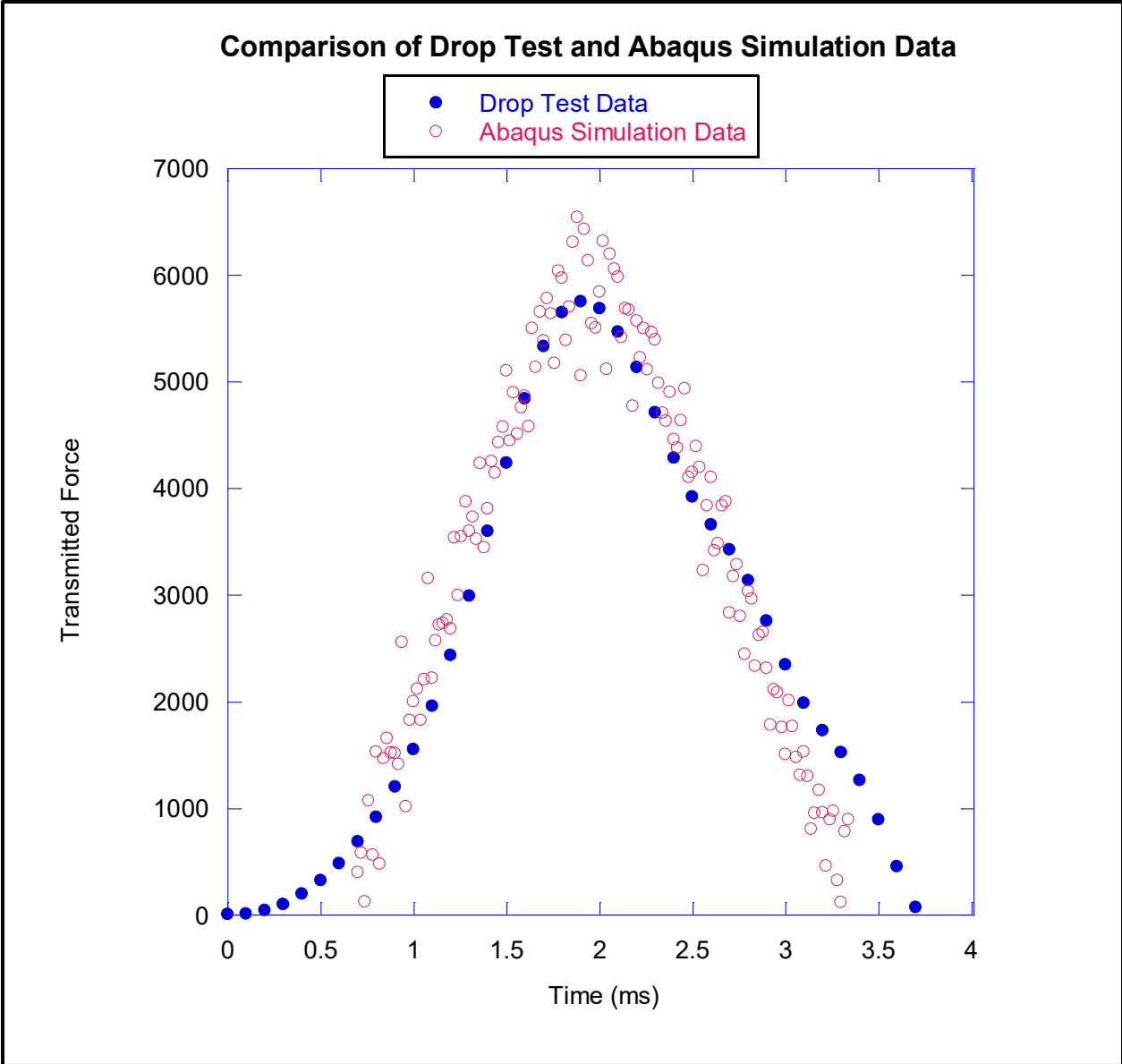
Figure C.12: A comparison of the impulse curves for the Abaqus® simulation (red) and experimental data (blue). Both curves have a similar shape and peak transmitted force. The simulation had a more rapid onset of impulse and finish, this is due to the fact that the liner elastic computation did not accommodate for the specific material behaviour or the plastic deformation in the model.

As illustrated in Figure C.12, both of the curves display a similar shape, with the simulation presenting a curve with more chatter. The peak force for the simulation was 5892 N (calculated in Figure C.6 above) and the peak force for the experiment was 5824 N. The simulation had a more rapid onset of impulse and finish, this is due to the fact that the liner elastic computation did not accommodate for the specific material behaviour or the plastic deformation in the model.

C.2.2.2.1 Using Impulse to fine tune

In the preliminary model, the material properties of each component were specified (see Appendix C). For example, the anvil was assigned the properties of an average steel. For the specimen, the Young's modulus, density, Poisson's ratio, and coefficient of friction were required as inputs in order to operate the preliminary model. The PVC, TPR, and silicone that were to be modelled had a known Young's modulus and density; however, the exact values of the coefficient of friction and Poisson's ratio were unknown. The data given by the GRANTA Edupack software presented the Poisson's ratio for each material as a range, and data from literature also gave a range for the coefficient of friction. For TPR, the Poisson's ratio range was 0.48-0.495 [9], and the coefficient of friction was 0.6-0.8 [10] [11]. Thus, multiple simulations were ran manipulating the Poisson's ratio and coefficient of friction in order to fine tune the peak force of the TPR specimen to match the testing data.

A complete analysis of the effects of Young's modulus, density, Poisson's ratio, and coefficient of friction was completed to see how each variable effects the peak transmitted force and time of the peak force. The data of the sensitivity analysis is presented in Appendix C.

C.2.3 Limitations to the Preliminary Model

The preliminary model was created and fine tuned for an 84 mm x 54 mm specimen. When the dimensions of the specimen were changed, there were many indications that the preliminary model was no longer accurate and is limited to accurately predicting the impact for only an 84 mm x 54 mm specimen. The most significant limitation of the preliminary model is that it does not model the failure of the material. The material failure was not added to the preliminary model as the failure data for the materials could not be obtained through literature and the tensile testing apparatus available did not have the capabilities to reach the yield strength of the materials. As a result, the simulation assumed that there was no failure to the specimen. If the specimen volume and size were too low, the cells created by the mesh would infinitely expand until they formed sharp geometric patterns during the simulation. The sharp geometric patterns were an indication that there should be failure in the model and that the simulation was not accurate. An example of the sharp geometric patterns produced are shown in Figure C.13 below.
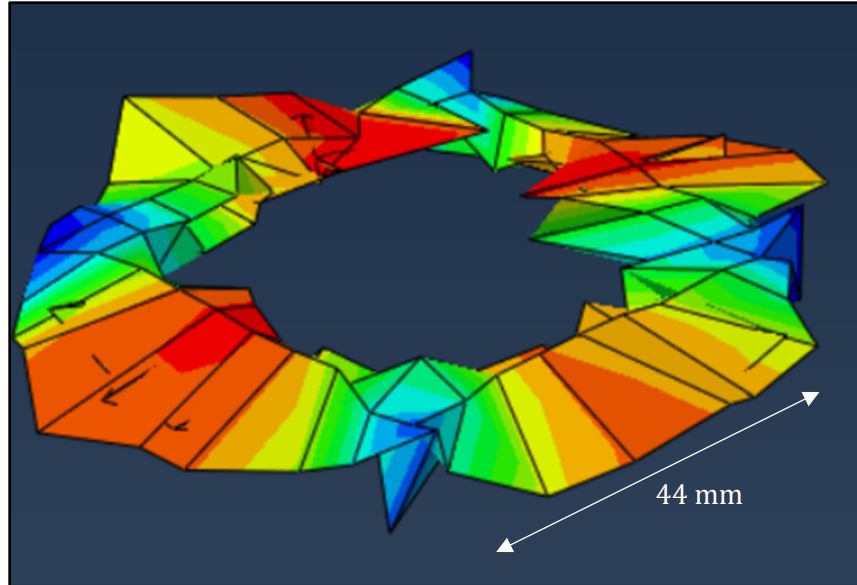
Figure C.13: An example of the sharp geometric patterns produced when the simulation is run with suspected failure that cannot be simulated. Due to the absence of a failure criteria, the cells of the original geometry infinitely stretch to unique geometric patterns.

Another indicator that the preliminary model was not accurate when the specimen size was deemed to be too small was that the total energy of the simulation would be greater than 5 J. In some simulations where the specimen size was significantly reduced, the total energy for the preliminary model was as high as 8 J, which is inaccurate. Any total energy above 5.001 J was deemed to be an indicator of inaccuracy in the preliminary model.

Due to the inability to model the failure of the material, the specimen size that can be used for the simulations is limited (i.e., small specimens cannot be used as they will lead to inaccurate results). This is a severe limitation as hands, which the gloves are designed for, require smaller geometries for a bumper than an 84 mm x 54 mm tile.

C.3 Analyzing Geometry

The purpose to analyze different geometries of bumpers is to determine if one geometry performs better than the other for the same surface area and volume of the material. The next section compares two geometries: a square based bumper and a circle-based bumper, as these geometries were most commonly tested in the axial compression testing in the reviewed literature [4],[5]. The literature also alluded that a hollow geometry would perform better than a solid geometry [4],[5]; therefore, variations of the circle and square shaped bumpers with holes in the center were analyzed. More specifically, specimens with a centered hole that was 25%, 50%, and 75% of the radius or length of

209

the original geometry were analyzed. The hypothesises of the experimental simulations were that the circle would reduce the transmitted force better than the square, and that the addition of the hole in the center of the specimen would reduce the transmitted force up to a point at which there was not enough material volume to absorb the impact. These hypothesises were drawn from the literature review of axial crush testing of steel beams where circle cross-sections absorbed more energy than square cross sections and hollow tubes absorbed more energy than solid rods (see section 2.5 of Chapter 2).

To select the initial dimensions of the specimen, a circular bumper with a radius of 10 mm and a thickness of 8 mm was originally used. The thickness was set to 8 mm as this is the maximum thickness the bumper was permitted to be by Superior Glove. A radius of 10 mm was used as this correlated to the critical surface area of TPR (where there was little plastic deformation to the specimen). TPR was selected as the material that was used for the bumper comparison as it was the material the simulatior was fine-tuned to model. Figure C.14 shows the result of the simulation for the10mm circular specimen, with the original geometry displayed in the upper right corner. As shown, the cells created by the mesh deformed to an extent that the bumper was unrecognizable. The mesh chosen was 5 mm, in order to be consistent with the original fine-tuned preliminary model; however, when the mesh was changed to be smaller, similar results occurred.
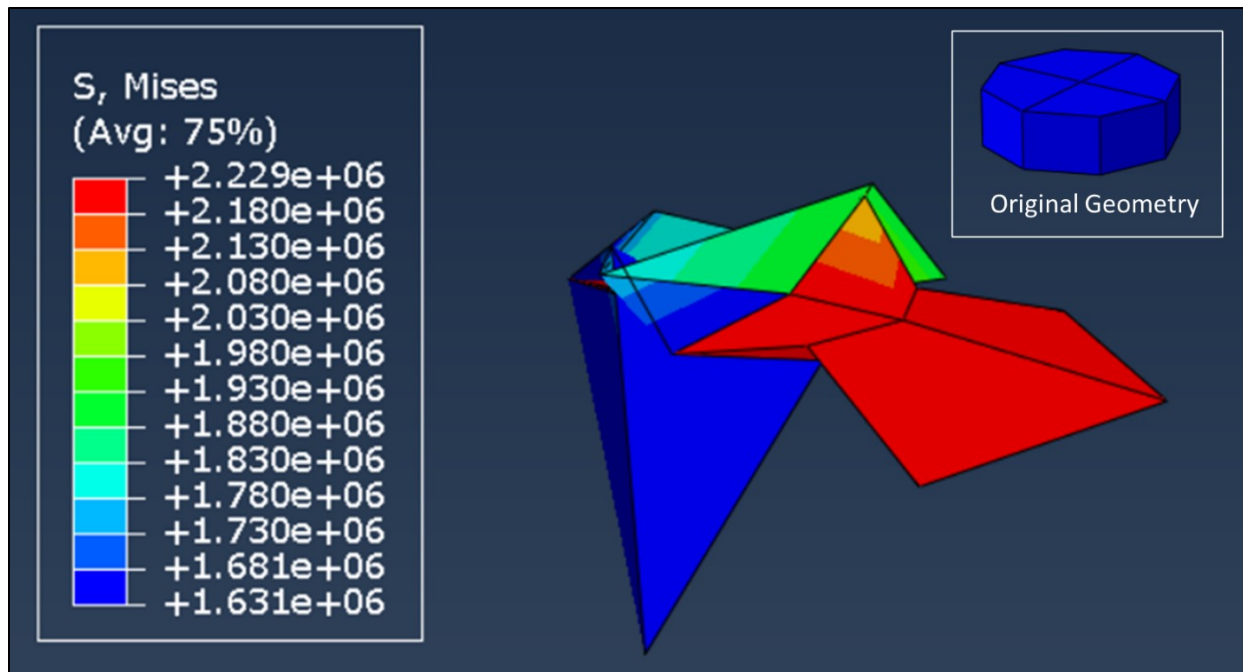
Figure C.14: A schematic of the extent of the deformation from a simulation of 8mm TPR 25A with a radius of 10mm. The original geometry is shown in the upper right corner. The four cells deformed to extreme geometries during the simulation; therefore, the simulation cannot be deemed accurate.

The results of the 10 mm radius bumper indicated that the specimen was too small for the impact and that plastic deformation was likely occurring (see limitations to preliminary model in Section C.2.3 above). Thus, the radius size was increased through trial and error until there was no increase in total energy to the system. This radius was 25 mm. The corresponding square of the same surface area (also volume) was calculated to have a length of 44.3 mm.

Figure C.15 illustrates the specimens that were created for the geometric analysis. The top row presents the circle specimens with a radius of 25 mm. Moving from left to right, the hole in the specimen increases by 25% of the radius. For example, the 25% hole has a radius of 6.75 mm and the 50% hole has a radius of 12.5 mm. The bottom row illustrates the square specimens with an outer length (L) of 44.3 mm. The hole size increased from left to right in the same manner as the circle.
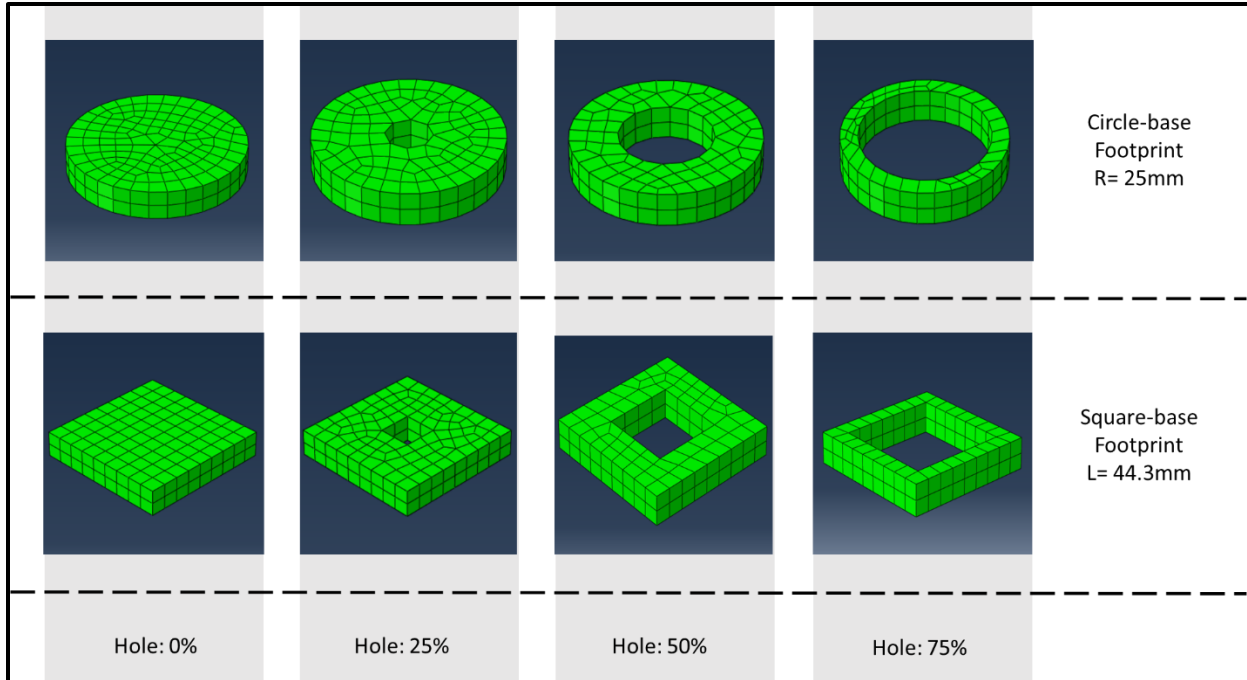
Figure C.15: Specimens used for the Abaqus® simulations. The top row is all circle-based with a radius (R) of 25 mm. The bottom row specimens have a square base with side length (L) of 44.3 mm. The columns represent the addition of a hole in the center of the specimen. The percentage represents the ratio to the length or radius to the respective dimension of the base.

C.3.1 Transmitted Force Analysis

Figure C.16 below presents the results of running the simulation for each of the eight specimen geometries created. Each specimen was tested five times with step increments of 100, 200, 300, 400, and 500 and curve fitted in the same way as the original simulation. In Figure C.16, the circles and squares with the same hole percentage are aligned for comparison and the maximum transmitted force as well as the time to achieve the peak transmitted force is displayed.
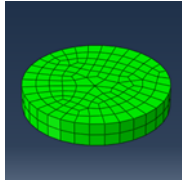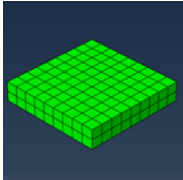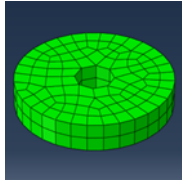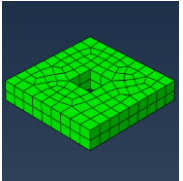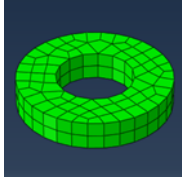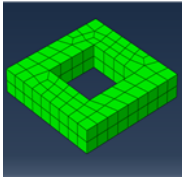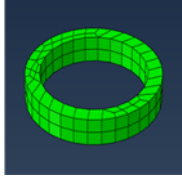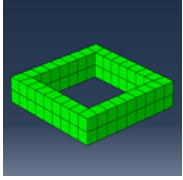
Geometry (Circles)	Maximum transmitted force (N)	Time to peak transmitted force (ms)	Geometry (Squares)	Maximum transmitted force (N)	Time to peak transmitted force (ms)
	4644	3.58		4192	3.58
	4528	3.62		4122	3.61
	3748	4.08		3220	4.12
	1771*	4.40		1937*	4.20

*Figure C.16: The maximum transmitted force and time to reach the peak transmitted force for each of the eight specimen geometries created. The specimens are ordered from no hole at the top, to 75% hole at the bottom. The * denotes a result that is inaccurate due to the amount of deformation to the cells and the shape of the force-time graph.*

As shown in Figure C.16, increasing the hole size results in the reduction of the transmitted force. In addition, the time to reach the bottom of the impact, or the maximum transmitted force, increases causing the impulse curve to shift to the right. The most interesting observation is that the squares

were calculated to have a lower transmitted force than the circles, which contradicts the findings of the axial crush experiments for steel tubes. The contradiction of the hypothesized result could be due to the different conditions of testing: a dynamic impact test vs a static impact test, specimen dimensions, and specimen material (steel vs polymer). The inaccuracy of the preliminary model could also be a contribution or the single factor of the contradiction of the hypothesized result. Further analysis is required to explore why the squares reduce the transmitted force more than the circles.

Due to the inaccurate nature of the simulation, the trade-off point of specimen volume and the size of the hole could not be determined. Although the 75% holes appeared to reduce the transmitted force further, the force-time graph generated from the simulation did not produce the typical impulse curve shape; therefore, the data cannot be deemed accurate. Figure C.17 shows a force-time graph for the 75% circle specimen as an example.
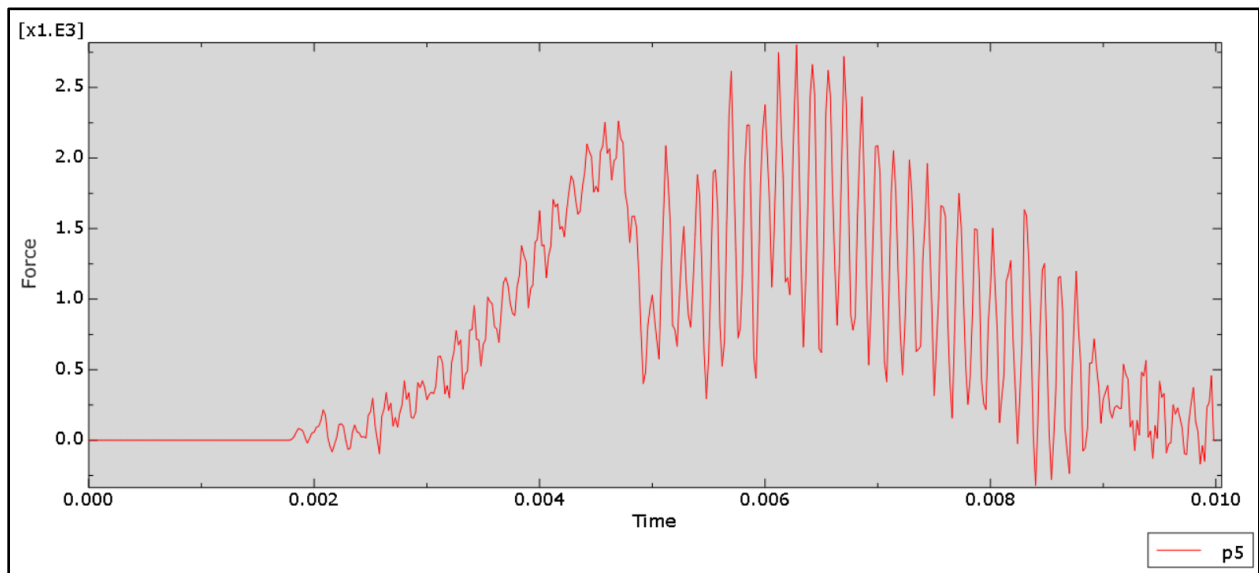
Figure C.17: The force-time output for the 75% circle geometry. As shown, there is a significant amount of chatter and no "ideal" impulse peak shape. Thus, the simulation is inaccurate for the 75% hole.

C.3.2 Visual Analysis
Figure C.18 and Figure C.19 below display the strain and stress contour plots of each of the specimens for the circle and square geometries at the bottom of the impact, respectively. For example, the no hole circle was isolated for the 0.0036 s frame. In each Figure, strain is shown on the top row and the stress on the bottom row. Each column from left to right increases the size of the hole (i.e., the no

hole geometry is on the left, adjacent to it is the 25% hole, then the 50% hole, and the 75% hole). As described in Section C.2, the red indicates areas of high stress and strain and the blue indicated the areas of low stress and strain. The maximum values for the strain and stress on a single cell for the specimen at the bottom of the impact are presented below the corresponding image. For example, the no hole circle had cells that reached 0.49 mm/mm in strain and 1.35 MPa in stress; the number of cells with the maximum value is unknown.
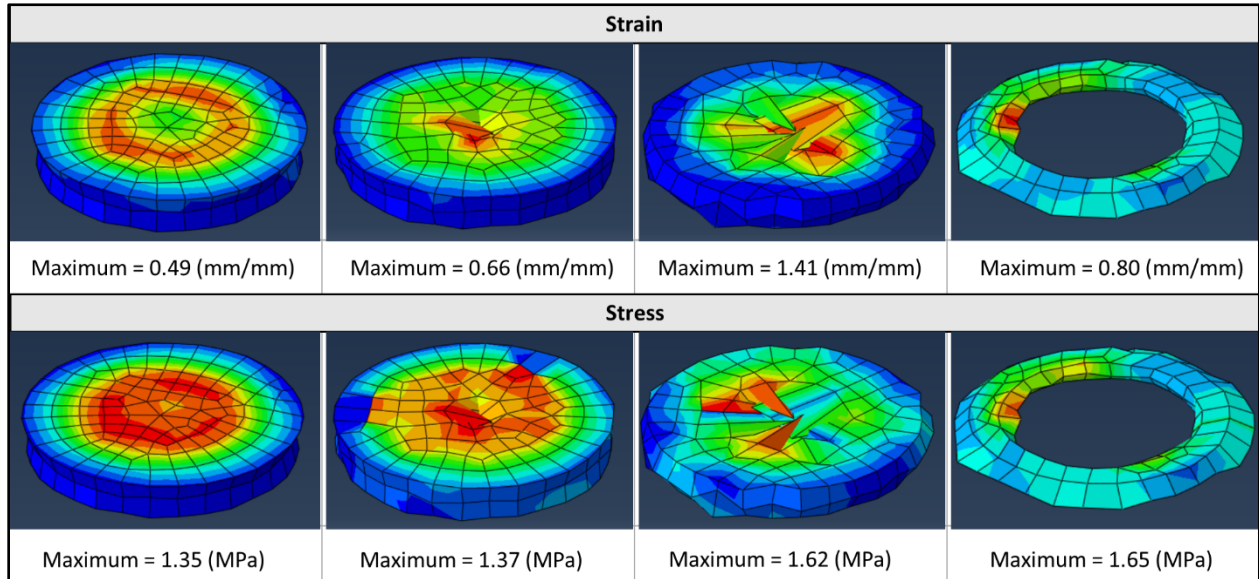
Figure C.18: The strain (top row) and stress (bottom row) contour plots for each circle geometry at the bottom of the impact. Moving from left to right the corresponding geometries are: no hole, 25% hole, 50% hole, and 75% hole. The red indicates areas of high strain and stress and the blue indicated areas of low strain and stress. The maximum strain and von mises stress on a single node is shown below the corresponding image and does not indicate the maxium values for the entire specimen.

Figure C.19: The strain (top row) and stress (bottom row) contour plots for each square geometry at the bottom of the impact. Moving from left to right the corresponding geometries are: no hole, 25% hole, 50% hole, and 75% hole. The red indicates areas of high strain and stress and the blue indicated areas of low strain and stress. The maximum strain and von mises stress on a single node is shown below the corresponding image and does not indicate the maxium values for the entire specimen.

In both Figure C.18 and Figure C.19, the holes of the 25% and 50% specimens were observed to be obsolete due to the stretching and overlap of the inner cells. Both the circle and the square geometry show an increase in the maximum strain as the hole size increase until the 75% hole. The increase in strain for both the circle and square geometry is significantly increased between the 25% hole and 50% hole when compared to the increase between no hole and 25% hole. When comparing maximum stress on a cell, the maximum stress continuously increases for the circle and increases until the hole becomes 50% for the square geometries.

The circle geometries (Figure C.18) illustrate that the stress and strain primarily occur in the center of the specimen. Thus, there is little stress and strain observed on the outer edge of the specimen, as indicated by the large blue ring on the outer specimen. As the geometric volume decreases (increase in hole size), the amount of global stress and strain increases. In comparison, the square geometries (Figure C.19) present stress and strain on a more global scale when compared to the circle geometries. This wider range of stress and strain could be the reason why the squares reduced the transmitted force better as there was more volume of material interacting in the energy absorption.

The contour plots of Figure C.18 and Figure C.19 draw attention to the areas where the strain and stress occur and show that they do not occur in the exact same way. For example, the no-hole circle

216

geometry shows a ring of strain halfway through the radius of the specimen, where as the stress contour plot displays a circle of stress at the center of the specimen. In addition, the strain had a higher concentration, or more severe colour contouring, at the center of the specimen where the hole was, whereas the same stress plot showed a larger contouring. This observation indicates that the cells in the center of the hole are absorbing more energy than the cells adjacent as they produce more strain for the same amount of stress. The increase of additional strain is likely the reason why the addition of a hole increases the energy absorption and reduces the transmitted force of the specimen.

As aforementioned, the 75% hole simulations are inaccurate, and the 75% specimens continued to deform past the bottom of the drop (the other specimens did not). The 75% specimens deformed to a point where the maximum strain reached 1.85 mm/mm for the circle and 1.57 mm/mm for the square and had a maximum stress of 1.76 MPa and 1.42 MPa for the circle and square, respectively. Figure C.20 illustrates an example of the maximum deformation of the 75% hole for the circle geometry. As visually indicated by Figure C.20, the 75% hole data is inaccurate due to the extreme deformation of the cells.
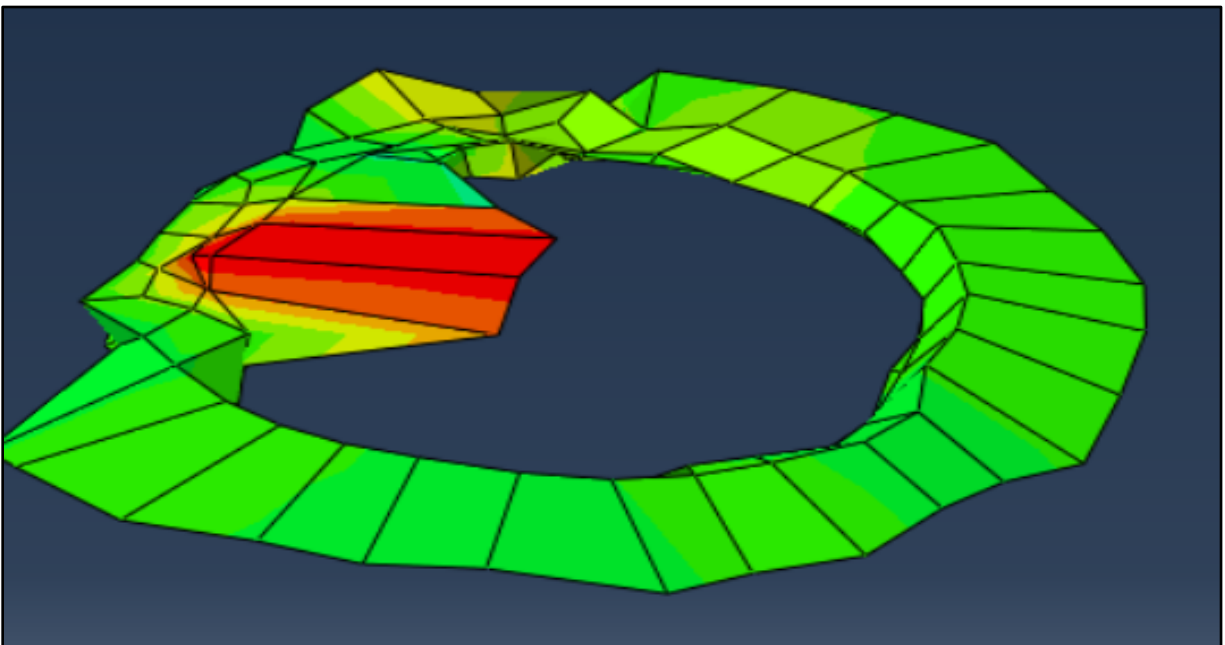
Figure C.20: The maximum deformation of the 75% hole circle geometry. As shown, the cells display extreme deformation, indicating that the simulation is inaccurate.

C.3.3 Summary of the Geometric Analysis
The simulation of the eight geometries show the importance to create a model with a failure criterion as the results for specimens with too small of an interaction volume, such as the 75% hole specimens,

produce inaccurate results as the cells of the mesh do not fail. Instead, the cells of the current preliminary model, infinitely stretch into irregular geometries that would not be observed in physical experiments as the cell would yield with the extreme deformation. Thus, the absence of a failure criterion prevents the accurate extrapolation of the data from the geometric analysis.

Although the data cannot be deemed accurate, there were some interesting observations and results from the geometric analysis. For example, squares performed better than circular geometries at reducing the transmitted force. This result could be due to the inaccuracies of the preliminary model; however, the visual analysis of the preliminary model suggests that the square geometries reduce the transmitted force more than the circles due to the greater number of cells that exhibit stress and strain. Thus, more strain and stress increase the area under the stress-strain curve, which correlates to the energy absorbed. The more energy the specimen absorbs, the better the specimen is at reducing transmitted force. The other observation that can be made, that was commensurate to the literature, was that the addition of a hole increases the energy absorption and decreases the transmitted force. The addition of the hole reduces the transmitted force as the hole increases the amount of strain that the geometry can exhibit (i.e., the cell walls are not inhibited by adjacent cells). The increase in strain allows for the material to use more area under the stress-strain curve, correlating to an increased energy absorption. The trade off point of the size of the hole and interaction volume was not able to be measured due to the lack of failure criterion in the preliminary model. Further development of the preliminary model is required to find the hole size-volume trade off as well as to confirm if the square geometry actually reduces the transmitted force better than the circle geometry. Manufacturing costs of the geometries will also need to be considered when selecting one over the other.

C.4 Summary

Table C.1: A summary of the research questions addressed in Appendix C and how they were evaluated.

Research Question	Method Used to Evaluate the Question	What was Learned
(5) What is the effect of geometry on transmitted force?	• Abaqus® • Drop testing	• Global strain on the specimen matters. If a geometry can increase the global strain it will reduce the transmitted force

		• Square geometries could perform better than circle geometries based on the output of transmitted force and the stress and strain observed in the simulation (simulation is not accurate)
(6) How can modelling be used to accurately predict a design's ability to reduce transmitted force?	• Abaqus® • HSV comparison • Drop testing	• The preliminary model was able to accurately simulate the visual appearance of deflections of a 6 mm thick TPR specimen tile measuring 84 mm x 54mm, when compared to the high speed videography. • The maximum transmitted force was obtained by adding the reaction forces on the bottom of the anvil in the preliminary model and plotting them against time. • The failure criterion for each material was not modelled. The lack of failure criterion was due to the lack of failure data available for the specific blend of materials tested. • Despite the lack of failure criterion, the preliminary model was able to predict the visual effects of the deformation for the specimen tested.

Appendix D : Abaqus® Modelling

D.1 Specifications of Abaqus® Model

Below is the code used to create the Abaqus® model for the 84 mm x 54 mm specimen of 25A TPR.

```
**
** PARTS
**

*Part, name=Anvil
*Element, type=C3D8R
*Nset, nset=Anvil-RefPt_, internal
*Surface, type=ELEMENT, name=anviltop
** Section: AnvilSection
*Solid Section, elset=_PickedSet6, material=Steel
,
*End Part
**

*Part, name=Striker
*Element, type=R3D4
*Nset, nset=Striker-RefPt_, internal
*Elset, elset=Striker, generate
*Element, type=MASS, elset=_PickedSet9_MassofStriker_
*Mass, elset=_PickedSet9_MassofStriker_
2.5,
*End Part
**

*Part, name=TPR
*Element, type=C3D8R
*Surface, type=ELEMENT, name=bottom
** Section: TPRSection
*Solid Section, elset=_PickedSet15, controls=EC-1, material="Thermoplatic Rubber"
,
*End Part
**
**
** ASSEMBLY
**
```

*Assembly, name=Assembly

**

*Instance, name=Anvil-1, part=Anvil

*End Instance

**

*Instance, name=Silicone_Sample-1, part=TPR

*End Instance

**

*Instance, name=Striker-1, part=Striker

*End Instance

**

*Nset, nset=BottomAnvil, instance=Anvil-1, generate

*Elset, elset=BottomAnvil, instance=Anvil-1, generate

*Nset, nset=Set-6, instance=Anvil-1

*Elset, elset=Set-6, instance=Anvil-1

*Surface, type=ELEMENT, name=_PickedSurf17, internal

*Rigid Body, ref node=Striker-1.Striker-RefPt_, elset=Striker-1.Striker

** Constraint: Nodetoanvil

*Coupling, constraint name=Nodetoanvil, ref node=_PickedSet20, surface=_PickedSurf17

*Kinematic

*End Assembly

**
** ELEMENT CONTROLS
**

*Section Controls, name=EC-1, DISTORTION CONTROL=YES, hourglass=ENHANCED
1., 1., 1.
**
** MATERIALS
**

```
*Material, name=Silicone

    *Density
    1100.,

    *Hyperelastic, mooney-rivlin, test data input, poisson=0.48

*Biaxial Test Data
 140000., 0.01
 270000., 0.02
 400000., 0.03
 520000., 0.04
 670000., 0.05
 760000., 0.06
 860000., 0.07
 970000., 0.08
 1.09e+06, 0.09
 1.19e+06, 0.1
 1.28e+06, 0.11
 1.39e+06, 0.12

*Uniaxial Test Data
 9000., 0.01
150000., 0.02
220000., 0.03
290000., 0.04
350000., 0.05
400000., 0.06
450000., 0.07
510000., 0.08
580000., 0.09
620000., 0.1
680000., 0.11
730000., 0.12

*Material, name=Steel

    *Density
    7800.,

    *Elastic
    2e+11, 0.25

*Material, name="Thermoplatic Rubber"

    *Density
    1200.,

    *Elastic
    1.8e+06, 0.4875
```

```
**
** INTERACTION PROPERTIES
**

*Surface Interaction, name=IntProp-1
    *Friction
    0.7,
**
** BOUNDARY CONDITIONS
**
** Name: BottomAnvil Type: Symmetry/Antisymmetry/Encastre

*Boundary
Set-6, ENCASTRE

** Name: RPMovement Type: Displacement/Rotation

*Boundary
_PickedSet15, 1, 1
_PickedSet15, 3, 3
_PickedSet15, 4, 4
_PickedSet15, 5, 5
_PickedSet15, 6, 6

**
** PREDEFINED FIELDS
**
** Name: StrikerVelocity   Type: Velocity

*Initial Conditions, type=VELOCITY
_PickedSet16, 1, 0.
_PickedSet16, 2, -2.
_PickedSet16, 3, 0.

**
** INTERACTIONS
**
** Interaction: GeneralContact

*Contact, op=NEW

*Contact Inclusions, ALL EXTERIOR

*Contact Property Assignment
 , , IntProp-1
```

```
** ----------------------------------------------------------------
**
** STEP: Impact
**
*Step, name=Impact, nlgeom=YES

*Dynamic, Explicit
, 0.01

*Bulk Viscosity
0.06, 1.2
**
** OUTPUT REQUESTS
**
*Restart, write, number interval=1, time marks=NO
**
** FIELD OUTPUT: F-Output-1
**
*Output, field, number interval=100

    *Node Output
    A, RF, U, V

    *Element Output, directions=YES
    BF, ENER, EVF, LE, PE, PEEQ, PEEQVAVG, PEVAVG, S, SVAVG

*Contact Output
CFORCE, CSTRESS
**
** HISTORY OUTPUT: H-Output-1
**
*Output, history, variable=PRESELECT
**
** HISTORY OUTPUT: BottomAnvil
**
*Output, history, time interval=2e-05

    *Node Output, nset=BottomAnvil
    RF2,

*End Step
```

D.2 Sensitivity Analysis for Material

The data collected to explore the sensitivity of Poisson ratio and coefficient of friction for the 25A TPR 84 mm x 54 mm specimens is shown in Table D.1 below. The increment column is defined as the number of data points taken in the 0.1 s simulation. The coefficient of friction was examined first and the first three groups of testing showed that increasing the coefficient of friction decreases the time for the drop to reach the bottom, creating a sharper impulse peak. The Poisson's ratio was examined with the first and last two batches of testing. Increasing the Poisson's ratio increased the transmitted force. The model was more sensitive (defined as magnitude of the change in transmitted force) to the changes in Poisson's ratio.

Table D.1: The data from the sensitivity analysis to fine tune the TPR 25 A 84 mm x 54 mm model. Changing the coefficient of friction had a small impact on transmitted force whereas changing the Poisson's ratio had a larger impact on transmitted force (i.e., the model was more sensitive to changes in Poisson's ratio).

Test Name	Coefficien	Poissons ratio	Density	Young's Modulus	Incrament	Time to KE =0 (ms)	KE max	KE finish	Transmitted Force (N)
TPR_a1	0.7	0.4875	1200	1800000	100	2.8	3.76016	3.72477	5910
TPR_a2	0.7	0.4875	1200	1800000	200	2.8	3.76016	3.72477	5935
TPR_a3	0.7	0.4875	1200	1800000	300	2.8	3.76016	3.72477	5827
TPR_a4	0.7	0.4875	1200	1800000	400	2.8	3.76016	3.72477	5857
TPR_a5	0.7	0.4875	1200	1800000	500	2.8	3.76016	3.72477	5858
								Average	5877.4
TPR_b1	0.6	0.4875	1200	1800000	100	2.9	3.30482	3.26565	5685
TPR_b2	0.6	0.4875	1200	1800000	200	2.9	3.30482	3.26565	5671
TPR_b3	0.6	0.4875	1200	1800000	300	2.9	3.30482	3.26565	5692
TPR_b4	0.6	0.4875	1200	1800000	400	2.9	3.30482	3.26565	5635
TPR_b5	0.6	0.4875	1200	1800000	500	2.9	3.30482	3.26565	5665
								Average	5669.6
TPR_c1	0.8	0.4875	1200	1800000	100	2.75	3.92153	3.88766	5910
TPR_c2	0.8	0.4875	1200	1800000	200	2.75	3.92153	3.88766	5818
TPR_c3	0.8	0.4875	1200	1800000	300	2.75	3.92153	3.88766	5891
TPR_c4	0.8	0.4875	1200	1800000	400	2.75	3.92153	3.88766	5841
TPR_c5	0.8	0.4875	1200	1800000	500	2.75	3.92153	3.88766	5920
								Average	5876
TPR_d1	0.7	0.48	1200	1800000	100	3	3.99364	3.97348	5512
TPR_d2	0.7	0.48	1200	1800000	200	3	3.99364	3.97348	5559
TPR_d3	0.7	0.48	1200	1800000	300	3	3.99364	3.97348	5419
TPR_d4	0.7	0.48	1200	1800000	400	3	3.99364	3.97348	5381
TPR_d5	0.7	0.48	1200	1800000	500	3	3.99364	3.97348	5545
								Average	5483.2
TPR_e1	0.7	0.495	1200	1800000	100	2.5	2.61613	2.56495	7101
TPR_e2	0.7	0.495	1200	1800000	200	2.5	2.61613	2.56495	7084
TPR_e3	0.7	0.495	1200	1800000	300	2.5	2.61613	2.56495	7130
TPR_e4	0.7	0.495	1200	1800000	400	2.5	2.61613	2.56495	7104
TPR_e5	0.7	0.495	1200	1800000	500	2.5	2.61613	2.56495	7113
								Average	7106.4

Appendix References

[1]Qiao P, Yang M, Bobaru F. Impact mechanics and high-energy absorbing materials: Review. Journal of Aerospace Engineering 2008 Oct 1,;21(4):235-248.

[2]Cetin E, Baykasoglu C. Energy absorption of thin-walled tubes enhanced by lattice structures. International Journal of Mechanical Sciences 2019 /07/01;157-158:471-484.

[3]Jones N. Energy-absorbing effectiveness factor. International Journal for Impact Engineering 2010 June;37(6):754-765.

[4]Guler MA, Cerit ME, Bayram B, Gerçeker B, Karakaya E. The effect of geometrical parameters on the energy absorption characteristics of thin-walled structures under axial impact loading. null 2010;15(4):377-390.

[5]Alavi Nia A, Haddad Hamedani J. Comparative analysis of energy absorption and deformations of thin walled tubes with various section geometries. Thin-Walled Structures 2010;48(12):946-954.

[6]Sulaiman S, AlHajji M, Jaafar CNA, Aziz FA, Zuhair T. Effect of composite material distribution and shape on energy absorption systems. null 2020:1-10.

[7]Zhang Z, Sun W, Zhao Y, Hou S. Crashworthiness of different composite tubes by experiments and simulations. Composites Part B: Engineering 2018;143:86-95.

[8]American national standard for performance and classification for impact resistant hand protection. . International Safety Equipment Association 2019 February.

[9]Granta Design Limited. Granta edupack . Level 3 2020;20.1.1.

[10]Harper CA. Handbook of plastics, elastomers, and composites. 4th ed. New York: McGraw-Hill; 2002.

[11]Friction and Friction Coefficients. Available from: https://www.engineeringtoolbox.com/friction-coefficients-d_778.html. [citedNov 6,2020] .